IRON CONTAINING LAYERED OXIDES FOR SODIUM ION BATTERY POSITIVE ELECTRODES

by

John S. Thorne

Submitted in partial fulfilment of the requirements
for the degree of Doctor of Philosophy

at

Dalhousie University
Halifax, Nova Scotia
June 2015

TABLE OF CONTENTS

LIST OF TABLES

LIST OF FIGURES

ABSTRACT

$Na_xFe_yM_{1-y}O_2$ phases with M = Mn, Ti, Sn, Co, $Co_{0.5}Ni_{0.5}$, Ni, and others including a P2-$Na_{2/3}Mn_{1/3}Fe_{1/3}Co_{1/3}O_2$ phase are synthesized and applied in Na-ion half cells for use as positive electrode materials. The potential use and application of Fe in Na-ion layered cathodes is explored. The feasibility of Fe for potential use in a commercial layered cathode material is assessed. On the basis of capacity retention, it is determined that the use of Fe in layered oxides may be prohibitive for commercial purposes unless coupled with Co in order to utilize high gravimetric and volumetric energy densities comparable to commonly used Li-ion systems. Using ^{57}Fe Mössbauer spectroscopy and a new model which aids in detection of Na-vacancies, it is found that Na vacancies in the Na layer have a measureable affect the quadrupole splitting of edge sharing octahedral Fe^{3+} sites. Using this model, it is hypothesized that the position of Na-vacancies during insertion and extraction play a key to stabilization of Fe in the transition metal layer when large amounts of Na are inserted and extracted from the host structures. Future directions for realization of commercial Fe-containing layered oxides are discussed.

LIST OF ABBREVIATIONS AND SYMBOLS USED

c	speed of light
°C	degrees Celsius
CE	coulombic Efficiency
CS	centre shift
C/10	10 hour discharge current
C/20	20 hour discharge current
dQ/dV	differential capacity
e	charge of an electron
eV	electron volt (unit)
E_γ	gamma ray energy
E_D	Doppler effect energy
E_K	thermal energy
E_R	recoil energy
EV	Electric Vehicle
FWHM	Full Width at Half Maximum
g/cc	grams per cubic centimeter
HWHM	Half Width at Half Maximum
I	Spin
ICP	Inductively Coupled Plasma
Li-ion	Lithium Ion
M	Mass or Transition Metal
mAh/cm^3	milliamp hours per cubic centimeter
mAh/g	milliamp hours per gram
mm/s	millimeters per second
Wh/kg	watt hour per kilogram
n	integer
Na-ion	Sodium Ion
ns	nanosecond

O3	3 layered transition metal oxide with octahedral environment around alkali atom (Delmas notation)
P2	2 layered transition metal oxide with prismatic environment around alkali atom (Delmas notation)
$P(E_\gamma)$	probability of gamma ray energy
QS	quadrupole splitting
SEI	Solid Electrolyte Interface
T	Temperature
V	Voltage
v	velocity
W	Watts
Wh/L	Watt hour per liter
x	atomic fraction Na or Fe
XRD	X-ray Diffraction
y	atomic fraction Fe
μ	chemical potential
λ	wavelength
θ	Bragg angle
ω	angular frequency
$\hbar$	Planck's constant
$\Psi_S(0)$	wave function at the nucleus

ACKNOWLEDGEMENTS

The author would like to thank his supervisors, Dr. Mark Obrovac and Dr. Richard Dunlap, for several conference opportunities and for providing equipment. Thanks to Dr. Jeff Dahn for use of the Mazerustar. Saptarshi Chowdhury was responsible for synthesis of the O3- $Na_xFe_xTi_{1-x}O_2$. David Dvorak and Chris Lee were very helpful for finalizing correct methods of synthesis for reliable formation of many novel layered oxide compositions (including $Na_{2/3}Mn_{1/3}Fe_{1/3}Co_{1/3}O_2$).

CHAPTER 1 INTRODUCTION

High energy density batteries made from inexpensive sustainable resources would be attractive for a number of applications, including automotive and grid storage. Such applications require batteries capable of excellent coulombic efficiency (>99.99%) and structural stability of the electrode materials. Na-ion batteries are a possible candidate technology for these applications. Major research in Na-ion batteries began in the 1980's [1-3], but research interest decreased as Li-ion batteries gained prominence [4-7, 8]. Because of heightened environmental concerns and new markets for secondary batteries in consumer electronics, grid storage and automotive applications, there has been a renewed research interest in Na-ion batteries in recent years, especially those which comprise electrodes made from sustainable inexpensive materials [9, 10]. Figure 1.1 shows accelerating research activity in Na-ion batteries between 2006 and 2014.

A necessary objective for widespread commercial application of Na-ion batteries is to achieve cost reduction in comparison to Li-ion batteries without substantially affecting the volumetric energy density and cycling capability. Achieving high gravimetric energy density is a secondary objective. Na-ion batteries with lower volumetric energy density and excellent cycling capability may also be applicable to grid energy storage. Iron based cathode materials are of particular interest because of the abundance and low cost of iron. While Fe^{3+} and Li^{+} cations tend to mix in lithium iron oxides [11], Fe^{3+} and Na^{+} have less tendency to mix. The P2-phase of $Na_{2/3}Fe_{1/2}Mn_{1/2}O_2$ has been reported to have an energy density over 500 Wh/kg [9] utilizing materials which are among the most abundant and

inexpensive on earth. This represents a promising step toward sustainable high energy density battery chemistries.

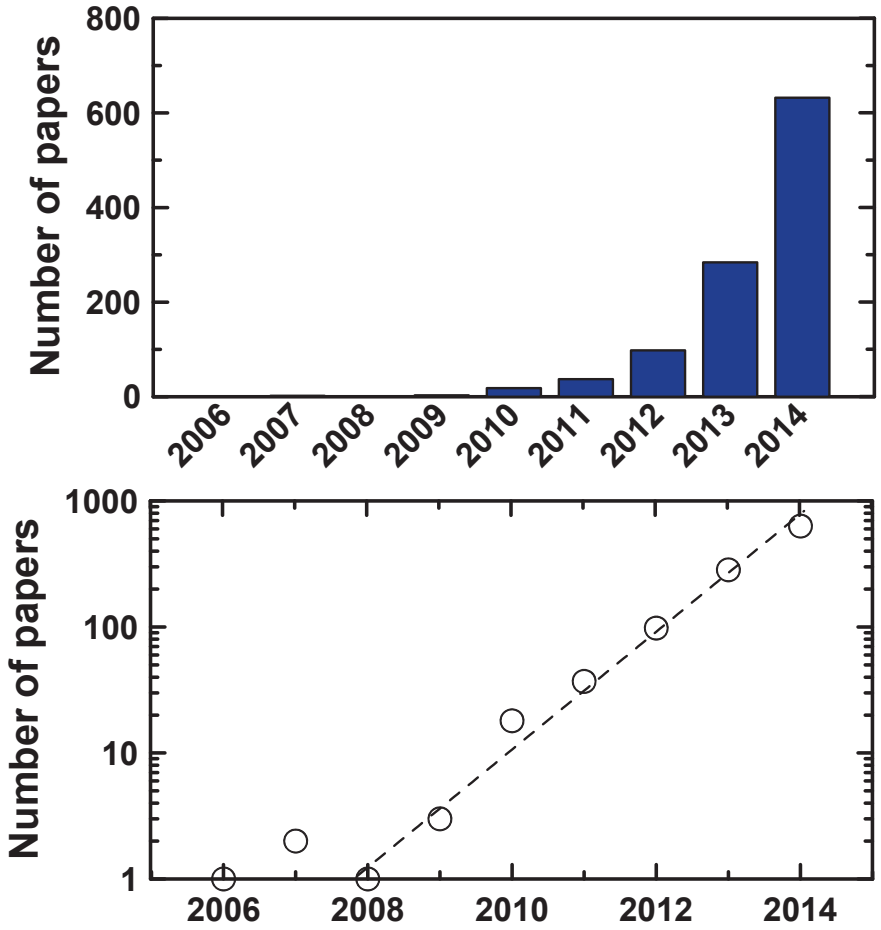

Figure 1.1: Number of papers located with keyword "Na-ion batteries" between 2006-2014 in the Google Scholar database (retrieved January 31st, 2015). A best fit line using an exponential function is shown for comparison.

Layered Na-ion cathode materials have been explored with energy densities in the 1100-1800 Wh/L (275-375 Wh/kg) range, including $NaCrO_2$ [12], $NaNi_{1/2}Mn_{1/2}O_2$ [13], $NaVO_2$ [14], and $NaFe_{1/3}Mn_{1/3}Ni_{1/3}O_2$ [15]. Higher energy densities around 2000 Wh/L

(500 Wh/kg) (compared to 3000 Wh/L for $LiCoO_2$) have been achieved with $NaNi_{1/2}Mn_{1/2}O_2$ [13], $NaMnO_2$ [16] and P3-$NaCoO_2$ [17] materials, but sufficient capacity retention has not been shown. Many other candidate P2 and O3 layered Na_xMO_2 cathodes for Na-ion batteries have been reported [18] including P2-Na_xCoO_2 [19-21], $Na_xMn_yCo_{1-y}O_2$ [22-25], O3- or P2- $Na_xFe_{1/2}Mn_{1/2}O_2$ [9] and $Na_xMn_yFe_{1-y}O_2$ [26-30]; Fe containing O3- $NaFe_{1/2}Co_{1/2}O_2$ [31], $NaFe_yNi_{1-y}O_2$ [32, 33], $NaNi_{1/3}Co_{1/3}Fe_{1/3}O_2$ [34], and $NaNi_{1/3}Mn_{1/3}Fe_{1/3}O_2$ [15]; and various $Na_xFe_yMn_{1-y-z}Ni_zO_2$ [35, 36] compounds. These have also been reported in full cells with anodes including hard carbon and SnSb-based materials [37-39]. New chemistries are showing great promise in development of 3 V Na-ion layered cathodes with high energy densities [40-42]. A number of Fe-containing layered cathodes with high energy densities have been reported including P2- $Na_{2/3}Fe_{1/2}Mn_{1/2}O_2$ [9] and P2- or O3- $Na_xMn_yFe_{1-y}O_2$ [27-29, 43, 44], Fe containing O3- $NaFe_{1/2}Co_{1/2}O_2$ [31], $NaFe_yNi_{1-y}O_2$ [33, 45], $NaFe_{1/3}Co_{1/3}Ni_{1/3}O_2$ [34], and $NaMn_{1/3}Fe_{1/3}Ni_{1/3}O_2$ [15]; and various $Na_xFe_yMn_{1-y-z}Ni_zO_2$ [35, 36, 46] compounds.

O3- $NaNi_{0.5}Ti_{0.5}O_2$ was recently reported, cycled between 2.0-4.0V which is assumed to have Ni^{2+} and Ti^{4+} oxidation states in the prepared material [41]. This is analogous to the $NaNi_{0.5}Mn_{0.5}O_2$ material in which the Ni was measured to be in the 2+ state while the Mn was found to be inactive in the 4+ state [13]. Since $Ti^{4+} \leftrightarrow Ti^{3+}$ occurs at much lower voltages in this system [47, 48], this sample is presumed to be driven by the $Ni^{2+} \leftrightarrow Ni^{4+}$ redox couple and 75% capacity retention after 300 cycles was achieved in Na half cells [41].

The addition of Fe to $NaNi_{0.5}Ti_{0.5}O_2$ [41] to produce $NaFe_x(Ni_{0.5}Ti_{0.5})_{1-x}O_2$ was recently reported [49], where the Fe is presumably in the 3+ state while the Ni and Ti are presumably in the divalent and tetravalent states, respectively. It was found that samples with x = 0.2 and x = 0.4 had electrochemical features similar to those reported for $NaNi_{0.5}Ti_{0.5}O_2$ [41]. Maximum achieved capacity retention was 72% after 75 cycles in Fe substituted $NaFe_{0.4}(Ni_{0.5}Ti_{0.5})_{0.6}O_2$ [49] despite a reduced voltage range of 2.6-3.75 V in the Fe-containing samples. Improvement is observed when the electrolyte salt was switched from $NaClO_4$ to sodium bis(fluorosulfonyl)imide (NaFSI) in Na half cells. Choice of electrolyte has the potential to significantly alter results in Na-half cells. For example, use of fluoroethylene carbonate (FEC) in propylene carbonate (PC) containing electrolytes improves reversibility in $NaNi_{1/2}Mn_{1/2}O_2$ Na-half cells [50]. Reactivity and degradation of the Na foil may influence cycling performance [50, 51].

Recently, a series of $NaNi_{0.4}Fe_{0.2}Mn_{0.4-x}Ti_xO_2$ was reported with x = 0, 0.2 and 0.4 [52]. The best capacity retention is achieved in this series in a 2.0-4.2 V window when x = 0.2, with 84% capacity retention achieved after 200 cycles. Mn and Ti are presumably in the 4+ state, the Ni in the 2+ state and the Fe in the 3+ state in the prepared material, where 80% of the theoretical capacity is attributed to the $Ni^{2+} \leftrightarrow Ni^{4+}$ couples. Stable ternary or quaternary Fe, Mn and Ti containing Ni-based electrodes may be primarily driven by the $Ni^{2+} \leftrightarrow Ni^{4+}$ redox couple. Further work is needed to confirm the oxidation states of the transition metal in these systems and to determine whether or not $Fe^{3+} \leftrightarrow Fe^{4+}$ is active during cycling.

Recently the quaternary $NaMn_{1/4}Fe_{1/4}Co_{1/4}Ni_{1/4}O_2$ electrode was reported [53]. The presence of Mn in the 4+ state enables the Ni to be in the 2+ state, while Fe and Co are both in the 3+ state. The use of Mn^{4+} or Ti^{4+} in the synthesized material coupled with Ni^{2+} may be useful to avoid low voltage regions associated with reversible the $Mn^{3+} \leftrightarrow Mn^{4+}$ redox couple [9, 10, 27], which results from using Mn^{3+} in the synthesized material, or reversible $Ti^{3+} \leftrightarrow Ti^{4+}$ [47, 48, 54, 55] when Ti^{3+} is used, and instead replace them with reversible $Ni^{2+} \leftrightarrow Ni^{4+}$.

Electrochemical performance of $NaFeO_2$ is adversely affected by the formation of Fe^{4+} [56]. Voltage hysteresis becomes a significant factor when the upper cutoff is extended beyond 3.4 V due to an increasing number of Na vacancies, resulting in what is hypothesized to be migration of Fe ions from the transitional metal layer (3a site) to the Na layer (3b and/or 6c sites) [56]. The substitution of other transition metals is necessary to attempt to stabilize or eliminate use of the $Fe^{3+} \leftrightarrow Fe^{4+}$ redox couple during cycling, especially at higher voltages, and instead replace it with $M^{3+} \leftrightarrow M^{4+}$ or $M^{2+} \leftrightarrow M^{4+}$ or other. This has been achieved by substitution of some of the iron in α-$NaFeO_2$ with other transition metals. Preferably these transition metals should also be low cost and earth abundant, as in the case of P2-type $Na_{2/3}Fe_{1/2}Mn_{1/2}O_2$ (~2182 Wh/L vs. Na), which has a high reversible energy density comparable to $LiMn_2O_4$ (~2060 Wh/L vs. Li) [9], but is still significantly less than $LiCoO_2$ (~3000 Wh/L). Mn substitution for Fe stabilizes the layered structure during cycling, although further improvements are needed for use in most practical applications. Fe^{4+} appears to be a source of capacity fade in Na_xFeO_2 [56],

$Na_xMn_yFe_{1-y}O_2$ [27] and $Na_xFe_yNi_{1-y}O_2$ [33] and other systems. In $NaFe_zNi_{1-z}O_2$ it was found that Fe and Ni are both 3+ in the prepared materials, and used mixed simultaneous $Ni^{3+} \leftrightarrow Ni^{4+}$ and $Fe^{3+} \leftrightarrow Fe^{4+}$ redox couples during cycling [33]. A study of the available literature supports the conclusion that Fe^{4+} is a source of capacity fade in the $NaNi_yFe_{1-y}O_2$ solid solution series when Ni is in the 3+ state ($0 \leq y \leq 1$) [33, 45, 57]. $Na_xFe_xTi_{1-x}O_2$ samples will be discussed in this thesis with Fe^{3+} and Ti^{4+} oxidation states in the starting material [54]. It was found that the $Fe^{3+} \leftrightarrow Fe^{4+}$ redox couple is raised to over 4 V when $x = 0.75$, compared to 3 V for $NaFeO_2$, and is a source of capacity fade, while the use of $Ti^{3+} \leftrightarrow Ti^{4+}$ and/or $Fe^{2+} \leftrightarrow Fe^{3+}$ redox couples below 2 V appear to result in good capacity retention. This was exactly analogous to the $Na_xFe_xMn_{1-x}O_2$ system, where the $Mn^{3+} \leftrightarrow Mn^{4+}$ redox couple (or $Fe^{2+} \leftrightarrow Fe^{3+}$ redox couple) appears to have better cycling stability than the $Fe^{3+} \leftrightarrow Fe^{4+}$ redox couple [27].

In the above survey, a number of new phases have been introduced as potential positive electrode materials having good gravimetric and volumetric energy densities in Na-ion half cells, but sources of instability during cycling are not frequently discussed. In order to achieve commercial applicability of iron-containing layered cathodes, sources of capacity fade in these materials must be systematically identified and eliminated. In this thesis, viability of the active $Fe^{3+} \leftrightarrow Fe^{4+}$ redox couple is evaluated when coupled with other transition metals. When necessary, ^{57}Fe Mössbauer effect spectroscopy is used to help determine if Fe is active in the material.

In one approach suggested in this thesis, iron could be used as an inactive filler atom in layered sodium transition metal oxide cathodes [27, 58]. In other words, the Fe in the layered oxide would only be present to maintain the layered crystal structure, but would not contribute to the electrochemistry and would remain in the Fe^{3+} oxidation state during cycling. However, it has been observed that in the binary $Na_xFe_yM_{1-y}O_2$ solid solutions, (where M = Mn, Ni, Co, Ti, and Cr) the Co might be effective to stabilize the $Fe^{3+} \leftrightarrow Fe^{4+}$ redox couple and has the highest energy density, and approaches that of layered Li-ion systems [31]. $NaFe_yCo_{1-y}O_2$ has exceptional theoretical volumetric and gravimetric energy density at voltages below 4.0 V, with y = 0.5 on the order of 2400 Wh/L (approaching 80% of the energy density of $LiCoO_2$) and has very good rate capability. With preliminary values of coulombic efficiencies in Na half cells approaching 0.995 or higher, this system appears very promising for the development of commercially feasible Fe-containing Na-ion batteries [31, 59]. In $Na_yMn_{1/3}Fe_{1/3}Co_{1/3}O_2$, evidence of Fe^{4+} was measured at 4.1 V using ^{57}Fe Mössbauer spectroscopy, with 76 mAh/g discharge capacity and excellent capacity retention achieved using the mixed simultaneous $Fe^{3+} \leftrightarrow Fe^{4+}$ and $Co^{3+} \leftrightarrow Co^{4+}$ couples, which resulted in 100% capacity retention in a 50 cycle test [60].

This thesis presents an overview of the available systematic studies on Fe-containing layered oxides and presents a number of novel layered oxide materials applied as a positive electrode material in Na-ion half cells. In Chapter 2, a brief overview of the theory necessary to understand the results of the thesis is presented. Chapter 3 provides an overview of the experimental procedures used to produce and study novel layered Fe-containing oxides.

In Chapter 4, comments are made regarding the moisture sensitivity of $NaFeO_2$ which is important to consider when working with Fe-containing cathodes. Additionally, a new model is introduced for analysis of ^{57}Fe Mössbauer spectra in charged $NaFeO_2$ which shows that introduction of Na vacancies has a measureable effect on the Fe environment. This model is later used to analyse materials charged in a Na-ion half cell, in which Na has been deintercalated from the host structure.

Chapter 5 presents a study of materials having composition $Na_xFe_xMn_{1-x}O_2$ with $0.5 \leq x \leq 1$. The Mössbauer model presented in Chapter 4 is used. It is shown that the substitution of Mn atoms in place of Fe in metal oxide layers is associated with significant stabilization of the structure during cycling. If acceptable coulombic efficiency can be achieved, these materials may be highly effective for commercial use in sustainable Na-ion batteries. Here the structural stabilization of iron-containing cathode materials by substitution with titanium to produce $Na_xFe_xTi_{1-x}O_2$ is also studied [54], along with ^{57}Fe Mössbauer effect spectra of as-synthesized and cycled materials. Earlier structural studies of this system showed that a single-phase O3 structure is maintained when $x \geq 0.72$ [61]. No previous Mössbauer or electrochemical studies on this system have been reported. In this study electrochemical cycling of these materials results in good cycling only when the voltage is restricted so that the $Fe^{3+} \leftrightarrow Fe^{4+}$ redox couple is not utilized, as determined by Mössbauer spectroscopy. This is shown to be analogous to the electrochemical behaviour of $Na_xFe_xMn_{1-x}O_2$ and $Na_xFe_xSn_{1-x}O_2$ materials [27].

Chapter 6 presents the effects of adding Fe to a new O3-$NaNi_{0.5}Co_{0.5}O_2$ solid solution, investigated in a series of $NaFe_x(Ni_{0.5}Co_{0.5})_{1-x}O_2$ samples with $0 \leq x \leq 0.5$. In previous work by Delmas, O3-$NaNi_{0.6}Co_{0.4}O_2$ was synthesized as a novel material and deintercalated to produce x = 0.80 and 0.58 samples. This material operates on the $Ni^{3+} \leftrightarrow Ni^{4+}$ redox couple. $NaFe_{1/3}Co_{1/3}Ni_{1/3}O_2$ was reported as a new cathode material [34] and utilizes the $M^{3+} \leftrightarrow M^{4+}$ redox couples with M = Fe, Co and Ni and has comparable energy density to the $NaFe_yCo_{1-y}O_2$ system when cycled to 4.2 V. In order to economically use Fe in a cathode material, minimization of Co is desired. In this light, a direct comparison is made between samples of $NaFe_xCo_{1-x}O_2$ and $NaFe_x(Co_{0.5}Ni_{0.5})_{1-x}O_2$ for x = 0.4 and 0.5, to observe effects of replacing Co with Ni.

The use of Co may be necessary to implement stable cycling of the $Fe^{3+} \leftrightarrow Fe^{4+}$ couple. An example is demonstrated in Chapter 7 by introduction of Fe to the P2-$Na_xMn_yCo_{1-y}O_2$ system in the form of the novel P2-$Na_{2/3}Mn_{1/3}Fe_{1/3}Co_{1/3}O_2$ material. Replacement of Co with Mn in P2-Na_xCoO_2 effectively suppresses formation of voltage plateaus resulting from Na ordering during discharge [24]. It is suggested that introduction of Mn into the $NaFe_yCo_{1-y}O_2$ system may have similar effects [31]. P2-$Na_xMn_{1/3}Fe_{1/3}Co_{1/3}O_2$ yields electrochemical properties similar to P2-$Na_xMn_{1/2}Co_{1/2}O_2$ [24], and surprisingly, capacity retention is maintained or improved by use of the $Fe^{3+} \leftrightarrow Fe^{4+}$ couple. The new P2-$Na_{2/3}Mn_{1/3}Fe_{1/3}Co_{1/3}O_2$ phase has average voltage 3.00 V (1.5-4.5 V) and an investigation of its electrochemical properties in Na half cells as a potential 500 Wh/kg (~ 2240 Wh/L) class positive electrode was conducted.

In Chapter 8, an overall assessment of these systems and other Fe-containing layered oxide systems is presented. With the combined results, Chapter 9 suggests future directions for Fe-containing layered cathodes for Na-ion batteries on the basis of capacity retention and energy density.

CHAPTER 2 THEORY

2.1 X-RAY DIFFRACTION

X-ray diffraction (XRD) is primarily used in this thesis to determine which layered phase or phases are present in synthesized materials. The XRD apparatus used corresponds to the theta-theta Bragg-Brentano geometry, in which the sample is in a fixed position and the X-ray source and detector positions are varied at constant distance from the sample with equal angle θ. Plots of the XRD patterns are expressed as intensity vs. scattering angle (2θ).

2.1.1 Bragg's Law

Consider incident X-rays reflected specularly from parallel lattice planes of a crystal, each separated by a distance d. Bragg's law of reflection is given by,

$$2d \sin\theta = n\lambda \qquad (2.1),$$

where θ is the incident angle of the X-ray beam, n is an integer and λ is the wavelength of the incident X-rays. For a given d and λ, equation 2.1 is only satisfied for particular angles θ and must be satisfied for reflected X-rays to interfere constructively. Otherwise, the reflected beams from each layer of the lattice interfere destructively [62]. Bragg's law

follows simply by considering the path length difference of the incoming and outgoing X-rays, illustrated in Figure 2.1.

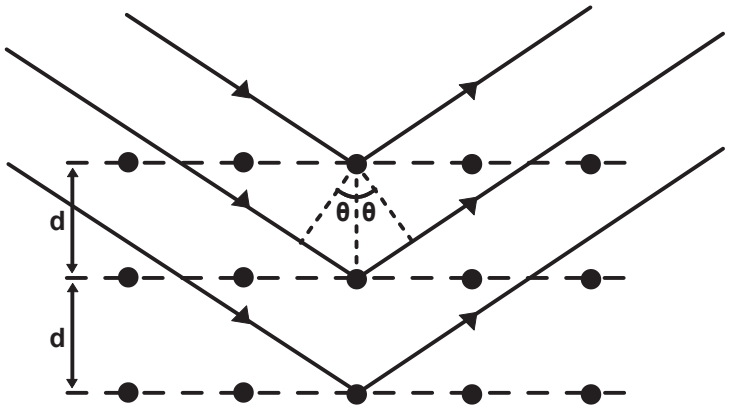

Figure 2.1: Schematic illustrating Bragg's law of diffraction, which comes from the difference in path length reflected from parallel lattice planes of a crystal.

2.1.2 Rietveld Refinement and the Bragg R-Factor

Methods first described by Hugo Rietveld [64, 65] are used to fit the XRD patterns presented in this thesis. Rietveld refinement was done using the Rietica software [66] which uses the following equation to calculate the diffraction pattern:

$$I_i = I_{ib} + \sum G_{ik} I_k \qquad (2.2),$$

where *Ii* is the intensity calculated at point *i*, I_{ib} is the calculated background at point i, and G_{ik} is a normalized pseudo-Voigt peak profile function for the k^{th} Bragg reflection,

and I_k, is the intensity of the k^{th} Bragg reflection. The intensity of the k^{th} Bragg reflection is given by:

$$I_k \propto L_k \left| F_k \right|^2 \qquad (2.3).$$

I_k is proportional to the Lorentz polarization factor L_k and the structure factor F_k. For incident unpolarized electromagnetic radiation, the scattering amplitude is proportional to the sine of the Bragg angle. Additionally, the scattering amplitude is dependent on the geometry of powder X-ray diffraction experiment. The polarization factor can be shown to be:

$$L = \frac{1 + \cos^2(2\theta)}{2\sin(2\theta)} \qquad (2.4),$$

which serves to reduce the intensity of the observed diffraction peaks at higher Bragg angle θ. The structure factor F_k is given by:

$$F_k = \sum f_j \exp(2\pi i(hx_j + ky_j + lz_j)) \qquad (2.5),$$

where f_j is the atomic scattering factor of the j^{th} atom, h, k and l are the Miller indices and x_j, y_j and z_j are the atomic coordinates of the j^{th} atom. The atomic scattering factor can be determined by:

$$f = \int \rho(r) e^{iQ \cdot r} d^3 r \qquad (2.6),$$

where $\rho(r)$ is assumed to be the density of a spherically symmetric scatterer, a function of position r, and Q is the momentum transfer. The Bragg R-Factor is used as a measure of goodness of fit of selected XRD patterns presented in this thesis. The Bragg R-Factor is defined by:

$$R = \frac{\sum |I_{obs} - I_{calc}|}{\sum I_{obs}} \qquad (2.7),$$

where I_{obs} and I_{calc} are the observed and calculated intensity summed over all points in the XRD pattern, respectively. This sum is expressed as a fraction.

2.2 ^{57}Fe MÖSSBAUER SPECTROSCOPY

Mössbauer effect spectroscopy is most commonly applied to iron containing materials but is also less frequently applied to other elements such as Sn and Sb. The Mössbauer effect in Fe is a valuable tool for probing the chemical environment and oxidation state of Fe-ions in Fe-containing materials.

In the case of ^{57}Fe Mössbauer spectroscopy, gamma rays produced from a source cause excitation of iron nuclei in the sample. These originate from metastable ^{57}Co (total spin 7/2), seen in Figure 2.2, which has a half-life of about 270 days. This decays to the unstable second excited state of ^{57}Fe (total spin 5/2) by electron capture. After decaying to the first excited state (total spin 3/2) a short time later, ^{57}Fe decays to the ½ state with a

half-life of about 100 ns. It is the transition from the first excited state (total spin 3/2) to the ground state (total spin 1/2) of ^{57}Fe which is used for Mössbauer spectroscopy.

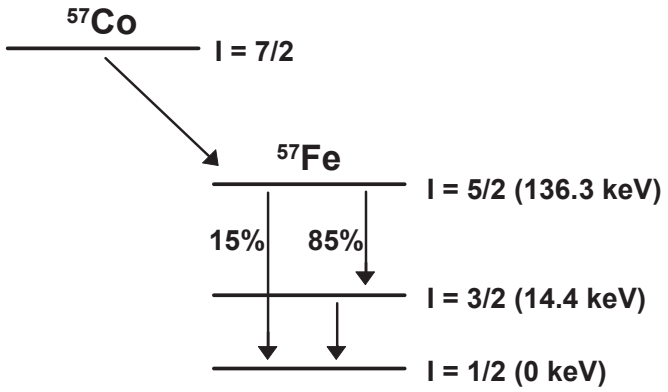

Figure 2.2: Decay scheme for ^{57}Fe, with spin, excited state energies, and the branching fractions. The 3/2 → 1/2 transition is the Mössbauer transition of interest. Adapted from previous work [67].

2.2.1 Recoil Free Fraction

When a photon is emitted from the nucleus of a free atom, conservation of energy and momentum state that the atom will recoil opposite to the momentum of the photon. The difference between nuclear transition energy and the emitted gamma ray photon is given by

$$E - E_{\gamma} = E_R + E_D \qquad (2.8),$$

the recoil energy E_R plus a Doppler effect energy E_D. The average Doppler effect energy over many events $<E_D>$ is given by [68],

$$\langle E_D \rangle = 2\sqrt{E_{Kavg} E_R} \qquad (2.9)$$

where the recoil energy is given by,

$$E_R = \frac{E_\gamma^{\,2}}{2Mc^2} \qquad (2.10)$$

and the average thermal energy is given by,

$$\langle E_K \rangle \approx 0.5 k_B T \qquad (2.11).$$

The Doppler shift in the gamma ray energy is caused by combinations of the recoil of the atom and random thermal motion. For a gas in which the emitter and absorber are both free atoms, the energy distributions of the emitted and absorbed gamma rays are shifted by the recoil energy. The mean width of the energy distribution is given by $<E_D>$.

Since the energy of the gamma ray must be exactly equal to the transition energy in the absorber in order to have resonance, this will only occur when the energy distributions of the emitter and absorber overlap. In general, the fraction of the overlap region is small [69]. In general, the recoil energy E_R is similar to the mean width $<E_D>$. Calculation of

the recoil energy using the mass for a ^{57}Fe atom, $E\gamma$ = 14.4 keV and T = 300 K yields E_R ≈ 10^{-3} eV, which corresponds to $\langle E_D \rangle \approx 10^{-2}$ eV. In the case of Fe, free atom absorption is non negligible. If atoms of the emitter are bound to a lattice, then the recoil mass effectively becomes that of the entire crystal, thus increasing M in equation 2.5 by factor of 10^{15} or more. For Fe, the proportional decrease in E_R reduces the value of E_R to 10^{-18} eV or less with corresponding $\langle E_D \rangle$ of 10^{-10}. The recoil energy is significantly less than the mean width.

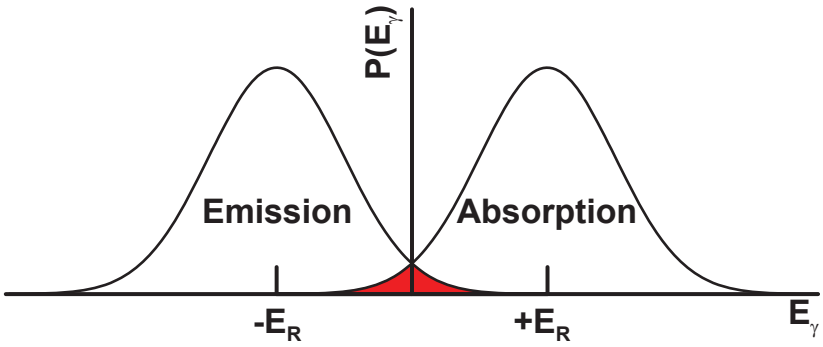

Figure 2.3: Diagram showing the distributions of energies produced from a recoiling nuclear emitter and absorber at finite temperature, with the overlap region highlighted in red. Not to scale. Adapted from previous work [68].

However, since recoil energies are on the same order as the lattice vibration phonon energies, a fraction of the emitted gamma rays will transfer a phonon with an energy $\hbar\omega$ to the lattice. Over many emission processes, the fraction of recoil-free events is given by

$$f = 1 - \frac{E_R}{\hbar\omega} \qquad (2.12)$$

[68]. For Fe, the existence of the recoil-free fraction affords a resolving power much less than 10^{-9} eV (i.e. the Heisenberg natural line width). This corresponds to a full width at half maximum (FWHM) of about 0.2 mm/s on the velocity scale. This is significantly less than energies from thermal effects ($<E_K>$ ~10^{-2} eV) or the free atom recoil energy (~10^{-3} eV for an Fe atom). Recoil-free fractions vary between materials depending on their properties. More in-depth descriptions for calculation of the recoil free fraction based on the Einstein and Debye-Waller models are found in the literature [68, 70].

2.2.2 Centre Shift

The actual energy of the transition between the ground and excited states is affected by the non-zero s-electron density in the nucleus. Changing the total electronic charge over the volume of the nucleus alters the coulombic potential at the nucleus and therefore the electron-nucleus interaction energy. This changes the 1/2 $\leftrightarrow$ 3/2 transition energy shown in Figure 2.3. The integral of the electron density over the volume of the nucleus is primarily affected by two things: first, excitation to the 3/2 state induces a volume change in the finite-sized nucleus, in turn altering the nucleus-electron interaction energy and the transition energy. Second, the chemical environment of the absorber atoms causes a change to the wave function of the s-electrons due to screening effects from p- and d-electrons and by bond formation. The source is Doppler shifted over a range of about ± 9 mm/s to ensure overlap of the emitter and absorber energies, which may even occur in higher values of the Doppler shift in some magnetic phases. The energy shift and

corresponding Doppler velocity *v(t)*, as determined by the time dependent velocity of the source material, are related by,

$$E_{shift}(t) = \frac{E_\gamma v(t)}{c} \qquad (2.13).$$

The deviation of isomer shift (also known as the centre shift at 0 K) of the absorber and the source (in mm/s) is given by,

$$CS = const \times \delta R \times \left(|\psi(0)_A|^2 - |\psi(0)_S|^2 \right) \qquad (2.14),$$

where δR is the change in the radius of the nucleus and $|\psi(0)_A|^2$ - $|\psi(0)_S|^2$ is the difference in the electron density (primarily due to s-electrons) in the absorber and source nuclei, respectively [68]. The centre shift is measured at temperatures higher than 0 K and is temperature dependent. For Fe, the sign of δR has been determined to be negative [70]. The sign and magnitude of the centre shift depends on $|\psi(0)_A|^2$, the electron density at the nucleus of the absorber.

For the purposes of this work, historical values of centre shifts are used as starting parameters in fitted Mössbauer spectra to estimate the amount of Fe^{3+} or Fe^{4+} contained in layered Fe-containing oxides such as Na_xFeO_2. Centre shifts of Fe^{2+}, Fe^{3+} and Fe^{4+} in similar layered materials have been clearly distinguished based on previous experimental results [71, 72, 73], with Fe^{3+} typically in the range of 0.15-0.4 mm/s and Fe^{4+} around 0

mm/s. In general, no clear or simple relationship between the number of d-electrons and the s- electron density at the nucleus has been determined.

2.2.3 Quadrupole Splitting

Electric quadrupole splitting can occur in nuclei with total spin greater than 1/2, for which the nucleus has a non-spherical charge distribution. When the electric potential about the centre of the non-spherically symmetric nucleus is expanded into a series of multipoles, the interaction energy resulting from the monopole and quadrupole term is non-zero. The dipole term and higher order terms are small or zero and the monopole term determines the centre shift. In the presence of an electric field gradient the quadrupole interaction energy of the nucleus is different for each orientation of the nucleus. The eigenvalues to the Hamiltonian posed by this problem are given by [68],

$$E_{QS} = e^2 Qq \frac{3I_Z{}^2 - I(I+1)}{4I(2I-2)} \qquad (2.15).$$

Where e is the charge of a proton and Q is the nuclear quadrupole moment. For a nucleus of total spin I in spin state I_z. For the I = 1/2 state, there is only one solution for sub states $I_z = \pm 1/2$. For the I = 3/2 state there are two solutions for substates $I_z = \pm 1/2$ and $\pm 3/2$, with the order of the 1/2 and 3/2 substates determined by the sign of the nuclear quadrupole moment. Splitting of the excited state is illustrated in Figure 2.4. Larger quadrupole splittings can occur, for example, in materials which have increasingly

electronically asymmetric Fe environments. Typical values of the quadrupole splitting for Fe^{3+} in Fe-containing layered oxides are near 0.5 mm/s.

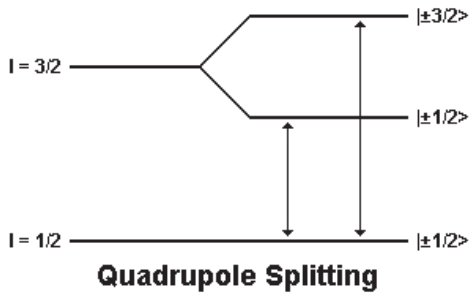

Figure 2.4: A diagram showing splitting of the excited 3/2 state of the nucleus in the presence of an electric field gradient.

2.2.4 Zeeman Effect

The Zeeman effect occurs when there is a non-zero magnetic field at the nucleus. There is an interaction energy associated with the nuclear magnetic dipole and the magnetic field dipole. The eigenvalues for the Hamiltonian which describes the magnetic dipole hyperfine interaction is given by [68]:

$$E_{QS} = -g\mu_N H m_I \qquad (2.16),$$

where g is the nuclear g-factor, $\mu_N = 5.04929\times10^{-24}$ J/T, H is the magnetic field and m_I is the magnetic quantum number (m_I = I, I-1 ... -I). There is a high probability that the change in m_I corresponding to the 3/2 → 1/2 transition is 0 or ±1 when transitioning

between the I = 3/2 and 1/2 levels due to the selection rules [68]. Therefore there are six transitions which may appear in the Mössbauer spectra, and resulting spectra can be fit with sextet components. Some samples in this thesis contain small amounts of magnetic impurity phases which were difficult to detect by other methods and did not affect results, therefore they are not treated in detail here.

2.3 ELECTROCHEMICAL METHODS

Materials generated in this thesis were incorporated into Na-ion half cells, in which the layered Fe-containing oxides were used as the cathode and pure Na metal was used as the anode. Since the chemical composition of the anode is constant, this means that the cell voltage is controlled only by the chemical potential (alternatively, the chemical composition) of the cathode.

2.3.1 Properties of Li-ion and Na-ion Batteries

Li-ion and Na-ion batteries take advantage of oxidation and reduction processes which occur in two electrode materials with different potentials to drive electronic charge through a circuit. As in any battery, there are several main components. These include the anode (negative electrode), the cathode (positive electrode), and the electrolyte. Other main components include the separator and the current collectors. The separator is electrically insulating, but allows for the passage of Li^+ or Na^+ ions and the electrolyte solution. The current collectors direct charge through an external circuit by interfacing

with the outside environment and the electrode. In a Li-ion or Na-ion battery, both the anode and the cathode must be able to react in some way with lithium or sodium. A schematic of the charge and discharge process of a Li-ion cell is shown in Figure 2.5.

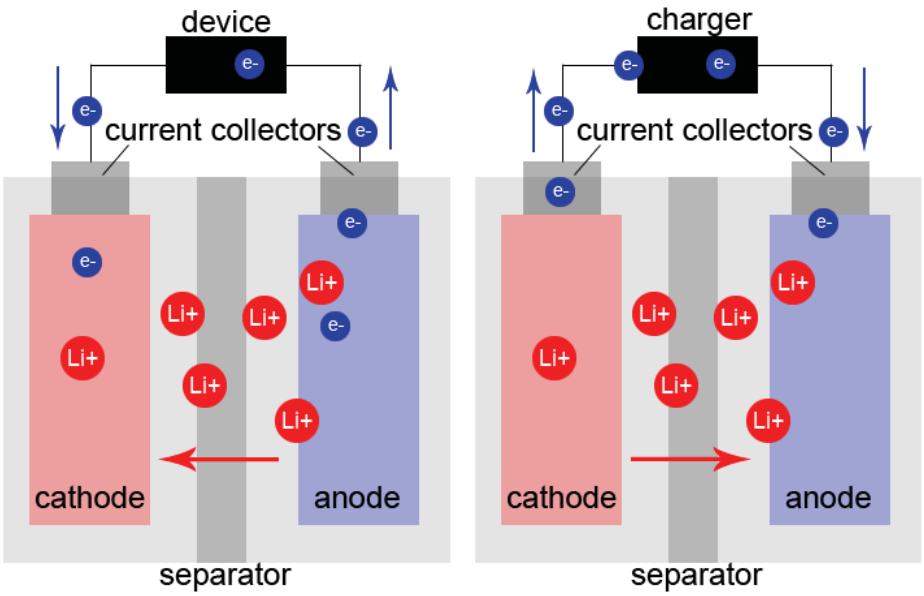

Figure 2.5: Schematic of the discharge (left) and charge (right) processes in a Li-ion cell. Key components include the anode, cathode, separator, electrolyte (light gray) and current collectors. One electron is transferred per lithium.

During discharge, the negative electrode is oxidized (loses electrons) producing lithium (or sodium) ions. The positive electrode is reduced. The cell is driven by the chemical potential between the cathode and anode. The chemical potential is defined by:

$$\mu_i = \left(\frac{\partial G}{\partial N_i} \right)_{T,P,N_j \neq i} \qquad (2.17),$$

the change in Gibbs free energy with respect to the change in number of the i^{th} species of particle, at constant pressure and temperature. The electrons travel through a closed external circuit and are driven by coulombic forces. The electric potential of the cell and the chemical potential of the electrodes are related by the formula:

$$-eV = \mu_{cathode} - \mu_{anode} \qquad (2.18),$$

where μ is the chemical potential (in electron volts) of the cathode or anode with respect to Na (or Li), and e is the magnitude of the charge of an electron. Applying a reversed, external electric potential causes the cathode to be oxidized and the anode to be reduced, meaning the opposite occurs and charging takes place. Electrons conduct through the circuit in the reverse direction, driven by the externally applied potential. Sodium is dissociated from the cathode and sent back to the anode. Ideally, the materials are reformed into their original states. The repeated charge and discharge process is sometimes referred to as a "rocking chair" process.

2.3.2 Peaks in dQ/dV

Electrochemical experiments using Na foil counter electrodes are generally presented as a differential capacity (dQ/dV) vs. voltage plot or a voltage vs. capacity plot. dQ/dV is the amount of charge dQ passed per change in voltage dV and is a measure of the change in composition per change in the chemical potential μ of the test material. The relationship

between the number N of Na atoms transferred to the cathode and the differential capacity at constant temperature is,

$$\frac{dQ}{dV} = const \times \left(\frac{dN}{d\mu} \right)_T \qquad (2.19)$$

[74]. Sharp peaks or divergences seen in dQ/dV are therefore indicative of a transfer of Na ions between the cathode and anode without a significant change in the chemical potential of the cell. In layered oxide materials, this can occur during insertion or removal of Na over the course of a phase transition, i.e. the O3 to P3 phase transition in $NaFe_{0.5}Co_{0.5}O_2$ [31]. The peak seen near 2.9 V during the charge curve of $NaFe_{0.5}Co_{0.5}O_2$ is indicative of the phase transition from the O3 phase to the P3 phase. The value of $\mu_{cathode}$ is constant until all the accessible O3 phase has been consumed to form the P3 phase.

In another example, peaks in differential capacity can occur during the course of a change in Na ordering, i.e. in the case of the P2-Na_xCoO_2, voltage plateaus are correlated with the location of the (008) diffraction peak [19]. In some segments of the voltage curve, the steep rises in the voltage curve to form a new plateau is associated with a sudden shift in a single (008) peak, indicative in a shift in the ordering of Na^+ ions and vacancies in the Na layer. For example, Figure 2.6 shows a steep change in the voltage at the ordered phase $Na_{2/3}CoO_2$ (region 3). The location of the (008) peak remains nearly constant until enough Na^+ has been deintercalated to cause another abrupt shift in the sodium ordering and corresponding c-axis lattice parameter.

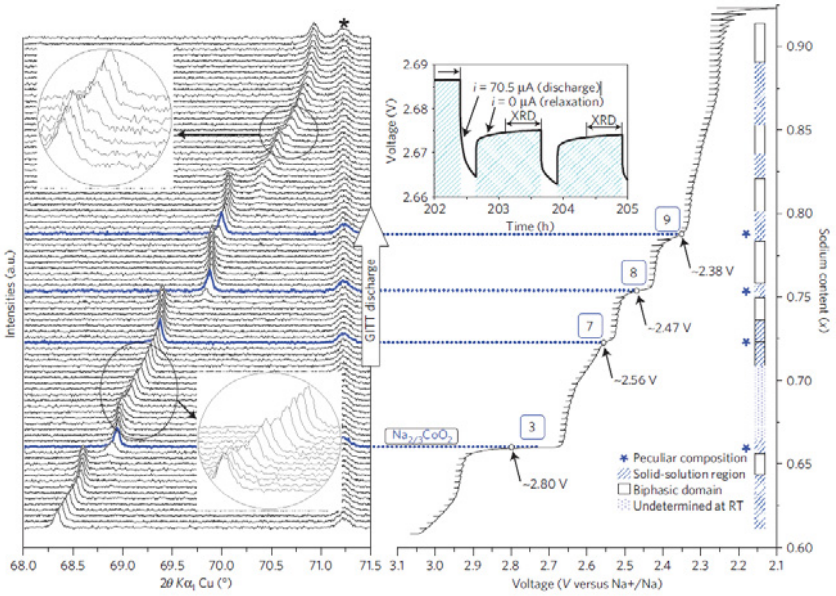

Figure 2.6: Location of the (008) diffraction peak as related to the voltage curve of P2-Na_xCoO_2. Reproduced from reference [19] with permission from Macmillan Publishers Ltd: Nature [19], copyright (2011)..

2.3.3 Coulombic Efficiency

In some instances, the coulombic efficiency (CE) is calculated, which is useful for better understanding electrode performance. Higher coulombic efficiency translates into better cycling performance in full cells. The coulombic efficiency is defined as:

$$CE = \frac{Q_{discharge}}{Q_{charge}} \qquad (2.20),$$

where $Q_{discharge}$ and Q_{charge} are the measured capacities (in mAh/g) of the corresponding discharge and charge of the cell for a specified cycle number. This value is typically

between 0.980 and 0.998 in Na half cells, but should be in excess of 0.9999 in a commercial full cell. Several factors contribute to the error in this quantity including the voltage and current accuracy of the charger, the time between measurements, and the temperature variation, which can affect the capacity of the cell from variation of the voltage, which may shift outside of the voltage cutoffs. Temperature was well controlled to within 0.1 ºC by use of temperature control boxes and has a small contribution to variation in recorded capacity. Error in the measured current and voltage is estimated to be between 0.02 - 0.05 % [78]. The maximum time between measurements of the voltage was every five minutes and is therefore the largest contribution to the error in the recorded capacity for a given charge. This error is given by:

$$\Delta Q = I\Delta t \qquad (2.21),$$

where I is the current in amps and Δt is the time between measurements. For a typical cell with current 10 mA/g, ΔQ is calculated to be in the 0.1 - 0.3 % range of the measured capacity. For example, in $NaFe_{0.5}Co_{0.5}O_2$ the measured capacity is near 160 mAh/g with calculated CE of 0.995 ± 0.001. Large fluctuations in the CE observed may be a result of structural damage occurring in the material and not resulting from instrumental error.

2.3.4 Hysteresis

In some cases, the “average hysteresis” or “hysteresis” of the second charge/discharge cycle of the voltage vs. time curve of the cell is calculated. This quantity may include a

combination of effects from voltage hysteresis inherent to the structure and rate dependent polarization caused by slow diffusion of Na when larger current densities are used. "Average hysteresis" or "hysteresis" in this work is defined by:

$$H = \frac{1}{t_{charge}} \int_0^{t_{charge}} V_{charge}(t)dt - \frac{1}{t_{discharge}} \int_0^{t_{discharge}} V_{discharge}(t)dt \qquad (2.22),$$

where $V_{charge}(t)$ and $V_{discharge}(t)$ are the voltage curves as a function of time for the charge and discharge respectively, integrated over the total time for the charge and discharge, t_{charge} and $t_{discharge}$ respectively. The integrals for this quantity were calculated as a Riemann sum from the voltage data. Rates are typically limited to C/10 or slower (i.e. where C is the theoretical current at which the material is fully charged or discharged in one hour) and therefore effects from polarization are expected to be small.

2.4 LAYERED OXIDE PHASES

2.4.1 Structures

Here, a brief discussion of layered oxide phases of synthesized materials in this thesis is presented. The relationship between the layered α-$NaFeO_2$ structure and the rocksalt structure can be seen in one instance by studying the (011) projection of the rocksalt structure, seen in Figure 2.7.

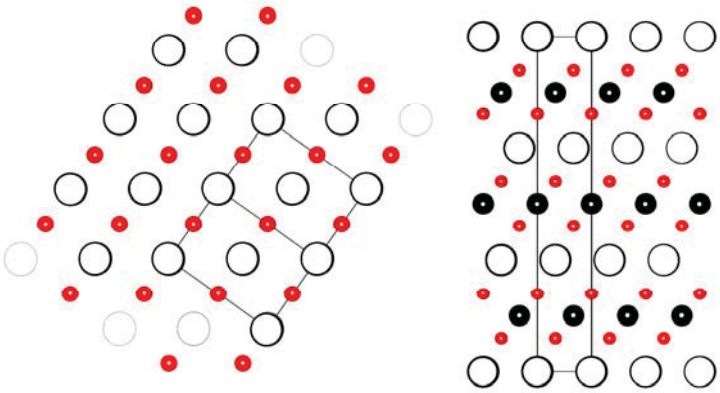

Figure 2.7: Rocksalt structure with (011) projection (left) having alternating Na and Cl layers compared to the α-$NaFeO_2$ structure with the (100) projection (right) where Na is white, Fe is black and oxygen is red.

The rocksalt structure is taken from the $Fm\bar{3}m$ space group with Na and Cl atoms placed in the (0.5, 0.5, 0.5) and (0, 0, 0) positions respectively. Each Na (or Cl) atom has octahedral coordination with the six nearest neighbor Cl (or Na) atoms respectively. The layered α-$NaFeO_2$ structure has the $R\bar{3}M$ structure and is shown in the (100) projection. In the case of the layered α-$NaFeO_2$ structure, when compared to the rocksalt structure, Cl atoms are replaced with O atoms, and every alternate layer of Na is replaced with Fe (or other transition metals).

Figure 2.8 shows how the rhombohedral description of the α-$NaFeO_2$ structure relates to the monoclinic description shown with three different projections. The (100) and (010) projections of the two unit cells are shown on the top right. On the left is the (100) projection in the monoclinic description. On the bottom is the (001) projection of the

rhombohedral cell. A distortion which cannot be described in the rhombohedral description can be obtained by adjusting parameters in the monoclinic description, i.e. the angle β.

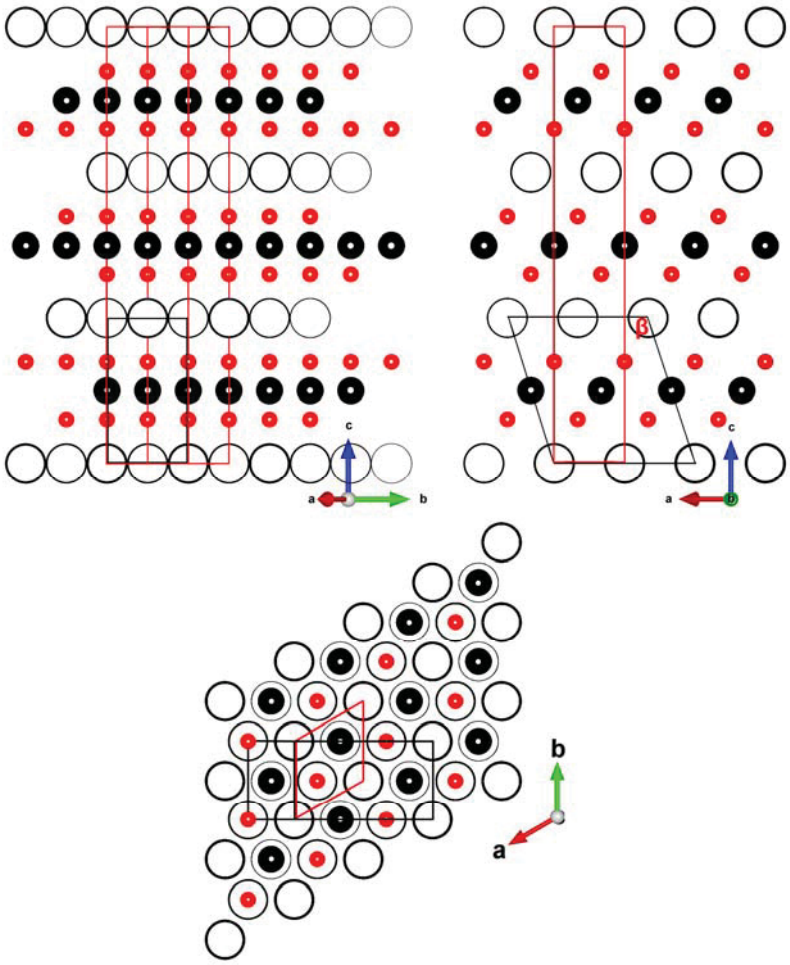

Figure 2.8: The α-$NaFeO_2$ structure is also described using a monoclinic cell (space group C2/m, black lines), which is equivalent to the rhombohedral cell (space group $R\bar{3}$ M, red lines). The (001) or (010) projection of the rhombohedral or monoclinic cells respectively are shown on the top right. The top left and bottom are 90° rotations with the orientation indicated. Na is white, Fe is black and oxygen is red.

In general, variations of this layered structure exist and the notation described by Delmas is used to denote layered sodium transition metal oxide phases in this thesis [75] such as P2- $NaMn_{1/3}Fe_{1/3}Co_{1/3}O_2$, P3- $NaCoO_2$, or O3- $NaFeO_2$ (α- $NaFeO_2$) In all of these structures, the transition metals form layers in which the metal ions are in octahedral sites. They are surrounded by layers of oxygen atoms which form the octahedra. The first character is used to indicate the relative location of the Na sites in the Na layer. In materials synthesized in this work, Na ions are in either prismatic sites (denoted P) in which 6 nearest neighbor oxygen atoms form a 5 sided prism, or octahedral sites (denoted O) in which 6 nearest neighbour oxygen atoms form an 8 sided prism. The second character denotes the number of transition metal layers in the unit cell in which the configuration is be assigned, i.e. 2, 3 or more. This notation is further summarized and described in more detail in the pioneering work by Delmas *et al.* [75]. Figure 2.9 shows how the (100) projection of the P2 and O3 structures are related. For $NaFeO_2$, the Na-O, Fe-O bond lengths are 2.37 Å and 2.05 Å, respectively [56].

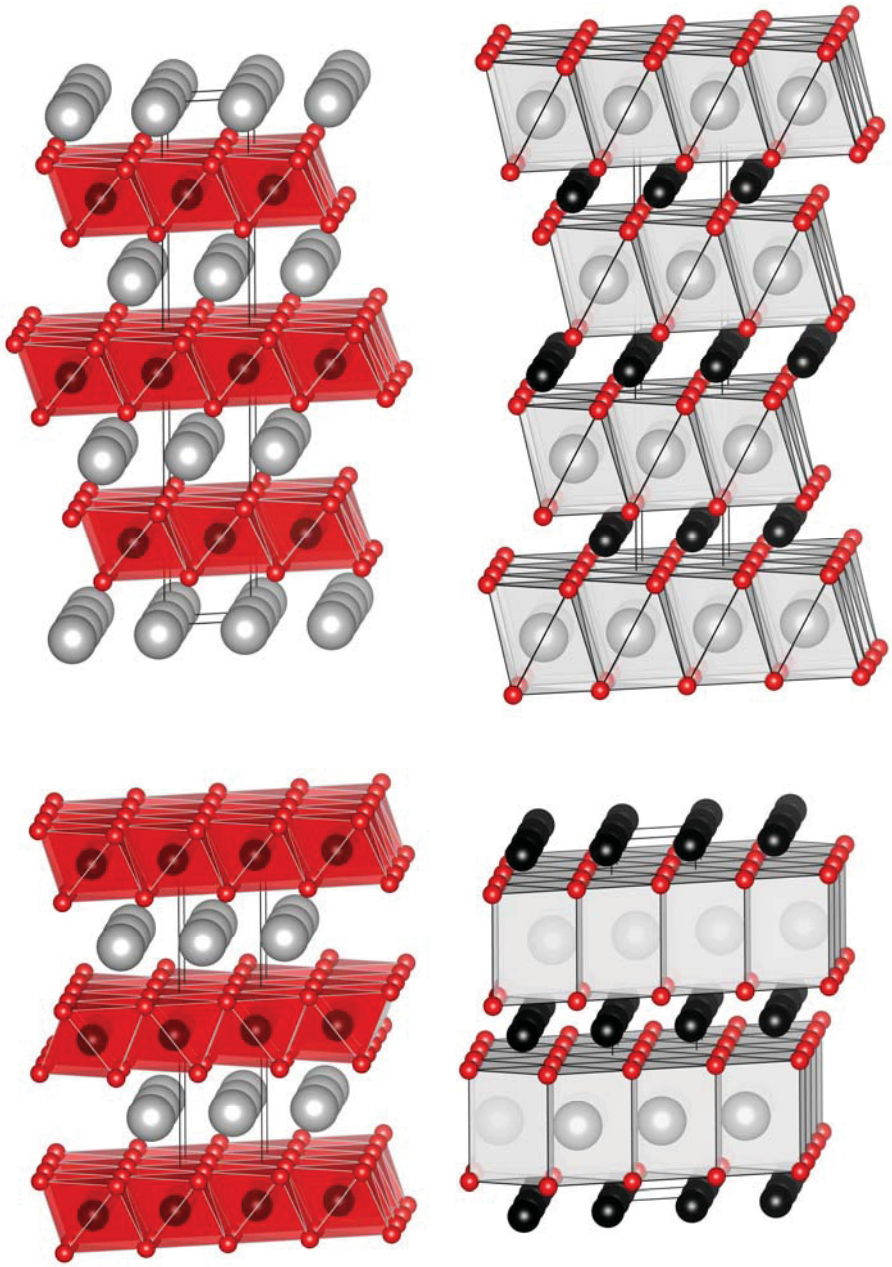

Figure 2.9: Tilted (100) projections of the O3 (top) and P2 (bottom) layered phases where the MO_6 octahedra are highlighted in red (left). Black atoms are the transition metal ions, red atoms are the oxygen, and white correspond to the sodium atoms. Na atoms are octahedral sites in the O3 phase (top right). Na atoms are in prismatic sites in the P2 phase (bottom right).

2.4.2 $Fe^{3+}(1)$ vs. $Fe^{3+}(2)$

As will be discussed in later sections, creation of Na site vacancies in the layered structures has a measureable effect on nearby Fe sites. This is shown in Figure 2.10 for the α-$NaFeO_2$. When a single Na^+ ion is removed, an edge sharing M^{3+} site is oxidized to create an M^{4+} site. If corresponding edge sharing $Fe^{3+}(1)$ sites exist, removal of Na causes $Fe^{3+}(2)$ sites to be created. The creation of $Fe^{3+}(2)$ sites may be detrimental to cycling performance when large amounts of Na vacancies are present. The creation of $Fe^{3+}(2)$ sites may increase the probability of an Fe^{3+} ion migrating into a face sharing tetrahedral site in the sodium layer. This transition metal migration occurs in $NaFeO_2$, $NaTiO_2$ and $NaCrO_2$ [56, 77].

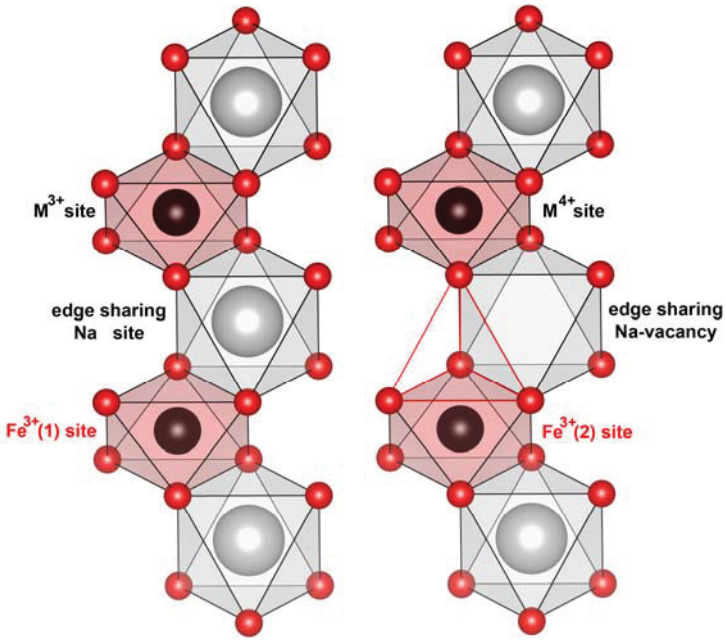

Figure 2.10: A comparison of $Fe^{3+}(1)$ sites (left) vs. $Fe^{3+}(2)$ sites (right) in the α-$NaFeO_2$ structure. In this structure, octahedral Na sites are edge sharing with octahedral transition metal sites. A face sharing tetrahedral site layer is highlighted with red lines.

2.5 JAHN-TELLER DISTORTION

Octahedral Fe^{4+}, Mn^{3+} and Ni^{2+} cations are all Jahn-Teller ions and therefore are considered briefly in the context of crystal field theory. In the octahedral setting in the layered oxides, transition metal ions are surrounded by six ligands corresponding to each oxygen bond, which are parallel to the d_z^2 and d_x^2-d_y^2 orbitals. In this environment, the five d-orbitals of the transition metal ion are split into two energy levels with energy difference Δ, referred to as the lower energy t_{2g} orbitals (the d_{xy}, d_{xz}, and d_{yz} orbitals) and the higher energy e_g orbitals (the d_z^2 and $d_{x^2-y^2}$ orbitals), respectively [79]. This is illustrated in Figure 2.11.

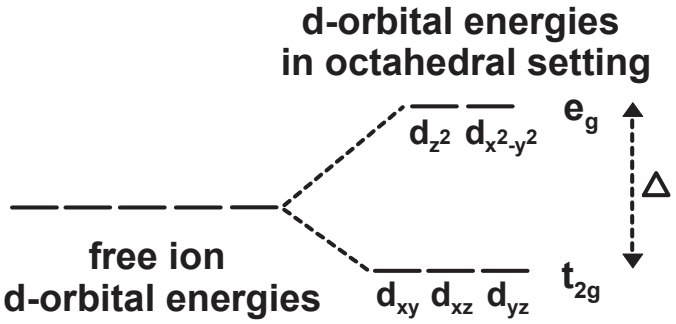

Figure 2.11: schematic representation of the energy splitting of the d-orbitals in an octahedral complex.

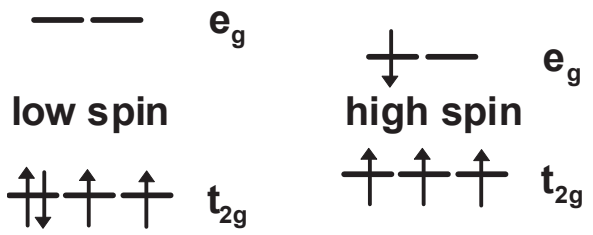

Figure 2.12: electron configuration for an Fe^{4+} or Mn^{3+} ion in the low spin (left) and high spin (right) states (not to scale).

For an Fe^{4+} ion, (four d-electrons), if the energy difference Δ (typically on the order of 10^0 eV or less) is smaller than the energy required to pair electrons from the exchange energy and coulombic repulsion (paired in accordance to Hund's rule), degeneracy of the d-electrons is lifted. The overall energy is reduced when the fourth electron is placed in the d_z^2 orbital. This is referred to as the high spin state (vs. the low spin state), illustrated in Figure 2.12. This may result in significant elongation or contraction of the M-O bond length parallel to the d_z^2 direction (or the $d_{x^2-y^2}$ direction) and is referred to as a Jahn-Teller distortion. When the octahedra are bound to a crystal lattice as in the case of an O3 or P2 material, distinct values of the M-O bond lengths may only occur if there are many such distortions present and may cause visible lattice distortions, as in the case of Na_xMnO_2 [80]. This often occurs when the average oxidation state of Mn is less than 3.5 [81]. A cooperative Jahn-Teller distortion may have negative implications for cycling performance when using the $Fe^{3+} \leftrightarrow Fe^{4+}$, $Mn^{3+} \leftrightarrow Mn^{4+}$ and $Ni^{2+} \leftrightarrow Ni^{4+}$ redox couples in the layered oxides which may result from internal stresses or strains induced in the material during cycling.

Noted is that no experimental evidence of a Jahn-Teller Fe^{4+} in materials presented in this thesis has been found. All discussion related to the Jahn-Teller effect is therefore speculative in the context of these materials. However, it has not been precluded as a possible contributing factor to capacity fade during after electrochemical cycling.

CHAPTER 3 EXPERIMENTAL METHODS

3.1 SYNTHESIS

Stoichiometric amounts of metal oxide precursors with sodium peroxide or sodium carbonate (as described in each section) were combined by high energy ball milling using a SPEX 8000 mill. In general, a 3:1 ball:sample mass ratio with a sample size of 3 g and two 0.5 inch diameter stainless steel balls were loaded into a 57.2 x 76.2 mm hardened steel milling vessel and milled for 2 hours. It is possible that slight excess of Fe was introduced into samples from degradation of the milling balls. The resulting powders were heated at specified temperatures under the specified conditions, anywhere from 2 – 48 hours as indicated in the relevant sections for each material.

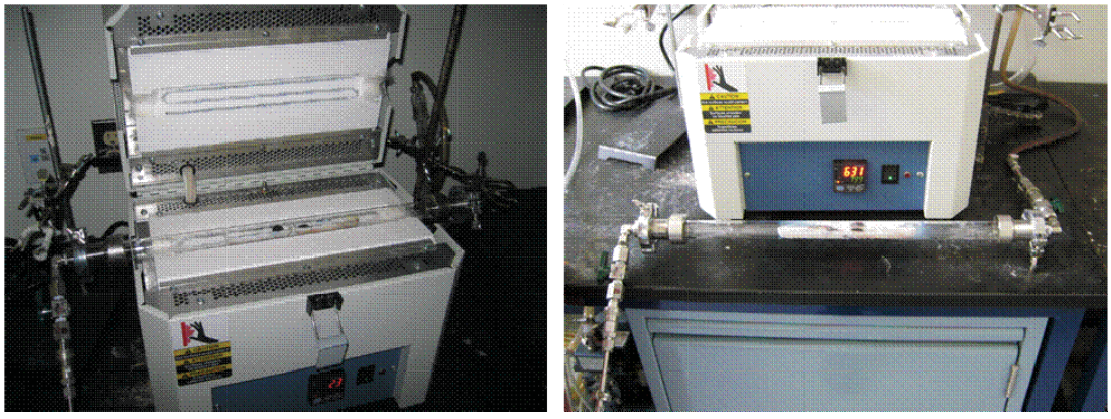

Figure 3.1: Precursor pellets in a gas tight quartz tube with controlled gas flow before annealing (left) and the resulting Fe-containing layered oxide after annealing (right) with evidence of Na-loss seen as white residue on the quartz tube.

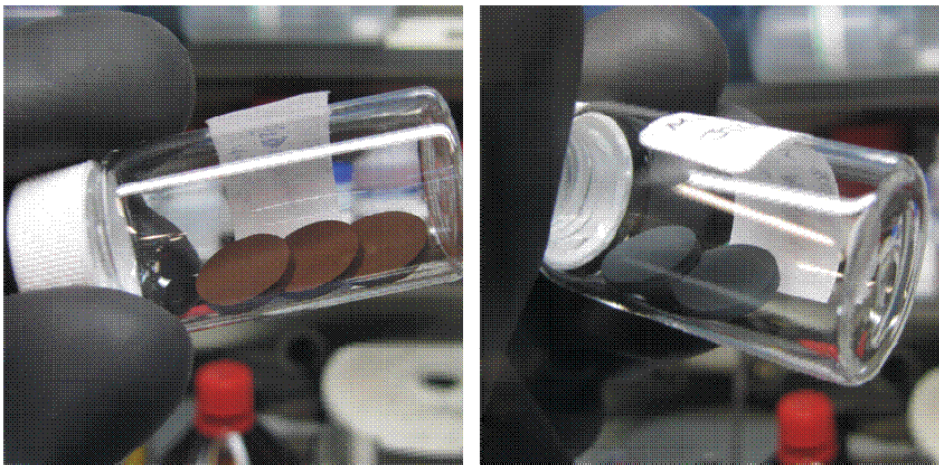

Figure 3.2: typical pellets before annealing (left) and after (right).

Synthesis of novel layered Na-ion oxides presented in this work is often more successful than loose powders when 1-2 g pellets are formed with ball milled precursors. Ball milled precursors were generally not exposed to atmospheric conditions when exploring new materials unless otherwise indicated. After pelletization, samples are transferred to the furnace in a quartz tube with closed (sealed) valves. Figure 3.1 shows the experimental setup. In this manner, atmospheric exposure can be avoided at all times. A controlled gas flow can be selected and samples can be immediately removed from the furnace after annealing to achieve a quench to room temperature. Evidence of sodium loss in the sample can be clearly observed after annealing in the form of white residue on the quartz tube. Figure 3.2 shows a pellet of the precursors for a typical iron contained layered oxide before annealing and after.

3.2 CELL CONSTRUCTION

Electrodes were coated with a slurry of 80% by weight active material, 12% Super-S carbon black and 8% PVDF binder dissolved in an appropriate amount of NMP to produce the correct viscosity of the mixture. The electrode material, carbon black and binder solution were mixed using a Mazerustar planetary mixer/deaerator. The slurries were spread on Al foil with a coating bar having a 0.006 inch gap and dried at 120 ºC in air for several hours. Circular electrodes with diameter 1.267 cm^2 were then punched from the coating and incorporated into 2325 size coin-type cells (illustrated in Figure 3.3) using the specified electrolyte. Two 3501 Celgard separators, one blown polypropylene microfiber separator (3M Co.) and a sodium foil counter/reference electrode (rolled from Na ingot to a few hundred microns thickness, reagent grade, Aldrich) were used in cell construction. Assembly took place in an Ar filled glove box. Cells were cycled using constant current using a Maccor Series 4000 Automated Test System at the specified current density.

In general, electrolyte containing 98% purity 1M $NaPF_6$ (Aldrich) dissolved in PC (Novolyte) was used in Chapters 3 and 4. In Chapters 5 through 8, 1M $NaClO_4$ (98% purity, Aldrich) dissolved in PC (Novolyte) with 2% by volume fluoroethylene carbonate (FEC) additive was used. Low purity electrolyte salts which are not battery grade such as those used in this thesis do not appear to adversely affect the cycling stability or the observed capacity, (discussed in later sections). Lower salt purities may adversely impact the measured coulombic efficiency.

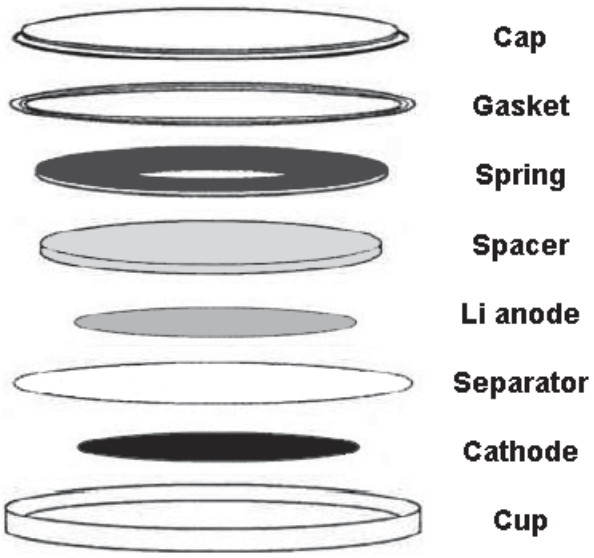

Figure 3.3: An illustration of the assembly of a 2325-type coin cell. From top to bottom: steel cap, gasket, spring, spacer, Li anode, separator, cathode, and cup.

3.3 CHARACTERIZATION BY XRD AND MÖSSBAUER

XRD measurements were performed using a Siemens D500 diffractometer, or a Rigaku Ultima IV X-Ray Diffractometer, equipped with a Cu anode X-ray tube and a diffracted beam monochromator. For Chapters 6 through 8, the XRD patterns were collected with samples under an argon atmosphere in a gas-tight sample holder with an aluminized polyester film window (DPM Solutions). Room temperature ^{57}Fe Mössbauer effect measurements were made using a SEE Co. constant acceleration spectrometer or a Wissel System II constant acceleration spectrometer equipped with a $\underline{\text{Rh}}^{57}$Co source. The velocity scale was calibrated relative to room temperature α-Fe.

3.4 EX-SITU MEASUREMENTS

Ex-situ measurements were performed by charging or discharging cells, followed by careful opening of cells in an Ar filled glove box and washing the electrodes in dimethyl carbonate (DMC). The electrode material was delaminated from the current collectors and the powders were then dried and placed in sealed holders for XRD or Mössbauer measurements. For ex-situ measurements, 4 to 8 cells were charged to various voltages at 10 mA/g current density (C/10 assuming 100 mAh/g). More than one cell was charged for each measurement in order to minimize the effects of shorting a cell during disassembly, and to increase the mass of the absorber in Mössbauer experiments. Electrodes were removed from cells and dissolved in DMC, dried and collected under Ar before being sealed and transferred to the spectrometer or X-ray diffractometer for measurement.

CHAPTER 4 STUDIES OF $NaFeO_2$

4.1 INTRODUCTION

There has been increased interest in layered oxides containing Fe for Na-ion cathode materials [10]. $NaFeO_2$ has two polymorphs. α-$NaFeO_2$ has the layered rock salt structure (O3-type) and is the prototype structure for the O3 type layered metal oxide phases. β-$NaFeO_2$ has an orthorhombic structure with space group $Pn2_1a$ [76] and has not been reported to be electrochemically active. The β- phase was incorporated in electrochemical Na half cells for this work but no activity was found at room temperature after charging to 4.5V and therefore will not be discussed further.

Na deintercalation from α-$NaFeO_2$ was first reported by Kikkawa *et al.* in 1985 [82], where $Na_{0.9}FeO_2$ was achieved using bromine as an oxidizing agent. It was shown to preserve its O3 structure when chemically deintercalated to Na_xFeO_2 with x = 0.9 [82]. The first electrochemical study of α-$NaFeO_2$ was reported in 1994 by Takeda *et al.*, where α-$NaFeO_2$ was incorporated into Li half cells using $LiClO_4$ as a lithium salt and a lithium foil counter electrode [71]. Takeda *et al.* observed that deintercalation of half the sodium results in the formation of a new monoclinic phase, suspected to be $Na_{0.5}FeO_2$ [71] (corresponding to a capacity of 120 mAh/g). The monoclinic distortion was proposed to appear in a two phase reaction during sodium removal. It was argued that the distortion was too small to be due to Jahn-Teller effects, but was more likely caused by structural distortion in response to Na-vacancies. Li could not be effectively

intercalated into the structure to form isostructural or other type Li_xFeO_2. In 2005, the discharge curve of a charged α-Na_xFeO_2 sample was reported in Na-half cells [83] and had a capacity near 80 mAh/g. A trace amount of Fe^{4+} was said to be observed for Na_xFeO_2 in the charged state. The Fe^{3+} to Fe^{4+} transition associated with deintercalation had not been shown to result in stable cycling of Na_xFeO_2.

More recently [56] it was shown that single phase deintercalation occurs for $1 \geq x \geq 0.5$ in Na_xFeO_2 when incorporated into Na half cells, and that the appearance of the monoclinic $Na_{0.5}FeO_2$ phase observed by Takeda *et al.* may have been a result of Li-ion exchange due to the incorporation into Li half cells. When cycling was restricted to below 3.4 V, reversible cycling was observed with a capacity of 80 mAh/g [56]. Cycling above 4.0 V ($x < 0.5$ in Na_xFeO_2) resulted in severe capacity fade. XRD analysis of Na_xFeO_2 cycled above 4.0 V showed a reduction in the (003) peak intensity. This is consistent with possible Fe migration into the Na layer during charging [56].

In this chapter, data are presented comparing exposed samples and comments are made on the atmospheric sensitivity of α-$NaFeO_2$. Adverse effects of exposure to ambient moist air on the discharge curve are discussed. Atmospheric exposure of layered Fe-containing Na-ion cathodes has a variable effect in binary, ternary and higher order systems. Harmful effects of moisture exposure and CO_2 are reduced with addition of other transition metals such as Mn [9, 27] and Co [31]. This information has implications for moisture exposed samples presented in this thesis, as will be commented on throughout the text.

Additionally, inspired by the work of Takeda *et al.* [71], three sites are used to analyse ^{57}Fe Mössbauer effect spectra collected from Fe-containing layered cathodes that contain Na vacancies. This model is used to analyse spectra in Chapters 4-7, and is used to fit the simplest case of Na_xFeO_2 in this chapter.

4.2 STRUCTURAL CHARACTERIZATION BY XRD

Figure 4.1 shows an XRD pattern from a powdered α-$NaFeO_2$ sample successfully prepared in open atmosphere at 650 °C for 48 hours, followed by a slow controlled cool to room temperature. Methods of preparing $NaFeO_2$ differ and conflict in various reports such as Richard *et al.* [84], Kikkawa *et al.* [82], Takeda *et al.* [71], and others [85]. $NaFeO_2$ can be synthesized by a variety of methods. In general, samples prepared in atmospheric conditions using a powdered sample were highly unreliable and difficult to avoid β-phase impurities.

Most often, the pure α- phase could be identified visually upon removal from the furnace (deep red, maroon colour), and had to be separated from β- phase impurities (green, or black colour). This is due to a variety of factors which may include cooling in atmospheric conditions and large temperature gradients during cooling. Most likely, since O3-$NaFeO_2$ hasn't been found to be particularly stable upon electrochemical deintercalation [56, 82], Na loss during annealing may facilitate early formation of the β-phase. Regardless, the formation of α-$NaFeO_2$ phase with an XRD pattern which does not

differ substantially from those previously reported [56, 82, 84] can be achieved even with atmospheric exposure.

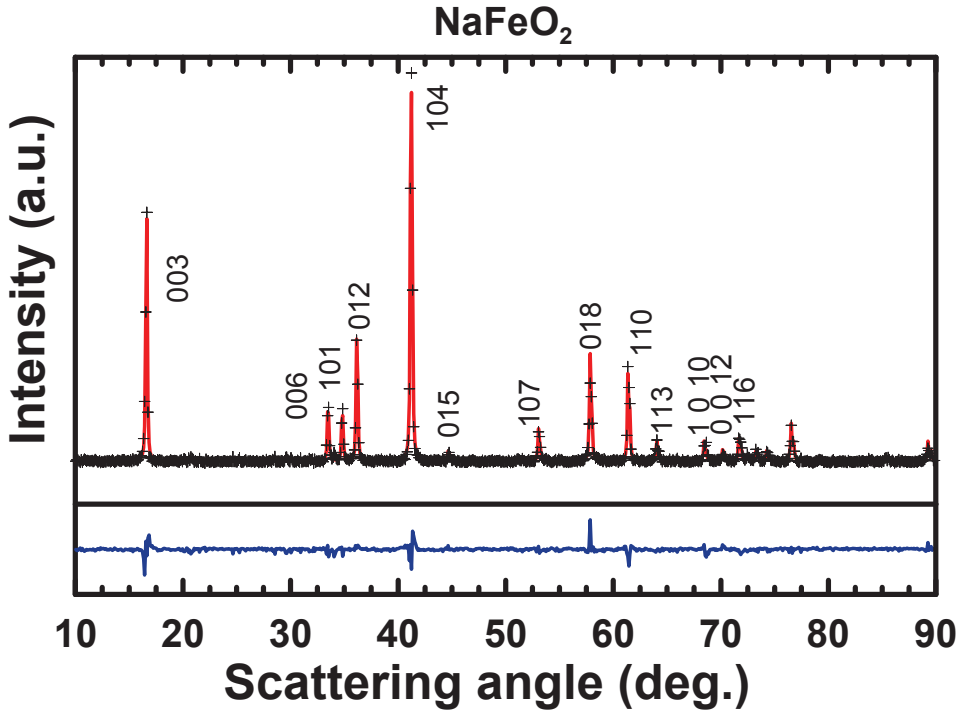

Figure 4.1: XRD pattern of an α- $NaFeO_2$ sample with results of Rietveld refinement and difference plot using a rhombohedral unit cell and space group $R\bar{3}m$. The first 13 Miller indices are shown. A difference plot is shown.

Atom	**Site**	**x**	**y**	**z**	**Occupancy**	**B (Å^2)**
Na	3b	0	0	0	0.932(3)	0.6
Fe	3a	0	0	0.500	1	0.6
O	6c	0	0	0.2284(2)	1	0.6
a_{hex} = 3.036(3) Å. c_{hex} = 16.072(4) Å. Bragg R-factor = 5.00.						

Table 4.1: Parameters used for Rietveld refinement of an α-$NaFeO_2$ sample including the isotropic temperature factors (B) (fixed).

Refined parameters for an α-$NaFeO_2$ phase are shown in Table 4.1. The method for reliable formation of the α- phase can be achieved by pelletizing, avoiding atmospheric exposure at all times, and annealing in a controlled dry air flow using methods discussed in Chapter 3 and using a 650 °C annealing temperature and 5% excess Na.

4.3 ELECTROCHEMISTRY

Figure 4.2 shows a comparison of samples of α-$NaFeO_2$ produced in this work which were exposed to atmospheric conditions. Trace amounts of moisture and/or slight sodium loss in the initial material are damaging and impact the electrochemical features. Samples that were prepared, handled, and stored in open atmospheric conditions in closed containers are classified as heavily exposed. Samples that were prepared and handled with days or less of atmospheric exposure, but stored in a glove box are classified as exposed.

Completely unexposed samples, such as those in the work of Yabuuchi *et al.* [56], are necessary to maximize the performance of $NaFeO_2$. The completely unexposed sample adapted from Yabuuchi *et al.* has an initial charge capacity of 141 mAh/g when charged to 4.0 V [56], while just 113 mAh/g was achieved when samples were primarily handled in atmospheric conditions. A heavily exposed sample offers dismal performance. Samples stored in atmospheric conditions are visually deteriorated after just a few months of storage. Despite potentially low materials cost, this material is impractical for commercial use.

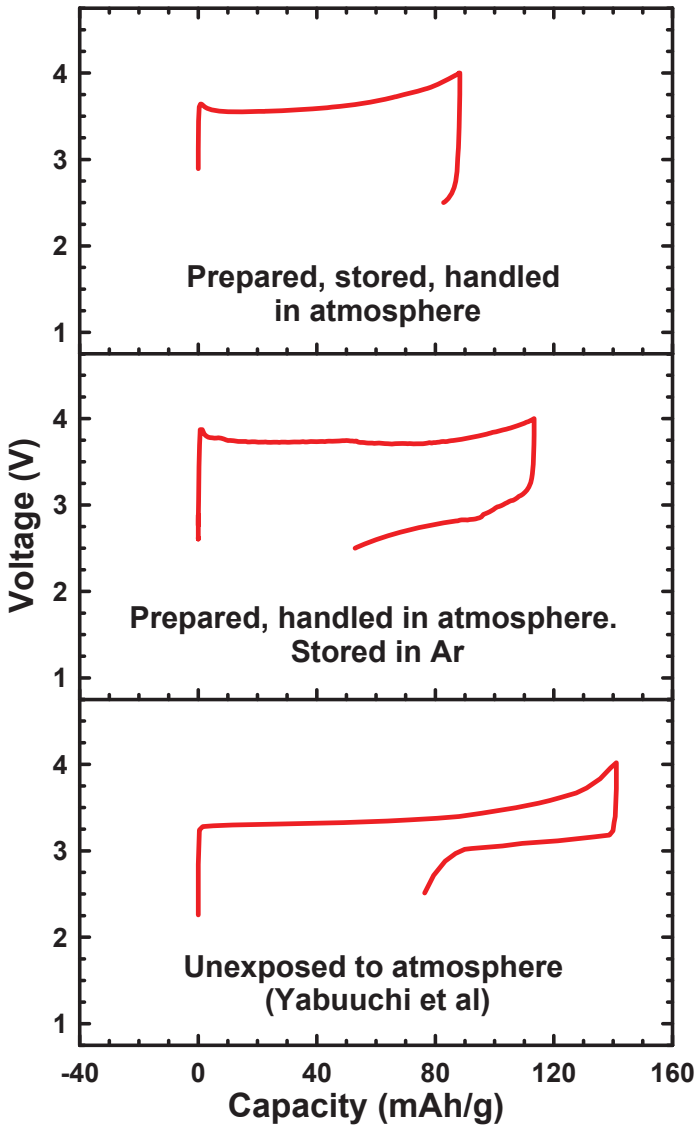

Figure 4.2: a comparison of a voltage curve for a sample which was heavily exposed to atmospheric conditions, a less exposed sample, and a completely unexposed sample adapted from Yabuuchi *et al.* [56].

Extensive handling in unexposed conditions is cost additive and less environmentally friendly compared to exposed conditions. Fe-containing samples which have some

transition metal substitution have significantly improved moisture tolerance, especially Mn-containing samples, as can be seen by comparison of $Na_{0.5}Fe_{0.5}Mn_{0.5}O_2$ [27] (handled in atmospheric conditions) with $Na_{2/3}Fe_{0.5}Mn_{0.5}O_2$ [9] (no atmospheric exposure). In this light, atmospheric exposure of Fe-containing layered cathodes in the later chapters has been limited to just a few hours after being mixed with PVDF and carbon black.

A recent study has shed light on the mechanism for damage to $Na_xFe_{0.5}Mn_{0.5}O_2$ caused by moisture and atmospheric exposure using neutron and X-ray diffraction, mass spectroscopy and thermal analysis. It was revealed that this material is sensitive to CO_2 as well as moisture. Exposure resulted in higher hysteresis and lower capacity resulting from the insertion of carbonate ions, which decompose during charging, and is balanced by the oxidation of Mn^{3+} to Mn^{4+} [86]. Effects of atmospheric exposure observed here in the electrochemistry of α-$NaFeO_2$ are similar to those discussed in the literature.

4.4 CHARACTERIZATION BY MÖSSBAUER SPECTROSCOPY

Takeda *et al.* [71] studied Mössbauer spectra of deintercalated α-Na_xFeO_2 with $x < 1$. The deintercalation of Na was associated with the oxidation of Fe^{3+} to form Fe^{4+} in the transition metal layers. With the emergence of Fe^{4+} accompanied by the formation of a monoclinic "$Na_{0.5}FeO_2$" phase, Fe^{3+} was shown to have two distinct environments, i.e. one for each respective phase: a more electronically symmetric environment for the $Fe^{3+}(1)$ in the O3- $NaFeO_2$ phase having a distinctly lower value of QS around 0.5 mm/s (where Fe^{3+} is uniformly surrounded by Fe^{3+}), and a less symmetric $Fe^{3+}(2)$ environment in what was referred to as the $Na_{0.5}FeO_2$ monoclinic phase with a distinctly higher value of QS near 0.8-0.9 mm/s (where Fe^{3+} is surrounded by both Fe^{4+} and Fe^{3+}). The emergence of the second Fe^{3+} site is coupled with the formation of Fe^{4+} and Na-site vacancies in the structure.

Here, an attempt is made to use a three site model to describe the Mössbauer spectra from an α-$NaFeO_2$ sample which was briefly handled in open air atmosphere. Mössbauer spectra of deintercalated $Na_xFe^{3+}{}_xFe^{4+}{}_{1-x}O_2$ ($0.78 \leq x \leq 1$) in an in-situ Na-ion half cell are presented, where it is assumed that the valence states of Na, Fe and O sum to zero. The following analysis confirms this assumption. Values of x are calculated from the measured capacity of the in-situ cell. Figure 4.3 shows ex-situ Mössbauer spectra of an exposed O3-$NaFeO_2$ electrode measured in an in-situ cell taken at different points in the voltage curve as indicated. A three site model using Lorentzian doublets, with two distinct Fe^{3+} sites as described in Takeda *et al.* [71], was employed to fit the Mössbauer

spectra. The sites used are designated $Fe^{3+}(1)$, $Fe^{3+}(2)$, and Fe^{4+} respectively, where the state of charge is estimated from the centre shift (i.e. Fe^{4+} having a centre shift near 0 mm/s and Fe^{3+} having a centre shift near 0.3-0.4 mm/s). Mössbauer spectra fitting parameters are listed in Table 4.2. The Mössbauer spectra of the as prepared α-$NaFeO_2$ corresponds almost entirely to $Fe^{3+}(1)$. The existence of trace amounts of Fe^{4+} and $Fe^{3+}(2)$ are questionable due to the very small area of these sites.

For spectra collected from samples with $x < 1$, the emergence of Fe^{4+} is seen to increase, as is evident by the increasing amplitude of the Fe^{4+} component. The area fraction of this component, determined by,

$$\alpha = \frac{A(Fe^{4+})}{A(Fe^{4+}) + A(Fe^{3+}(1)) + A(Fe^{3+}(2))} \qquad (4.1)$$

The fitted fraction of Fe^{4+} agrees well with the values predicted by the capacity of the cell. The expected relative area of Fe^{4+} was used as starting values for the fits and were later freed, as indicated in Table 4.2. Excellent fits were achieved. In Figure 4.4 the following parameter is plotted versus x:

$$\beta = \frac{A(Fe^{3+}(2))}{A(Fe^{3+}(1)) + A(Fe^{3+}(2))}, \qquad (4.2).$$

This is the area of the $Fe^{3+}(2)$ component divided by the total Fe^{3+} component area, i.e. the fraction of $Fe^{3+}(2)$ sites relative to the total amount of Fe^{3+}, the $Fe^{3+}(1) + Fe^{3+}(2)$.

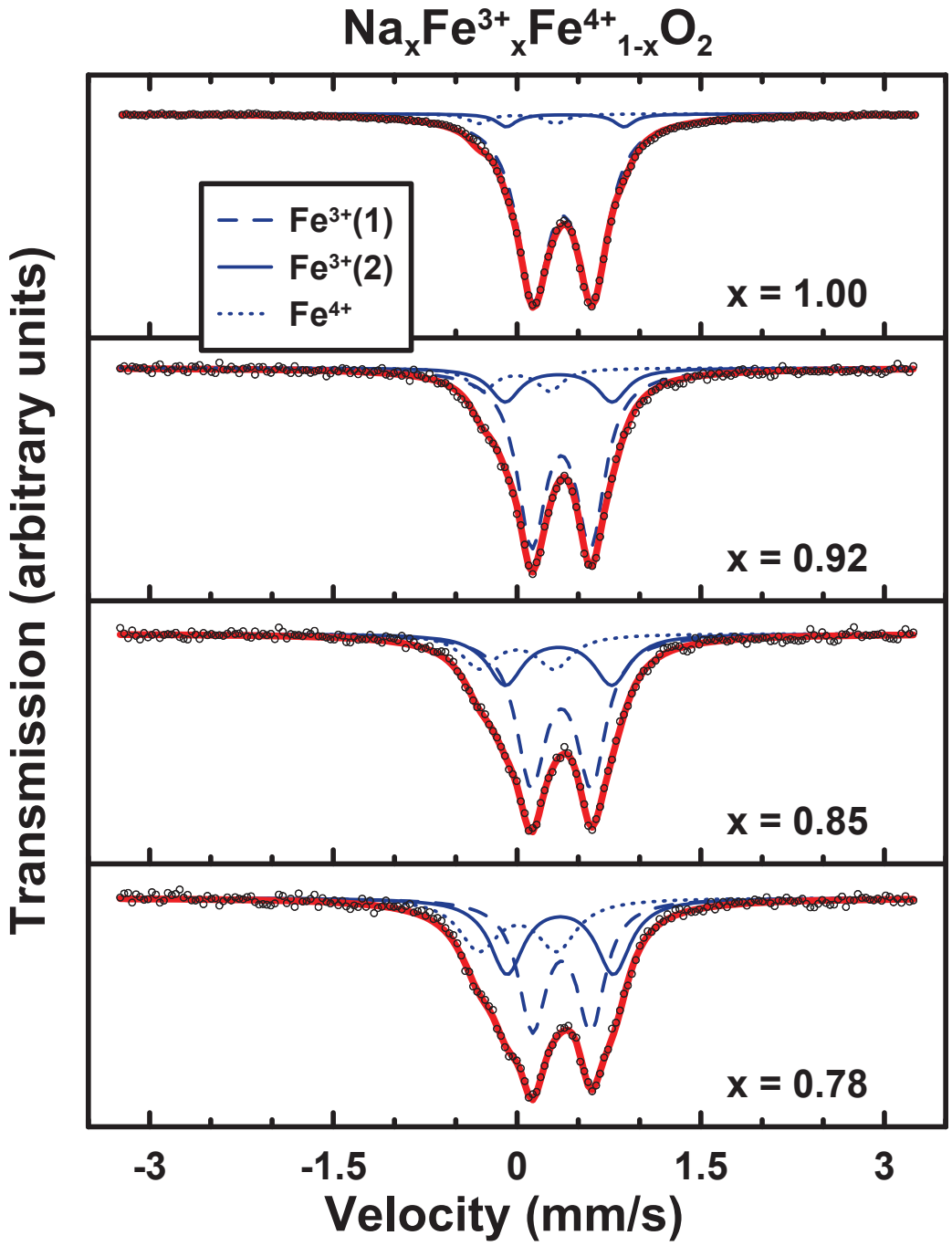

Figure 4.3 ^{57}Fe Mössbauer effect spectra from $Na_xFe^{3+}{}_xFe^{4+}{}_{1-x}O_2$ for $1.00 \geq x \geq 0.78$. Fitting components are shown as blue lines, with their sum shown as red lines. Data are shown as circles.

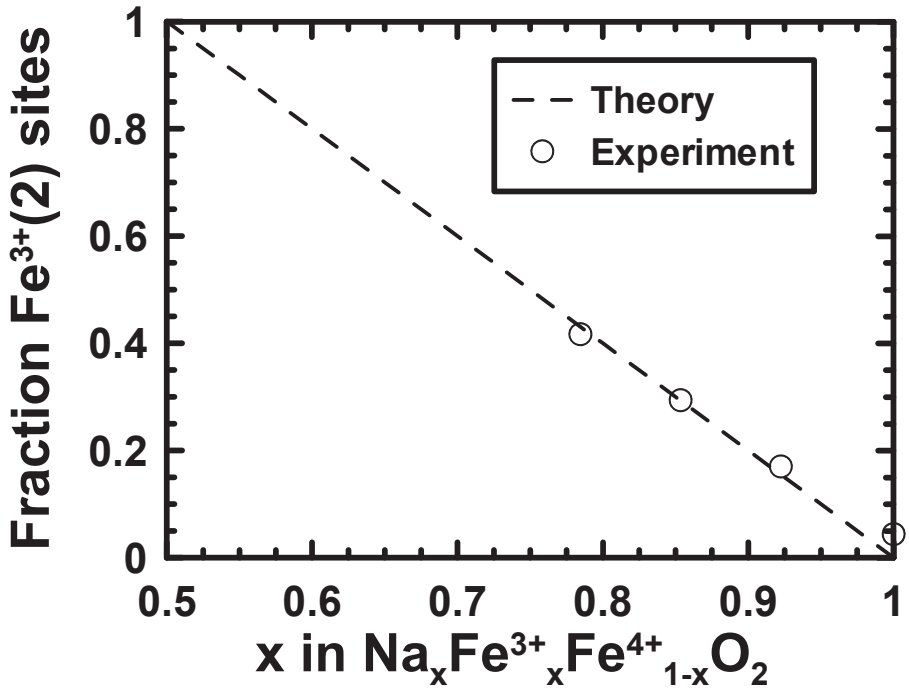

Figure 4.4: Normalized fractional area of Fe^{3+}(2) sites relative to the total Fe^{3+} area for $Na_xFe^{3+}{}_xFe^{4+}{}_{1-x}O_2$ samples (the parameter β) as a function of x in $Na_xFe^{3+}{}_xM^{4+}{}_{1-x}O_2$.

The observed trend in β may be explained by additional asymmetry created by different Na occupancies on the adjacent layers. A distinctly lower value of the QS may be observed if Fe^{3+} when all adjacent Na sites are occupied. Removal of an Na^+ ion causes symmetry to be broken among equivalent Fe sites via the creation of an Fe^{4+} ion. Similarly, a higher value of the QS in one Fe^{3+} site is observed in the creation of one Fe^{4+} ion for each Na vacancy. This would result in the linear trend in beta as the probability of a Na vacancy (or Fe^{4+} ion) near an Fe^{3+} atom is 0 in $NaFe^{3+}O_2$ and approaches 1 in $Na_{0.5}Fe^{3+}{}_{0.5}Fe^{4+}{}_{0.5}O_2$. This linear trend in β indicates that for each Fe^{4+}, (also seen from the previous work [71]) and Na-vacancy there is associated one Fe^{3+}(2) site, at the expense of an Fe^{3+}(1) site.

Sample	Site	CS (mm/s)	QS (mm/s)	Area (%)
$NaFeO_2$	$Fe^{3+}(1)$	+0.373*	0.483	94
x = 1.00	$Fe^{3+}(2)$	+0.394	0.960	4
	Fe^{4+}	+0.022*	0.631	2
$Na_xFe^{4+}_{0.09}Fe^{3+}_{0.91}O_2$	$Fe^{3+}(1)$	+0.361*	0.480	76
x = 0.92	$Fe^{3+}(2)$	+0.339	0.874	15
	Fe^{4+}	-0.009*	0.554	9
$Na_xFe^{4+}_{0.16}Fe^{3+}_{0.84}O_2$	$Fe^{3+}(1)$	+0.361*	0.490	59
x = 0.85	$Fe^{3+}(2)$	+0.337	0.871	25
	Fe^{4+}	+0.000*	0.612	16
$Na_xFe^{4+}_{0.24}Fe^{3+}_{0.76}O_2$	$Fe^{3+}(1)$	+0.364*	0.476	44
x = 0.78	$Fe^{3+}(2)$	+0.352	0.870	31
	Fe^{4+}	+0.007*	0.635	25

* fixed parameter.

Table 4.2: Fitted room temperature ^{57}Fe Mössbauer effect parameters for the symmetric doublet sites in charged samples as indicated. A three site model was used to extract the ratio of Fe^{4+} and the ratio of $Fe^{3+}(1)$ to $Fe^{3+}(2)$. Only one parameter was fixed in each fit. Typical uncertainties for measured values of the centre shifts (CS) and quadrupole splittings (QS) are about ± 0.005 mm/s.

4.5 CONCLUSIONS

Samples presented in later chapters have been handled in atmospheric conditions. The relevant discussion on atmospheric exposure of samples in later chapters is presented. In some samples, voltage curves can be directly compared to literature data. The exposure of the moisture sensitive Fe-containing layered materials to atmospheric conditions results in lower specific capacity and increased voltage hysteresis which may result from damage caused by exposure. Damaged Fe^{3+} containing regions may limit or impede access to active or undamaged areas, which has a variable effect in binary, ternary or higher Fe-containing layered systems.

In this section, a model was introduced based on the initial work of Takeda *et al.* in deintercalated $NaFeO_2$ [71] where Na vacancies are detected by use of a second $Fe^{3+}(2)$ site with higher quadrupole splitting in comparison to the $Fe^{3+}(1)$ sites. This model was used to obtain excellent fits of deintercalated Na_xFeO_2 for $1 < x < 0.78$ and is used in later sections.

CHAPTER 5 STUDIES OF $Na_xFe^{3+}_xM^{4+}_{1-x}O_2$ (M=Mn, Ti, Sn)

5.1 INTRODUCTION

Here an investigation of new layered $Na_xFe^{3+}_xMn^{4+}_{1-x}O_2$ electrode materials is presented, which was published in 2012 [27] and has primarily O3 structure when $x < 0.65$. The electrochemistry of layered O3-$Na_xFe^{3+}_xTi^{4+}_{1-x}O_2$ (published in 2014 [54]) and O3-$Na_xFe^{3+}_xSn^{4+}_{1-x}O_2$ is also described and these systems are found to have an analogous oxidation/reduction mechanism to the Mn-containing samples. The oxidation of Fe^{3+} to Fe^{4+} during electrochemical cycling is shown to be a major source of hysteresis and capacity fade, while the use of the $Fe^{2+} \leftrightarrow Fe^{3+}$, $Mn^{3+} \leftrightarrow Mn^{4+}$, $Ti^{3+} \leftrightarrow Ti^{4+}$ and/or $Sn^{3+} \leftrightarrow Sn^{4+}$ redox couples results in more stable cycling performance in the binary systems.

It was confirmed in this work that Mössbauer spectra can accurately detect Na vacancies in $Na_xFe^{3+}_xM^{4+}_{1-x}O_2$ materials with M = Fe, Mn [27], Ti [54] and Sn from their effects on neighboring Fe^{3+} ions and this model can be used to analyse materials at different stages of charge or discharge. This Na vacancy model potentially has broader implications and is useful as a probe for Na-vacancies in iron containing Na-ion cathode materials in general (such as those presented in Chapters 6 and 7). Possible reasons for capacity fade and hysteresis are discussed in terms of ex-situ Mössbauer and XRD studies.

5.2 SYNTHESIS

Stoichiometric amounts of Fe_3O_4, MnO_2 and Na_2CO_3 were ball milled for 2 hours sealed in air. The resulting loose powders were annealed in open air atmosphere for 2 hours at 750 °C to obtain samples of $Na_xFe_xMn_{1-x}O_2$. Samples were immediately removed from the furnace after annealing and transferred in the glove box ante chamber.

Stoichiometric amounts of Fe_3O_4 (98%, Aldrich), TiO_2 (99%, Aldrich), and Na_2CO_3 (98%, Aldrich) were ball milled for 2 hours in air. The resulting powders were then heated in open air atmosphere according to the temperatures and annealing times previously described by Li *et al.* [61] to obtain samples of $Na_xFe^{3+}{}_xTi^{4+}{}_{1-x}O_2$.

Stoichiometric amounts of Fe_3O_4 (98%, Aldrich), SnO_2 (99%, Aldrich), and Na_2CO_3 (98%, Aldrich) were ball milled for 8 hours in air. The resulting powders were then heated in open air atmosphere at 900 °C for 16 hours to obtain $Na_{0.85}Fe_{0.85}Sn_{0.15}O_2$. When x is less than 0.85 in $Na_xFe_xSn_{1-x}O_2$, an impurity phase identified as $NaSnFeO_4$ was found, which is isostructural with $NaTiFeO_4$, indicating the solubility limit is near x = 0.85. This system is analogous to the $Na_xFe_xTi_{1-x}O_2$ with solubility limit x = 0.72 [61].

5.3 STRUCTURAL CHARACTERIZATION BY XRD

Figure 5.1 shows XRD patterns of $Na_xFe_xMn_{1-x}O_2$ with the values of x indicated. The peak positions of α-$NaFeO_2$ are shown as dashed lines for comparison. Patterns for

samples with x > 0.65 were fit by Rietveld refinement using a rhombohedral unit cell and space group $R\bar{3}m$. For the refinement, sodium atoms with occupancy x were placed in the fixed 3a sites at the origin (0, 0, 0), iron and manganese with composition Fe_xMn_{1-x} were placed in the fixed 3b sites with atomic coordinates (0, 0, 0.5) and oxygen atoms were placed in the 6c sites (0, 0, z), with z = 0.25 as a starting value which was allowed to vary during the fit. The lattice constants were also allowed to vary. The oxygen position refined to values near z = 0.23, which is in close agreement with the oxygen positions reported for $Na_xFe_xTi_{1-x}O_2$ [61].

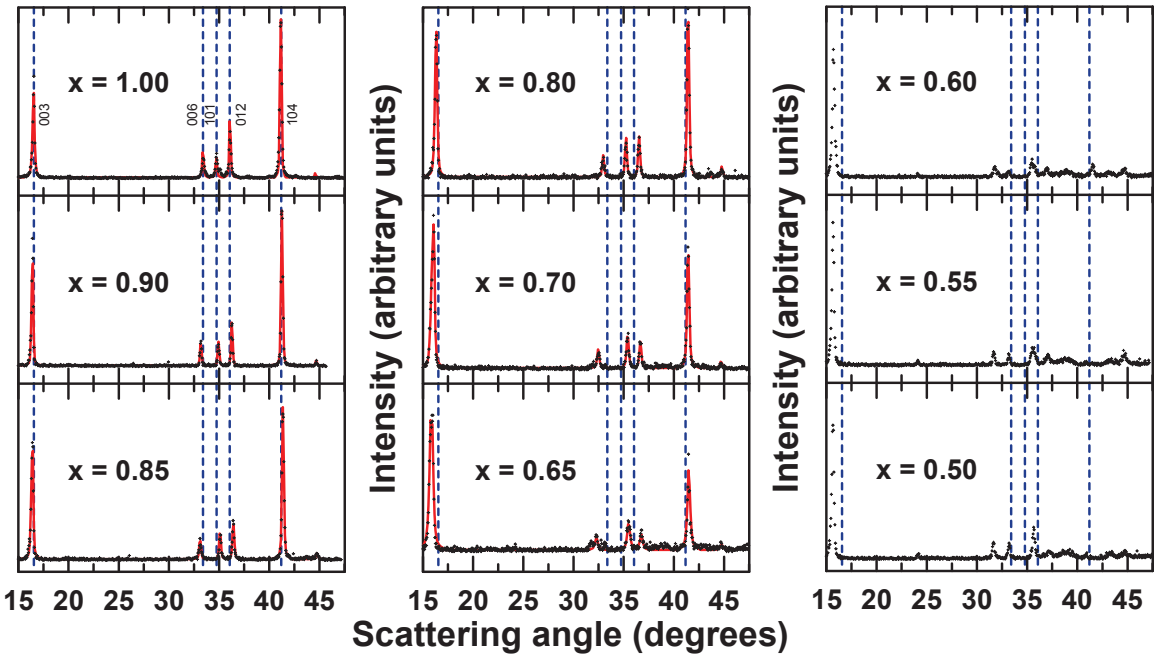

Figure 5.1: Measured X-ray diffraction patterns (crosses) with results of Rietveld refinement where applicable (solid lines) for given values of x in $Na_xFe_xMn_{1-x}O_2$. The peak positions of α-$NaFeO_2$ are shown as dashed lines for comparison.

Bragg R-factors for the fitted patterns were found to be less than 2.5 with the exception of the x = 0.65 sample, for which the (006) has split. For x < 0.65, an additional peak appears at a scattering angle near 24° which grows in intensity as x gets smaller. It is speculated that this effect may be attributed to the early onset of a staged phase or phases in which Na vacancies are grouped together such that two or more distinct values of the (006) distance can be measured. The broadening of the (003) line in the x=0.65 sample (compared to $NaFeO_2$) is consistent with this. Figure 5.2 shows evidence for the emergence of a second phase when x < 0.70, indicated by the onset of new peaks emerging near the (006) peak as the value of x decreases, as well as new peaks emerging between scattering angles of 38-40°. These peaks have not been accounted for in the fits.

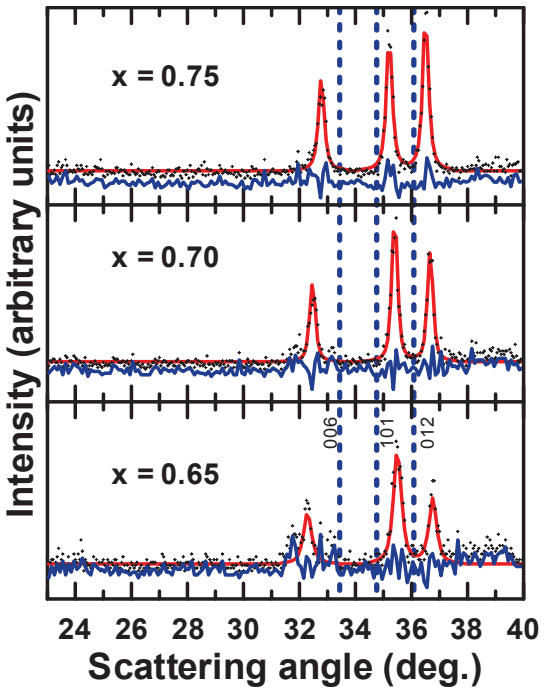

Figure 5.2: Expanded view of selected XRD patterns from Figure 5.1 with x value indicated. Shown is the measured data (crosses) with results of Rietveld refinement (solid red lines). The peak positions of α-$NaFeO_2$ are shown as dashed lines for comparison. Difference plots are shown in blue.

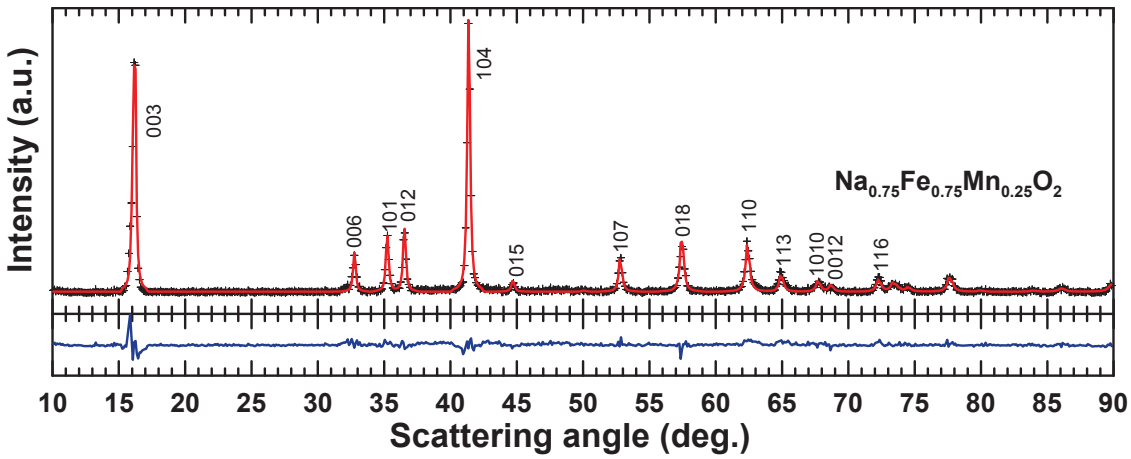

Figure 5.3 Expanded view of the Rietveld refinement for the x=0.75 sample, reporting a single phase O3 material [88]. The first 13 Miller indices are indicated. A difference plot is shown.

Figure 5.3 shows an expanded view of the XRD pattern and fit with an extended angular range for the $Na_{0.75}Fe_{0.75}Mn_{0.25}O_2$, including a residual plot shown on the same scale. The sample is well described by single phase O3 structure with no monoclinic impurity, similar to that of deintercalated Na_yFeO_2. The asymmetry in the (003) peak can be attributed to an instrumental artifact resulting from the geometry of the X-ray diffractometer. The Na occupancy for this sample was allowed to vary in the Rietveld refinement and stabilized to a value near 0.72, which is in reasonable agreement with the target stoichiometry and suggests that some Fe is in the 4+ oxidation state. Values of the Na occupancy stabilized just below the intended value for other samples, indicating slight Na loss during synthesis is likely.

Rietveld refinement analysis was not performed for samples with $x < 0.65$. The large number of Na vacancies may cause lattice distortions and the splitting of or emergence of

multiple new peaks compared to the O3 phase. The layered transition metal oxide stacking distance continues to be a prominent trend in the atomic arrangement as indicated by the continued linear trend in the position of the low angle (003) peak (as seen in Figure 5.5). For instance, the c-axis lattice constant for the x = 0.5 sample indexed to the O3 structure would be roughly 16.9 Å, which is close to the value of c = 16.8 Å as predicted from linear extrapolation from the line of best fit in Figure 5.5.

The majority of peaks seen in the x = 0.5 pattern can be indexed if two different values of the c-axis parameter are used for hexagonal unit cells. These two unit cells are referred to as unit cell A and unit cell B and are shown in Table 5.1. The best agreement with the XRD patterns was obtained when unit cell A had lattice constants of a = 2.91 Å and c = 33.9 Å and when unit cell B had lattice constants of a = 2.91 Å and c = 22.6 Å. In both unit cells A and B, the a-axis lattice parameter is found to be similar to the value found by Yabuuchi *et al.* in $Na_{2/3}Fe_{1/2}Mn_{1/2}O_2$ [9]. However, the c-axis parameter of unit cells A and B are double the c-axis parameter of the O3 or P2 structure respectively. For instance, half of the c-axis of unit cell A is 16.9 Å, which is close to the predicted value of 16.8 Å from equation 5.1 for the O3 structure. Similarly, half of the c-axis of unit cell B is roughly 11.3 Å, which is near the value of 11.2 Å for the P2 $Na_{2/3}Fe_{1/2}Mn_{1/2}O_2$ phase [9]. This suggests that Na staging is likely occurring in these compositions. Examples of staged phases can be found in charged Li_xCoO_2, further described in the literature [87].

Using these cell constants, the peak near 37.2 º can be uniquely assigned to a (014) reflection in unit cell A (O3-like phase), while the peak near 41.0 º can be uniquely

assigned to a (015) reflection in unit cell B (P2-like phase). Similarly, the (015) and (014) peaks must be assigned to either cell A or B, necessitating at least two crystallographic layered phases. Other peaks in the diffraction pattern shown for x = 0.5 in Figure 5.1 can be assigned to either of unit cells. For example, what would normally be assigned to the (003) peak in α-$NaFeO_2$ can assigned to a (006) peak in unit cell A, or a (004) peak in unit cell B. Other peaks, such as that near 33 º, cannot be assigned to either unit cell A or B, and may be indicative of a third non-layered impurity phase. Similar behaviour is seen for all compositions with $x < 0.65$.

Figure 5.4 shows selected XRD patterns for the prototypical O3-type α-$NaFeO_2$ and $Na_xFe_xTi_{1-x}O_2$ samples. All the samples in this series are single phase with the O3 structure, in agreement with previous studies [61]. X-ray diffraction patterns for samples in Figure 5.4 were fit by Rietveld refinement using a rhombohedral unit cell and space group $R\bar{3}m$. For the refinement, sodium atoms with occupancy x were placed in the 3a sites, iron and titanium with composition Fe_xTi_{1-x} were placed in the 3b sites and oxygen atoms were placed in the 6c sites. The lattice constants were allowed to vary. The oxygen position refined to values near (0, 0, 0.23), which is in close agreement with the oxygen positions previously reported for $Na_xFe_xTi_{1-x}O_2$ [61]. Bragg R-factors for the fitted patterns were found to be less than 4.5.

Unit cell A a = 2.909 Å c = 33.975 Å		**Unit cell B** a = 2.908 Å c = 22.649 Å	
Miller indices	Calculated Scattering Angle	Miller Indices	Calculated Scattering Angle
(0 0 6)	15.648	(0 0 4)	15.649
(0 0 9)	23.565	(0 0 6)	23.567
(0 0 12)	31.598	(0 0 8)	31.601
(0 1 1)	35.740		
		(1 0 0)	35.650
(0 1 2)	36.042		
(0 1 4)	37.228		
		(1 0 3)	37.650
(0 1 6)	39.137	(1 0 4)	39.147
		(0 0 10)	39.797
(0 1 7)	40.336		
		(1 0 5)	41.003
(0 1 8)	41.685		
(0 1 9)	43.171	(1 0 6)	43.181
(0 1 10)	44.785		
		(1 0 7)	45.647
(0 1 11)	46.517		
(0 1 12)	48.359	(1 0 8)	48.370
(0 1 13)	50.304		
		(1 0 10)	54.485

Table 5.1: Calculated scattering angles with unit cell A (left columns) and unit cell B (right columns), discussed in text for the $Na_{0.5}Fe_{0.5}Mn_{0.5}O_2$ material.

Refined values of lattice parameters and the c/a ratio for the $Na_xFe_xMn_{1-x}O_2$ samples are shown in Figure 5.5. The a-axis increases linearly while the c-axis decreases linearly with x. This results in a small increase in the cell volume as x is increased. However, the calculated crystallographic density increases substantially (linearly from 4.10 g/cc to 4.33 g/cc) over this range, since the molar mass of the samples increases with x. The values of

c/a diverge significantly from the ideal rocksalt structure which has a value of c/a = 4.9, indicating significant elongation of the c-axis due to a well-defined layered structure.

Figure 5.5 also shows the lattice parameters of $Na_xFe_xTi_{1-x}O_2$ as determined by Rietveld refinement, in comparison to those synthesized by Li *et al.* [61]. The lattice parameters are very similar to those previously reported and best fit lines to all available data are shown for comparison. Values of the calculated densities are also shown. Calculated crystallographic densities of the $Na_xFe_xTi_{1-x}O_2$ vary linearly from 4.33 to 4.02 g/cm^3 as x decreases from 1 to 0.75. Values of c/a are substantially larger than the ideal value of c/a = 4.9 for the rocksalt structure, due to expansion along the c-axis, as caused by Na vacancies in an ordered layered structure.

The c-axis lattice constant is the same for both $Na_xFe_xMn_{1-x}O_2$ and $Na_xFe_xTi_{1-x}O_2$ over the entire range $0.65 \leq x \leq 1$. From this it can be reasoned that the c-lattice constant is strongly dependent on the Na occupancy. The value of the a-axis lattice constant appears to depend on the identity of the substituted transition metal, as evidenced by the difference in slope seen for Ti and Mn, and may be attributed to the different ionic radius of the Mn and Ti ions.

Figure 5.6 shows the XRD pattern for a single phase O3-$Na_{0.85}Fe_{0.85}Sn_{0.15}O_2$. The lattice parameters for this compound stabilized toward a = 3.04 Å and c = 16.34 Å. The value of the c-axis parameter is similar to those for the Ti and Mn substituted samples, but the a-axis parameter is significantly larger.

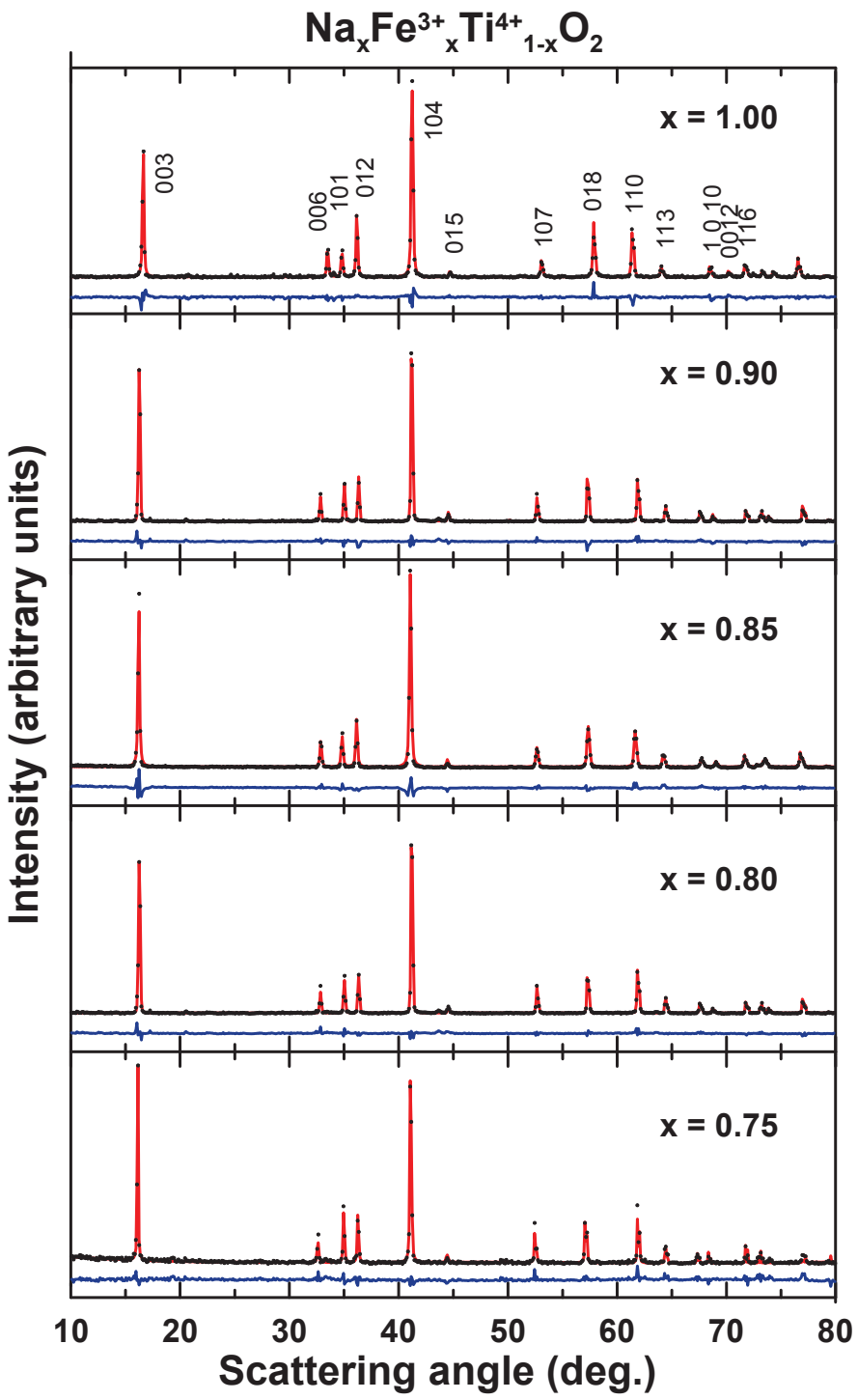

Figure 5.4. XRD patterns for $Na_xFe_xTi_{1-x}O_2$ samples with x values indicated. Difference plots are shown in blue.

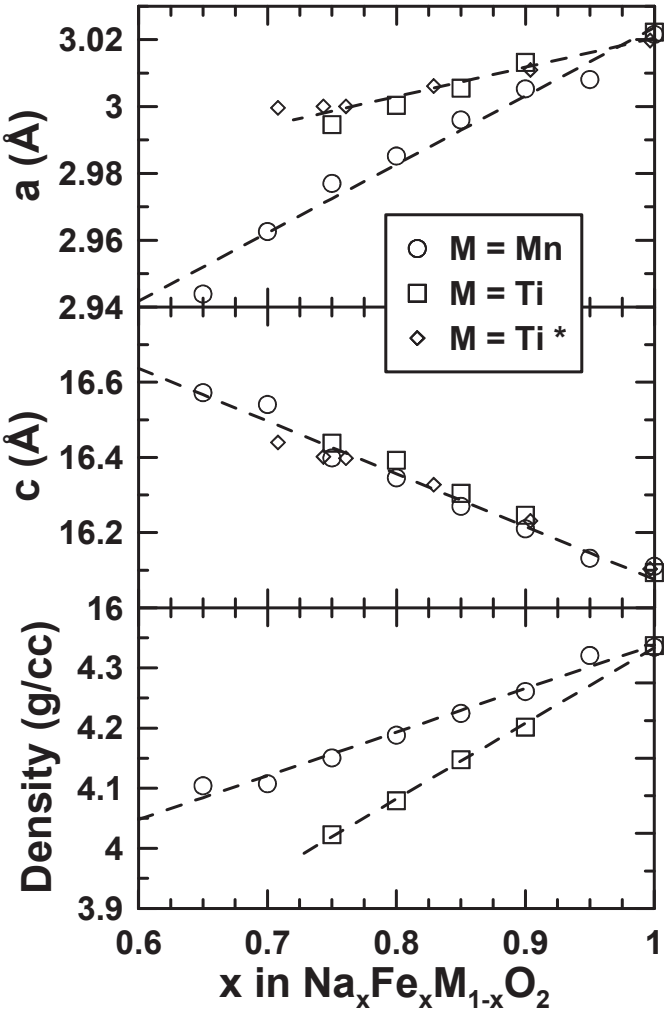

Figure 5.5: Lattice parameters of the rhombohedral unit cell and calculated crystallographic density for O3- $Na_xFe_xMn_{1-x}O_2$. Lattice parameters and densities for $Na_xFe_xTi_{1-x}O_2$ are shown for comparison. Data from Li *et al.* (highlighted *) for $Na_xFe_xTi_{1-x}O_2$ [61] are also shown.

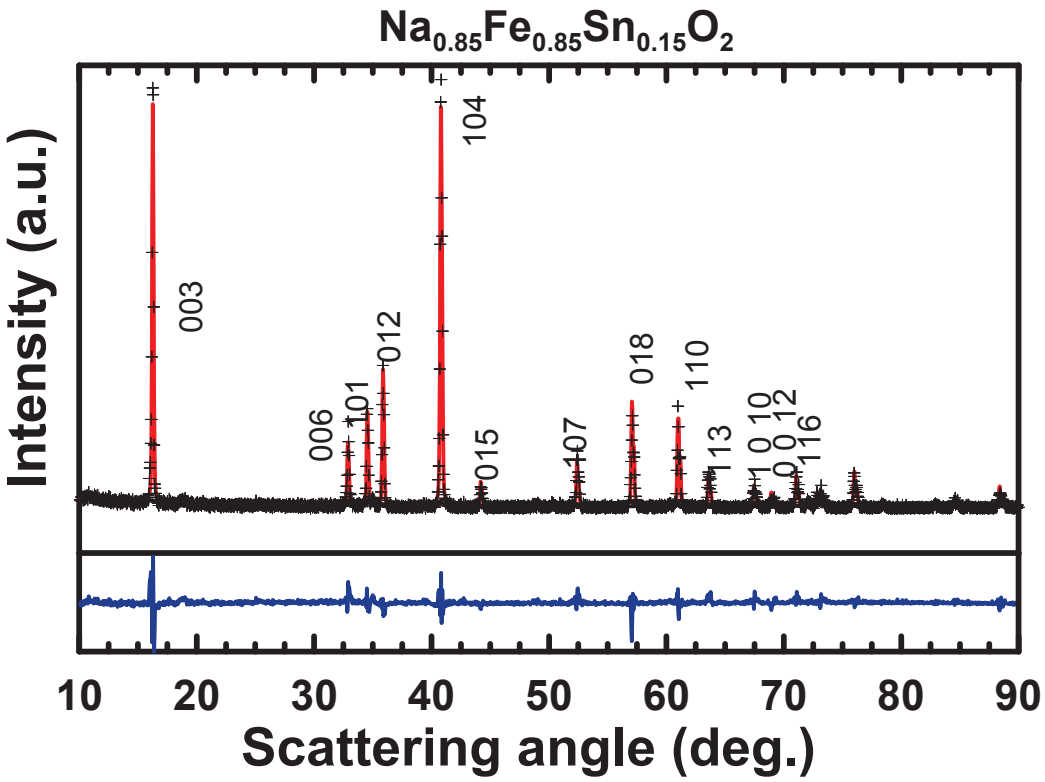

Figure 5.6: Fitted XRD pattern of $Na_{0.85}Fe_{0.85}Sn_{0.15}O_2$ with difference plot.

5.4 CHARACTERIZATION BY MÖSSBAUER SPECTROSCOPY

Figure 5.7 (a) and (b) shows ^{57}Fe Mössbauer spectra for $Na_xFe_xMn_{1-x}O_2$ samples with $0.5 \leq x \leq 1.0$. Figure 5.8 shows Mössbauer spectra for $Na_xFe_xTi_{1-x}O_2$ samples and were found to be similar to the $Na_xFe_xMn_{1-x}O_2$ samples. All spectra were fit using a combination of three (or when necessary four) distinct Fe sites. Negligible amounts of Fe^{4+} were detected in all samples (i.e. 2% or less), which suggests that the transition metal layer can be assigned to oxidation states $Fe^{3+}{}_xMn^{4+}{}_{1-x}$ and $Fe^{3+}{}_xTi^{4+}{}_{1-x}$, or $Fe^{3+}{}_xSn^{4+}{}_{1-x}$ (not shown) based on the condition of charge neutrality. Two distinct Fe^{3+} environments can be detected when $x < 1$. These sites are labeled here as $Fe^{3+}(1)$ sites and $Fe^{3+}(2)$ sites.

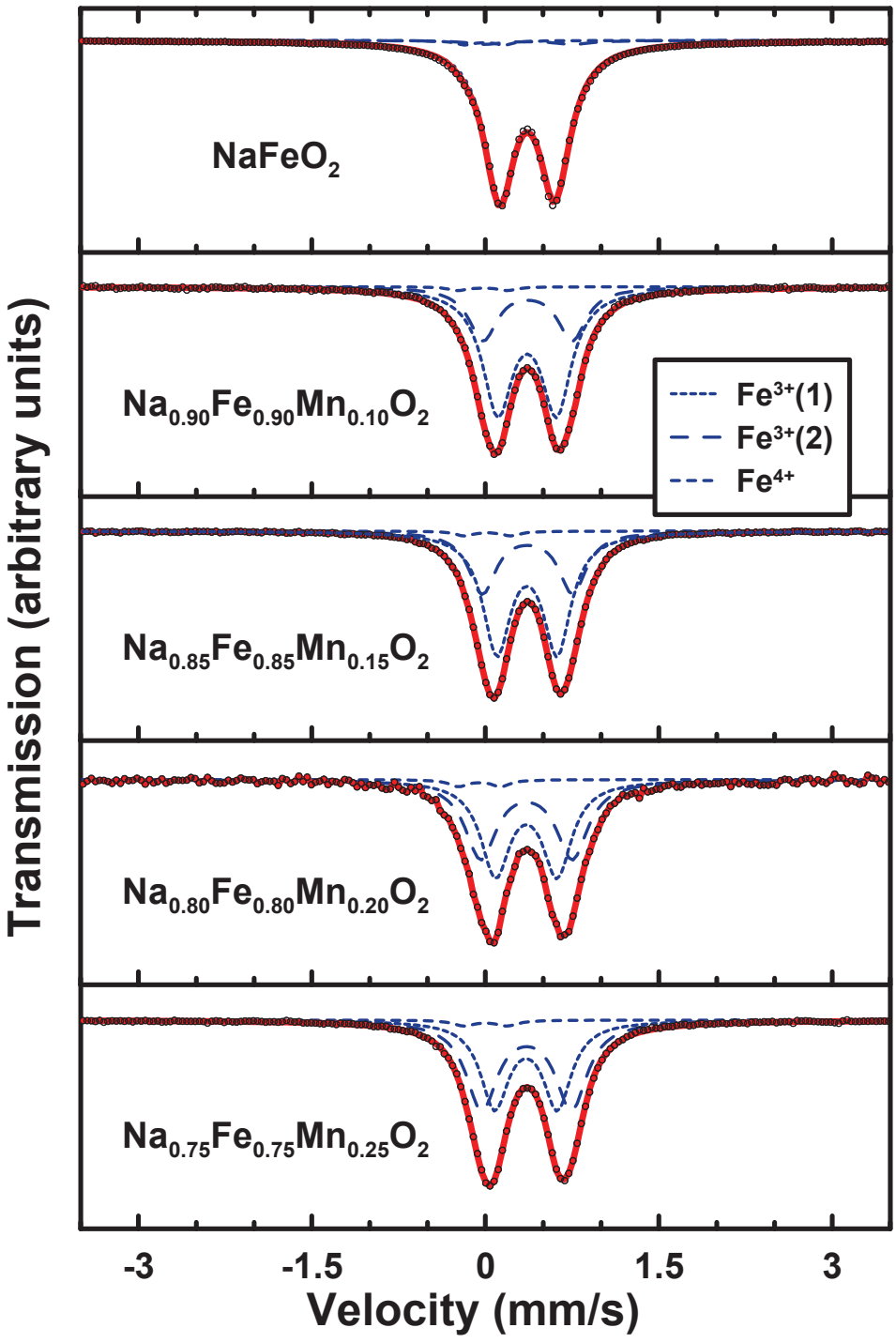

Figure 5.7 (a) ^{57}Fe Mössbauer effect spectra from $Na_xFe_xMn_{1-x}O_2$ for $1.00 \geq x \geq 0.75$. Fitting components are shown as broken lines, with their sum shown as solid lines. Data are shown as circles.

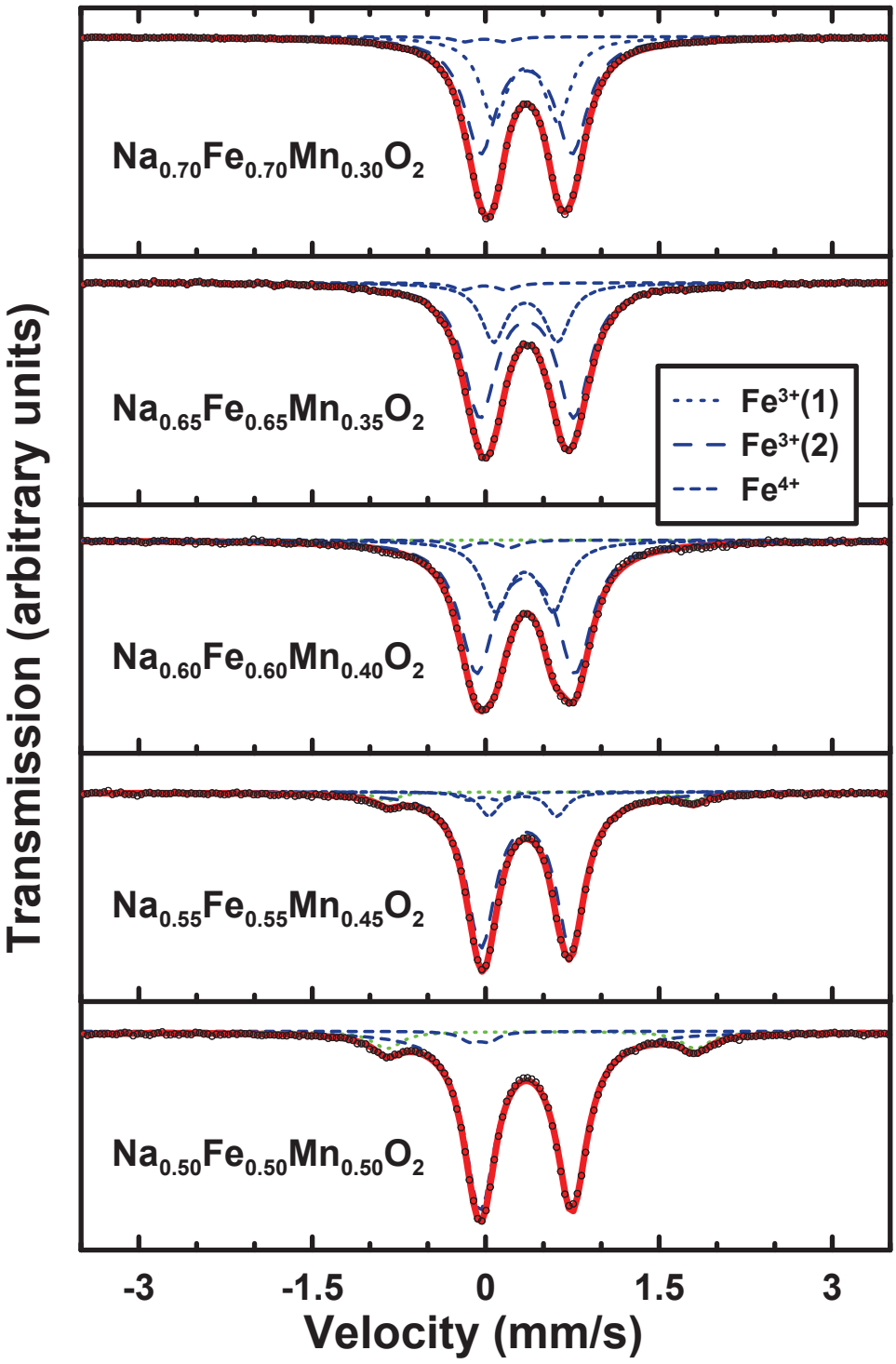

Figure 5.7 (b) ^{57}Fe Mössbauer effect spectra from $Na_xFe_xMn_{1-x}O_2$ for $0.7 \geq x \geq 0.5$. Fitting components, their sum and the data points are shown. The magnetic Fe^{3+} component is shown in green.

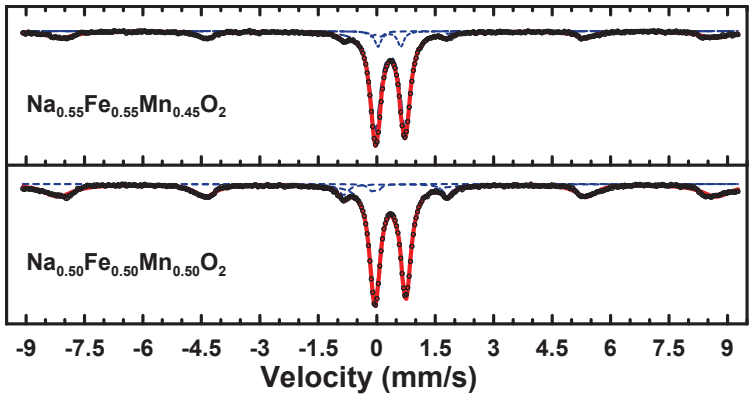

Figure 5.7 (c): Expanded ^{57}Fe Mössbauer effect spectra for the x = 0.5 and 0.55 samples to show the magnetic component.

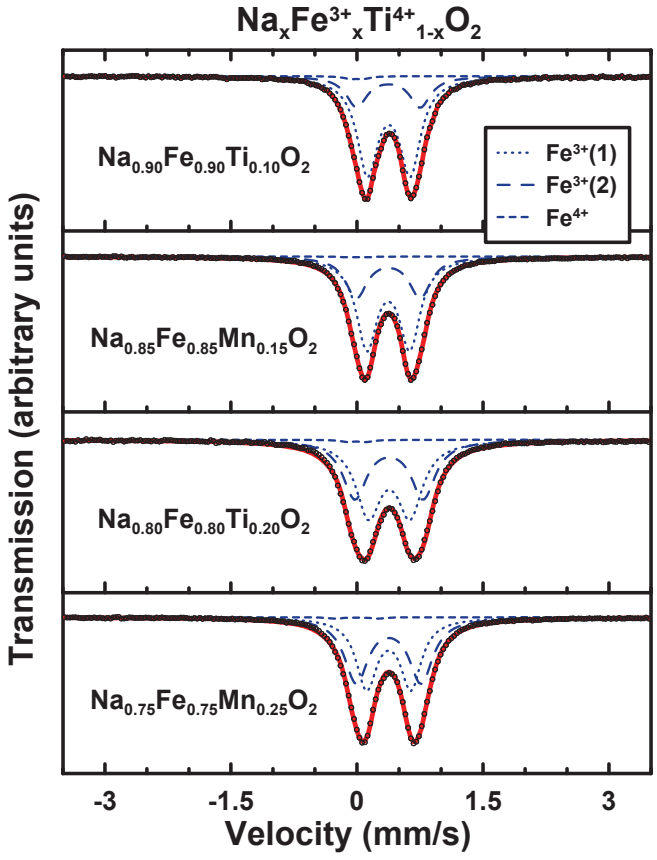

Figure 5.8. Room temperature ^{57}Fe Mössbauer spectra for $Na_xFe^{3+}{}_xTi^{4+}{}_{1-x}O_2$ with x values given, fit using the Na occupancy model described in the text.

x	Site	CS (mm/s)	QS (mm/s)	H (T)	Area (%)
1.00	Fe^{3+}(1)	+0.360	0.477	-	96
	Fe^{3+}(2)	+0.368	0.775	-	3
	Fe^{4+}	+0.008	0.338	-	2
0.90	Fe^{3+}(1)	+0.361	0.507	-	70
	Fe^{3+}(2)	+0.365	0.770	-	29
	Fe^{4+}	-0.023	0.426	-	1
0.85	Fe^{3+}(1)	+0.360	0.521	-	65
	Fe^{3+}(2)	+0.364	0.781	-	33
	Fe^{4+}	+0.018	0.403	-	2
0.80	Fe^{3+}(1)	+0.354	0.534	-	52
	Fe^{3+}(2)	+0.356	0.792	-	46
	Fe^{4+}	-0.050	0.363	-	2
0.75	Fe^{3+}(1)	+0.352	0.542	-	46
	Fe^{3+}(2)	+0.356	0.775	-	52
	Fe^{4+}	+0.001	0.372	-	2
0.70	Fe^{3+}(1)	+0.347	0.550	-	36
	Fe^{3+}(2)	+0.351	0.791	-	62
	Fe^{4+}	-0.011	0.350	-	2
0.65	Fe^{3+}(1)	+0.345	0.551	-	24
	Fe^{3+}(2)	+0.346	0.810	-	74
	Fe^{4+}	-0.009	0.373	-	2
0.60	Fe^{3+}(1)	+0.338	0.499	-	26
	Fe^{3+}(2)	+0.349	0.851	-	62
	Fe^{4+}	-0.003	0.425	-	2
	Fe(magnetic)	+0.385	-	51.9	10
0.55	Fe^{3+}(1)	+0.323	0.586	-	7
	Fe^{3+}(2)	+0.347	0.774	-	66
	Fe^{4+}	-0.022	0.267	-	2
	Fe(magnetic)	+0.374	-	52.0	25
0.50	Fe^{3+}(1)	-	-	-	0
	Fe^{3+}(2)	+0.349	0.794	-	59
	Fe^{4+}	-0.054	0.168	-	2
	Fe(magnetic)	+0.374	-	52.3	39

Table 5.2: Fitted room temperature ^{57}Fe Mössbauer effect parameters for the three doublet sites and (where applicable) the sextet component in $Na_xFe^{3+}{}_xMn^{4+}{}_{1-x}O_2$. Typical uncertainties for measured values of the centre shifts (CS) and quadrupole splittings (QS) are about ± 0.005 mm/s.

x	Site	CS (mm/s)	QS (mm/s)	Area (%)
1.00	$Fe^{3+}(1)$ $Fe^{3+}(2)$ Fe^{4+}	+0.373 +0.394 +0.022	0.483 0.960 0.631	93 4 2
0.90	$Fe^{3+}(1)$ $Fe^{3+}(2)$ Fe^{4+}	+0.380 +0.375 -0.019	0.507 0.757 0.158	75 24 1
0.85	$Fe^{3+}(1)$ $Fe^{3+}(2)$ Fe^{4+}	+0.374 +0.372 -0.041	0.511 0.760 0.212	68 32 0
0.80	$Fe^{3+}(1)$ $Fe^{3+}(2)$ Fe^{4+}	+0.385 +0.382 -0.036	0.493 0.814 0.217	56 43 1
0.75	$Fe^{3+}(1)$ $Fe^{3+}(2)$ Fe^{4+}	+0.379 +0.378 +0.069	0.527 0.771 0.515	48 51 1

Table 5.3. Fitted room temperature ^{57}Fe Mössbauer effect parameters for the three doublet sites in $Na_xFe^{3+}_xTi^{4+}_{1-x}O_2$. Typical uncertainties for measured values of the centre shifts (CS) and quadrupole splittings (QS) are about ± 0.005 mm/s.

The fitting parameters for Figure 5.7(a) and (b) are listed in Table 5.2. Table 5.3 lists the fitting parameters for spectra presented in Figure 5.8. The $Fe^{3+}(1)$ and $Fe^{3+}(2)$ have similar centre shifts (CS) in the range of 0.32 - 0.37 mm/s. Site 3 is a doublet with a centre shift near 0 mm/s, indicative of Fe^{4+}. Yabuuchi *et al.* [9] report $Fe^{3+}(2)$ having a CS near 0.25 mm/s and a quadrupole splitting (QS) near 0.81 mm/s in P2 $Na_{2/3}Fe_{1/2}Mn_{1/2}O_2$, which is similar to those reported here for the $Fe^{3+}(2)$ sites in $Na_{0.5}Fe_{0.5}Mn_{0.5}O_2$. A significantly lower value of the centre shift in Yabuuchi's work is

due to the low temperature measurement at 5 K, compared to room temperature in this work

Samples with $x < 0.65$ showed an additional spectral component due to an Fe-containing magnetic phase with parameters similar to Fe_2O_3 (with CS near 0.38 and H(T) near 50.5 T) [68] This is evidenced by the additional peaks shown in these spectra in Figure 5.7, and appropriate higher velocity peaks (shown in Figure 5.7 (c)) for a magnetically split sextet. A sextet component with parameters as indicated in Table 5.2 was included in the fits for these spectra. An Fe-containing magnetic phase was also detected in the Mössbauer spectra for P2- $Na_{2/3}Fe_{1/2}Mn_{1/2}O_2$ [9], but had a significantly larger relative area in the fits. XRD patterns showed minimal impurity phases, which do not likely have significant effect on the electrochemical features. Area of the fitting components is not indicative of the proportion of the magnetic phase and layered $Na_xFe_xMn_{1-x}O_2$ phase present which may result from differences in the recoil free fraction of Fe in each respective phase. This is evidenced by the charge capacity of the sample, near 190 mAh/g, which would be significantly different in comparison to the literature [9] where a magnetic phase is detected with a much larger area fraction.

For the $Na_xFe_xMn_{1-x}O_2$ and $Na_xFe_xTi_{1-x}O_2$ solid solution series, the Fe^{4+} site area is approximately constant, comprising about 1-2% of the total spectral area in all samples. Inclusion of the Fe^{4+} site near 0 mm/s resulted in fairly significant visual improvement of homogeneity of the residuals and refined the relative area trend of the Fe^{3+} sites. The area of the $Fe^{3+}(2)$ site increases relative to that of $Fe^{3+}(1)$ as the value of x increases, but it is

not coupled with emergence of Fe^{4+} as it is in deintercalated Na_xFeO_2 [71]. From this it can be inferred from the condition of charge neutrality that that the sodium vacancies are preferentially accompanied by the formation of Mn^{4+} or Ti^{4+} (or Sn^{4+}) and not Fe^{4+}.

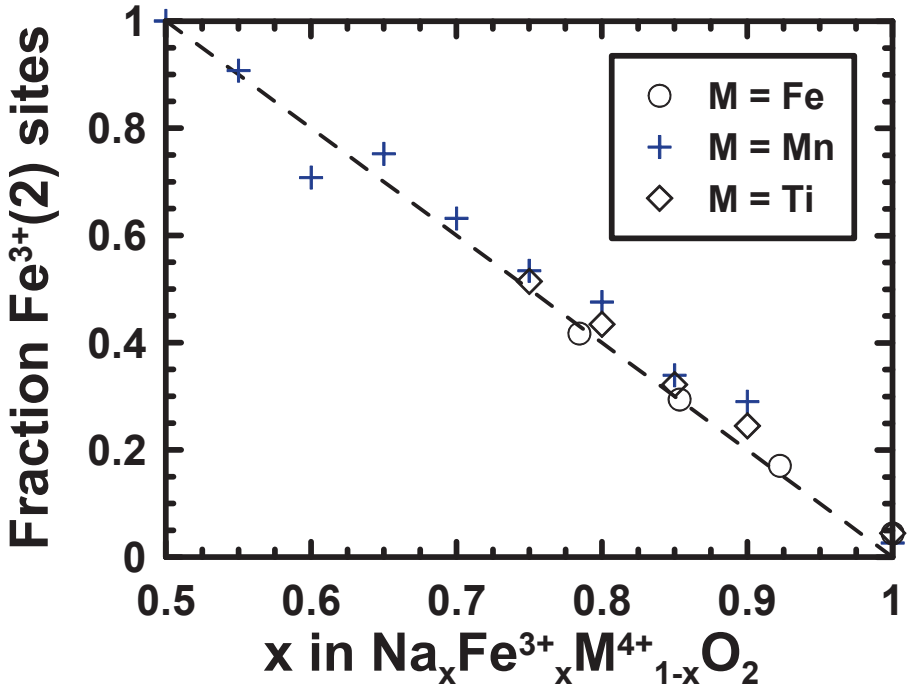

Figure 5.9. Normalized fractional area of Fe^{3+}(2) sites relative to the total Fe^{3+} area for $Na_xFe^{3+}{}_xM^{4+}{}_{1-x}O_2$ samples (the parameter β) with M = Fe, Ti and Mn [27] as a function of x in $Na_xFe^{3+}{}_xM^{4+}{}_{1-x}O_2$.

In the work of Takeda *et al.* [71], elongation is observed for two of the six Fe-O bond lengths in the monoclinic $Na_{0.5}FeO_2$. It was thought that the monoclinic lattice distortion resulting from Na deintercalation was caused by sodium vacancies and not by a cooperative Jahn-Teller distortion from Fe^{4+} ions in the structure. Here, Mössbauer results suggest an assignment of oxidation states according to $Na_xFe^{3+}{}_xM^{4+}{}_{1-x}O_2$ with M = Mn, Ti or Sn. Therefore there are virtually no Jahn-Teller ions present in these samples.

If the interpretation of Takeda is correct, then a monoclinic distortion due to Na-vacancies should also occur for $Na_xFe_xM_{1-x}O_2$. However, no distortion is observed here for $x > 0.7$, as is shown, for instance, in the diffraction pattern in Figure 5.3. This may lead one to suspect that the monoclinic distortion in samples with $y < 1$ in Na_yFeO_2 is induced at least partly by the Jahn-Teller distortion in $Fe^{4+}O_6$ octahedra and not solely by structural compensation for sodium vacancies. Alternatively, and more likely, Li-ion exchange with Na ions in the structure is the source of the monoclinic distortion in Takeda's work [56].

The relative amount of each Fe^{3+} site in $Na_xFe^{3+}{}_xM^{4+}{}_{1-x}O_2$ (the β parameter, defined in Chapter 4) where M = Mn, Ti or Fe is plotted in Figure 5.9 and shows a linear increase in the $Fe^{3+}(2)$ sites at the expense of $Fe^{3+}(1)$ sites as x is increased. Samples having M = Fe^{4+} formed electrochemically [71] and M = Mn^{4+} formed by solid state reaction both appear to have linear trends in β and also have the same endpoints near 0 and 1. This linear trend indicates that for each M^{4+}, where M = Fe, Mn, Ti or Sn, the creation of $Fe^{3+}(2)$ sites is correlated with the introduction of Na^+ vacancies. Introduction of one Na^+ vacancy results in the creation of one $Fe^{3+}(2)$ site at the expense of one $Fe^{3+}(1)$ site, as well as the creation of an M^{4+} site (M^{4+} = Fe^{4+}, Mn^{4+}, Ti^{4+}, Sn^{4+}). This result appears independent of the long range crystallographic arrangement, which may influence precise values of parameters such as CS and QS. Best fit values from Table 5.2 are consistent with the continued trend even though the well ordered α-$NaFeO_2$ type structure is not observed for samples with $x < 0.65$. The $Fe^{3+}(1)$ and $Fe^{3+}(2)$ sites have the same centre shifts in the 0.33-0.38 mm/s range (indicative of their charge) but can be distinguished

based on the value of their quadrupole splittings. It is believed that the creation of the $Fe^{3+}(2)$ is a result of additional electronic asymmetry created by the introduction of a Na^{+} vacancy in the adjacent layer near the Fe^{3+} site and therefore has a higher quadrupole splitting (near 0.8 mm/s) in comparison to the $Fe^{3+}(1)$ site (near 0.5 mm/s). This Na vacancy model potentially has broader implications and may be useful as a probe for Na-vacancies in iron containing Na-ion cathode materials in general, as is explored in later sections.

5.5 ELECTROCHEMISTRY

Figure 5.10 with Figure 5.11, Figure 5.12 with Figure 5.13, and Figure 5.14 with Figure 5.15 show voltage curves of the $Na_xFe_xMn_{1-x}O_2$ samples and plots of specific capacity as a function of cycle number (where both the discharge capacity and coulombic efficiency are shown) when cycled between 1.5 - 4.0 V and 1.5 - 4.25 V, as indicated in the figures. These figures show the trends which occur as Fe^{3+} oxidation is decreased as Mn is added to the system. The Mössbauer results above suggest that the oxidation states in $Na_xFe_xMn_{1-x}O_2$ are Fe^{3+} and Mn^{4+}. Therefore the first desodiation of this material corresponds to the oxidation of Fe^{3+} to Fe^{4+} as seen by the high voltage charge plateau in Figures 5.9, 5.11 and 5.13, while during the sodiation of $Na_xFe_xMn_{1-x}O_2$, Mn^{4+} will be reduced to Mn^{3+} (also a Jahn-Teller ion). It is possible that $Fe^{3+} \rightarrow Fe^{2+}$ also occurs during sodiation.

A study of Figure 5.11, 5.12, and 5.14 reveals that the x = 0.5 sample has the best capacity retention and highest capacity after 20 cycles in each respective voltage range. Table 5.4 shows the average voltage, maximum capacity, gravimetric energy density and the percentage capacity retention after 20 cycles. The volumetric energy density was not calculated for these samples, as the lattice parameters of the multi phase mixtures could not determined. The capacity retention is calculated by dividing the 20^{th} discharge capacity by the maximum observed discharge capacity.

The maximum energy density achieved for these samples is about 450-460 Wh/kg for the x=0.5 sample when cycled between 1.5 - 4.25 V. For comparison, the pure phase P2 material with starting composition $Na_{2/3}Fe_{1/2}Mn_{1/2}O_2$ has been shown to have an estimated energy density 520 Wh/kg [9]. The $Na_xFe_xMn_{1-x}O_2$ samples presented here have volumetric energy densities in the 1300-1800 Wh/L range, with up to 2130 Wh/L reported These values are low due to the large number of Na-vacancies in the synthesized materials which causes a decrease in density, as well as the need for a source of additional Na in a full cell application when negative capacity is used.

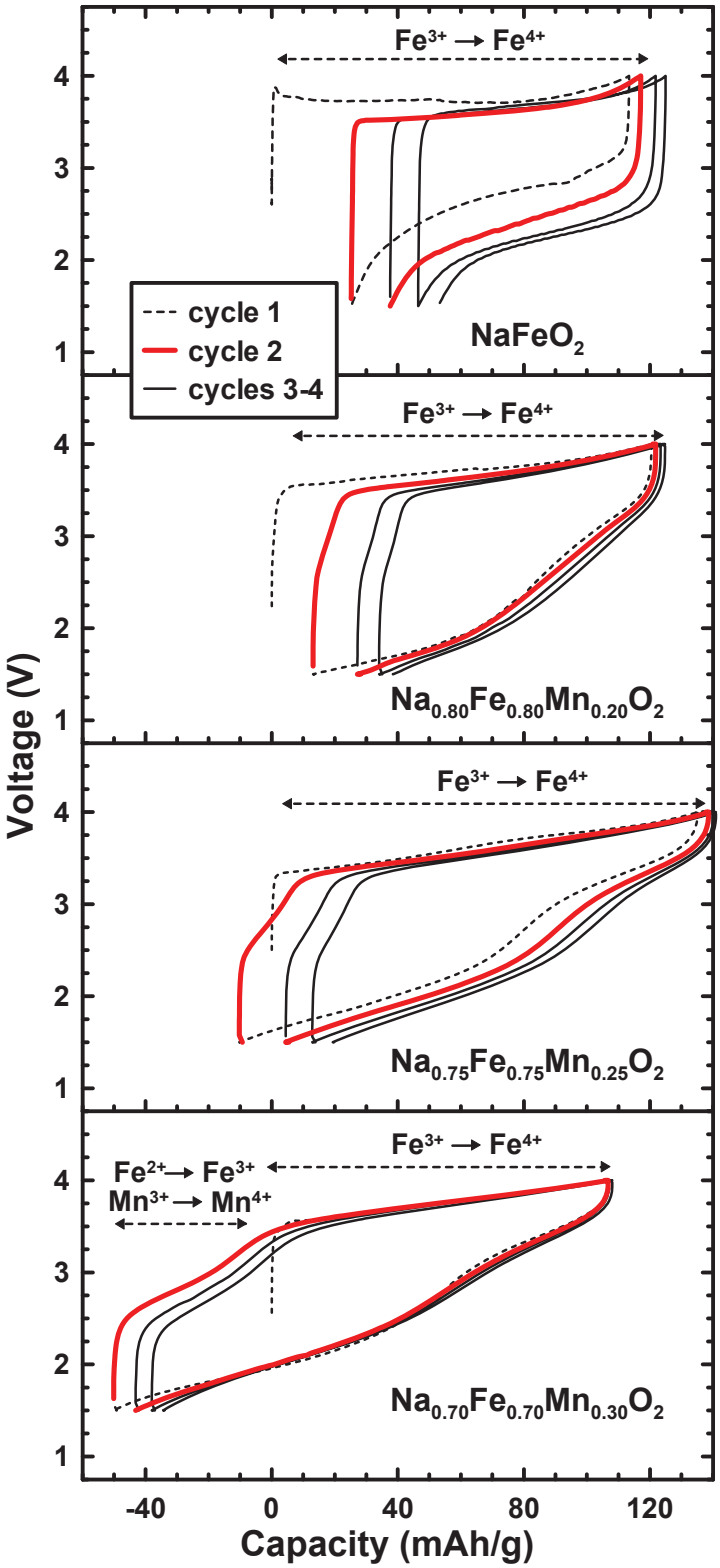

Figure 5.10: Voltage profiles of $Na_xFe_xMn_{1-x}O_2$ for values of x indicated cycled between 1.5-4.0 V and between 1.5-4.0 V. Cycles 1, 2 and 3-4 are shown for comparison.

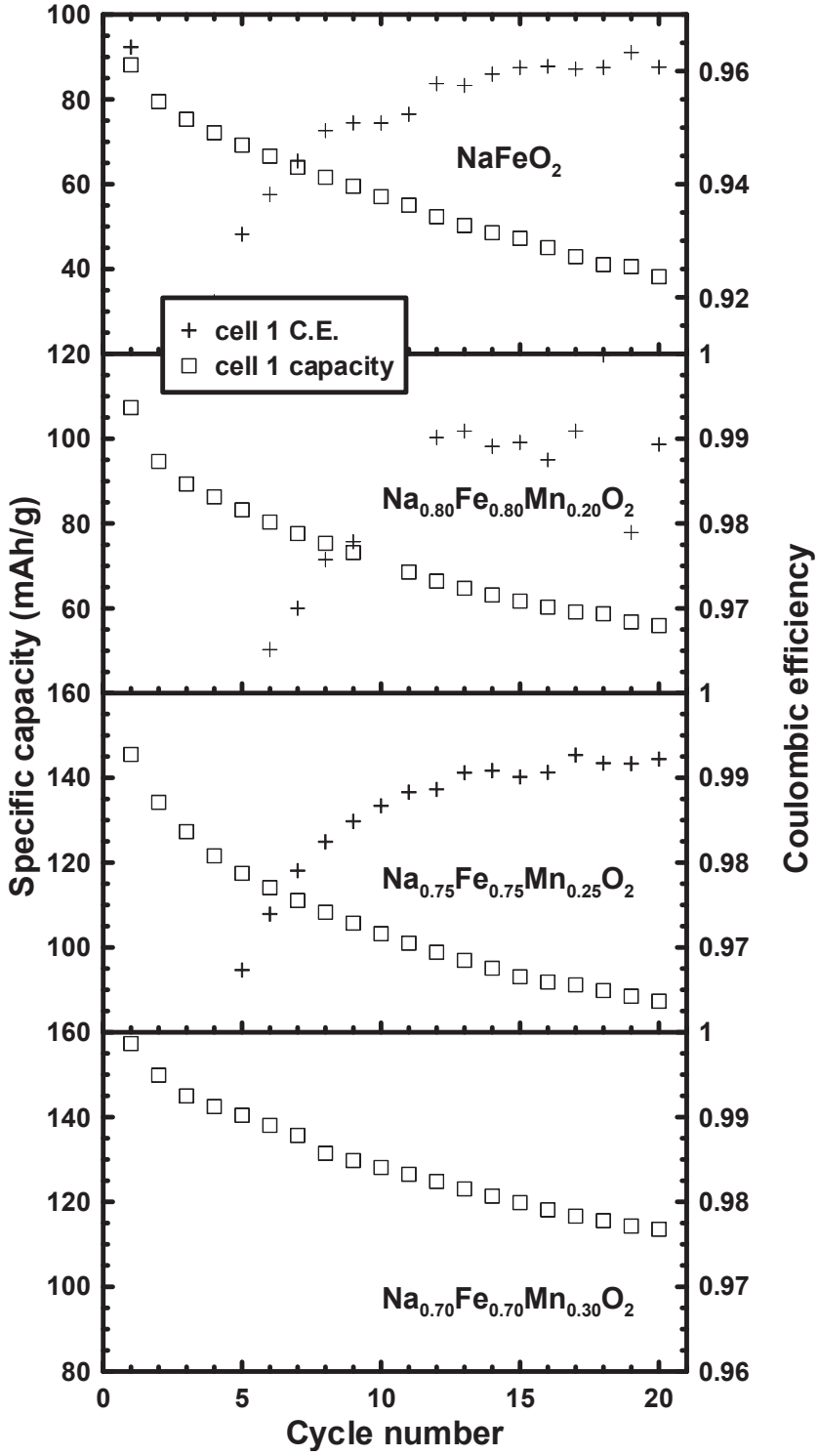

Figure 5.11: Cycle number vs. specific capacity and cycle number vs. coulombic efficiency for cycles 1-20 for selected $NaFe_xMn_{1-x}O_2$

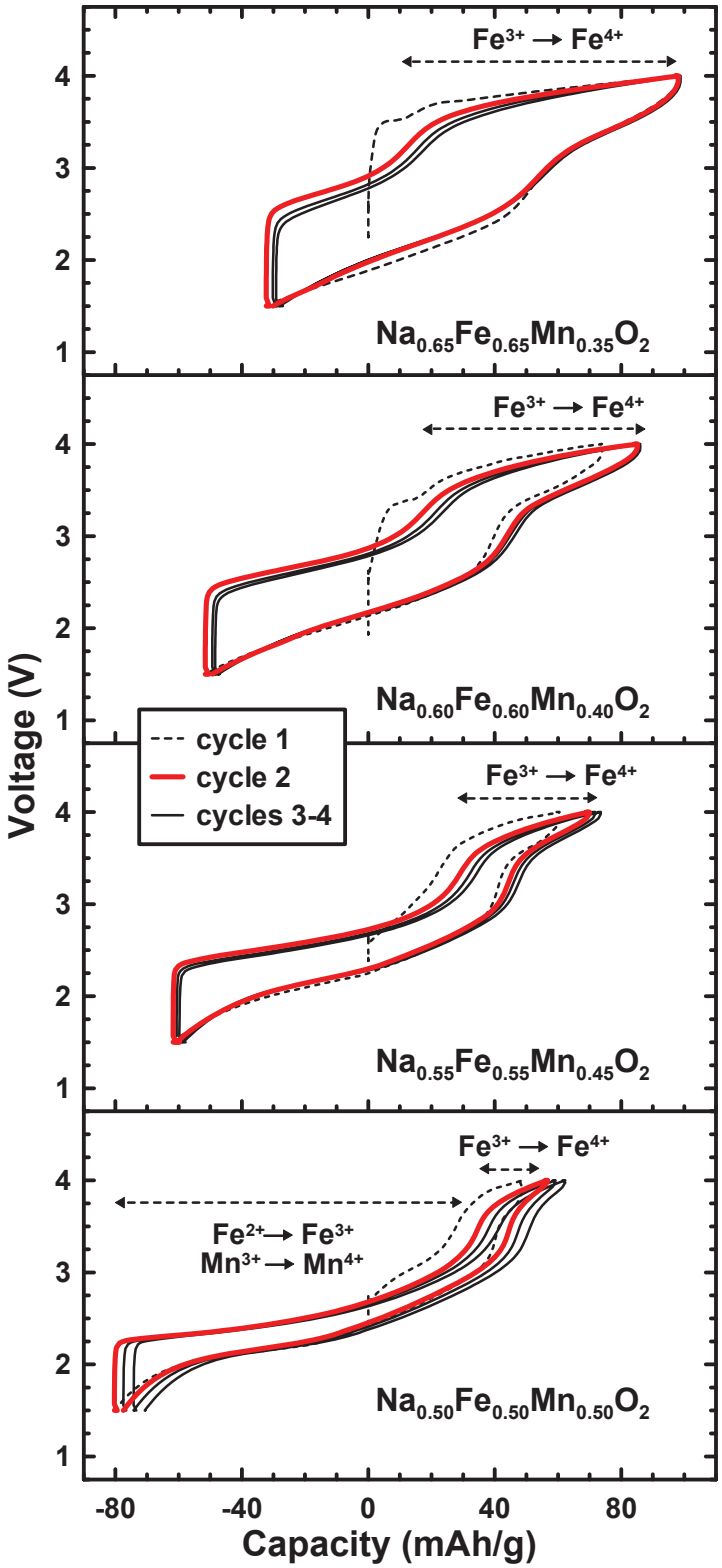

Figure 5.12: Voltage profiles of $Na_xFe_xMn_{1-x}O_2$ for values of x indicated cycled between 1.5-4.0 V. Cycles 1, 2 and 3-4 are shown for comparison.

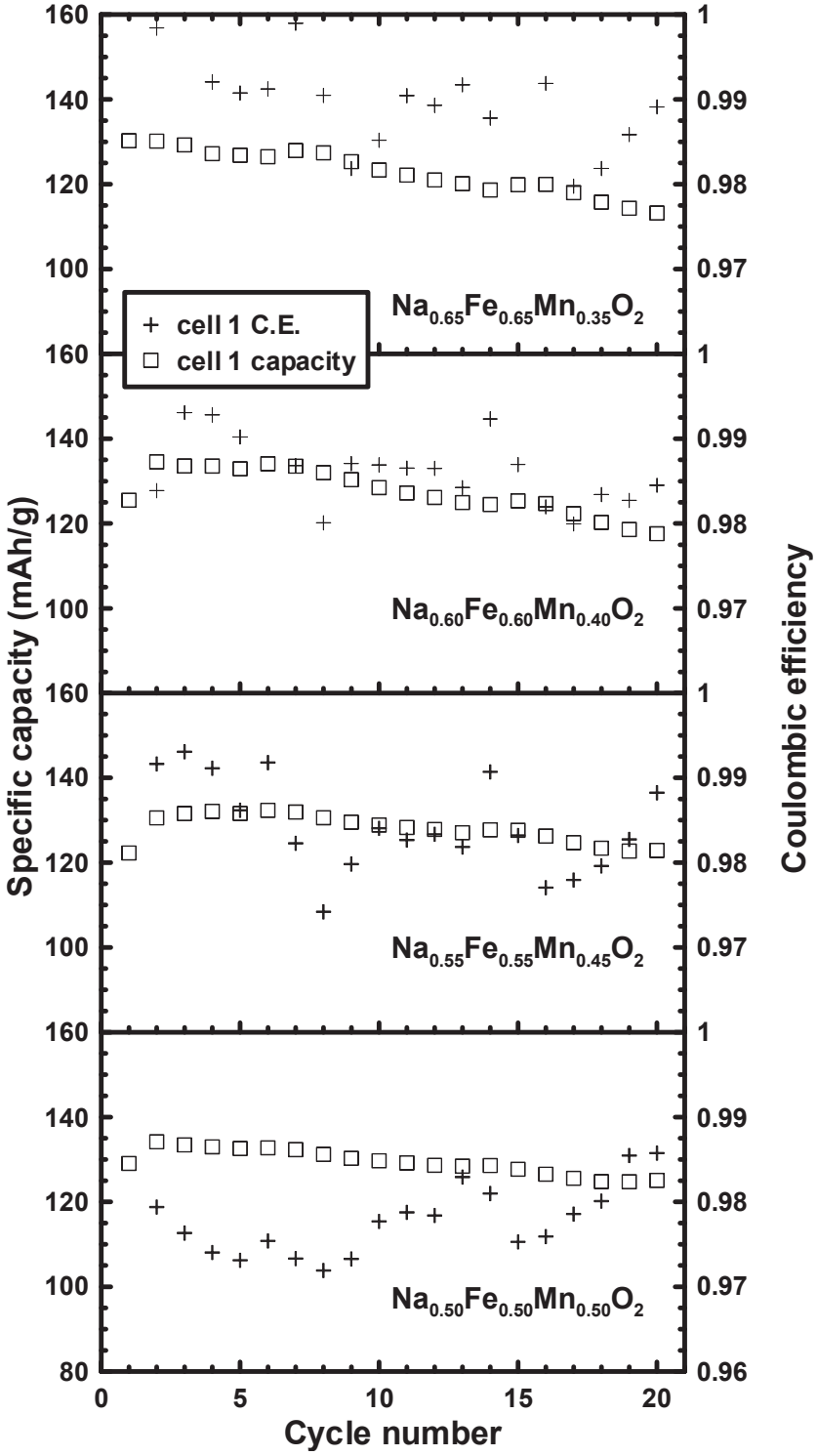

Figure 5.13: Cycle number vs. specific capacity and cycle number vs. coulombic efficiency for cycles 1-20 for selected $NaFe_xMn_{1-x}O_2$.

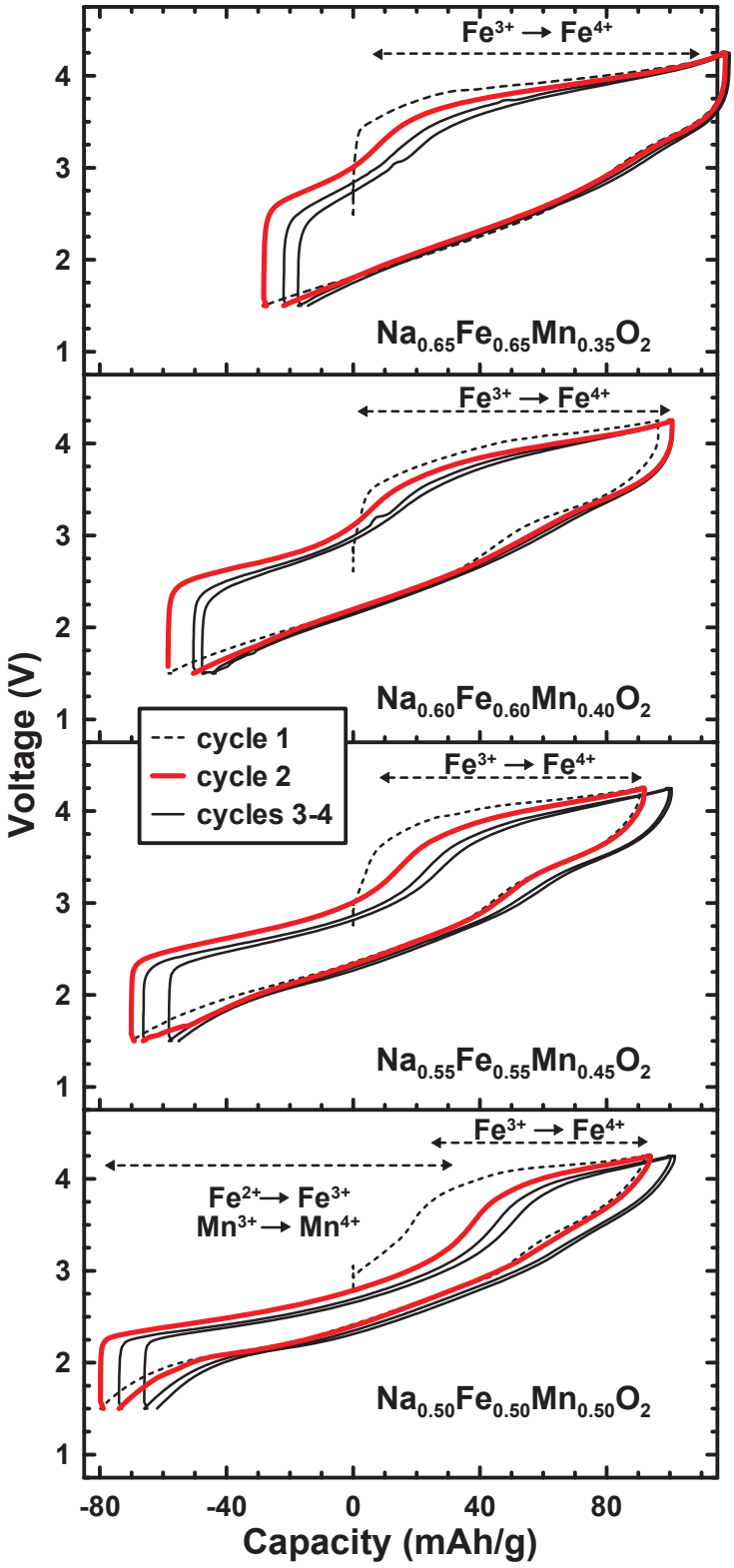

Figure 5.14: Voltage profiles of $Na_xFe_xMn_{1-x}O_2$ for values of x indicated cycled between 1.5-4.25 V. Cycles 1, 2 and 3-4 are shown for comparison.

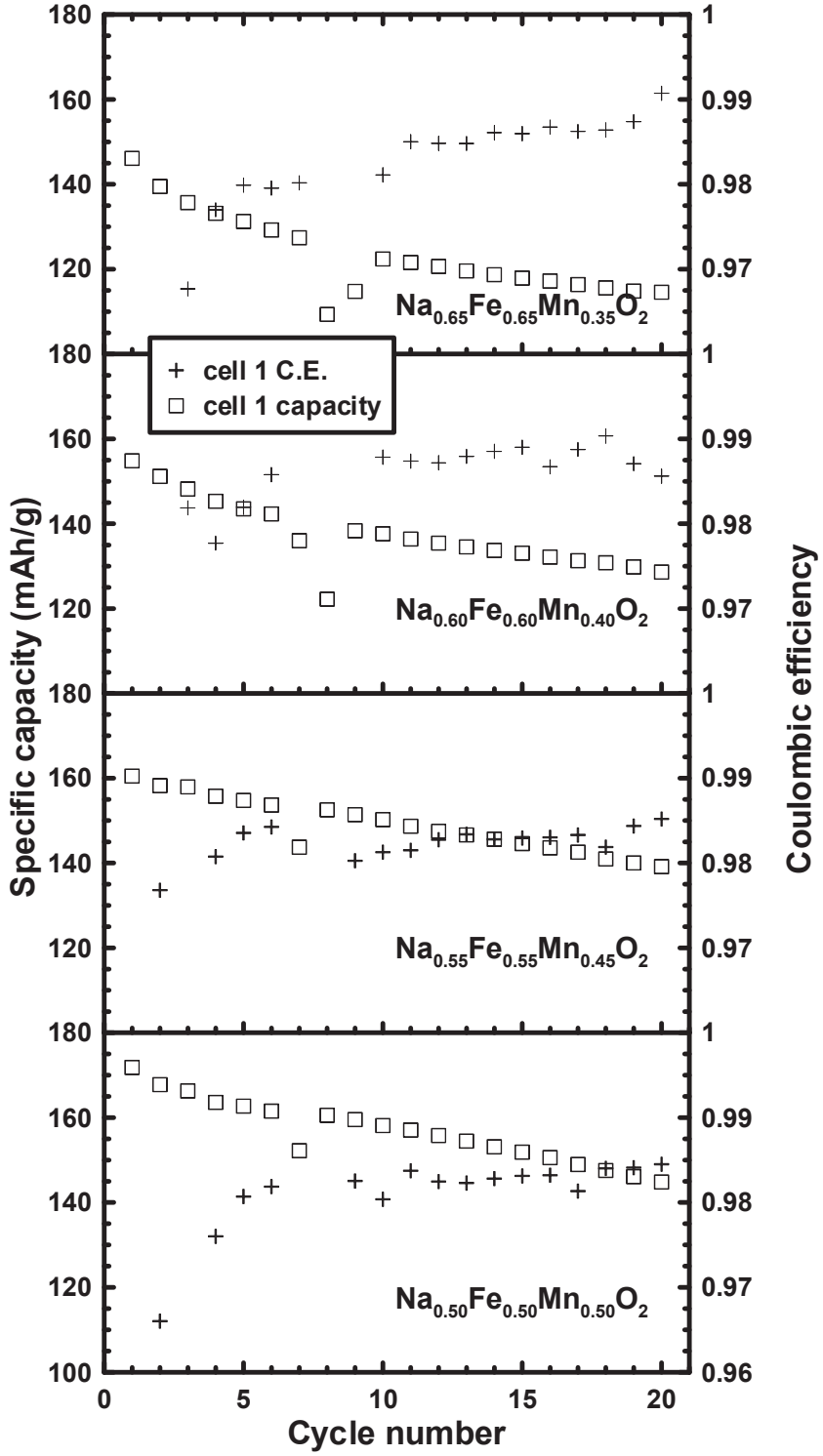

Figure 5.15: Cycle number vs. specific capacity and cycle number vs. coulombic efficiency for cycles 1-20 for selected $NaFe_xMn_{1-x}O_2$.

x	Voltage range (V)	Capacity (mAh/g)	Average voltage (V)	Energy density (Wh/kg)	Energy density (Wh/L)	Capacity retention (%)
0.50	1.5-4.0	135	2.50	338	1344	94
	1.5-4.25	173	2.63	455	1809	85
0.55	1.5-4.0	133	2.56	341	1368	93
	1.5-4.25	161	2.60	420	1685	87
0.60	1.5-4.0	135	2.58	350	1417	88
	1.5-4.25	156	2.55	397	1607	83
0.65	1.5-4.0	131	2.52	331	1352	87
	1.5-4.25	147	2.45	360	1470	78

Table 5.4: Results of electrochemical studies of samples with $0.50 \leq x \leq 0.65$.

Figure 5.16 shows the first cycle voltage curves for $Na_xFe_xMn_{1-x}O_2$ vs. Na cells cycled between 1.5 - 4.0 V and 1.5 - 4.25 V, from which the oxidation states of Fe can be estimated. A small amount of shorting may have occurred for some of these cells during their construction, which shifts the first cycle voltage curve slightly (i.e. a small amount of Mn^{4+} reduction or excess Na in starting materials). Subsequent cycles were not affected by this. The length of the first desodiation plateau increases with x in the sample. Similarly the length of the first sodiation plateau decreases as x is increased (i.e. more sodium vacancies in $Na_xFe_xMn_{1-x}O_2$), which shows that the amount of Fe^{4+} in the charged materials are reduced with higher values of x.

Figure 5.17 shows a proposed mechanism that may be clearly observed for pure single phase $Na_{0.70}Fe^{3+}_{0.70}Mn^{4+}_{0.30}O_2$. The first charge plateau (measured and reproduced identically several times) is similar to that seen in α-$NaFeO_2$. After the first cycle, a lower voltage plateau can be initially seen during charging before the first high voltage charge plateau is repeated identically. The voltage curves show two distinct deintercalation

plateaus with capacities that correspond to the Fe and Mn stoichiometry in the sample, as is illustrated clearly in Figure 5.16 and Figure 5.17. The high voltage deintercalation plateau corresponds to $Fe^{3+} \rightarrow Fe^{4+}$ oxidation, while the low voltage deintercalation plateau corresponds to the $Mn^{3+} \rightarrow Mn^{4+}$ and/or $Fe^{2+} \rightarrow Fe^{3+}$ oxidation. Intercalation from the charged materials has negative capacity when 1.5 V is selected as the lower cutoff. Therefore, the intercalation may contain mixed $Fe^{4+} \rightarrow Fe^{3+}$, $Mn^{4+} \rightarrow Mn^{3+}$, and $Fe^{3+} \rightarrow Fe^{2+}$.

There is a substantial increase in the reversibility and specific capacity as the value of x decreases, for cells cycled in the range of 1.5 - 4.0 V. Substitution of Mn for Fe appears to stabilize these sodium deficient materials and allows for improved energy density and capacity retention in the selected voltage ranges. There is also a steady decrease in the overall polarization or hysteresis in respective voltage ranges as the value x increases. This is shown in Figure 5.18, in which is plotted the average hysteresis as a function of x for samples having $x < 0.7$ cycled between 1.5 - 4.0 V and 1.5 - 4.25 V. There are significantly different values of hysteresis for O3-$NaFe_{1/2}Mn_{1/2}O_2$ vs. P2-$Na_{2/3}Fe_{1/2}Mn_{1/2}O_2$ [9]. Therefore a presence of two phases may contribute to the additional hysteresis introduced as Fe is added. However, it is noted that this difference is much smaller in a comparison of P2- and O3- $Na_{2/3}Fe_{2/3}Mn_{1/3}O_2$ samples, indicating that this difference becomes much less significant as x increases to 2/3 [89].

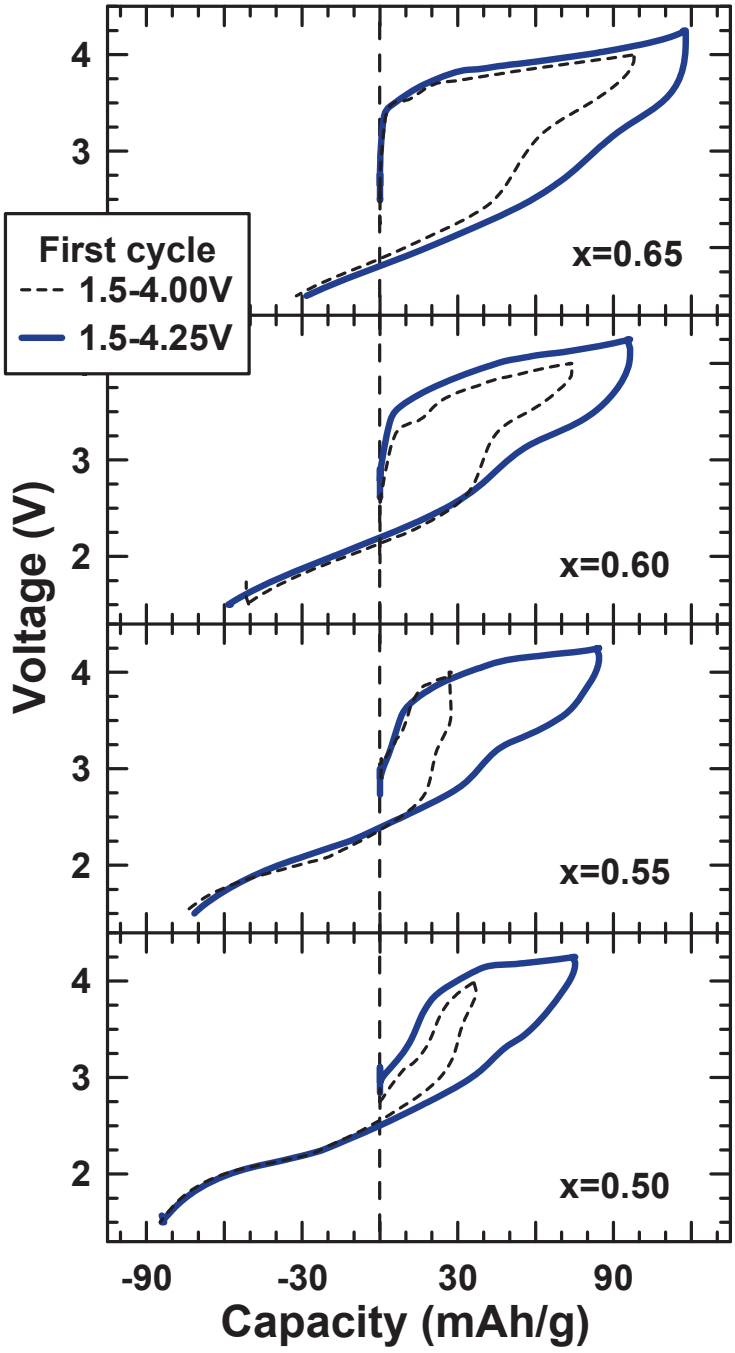

Figure 5.16: First cycle for 1.5-4.0 V (dashed lines) and 1.5-4.25 V (solid lines) for selected cells of $Na_xFe^{3+}{}_xMn^{4+}{}_{1-x}O_2$ as shown. A small amount of shorting may have occurred in some cells, which would result in a slight excess of Na (or Mn^{3+}) in the starting materials.

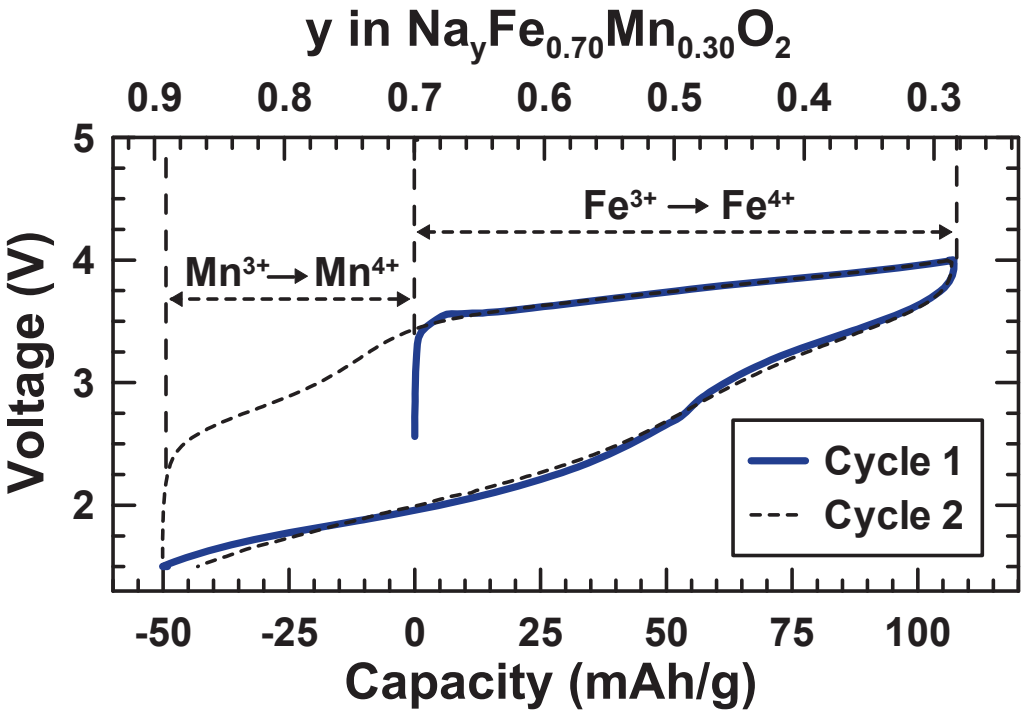

Figure 5.17: Proposed mechanism for the deintercalation voltage plateaus of $Na_{0.70}Fe^{3+}_{0.70}Mn^{4+}_{0.30}O_2$.

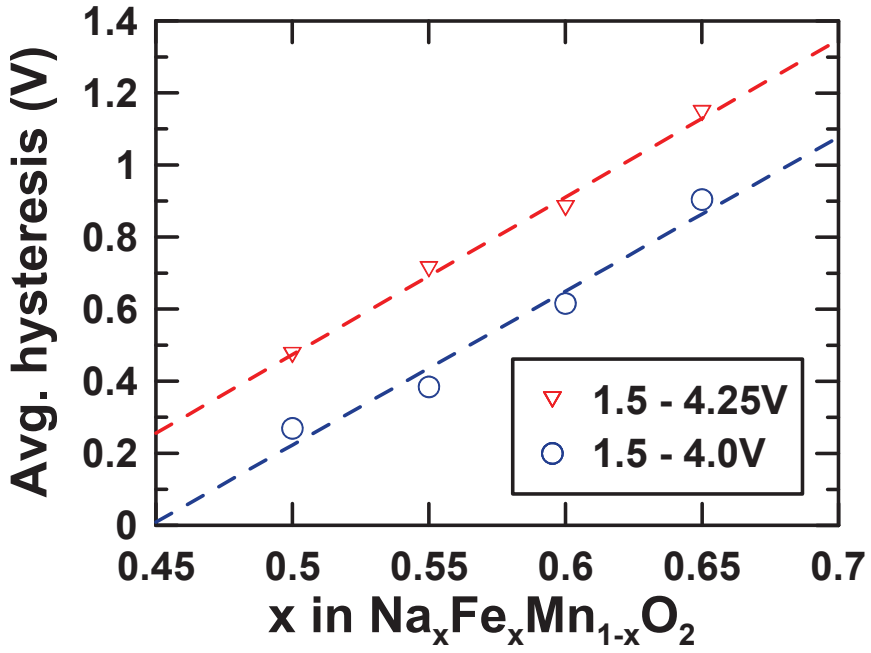

Figure 5.18: The average hysteresis vs. x in $Na_xFe^{3+}_xM^{4+}_{1-x}O_2$ when cycled between 1.5-4.0 V and 1.5-4.25 V. Best fit lines are shown for comparison.

It is possible that consideration of the Jahn-Teller effect may provide clues to the observed stabilization of cycling performance, lower hysteresis and improved energy density for samples with lower values of x. The presence of a network of Mn^{4+} in the $Na_xFe_xMn_{1-x}O_2$ structure during Fe^{3+} oxidation reduces the number of Jahn-Teller ions that are simultaneously active during cycling. One might speculate that this Jahn-Teller inhibiting effect would be maximized near the x = 0.5. This sample has the least voltage hysteresis of the series, as shown in Figure 5.18. Lattice distortions which may be caused by the Jahn-Teller effect might be a contributing factor for the capacity fade observed for samples having higher Fe content. However, no experimental evidence has been found.

Figure 5.19 shows the voltage curve of the x = 0.5 sample first sodiated to 1.5 V before being cycled between 1.5 - 4.25 V. The first charge capacity is in excess of 190 mAh/g. However, this capacity is not observed in subsequent discharge cycles where the capacity was then found to be near 160 mAh/g. Figure 5.19(a) shows an XRD pattern of an x = 0.5 sample discharged to 1.5 V compared with the starting material. A pure phase P2 structure is not formed electrochemically, but appears to be part of a multiphase mixture which resembles the P2 type material.

The voltage curve shown in Figure 5.19(b) in addition to the results in Figure 5.14 show that cycling through the high voltage plateau is a large source of structural instability and capacity fade. Furthermore, cells constructed here contain low purity electrolyte salt and no FEC additive as used in the work of Yabuuchi *et al.* [9], which can also lower

impedance growth on the Na electrode. The formation of the solid electrolyte interface (SEI) layer on the first charge has been shown by Yabuuchi *et al.* [9, 38] to a major factor to high irreversible capacity on the first charge of P2-type $Na_{2/3}Fe_{1/2}Mn_{1/2}O_2$ and may be the main factor here. However, the slope of the capacity fade on a percentage basis is similar to that seen in the previous work [9], indicating that another mechanism is likely responsible for the structural instability during cycling.

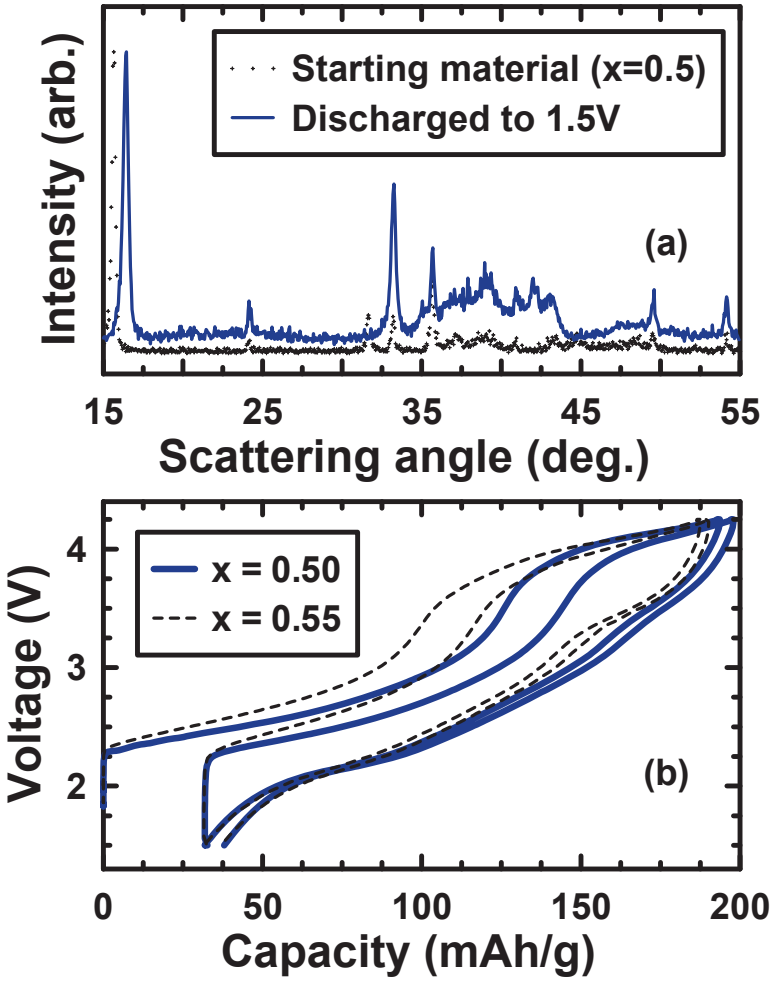

Figure 5.19: (a) XRD of the x = 0.5 composition before discharge (crosses) and after discharging to 1.5 V (solid line) and (b) voltage curves for x = 0.5 (solid line) and x = 0.55 (dashed line) samples cycled to 4.25 V after first discharging to 1.5 V.

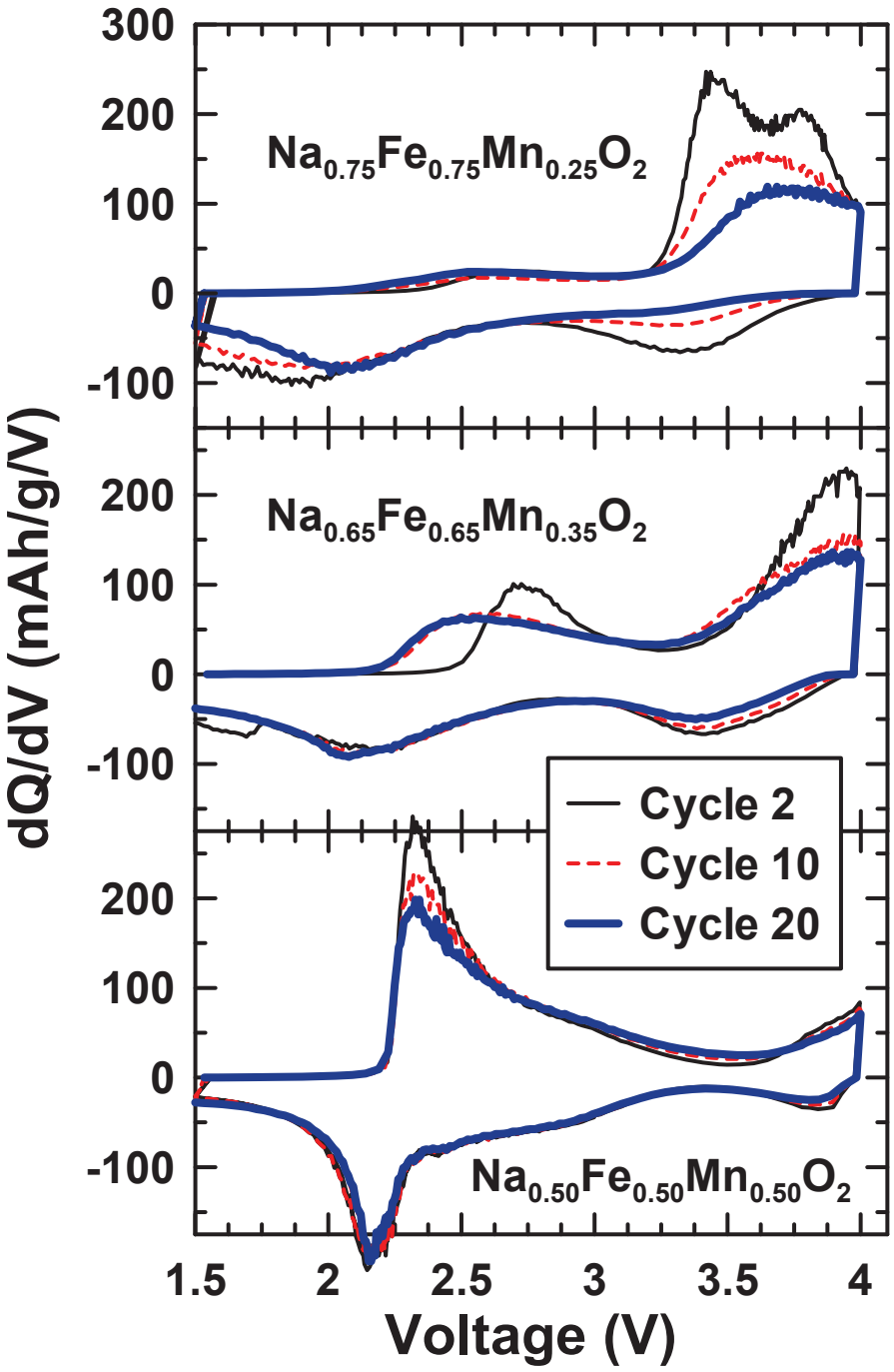

Figure 5.20: dQ/dV as a function of voltage for selected samples. A gradual improvement in cycling stability is observed as the Fe oxidation is replaced with Mn.

All samples that access the high voltage charge plateau (i.e., oxidation of the Fe^{3+}) have poorer capacity retention compared to those that access less of the high voltage plateau. Figure 5.20 shows the differential capacity as a function of voltage for selected samples from Figures 5.9 and 5.11. As the manganese content increases, less of the $Fe^{3+} \rightarrow Fe^{4+}$ deintercalation plateau is accessed, which leads to more stable cycling and less hysteresis. Higher hysteresis and poor capacity retention may be a result of Fe ions migrating away from the transition metal layer when significant amounts of Na vacancies are present in the structure during deintercalation at high voltages.

The capacity retention achieved here for $Na_{0.5}Fe_{0.5}Mn_{0.5}O_2$ (85% after 20 cycles when cycled between 1.5 - 4.25 V) is similar to that for P2 type $Na_yFe_{0.5}Mn_{0.5}O_2$ reported recently (85% after 20 cycles when cycled between 1.5 - 4.3 V) [9]. This may imply that the similar failure mechanism may be occurring when these materials are cycled to a high voltage. If the voltage range is restricted to 1.5 - 4.0 V or less such that access to Fe oxidation is restricted, Figure 5.20 shows that dramatically improved cycling stability can be achieved. Capacity retention well in excess of 90% after 20 cycles is observed for samples with x = 0.5, although the cathode energy density is limited to about 330 - 350 Wh/kg when the negative capacity (excess Na) is included.

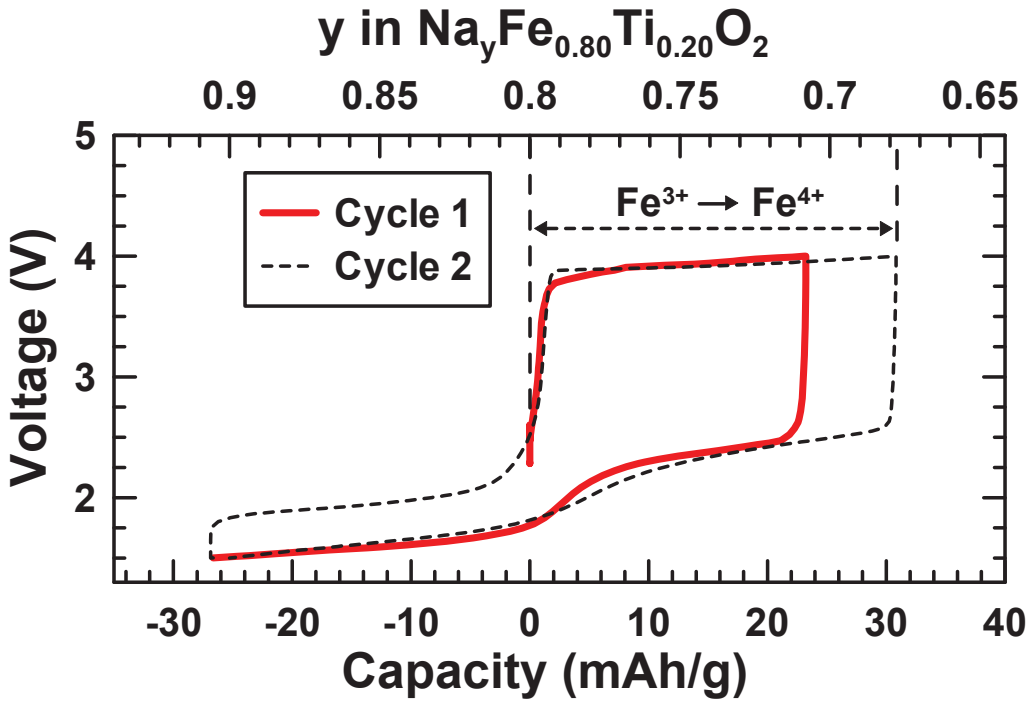

Figure 5.21: First and second cycles of $Na_{0.80}Fe_{0.80}Ti_{0.20}O_2$ showing the region where Fe^{3+} oxidation occurs.

Figure 5.21 shows the voltage profile for the first and second cycles of $Na_{0.80}Fe^{3+}_{0.80}Ti^{4+}_{0.20}O_2$. The oxidation states of the ions in this composition imply that Fe^{3+} oxidation occurs during the first charge, which is exactly analogous to the Mn system. The subsequent discharge half-cycle has a plateau of the same length as the first charge half-cycle, but is separated by considerable hysteresis. This hysteresis is associated with access of the $Fe^{3+} \rightarrow Fe^{4+}$ deintercalation plateau. Moisture exposure may also be a contributing factor. Discharge beyond this plateau results in reduction of Ti^{4+} to Ti^{3+} and/or Fe^{3+} to Fe^{2+}, and is associated with significantly less hysteresis.

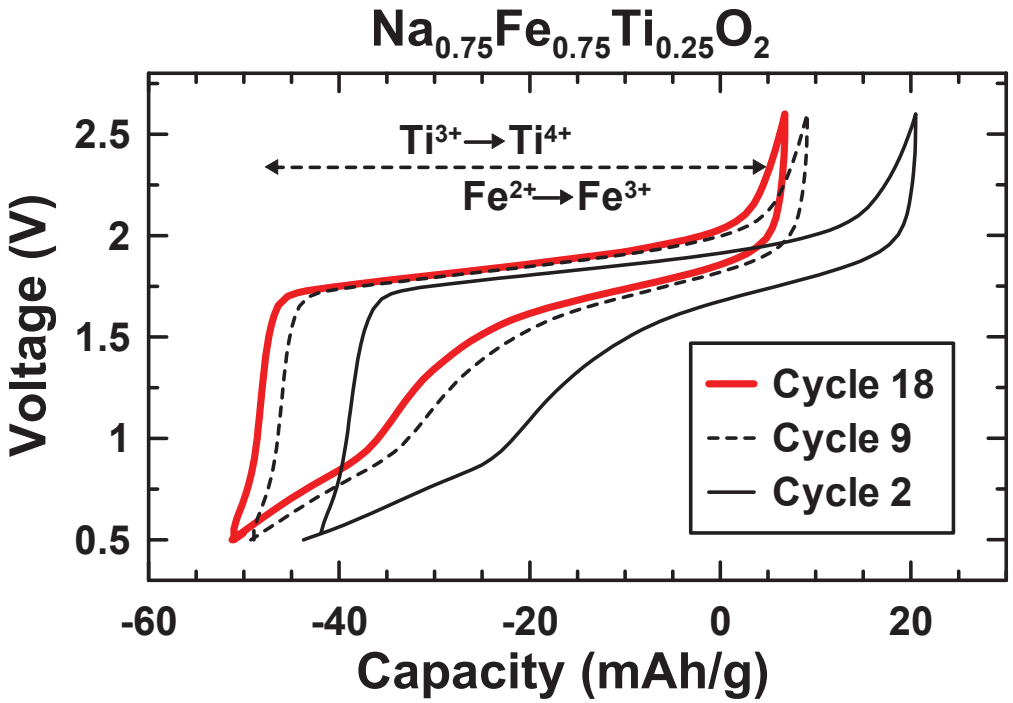

Figure 5.22: Voltage curve of $Na_{0.75}Fe_{0.75}Ti_{0.25}O_2$ cycled in the voltage range 0.5 – 2.6 V, which operates on the $Ti^{3+} \leftrightarrow Ti^{4+}$ and $Fe^{2+} \leftrightarrow Fe^{3+}$ redox couples.

Figure 5.22 shows cycling of $Na_{0.75}Fe_{0.75}Ti_{0.25}O_2$ in the voltage range 0.5 – 2.6 V where cycling was commenced by discharging directly from the starting material. Since all Fe is 3+ in the starting material and Fe^{2+} is measured at 0.5 V, only the $Fe^{2+} \leftrightarrow Fe^{3+}$ and $Ti^{3+} \leftrightarrow Ti^{4+}$ redox couples are accessed during the 2 V plateau. Stable cycling with a capacity of roughly 60 mAh/g or $\Delta y = 0.23$ in $Na_{(0.75 + \Delta y)}Fe_{0.75}Ti_{0.25}O_2$ is observed in the low voltage region. During charging, the low voltage plateau is reversible and has significantly less hysteresis than the high voltage plateau, which is associated with the $Fe^{3+} \leftrightarrow Fe^{4+}$ redox couple. Additionally, charging above 3 V through the high voltage plateau alters the low voltage characteristics in comparison to those cycled below 3 V.

Figure 5.23 shows the voltage vs. specific capacity curves for $Na_xFe_xTi_{1-x}O_2$ with $1 \leq x \leq 0.75$. Figure 5.24 shows the corresponding capacity (or coulombic efficiency) vs. cycle number for $Na_xFe_xTi_{1-x}O_2$ with $1 \leq x \leq 0.75$. These show the trends which occur as Ti is added to $NaFeO_2$. All samples are cycled in the 1.5-4.0 V window unless otherwise indicated. The length of the high voltage $Fe^{3+} \rightarrow Fe^{4+}$ deintercalation plateau decreases as Ti is added or if the voltage window is decreased for each sample. This occurs in a similar manner as discussed for the $Na_xFe_xMn_{1-x}O_2$ samples. Performance on the basis of percentage capacity retention is improved as Ti is added.

Figure 5.25 highlights the similarities between each system, showing voltage curves for later cycles of selected $Na_xFe^{3+}{}_xMn^{4+}{}_{1-x}O_2$ and selected $Na_xFe^{3+}{}_xTi^{4+}{}_{1-x}O_2$ samples. The Fe^{3+} oxidation plateau is shifted to higher voltages with increasing Mn or Ti substitution. This results in less of the Fe^{3+} oxidation plateau being accessed as the amount of Mn or Ti substitution is increased. The poorest reversibility is observed for α-$NaFeO_2$, while steadily increasing capacity retention is observed as less Fe is accessed via the high voltage deintercalation plateau. When primarily $Mn^{3+} \leftrightarrow Mn^{4+}$, $Ti^{3+} \leftrightarrow Ti^{4+}$ and/or $Fe^{2+} \leftrightarrow Fe^{3+}$ redox couples are occurring in the respective systems, the most reversible behaviour is observed, with capacity retention in excess of 90% after 18 cycles [27]. Avoidance of the $Fe^{3+} \leftrightarrow Fe^{4+}$ couple may be essential for stable cycling in $Na_yFe_xM_{1-x}O_2$ when M = Mn and Ti.

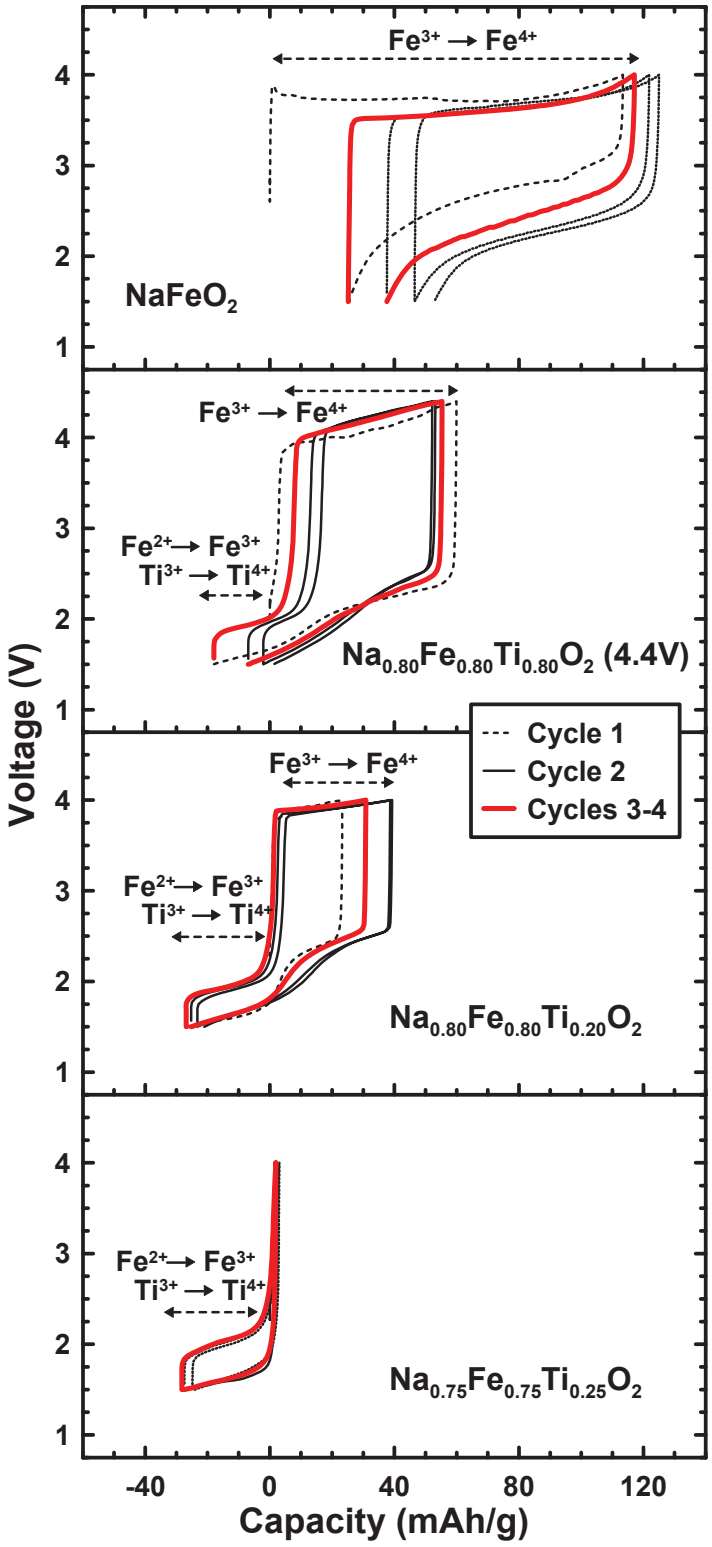

Figure 5.23: Voltage profiles of $Na_xFe_xTi_{1-x}O_2$ for values of x indicated cycled between 1.5-4.0 V and between 1.5-4.4 V (second panel). Cycles 1, 2 and 3-4 are shown.

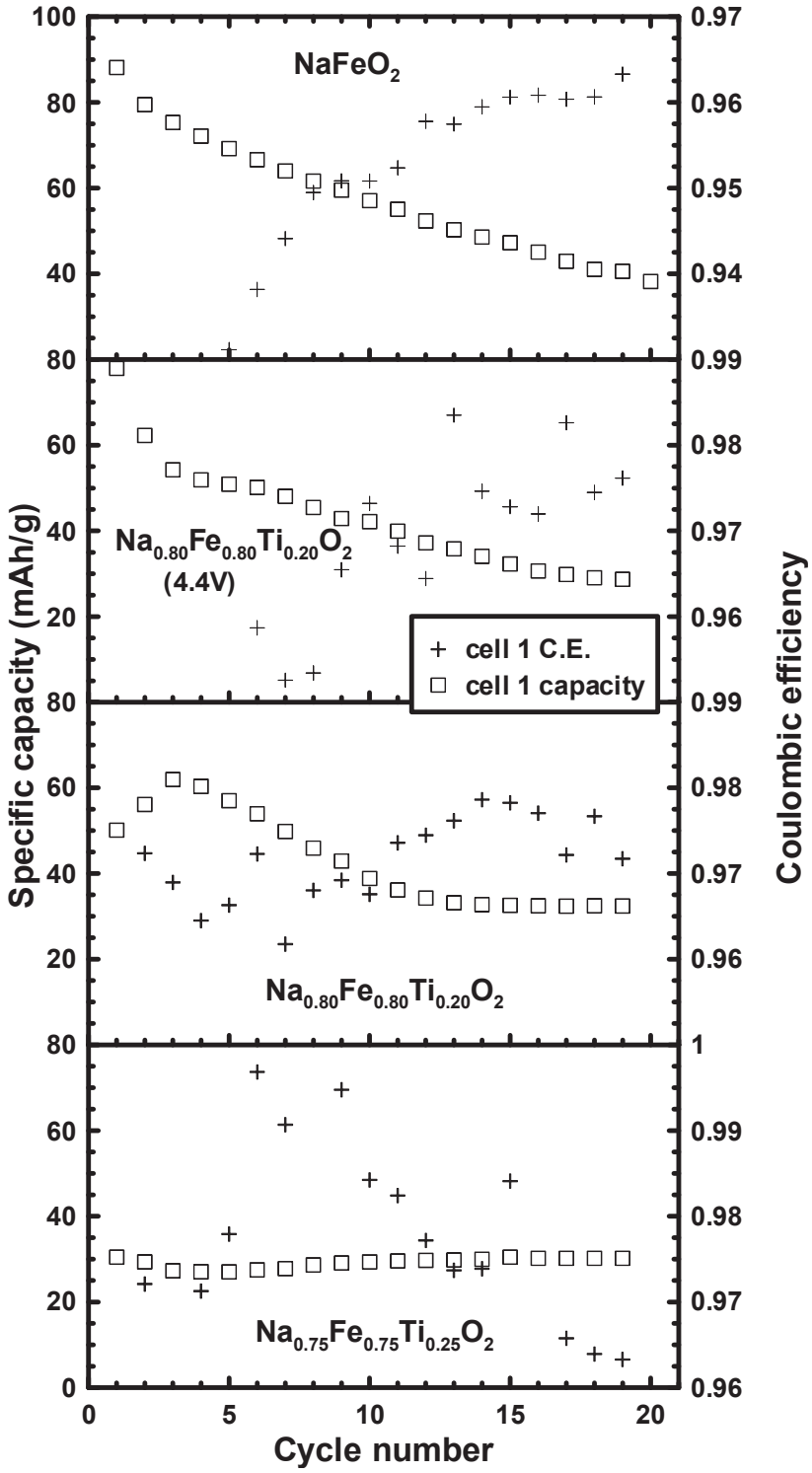

Figure 5.24: Cycle number vs. specific capacity and cycle number vs. coulombic efficiency for cycles 1-20 for $NaFe_xTi_{1-x}O_2$ samples.

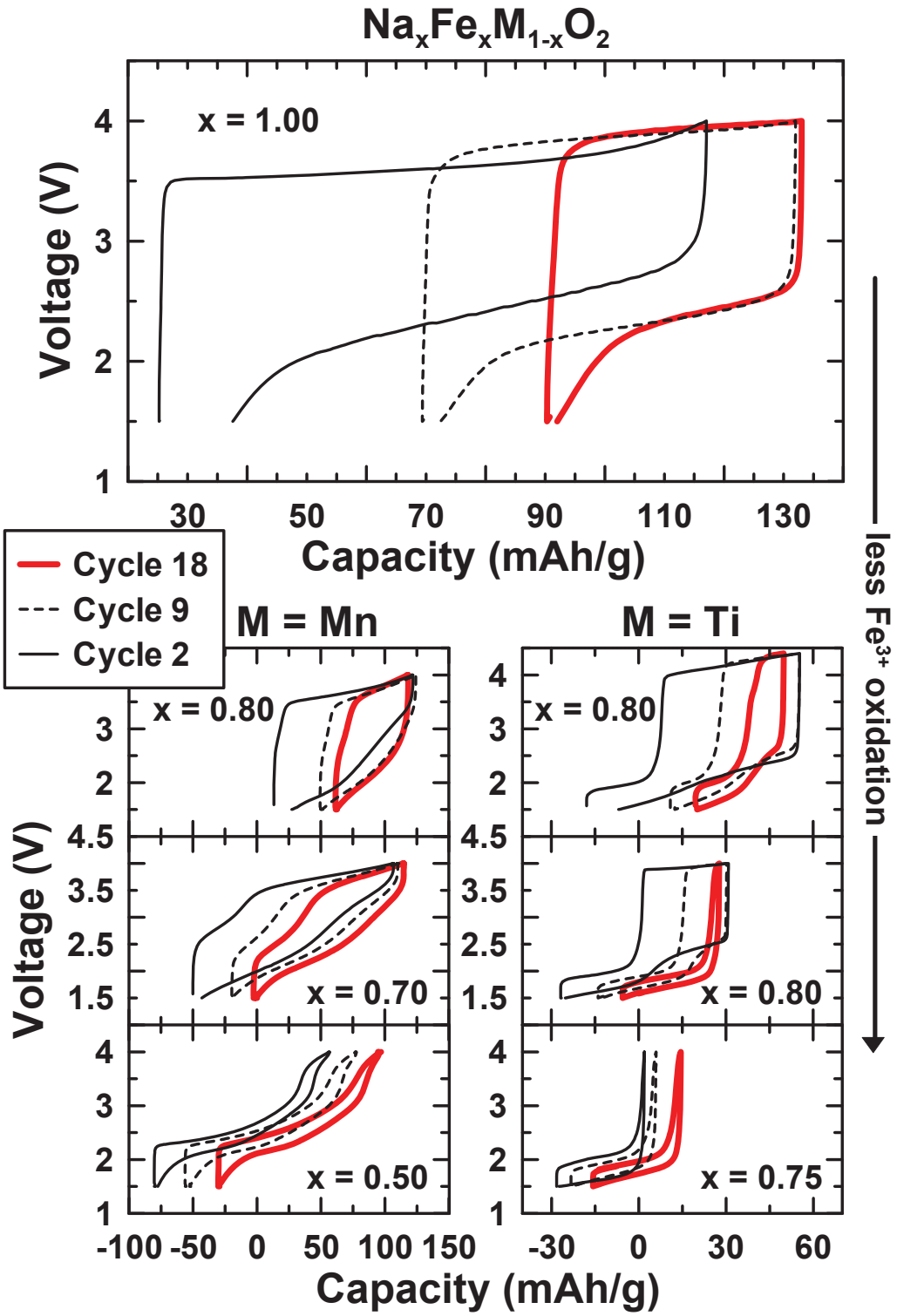

Figure 5.25: Voltage curve of $NaFeO_2$ compared with selected $Na_xFe_xM_{1-x}O_2$ with M = Mn and M = Ti samples sorted based on how much Fe^{3+} oxidation occurs in each cell.

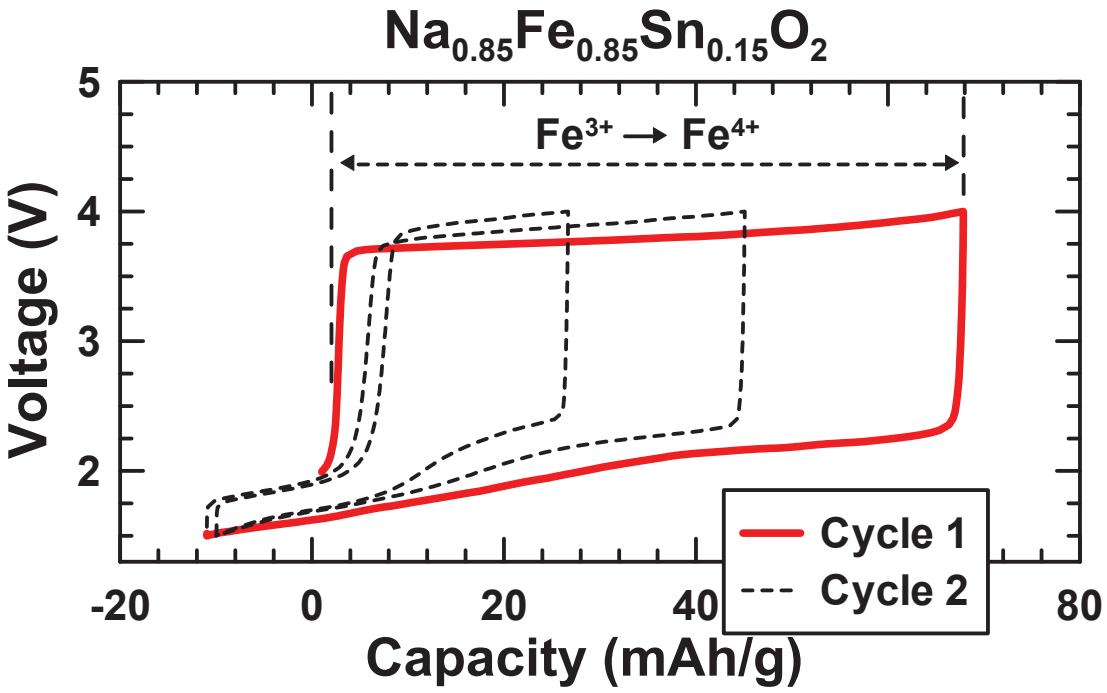

Figure 5.26: First, second and third cycles of $Na_{0.85}Fe_{0.85}Sn_{0.15}O_2$ showing the region where Fe^{3+} oxidation occurs.

Figure 5.26 shows the voltage profile for the first three cycles of O3-$Na_{0.85}Fe^{3+}_{0.85}Sn^{4+}_{0.15}O_2$. The oxidation states of the ions in this composition imply that Fe^{3+} oxidation occurs during the first charge. The subsequent discharge half-cycle has a plateau are shorter in length as compared to the first charge half-cycle, and is separated by considerable hysteresis. This hysteresis and capacity fade is associated with the $Fe^{3+} \leftrightarrow Fe^{4+}$ couple, and moisture exposure may also be a contributing factor. Discharge beyond this plateau results in reduction of Sn^{4+} to Sn^{3+} and/or Fe^{3+} to Fe^{2+}, and is associated with significantly less hysteresis. These results are analogous to those discussed for $Na_xFe_xMn_{1-x}O_2$ and $Na_xFe_xTi_{1-x}O_2$, which provides yet another example indicating that varying the transition metal substitution does not appear to eliminate negative effects of using the $Fe \leftrightarrow Fe^{4+}$ redox couple in these materials.

5.6 CHARACTERIZATION BY EX-SITU MÖSSBAUER AND XRD

Figure 5.27 shows ex-situ Mössbauer effect measurements for $Na_{0.75}Fe_{0.75}Ti_{0.25}O_2$ charged directly to 4.4 V and discharged directly to 0.5 V at 10 mA/g current. Table 5.5 shows the parameters from fits shown in Figure 5.27. After being charged to 4.4 V, the relative area of the $Fe^{3+}(2)$ site remains constant in comparison to the uncharged material, but the area of the $Fe^{3+}(1)$ site has decreased.

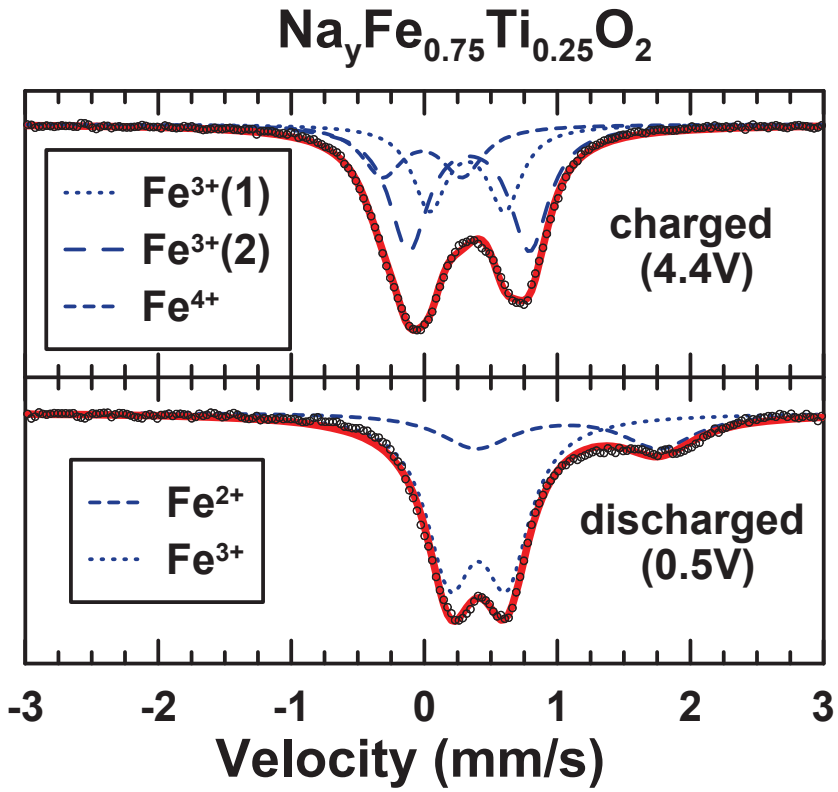

Figure 5.27: Room temperature ^{57}Fe Mössbauer spectra for $Na_yFe_{0.75}Ti_{0.25}O_2$. Five cells per measurement were charged or discharged to the indicated voltages. The spectrum of the charged material was fit using the three site model described in the text.

This decrease is accompanied by an equal increase in the area of the Fe^{4+} site. The equal change in area strongly suggests that the first charge capacity of $Na_{0.75}Fe^{3+}_{0.75}Ti^{4+}_{0.25}O_2$ is entirely from Fe^{3+} oxidation. This mechanism also supports the vacancy model proposed above based on energetic considerations, since it should be more difficult to remove Na^+ from a site that is near a Na^+ vacancy than one that is in a lattice with no vacancies. Therefore the Na^+ ions that are not near vacancies (i.e. those that are near Fe^{3+}(1) sites) are first removed during charging.

Capacity ($Na_yFe_{0.75}Ti_{0.75}O_2$)	**Voltage**	**Site**	**CS (mm/s)**	**QS (mm/s)**	**A (%)**
68 mAh/g ("y=0.49")	4.4 V	Fe^{3+}(1) Fe^{3+}(2) Fe^{4+}	+0.323 +0.337 -0.015	0.563 0.909 0.601	29 50 21
-85 mAh/g ("y=1.08")	0.5 V	Fe^{2+} Fe^{3+}	+1.08 +0.405	1.38 0.427	26 74

Table 5.5: Fitted room temperature ^{57}Fe Mössbauer effect parameters for the doublet sites in charged or discharged $Na_{0.75}Fe^{3+}_{0.75}Ti^{4+}_{0.25}O_2$. Typical uncertainties for measured values of the centre shifts (CS) and quadrupole splittings (QS) are about ± 0.005 mm/s.

After being discharged to 0.5 V from the as-prepared material, Fe^{2+} is observed in the Mössbauer spectrum, confirming that the reduction of Fe^{3+} occurs on the low voltage plateau. The amount of Fe^{2+} determined from the fit to the Mössbauer spectrum only accounts for roughly 60% of the observed discharge capacity. Therefore, it is likely that the reduction of both Fe^{3+} and Ti^{4+} has occurred. There is a noticeable increase in the half

width of the Fe^{3+} doublet for the discharged material and a reduction in the quadrupole splitting in comparison to the Fe^{3+}(1) site found in α-$NaFeO_2$. The presence of Fe^{2+} coupled with the theoretical formation of $Na_{1.08}Fe_{0.75}Ti_{0.25}O_2$ suggests that Na may be clustering near the Fe sites at low voltages.

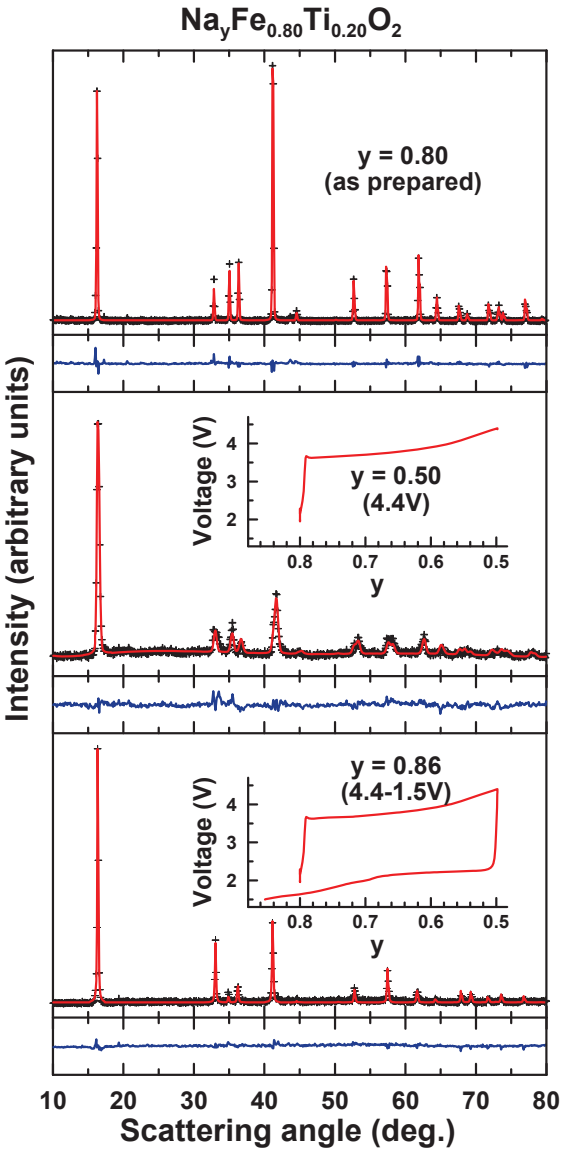

Figure 5.28: Ex-situ XRD and the results of Rietveld analysis of $Na_yFe_{0.80}Ti_{0.20}O_2$ samples as prepared or obtained electrochemically in Na-ion half cells with the voltage curves and y values shown. Difference plots are shown in blue.

Figure 5.28 shows ex-situ X-ray diffraction patterns of $Na_{0.8}Fe_{0.8}Ti_{0.2}O_2$ after charging to 4.4 V, as well as after discharging to 1.5 V from 4.4 V in comparison to the as-prepared sample. Rietveld refinements and difference plots are shown on the same scale along with a plot of the resulting voltage curve for each material. Both the starting material and the fully sodiated material are well described by the pristine O3 structure. The a-axis remains unchanged from the starting material with a = 3.01 Å, while the c-axis decreases from c = 16.39 Å to c = 16.28 Å in the cycled material, confirming that additional Na can be reversibly incorporated into the structure via Ti^{4+} reduction. Based on the correlation of the c-axis lattice parameter and x shown in Figure 5.5, the measured c-axis lattice parameter of fully sodiated $Na_{0.8}Fe_{0.8}Ti_{0.2}O_2$ corresponds to a composition of $Na_{0.87}Fe_{0.80}Ti_{0.20}O_2$. This is similar to the composition that was predicted from the electrochemistry and the Na occupancy that resulted from Rietveld refinement. No improvement of the fit could be achieved by placing Fe in the Na layer, however, improved powder XRD results are necessary for a more detailed analysis.

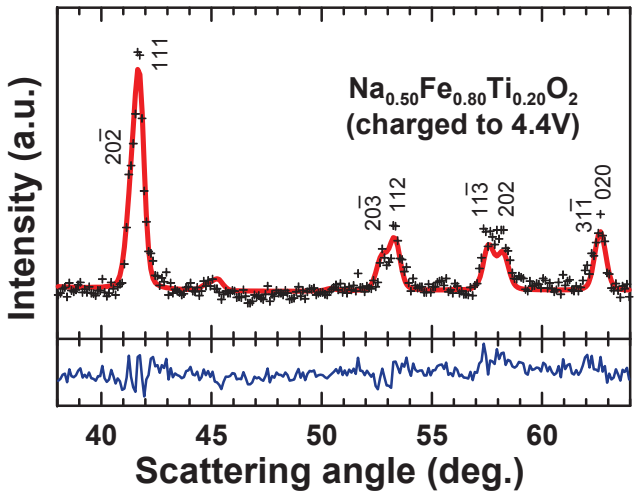

Figure 5.29: Results of the monoclinic fit for the y = 0.5 sample from Figure 5.28. A difference plot is shown.

In the charged (desodiated) sample having composition near $Na_{0.5}Fe_{0.8}Ti_{0.2}O_2$, splitting of the (107), (108) and (110) peaks from the rhombohedral description are clearly observed. Figure 5.29 shows that the peak splitting can be described with good agreement when this sample is fit with a monoclinic cell (space group C2/m). Na atoms were placed in the 2d site (0, 0.5, 0.5) and the occupancy was freed, with Fe and Ti placed in the 2a site (0, 0, 0) with occupancy x and 1-x respectively, and O placed in the 4i site with variable positions. Since the sample was smaller than the X-ray beam at low angles in the air-sensitive sample holder used, the refinement is only an estimation, although the lattice constant and space group should be accurate.

Capacity ($Na_yFe_{0.80}Ti_{0.20}O_2$)	**Voltage**	**a**	**b**	**c**	**β**
0 mAh/g ("y=0.80")	Start	5.204(1) Å	3.004(2) Å	5.734(4) Å	107.59(3)
76 mAh/g ("y=0.5")	4.4 V	5.141(5) Å	2.964(3) Å	5.702(2) Å	108.14(2)
-14 mAh/g ("y=0.87")	4.4-1.5 V	5.208(2) Å	3.011(3) Å	5.694(6) Å	107.78(5)

Table 5.6: Fitted lattice parameters in the monoclinic description for y = 0.8, 0.5 and 0.87 in $Na_yFe_{0.8}Ti_{0.2}O_2$.

Table 5.6 shows how this monoclinic distortion relates to the starting material and the discharged materials. The relationship between the equivalent rhombohedral and monoclinic descriptions of the α-$NaFeO_2$ structure is also described in Takeda *et al.* [71].

There are only small differences in the lattice constants between the fully charged and fully discharged material. This is unexpected, since, according to Figure 5.5, the c-axis lattice parameter should increase with increasing Na vacancies. Expansion of the c-axis during deintercalation is typically observed in layered Na-ion cathodes such as Na_xVO_2 [90] Na_xCoO_2 [19], and $Na_xCo_{2/3}Mn_{1/3}O_2$ [23]. The c-axis lattice parameter in the charged material is much smaller than expected at this level of Na occupation. The occurrence of a significant monoclinic distortion of the charged material may be a contributing factor to the hysteresis observed in the voltage curve during the $Fe^{3+} \rightarrow Fe^{4+}$ high voltage plateau. Hysteresis is often associated with the energy barriers that accompany structural distortion [91, 92]. The reversible migration of Mn between octahedral and tetrahedral sites in $LiMn_2O_4$ during delithiation corresponds to observed hysteresis in that system [93, 94]. While no improvement in the fit was seen when Fe was placed in the Na layer, occurrence of Fe migration during charge is not necessarily eliminated as a possible factor in these systems [56]. Other factors such as transition metal dissolution or slow kinetics are possible contributors to large hysteresis at high voltage.

5.7 CONCLUSIONS

Investigations of $Na_xFe_xMn_{1-x}O_2$ with $x > 0.65$ belonging to the α-$NaFeO_2$ type structure are reported. Compositions with $x > 0.65$ were found to have the O3 type structure while compositions with $x < 0.65$ were found to be a combination of two or more O3- and P2-like phases. A large amount of sodium vacancies in the structure may cause staged phases to form when $x < 0.65$. Despite this, the local transition metal structure is similar for the

entire composition range. This is evidenced by the continuous trends in lattice constants and the Mössbauer spectra along the entire composition range.

The substitution of Mn for Fe results in significant reduction in voltage hysteresis and increased capacity retention during cycling. The x = 0.5 composition has the best performance given the chosen testing protocols. When sodiation and desodiation occur in this composition, less Jahn-Teller ions are present than pure $NaMnO_2$ or α-$NaFeO_2$. It is possible that this situation may inhibit co-operative Jahn-Teller distortions and may be one contributing source of improved electrochemical performance compared to α-$NaFeO_2$, though it is noted that no evidence for a cooperative Jahn-Teller distortion has been found. Samples having x = 0.5 were found to cycle reversibly at a capacity over 170 mAh/g (corresponding to a theoretical energy density of approximately 460 Wh/kg) with 85% capacity retention after 20 cycles. When the capacity is restricted to 135 mAh/g (340 Wh/kg), capacity retention approaches 95% after 20 cycles.

Upon closely inspecting and comparing the capacity fade and voltage curves, it becomes apparent that samples have improved capacity retention if less Fe^{3+} is oxidized during sodium deintercalation. In fact, the capacity retention of the 0.5 composition is directly related to how much Fe is accessed during insertion and removal of Na. When less Fe is oxidized, capacity fade becomes less prominent, and this condition appears to be independent of which layered phase is present.

Electrochemical performance of x = 0.5 and 0.55 samples shows similarity to the P2-type $Na_{2/3}Fe_{1/2}Mn_{1/2}O_2$ recently reported [9], generally having capacity retention of about 85% after 20 cycles when cycled in the 450-520 Wh/kg range (1850-2130 Wh/L). However, when the x=0.5 materials are limited to cycling between 300-400 Wh/kg (1600 Wh/L) at 30 °C their capacity retention was found to be well in excess of 90% after 20 cycles. Improved capacity retention may be achieved for samples containing more iron if the voltage cutoff is further restricted below 4.0V.

The role of transition metals in stabilizing the O3 phase in Fe containing layered Na-ion cathode materials has been further investigated in the analogous series $Na_xFe^{3+}{}_xM^{4+}{}_{1-x}O_2$ with M = Ti and Sn. The present work provides evidence that the activation of the $Fe^{3+} \leftrightarrow Fe^{4+}$ couple in the binary $Na_yFe_xM_{1-x}O_2$ systems (M = Ti and Sn) also leads to capacity fade. This may be due to significant structural distortion that accompanies the formation of Fe^{4+} as well as the creation of too many Na-vacancies near Fe^{3+} sites during deintercalation, which may increase the probability of Fe migration into the Na layer. Good performance may be achieved in these materials if the $Fe^{3+} \leftrightarrow Fe^{4+}$ couple is not accessed and the structural distortion is avoided. In this way, Fe can be used as a "filler" atom in these binary systems, so as to reduce the amount of more expensive or less sustainable active transition metals used.

These preliminary studies also indicate that the relevance of the three site Mössbauer model introduced in Chapter 4 appears to be independent of the layering type and transition metal M in $Na_xFe_yM_{1-y}O_2$ (M = Fe, Mn, Ti, and Sn), i.e. monoclinic C2/m as in

$Na_{0.5}FeO_2$ or $NaMnO_2$, P2-type ($Na_{2/3}Fe_{1/2}Mn_{1/2}O_2$), O3-type ($NaFeO_2$), or other. A more electronically asymmetric Fe^{3+}(2) environment compared to a more symmetric Fe^{3+}(1) environment can be distinguished solely based on how many Na vacancies are present on the adjacent layer in the $Na_xFe^{3+}_xM^{4+}_{1-x}O_2$ materials when M = Fe, Mn, Ti and Sn. Evidence has been presented which suggests that introduction of vacancies in the Na-layer influences the quadrupole splitting of the Fe sites in the transition metal layer. This model will be used to analyse and interpret spectra in Chapters 6 and 7.

CHAPTER 6 STUDIES OF $NaFe^{3+}_xM_{1-x}O_2$ (M=Ni, $Ni_{0.5}Co_{0.5}$, Co)

6.1 INTRODUCTION

In this chapter, the synthesis and structure of $NaFe_xM_{1-x}O_2$ materials with M = Ni, Co and $Ni_{0.5}Co_{0.5}$ are reported. Ni and Co are commonly used in layered Li-ion cathodes due to the high voltage and good cycling performance associated with the Ni and Co redox couples in the layered material, and are therefore applied here coupled with active Fe. The electrochemistry of unreported $NaFe_xM_{1-x}O_2$ materials with M = $Ni_{0.5}Co_{0.5}$ and $0 \leq x \leq 0.5$ is explored. In previous work in the 1980's, O3-$Na_xNi_{0.6}Co_{0.4}O_2$ was synthesized and deintercalated to produce x = 0.80 and 0.58 samples, where Ni and Co are measured to be in the 3+ state in the synthesized material. It was found that $Ni^{3+} \rightarrow Ni^{4+}$ was preferred over $Co^{3+} \rightarrow Co^{4+}$ during Na deintercalation at voltages measured below 2.94 V [95]. Here, some effects of adding Fe to unreported $NaNi_{0.5}Co_{0.5}O_2$ are investigated.

Of the binary $NaFe_xM_{1-x}O_2$ with M = Mn, Ni, Co, Ti, Sn, and others found in the literature, Co offers the highest energy density in the narrowest voltage range, with the best cycling performance. Here, an evaluation of $NaFe_xNi_{1-x}O_2$, of $NaFe_x(Ni_{0.5}Co_{0.5})_{1-x}O_2$ and $NaFe_xCo_{1-x}O_2$ is made to help understand why this is the case. A comparison of the ex-situ Mossbauer spectra of charged $NaFe_xCo_{1-x}O_2$ and $NaFe_x(Co_{0.5}Ni_{0.5})_{1-x}O_2$ with x = 0.4 and 0.5 is made, and discussed in terms of cycling stability.

6.2 SYNTHESIS

Stoichiometric amounts of Fe_3O_4, Co_3O_4, NiO and Na_2O_2 were combined by high energy ball milling for 4 hours in Ar. For $NaFe_x(Co_{0.5}Ni_{0.5})O_2$ samples, the resulting powders were then pressed into a pellet and heated in O_2 for 14 hours at 800 °C, followed by immediate removal from the furnace.

$NaFe_xCo_{1-x}O_2$ samples were made in open air atmosphere and loose powder was annealed at 900 °C for 12 hours followed by natural cooling to room temperature. When $x < 0.2$, the temperature was lowered in order to avoid Na loss. A single phase was obtained using 800 °C when $x = 0.2$.

$NaFe_xNi_{1-x}O_2$ samples were made using both loose powders and pellets and were annealed at 650 °C for 30 hours. It was found that samples with $x > 0.2$ could be synthesized into a single phase in a dry air flow or open air atmosphere for 30 hours. $x < 0.2$ had to be made into pellets and annealing time was reduced to avoid Na loss. Samples with $x < 0.2$ are particularly sensitive to moisture. For $x = 0.2$ the annealing time was 20 hours. For $x < 0.2$ the annealing time was 14 hours.

6.3 STRUCTURAL CHARACTERIZATION BY XRD

Figure 6.1 shows the results of X-ray diffraction experiments on $NaFe_x(Co_{0.5}Ni_{0.5})_{1-x}O_2$ samples with $0 \leq x \leq 0.5$. All patterns were fit by Rietveld refinement using a rhombohedral unit cell and space group $R\bar{3}m$ (O3-type). For the refinement, sodium atoms with occupancy 1 were placed in the 3a sites, iron, cobalt and nickel with composition $Fe_xCo_{0.5(1-x)}Ni_{0.5(1-x)}$ were placed in the 3b sites and oxygen atoms were placed in the 6c sites. The lattice constants were allowed to vary. The oxygen positions were refined to values near (0, 0, 0.232), (0, 0, 0.234) for the x=0.3 and x=0.4 samples respectively, which are in close agreement with the oxygen positions previously reported for $NaFe_{1/3}Co_{1/3}Ni_{1/3}O_2$ [34].

Figure 6.2 shows the XRD data of $NaFe_xNi_{1-x}O_2$ samples which are not indexed with the O3 structure. Samples with $x \leq 0.14$ were indexed with a monoclinic unit cell (C2/m), isostructural with $NaNiO_2$ [57]. For samples with $0.14 < x < 0.2$ there is a two phase region having monoclinic and O3 phases at selected conditions. Samples with $x \leq 0.2$ were found to be particularly sensitive to moisture. Samples could not be handled or synthesized in the atmosphere without significant changes in material properties resulting from exposure. $NaNiO_2$ and $NaFeO_2$ are both hygroscopic. However, significant differences were not observed in XRD patterns taken from samples that were exposed to air for a few hours vs. those which were not air exposed in the composition range $0.3 < x < 0.6$. Large noticeable changes have been observed, however, after periods of months of being exposed to atmospheric conditions.

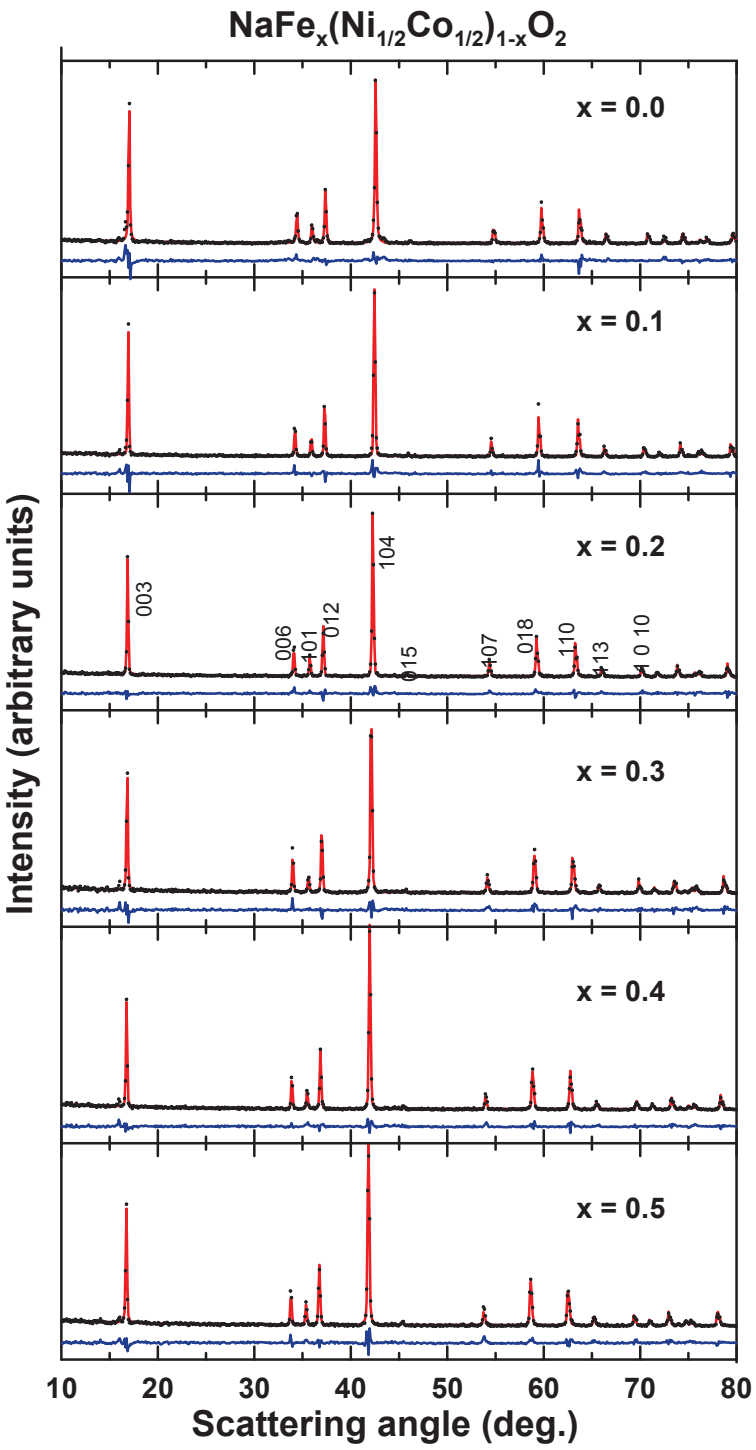

Figure 6.1: XRD patterns of the $NaFe_x(Co_{0.5}Ni_{0.5})_{1-x}O_2$ samples ($0 \leq x \leq 0.5$) with results of Rietveld refinement shown in red. Miller indices for the O3 structure are indicated. Difference plots are shown in blue.

Structural changes were measured when $NaNiO_2$ was mixed with PVDF in NMP, compared to $NaNiO_2$ mixed with EPDM in cyclohexane in which the pristine structure is preserved, which may result from solvent or water intercalation [96]. The $NaFe_xNi_{1-x}O_2$ series, especially with those having $x < 0.2$, appear less practical in comparison to other systems such as Mn-containing or ternary compositions, where moisture or solvent sensitivity becomes less significant.

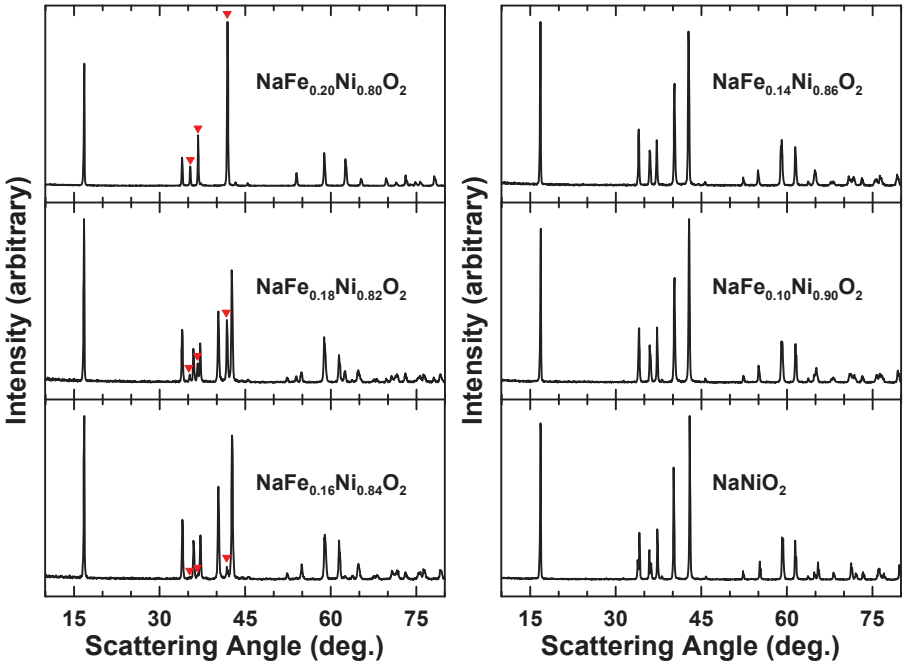

Figure 6.2: XRD patterns of $NaFe_xNi_{1-x}O_2$ with $x \leq 0.2$ showing a two phase region between $0.14 < x < 0.2$, having monoclinic and rhombohedral unit cells. The reduction of the (101), (012) and (104) peaks of the O3 unit cell with respect to the monoclinic unit cell is highlighted with red triangles.

Atmospheric exposure to $Na_x(Ni,Fe,Mn)O_2$ samples has recently been studied [91], where addition of Ni^{2+} to the $Na_x(Fe,Mn)O_2$ samples was found to reduce atmospheric sensitivity. Bucholz *et al.* have reported a moisture study on P2- or P3-

$Na_xNi_{0.22}Co_{0.11}Mn_{0.66}O_2$ in which samples with $x \leq 0.33$ were found to be particularly hygroscopic [97].

Figure 6.3 shows the lattice parameters, calculated densities and best fit lines for the $NaFe_x(Co_{0.5}Ni_{0.5})_{1-x}O_2$, $NaFe_xCo_{1-x}O_2$, and $NaFe_xNi_{1-x}O_2$ samples. $NaFe_xNi_{1-x}O_2$ has been previously reported for the composition range $0.3 \leq x \leq 0.5$ [33]. All samples are O3 when $0.2 \leq x$ in $NaFe_xNi_{1-x}O_2$. Contrary to what was suggested in the literature [33] the O3-type solid solution can be extended in to the range $0.2 \leq x \leq 0.7$ in $NaFe_xNi_{1-x}O_2$. It is possible that the solid solution can be extended through to $x = 1$. However, samples with $0.7 \leq x$ became more difficult to synthesize without formation of the β-$NaFeO_2$ impurity phase. Further experiments are necessary to determine the extent of the single phase solid solution region. All layered phases with $0.2 \leq x \leq 0.7$ are single phase with little noticeable impurities present and appear to follow Vegard's law after annealing at 650 °C in the single phase regions.

$NaFe_xCo_{1-x}O_2$ samples have been previously reported for $x = 0.4$, 0.5 and 0.6 [31, 59]. However, capacity retention is not described. Lattice parameters are shown across the solid solution series in Figure 6.3. Values of the c-axis parameter in this work were found to be similar or slightly higher for the $x = 0.5$ compared to that reported by Yoshida *et al.* [31]. A slightly higher value may have resulted from slight Na loss during annealing, though no Fe^{4+} was detected in the synthesized material by use of ex-situ Mössbauer spectroscopy, as will be discussed below.

Samples of composition $NaFe_x(Co_{0.5}Ni_{0.5})_{1-x}O_2$ connect the $NaFe_xCo_{1-x}O_2$ and the $NaFe_xNi_{1-x}O_2$ solid solution series. Single phase O3 structure in the $NaFe_xCo_yNi_zO_2$ ternary system appear to follow Vegard's law as x, y or z are varied over a region of the composition space with the selected synthesis conditions. In general, addition of Ni or Fe results in a decrease in density in comparison to samples with more Co, in which higher densities appear to result from a decreasing value of the a-axis parameter.

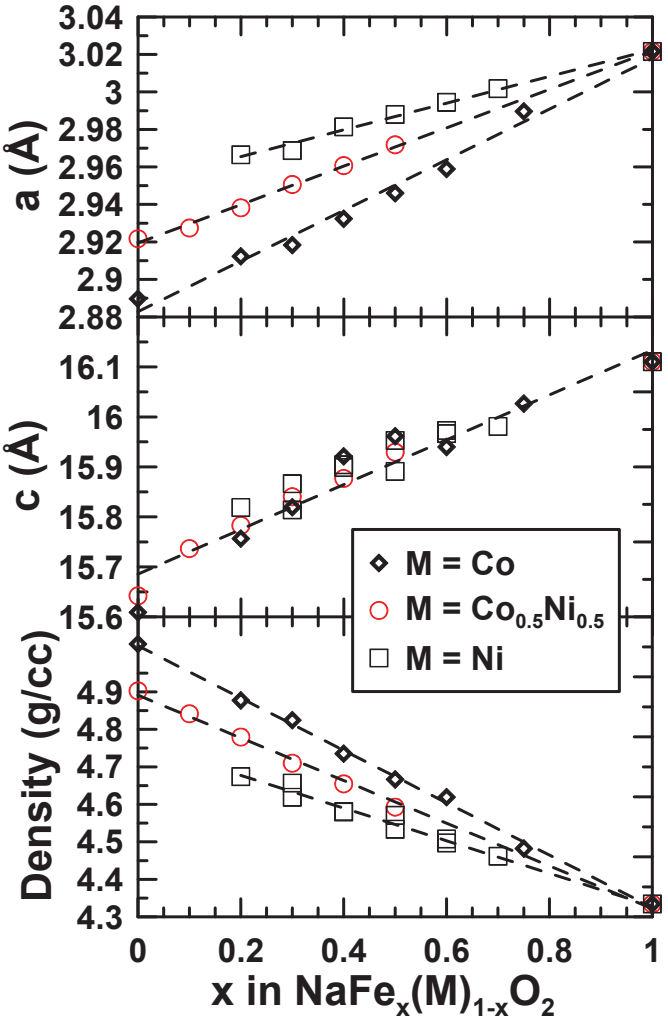

Figure 6.3: Lattice parameters extracted from Rietveld analysis for O3-type $NaFe_xM_{1-x}O_2$ (M = Co, $Co_{0.5}Ni_{0.5}$, Ni) with calculated densities.

6.4 ELECTROCHEMISTRY

Figures 6.4 and 6.5 show the voltage vs. specific capacity, and the specific capacity (or coulombic efficiency) vs. cycle number respectively for $NaFe_x(Co_{0.5}Ni_{0.5})_{1-x}O_2$ with $0 \leq x \leq 0.3$, which show the initial trends which occur as Fe is added to this system. Good reproducibility in the measurements can be seen by comparison of the coulombic efficiencies and the discharge capacities for each set of cells. It can be seen from the voltage curves that the reversible capacity becomes larger as the Fe content is increased from 0. Additionally, the average hysteresis, (the difference in average voltage of the second charge and discharge cycle) is reduced as Fe is added.

The addition of Fe is also associated with a reduction in first cycle irreversible capacity from 21 mAh/g (16%) for the x = 0 sample to 5 mAh/g (4%) for the x = 0.3 sample. A similar capacity in the same voltage range has been observed for $NaFe_{1/3}Co_{1/3}Ni_{1/3}O_2$, and an irreversible capacity of 7 mAh/g (4 %) resulted, even when using a higher cutoff potential of 4.2 V [34]. The optimal sample on the basis of irreversible capacity appears to be that of the x = 1/3 material.

It is likely that the $NaCo_{0.5}Ni_{0.5}O_2$ sample was damaged by trace moisture exposure, as can be seen by the initial sharp over potential required to initialize the first cycle. This might suggest that some fraction of samples with x = 0 or 0.1 were damaged by traces of moisture and may have an adverse effect on their electrochemical features as previously described. As Fe, Co and Ni transition metals are mixed. However, this effect becomes

less noticeable, especially in later cycles. There are minor differences in first cycle features in the unexposed $NaNi_{1/3}Fe_{1/3}Co_{1/3}O_2$ reported by Ceder's group [34], suggesting that this combination is acceptable on the basis of moisture sensitivity, having small or minimal effects on specific capacity and hysteresis.

Figures 6.6 and 6.7 show the comparison of voltage vs. capacity and capacity retention (or coulombic efficiency) vs. cycle number respectively for $NaFe_x(Co_{0.5}Ni_{0.5})_{1-x}O_2$ with x = 0.4 and x = 0.5 and $NaFe_xCo_{1-x}O_2$ with x = 0.4 and x = 0.5. It can be seen from the voltage curves that the average hysteresis increases for samples with less Co (more Fe or Ni). When x = 0.5 in $NaFe_x(Co_{0.5}Ni_{0.5})_{1-x}O_2$, the 2nd cycle hysteresis is 189 mV. When x = 0.5 in $NaFe_xCo_{1-x}O_2$, the hysteresis is reduced to 146 mV. Similarly, for the x = 0.4 samples, the voltage hysteresis is 144 mV and 117 mV respectively. The use of Ni^{3+} in place of Co^{3+} results in increased voltage hysteresis. More Fe^{4+} at the top of charge has been hypothesized to be a source of increased voltage hysteresis for samples with x > 0.5 in $NaFe_xCo_{1-x}O_2$ [31, 59] and the $Na_xFe_xM_{1-x}O_2$ (M = Mn, Ti, and Sn) samples presented in Chapter 5.

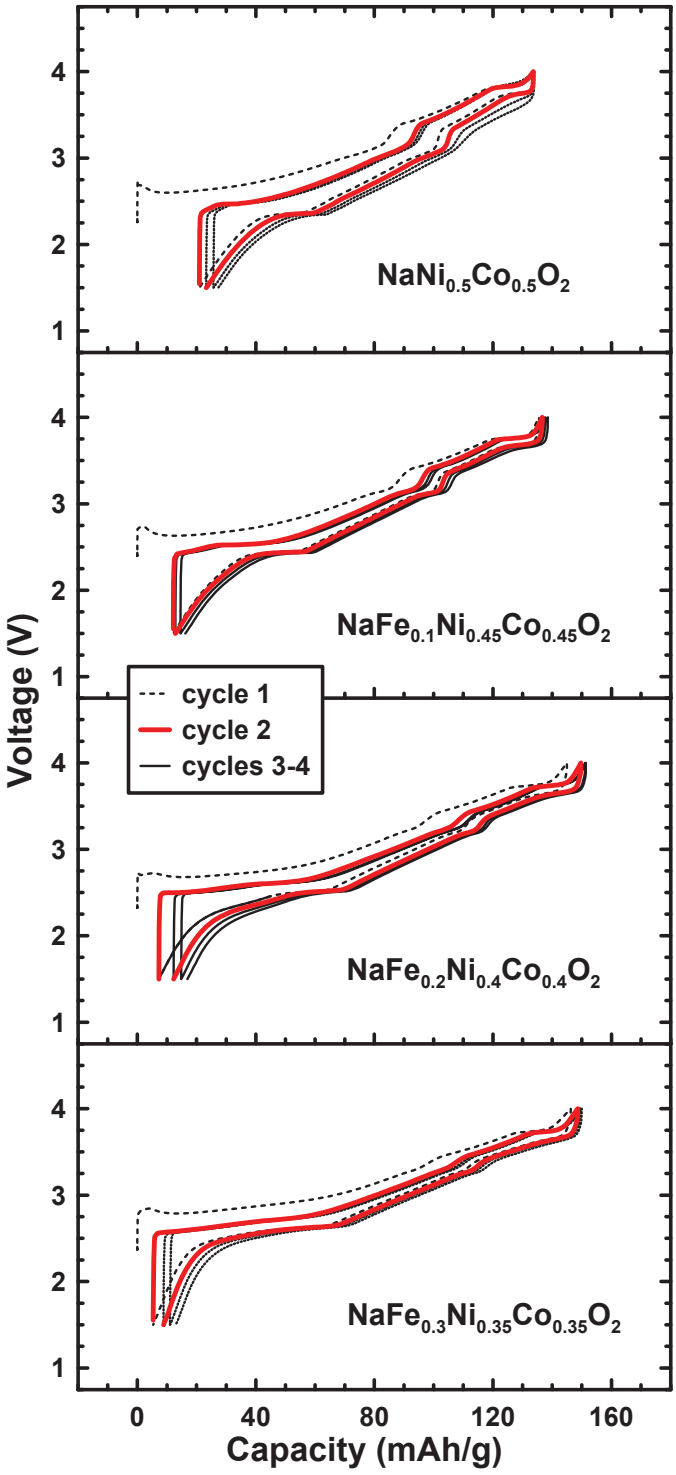

Figure 6.4: Voltage vs. capacity of cycles 1-4 as indicated for $NaFe_x(Co_{0.5}Ni_{0.5})_{1-x}O_2$ samples having $0 \leq x \leq 0.3$.

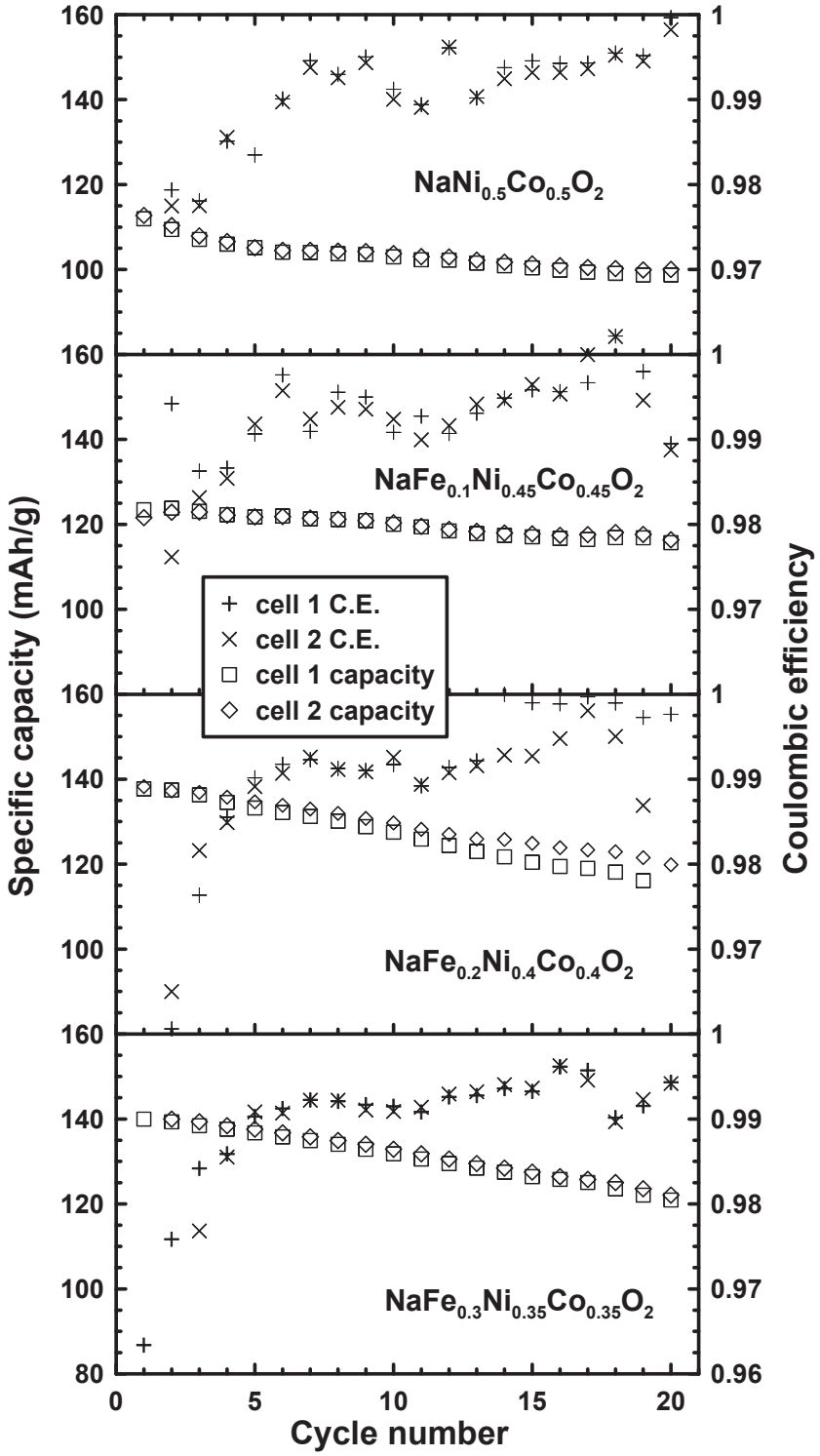

Figure 6.5: Specific capacity vs. cycle number and coulombic efficiency (defined as discharge capacity divided by charge capacity) vs. cycle number for cycles 1-20 for $NaFe_x(Co_{0.5}Ni_{0.5})_{1-x}O_2$ samples having $0 \leq x \leq 0.3$.

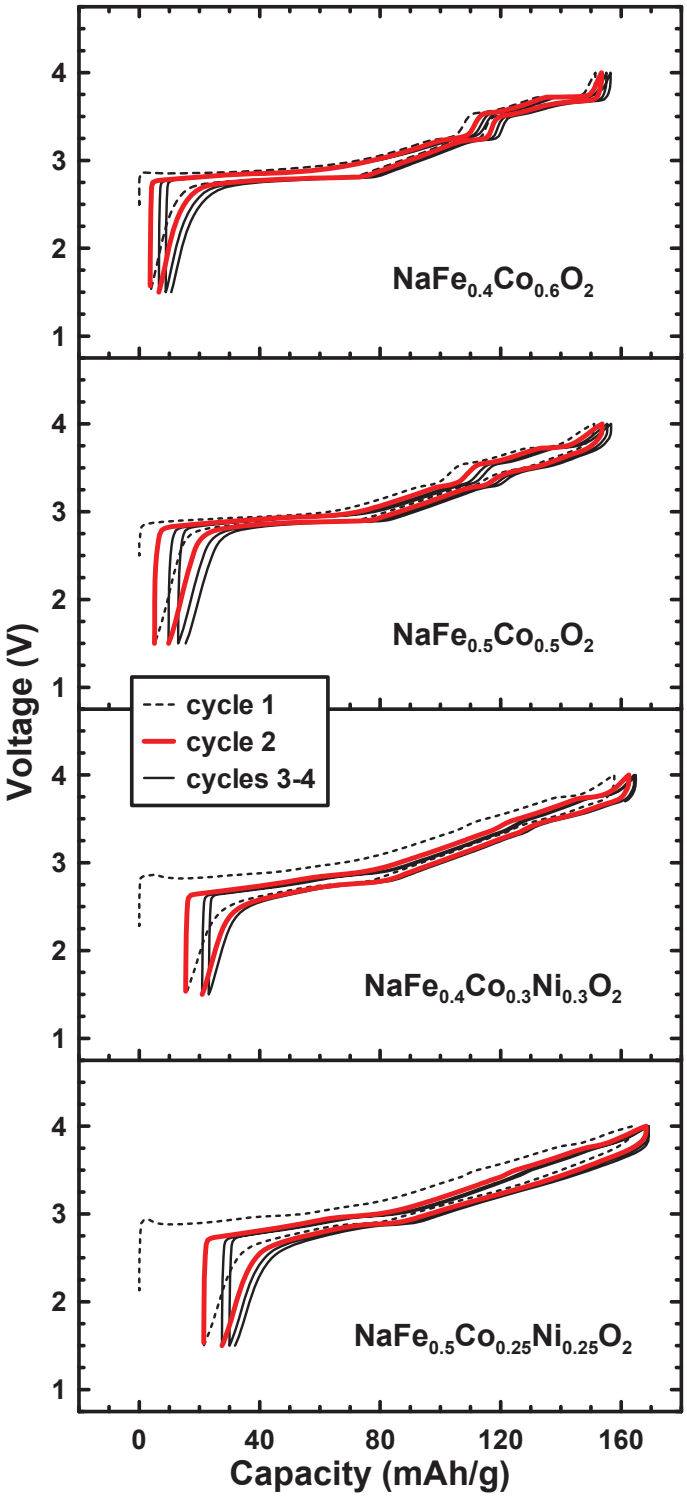

Figure 6.6: Voltage vs. capacity of cycles 1-4 as indicated for $NaFe_xM_{1-x}O_2$ samples having $0.4 \leq x \leq 0.5$ and M = Co, $Co_{0.5}Ni_{0.5}$.

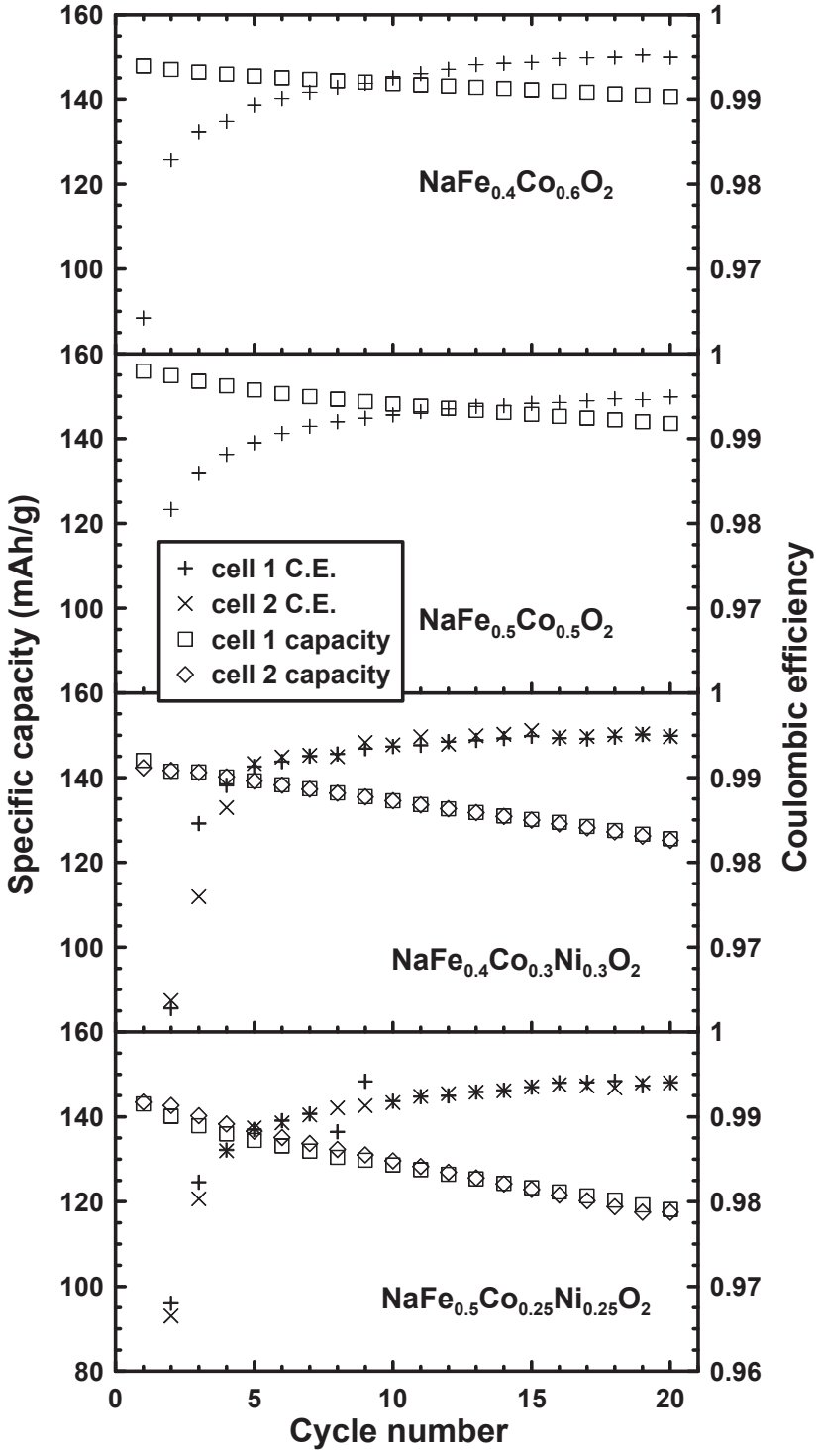

Figure 6.7: Specific capacity vs. cycle number and coulombic efficiency (defined as discharge capacity divided by charge capacity) vs. cycle number for cycles 1-20 for $NaFe_xM_{1-x}O_2$ samples having $0.4 \leq x \leq 0.5$ and M = Co, $Co_{0.5}Ni_{0.5}$.

Figure 6.8 highlights the positive effects of addition of Fe by comparing voltage curves directly. The decreasing slope of the discharge curve and the increase in average voltage are clearly observed as x is increased, as well as the increase in reversible capacity. Capacity retention is similar for samples $0.2 \leq x \leq 0.4$ in $NaFe_x(Ni_{0.5}Co_{0.5})_{1-x}O_2$, but the observed increase in volumetric energy density is 7%.

Figure 6.9 shows differential capacity (dQ/dV) vs. voltage for the first five cycles as indicated excluding the first charge. Although the calculated average voltage hysteresis is initially reduced during discharge as x is increased from 0 to 0.3, the shape of the charge and discharge becomes less symmetric as more Fe is added. When $0.4 \leq x \leq 0.5$, this effect becomes very pronounced and the voltage hysteresis increases as x is increased from 0.3 to 0.5.

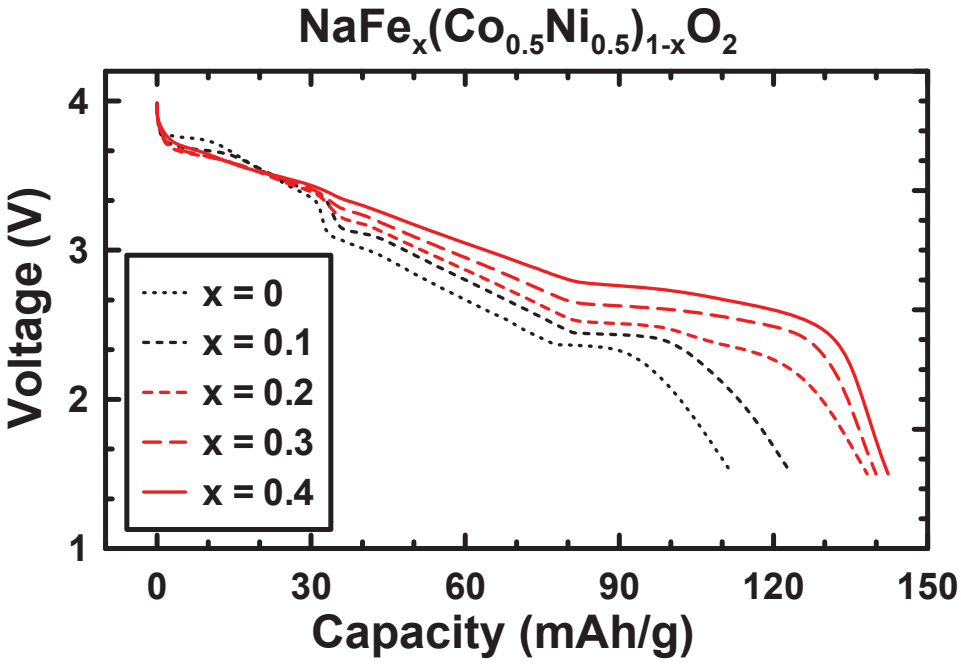

Figure 6.8: Voltage vs. capacity of the first discharge for $NaFe_x(Co_{0.5}Ni_{0.5})_{1-x}O_2$ samples having $0 \leq x \leq 0.4$.

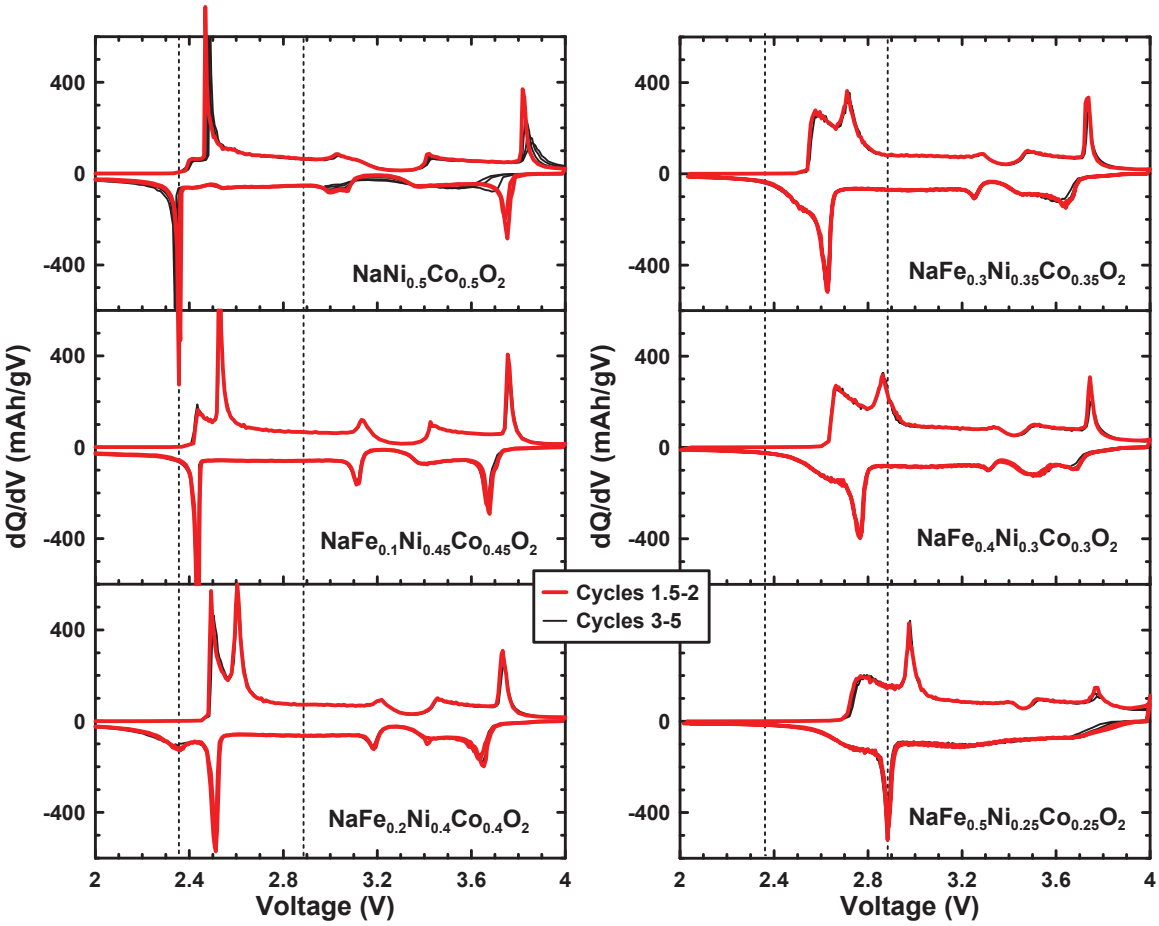

Figure 6.9: Voltage vs. dQ/dV of cycles 1.5-5 for $NaFe_x(Co_{0.5}Ni_{0.5})_{1-x}O_2$ samples having $0 \leq x \leq 0.5$.

Addition of Fe as a way to reduce the sharp peaks seen in dQ/dV has been reported for the $NaFe_xNi_{1-x}O_2$ system [33, 45], $NaFe_xCo_{1-x}O_2$ [31, 59], and $NaFe_x(Ni_{0.5}Mn_{0.5})_{1-x}O_2$ [35] This is the result of the suppression or elimination of two-phase regions such as those seen in deintercalated Na_xNiO_2 [57] and/or suppression of voltage plateaus formed from Na-ordering such as those seen in deintercalated P2- Na_xCoO_2 [19, 93]. In the $NaFe_xNi_{1-x}O_2$ and $NaFe_x(Ni_{0.5}Mn_{0.5})_{1-x}O_2$ systems the addition of Fe caused a deterioration in electrochemical features such as voltage hysteresis or asymmetry, capacity retention and energy density. For the $NaFe_xCo_{1-x}O_2$ system, increasing x from 0

causes improvement in electrochemical features across the board. Further optimization on the basis of capacity retention in the range $0 < x \leq 0.4$ is necessary in this system.

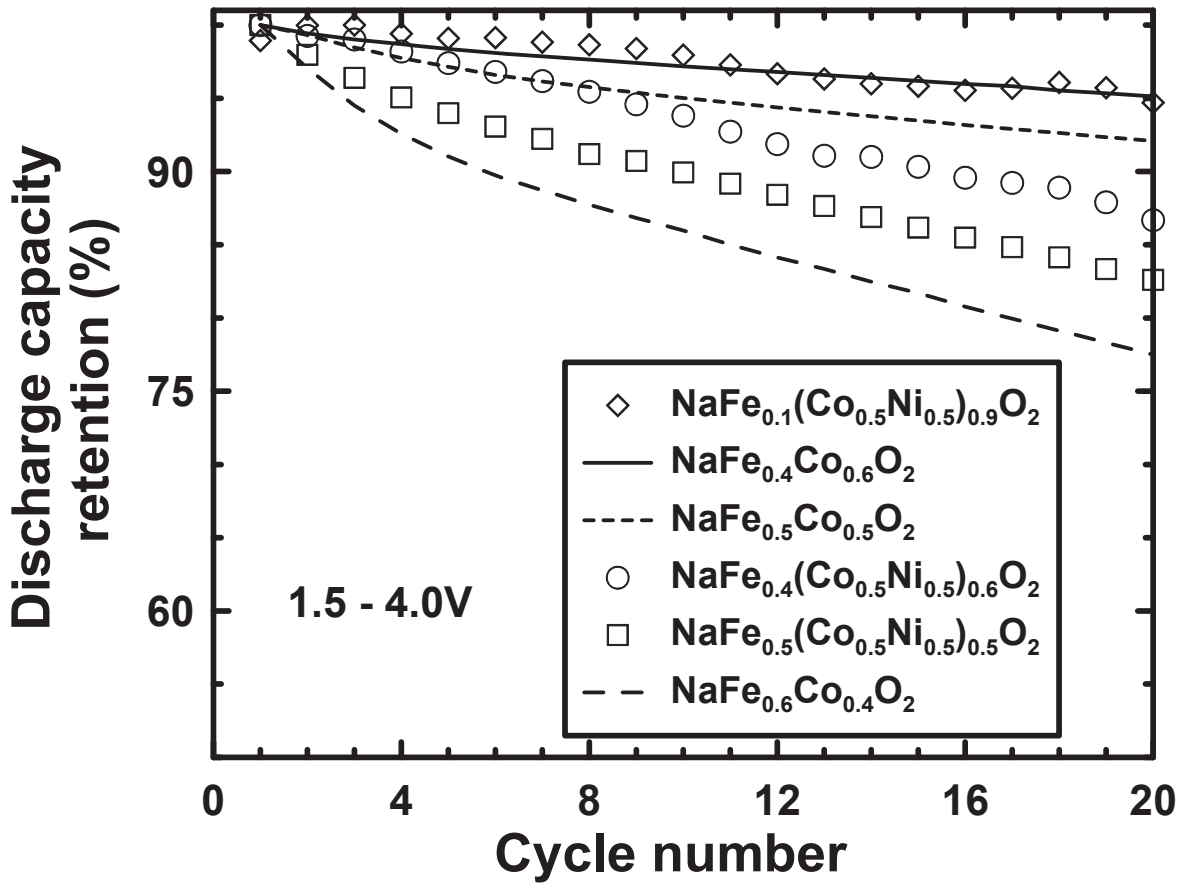

Figure 6.10: Percentage capacity retention as a function of cycle number for selected $NaFe_xM_{1-x}O_2$ samples with M = Co, $Co_{0.5}Ni_{0.5}$.

Figure 6.10 shows the cycling performance for selected samples synthesized in this work on the basis of percentage capacity retention. It is found that the capacity retention of $NaFe_x(Ni_{0.5}Co_{0.5})_{1-x}O_2$ deteriorates for samples with increasing values of x in the range $0.1 < x \leq 0.5$, and the capacity retention of $NaFe_xCo_{1-x}O_2$ deteriorates for samples with increasing values of x when $x \geq 0.4$. The performance of the $NaFe_{0.4}Co_{0.6}O_2$ with a lower

cutoff potential of 1.5 V on the basis of percent capacity retention exceeds that of the $NaFe_{0.5}Co_{0.5}O_2$ recently reported by Yoshida *et al.* [31] and that reported here, contrary to previous claims that capacity retention of x = 0.4 and 0.5 are the same [31].

Material	**Capacity (mAh/g)**	**Voltage (V)**	**Gravimetric Energy (Wh/kg)**	**Volumetric Energy (Wh/L)**	**Capacity retention**
$NaNi_{0.5}Co_{0.5}O_2$	113	2.81	318	1559	90%
$NaFe_{0.1}(Ni_{0.5}Co_{0.5})_{0.9}O_2$	123	2.83	348	1685	95%
$NaFe_{0.2}(Ni_{0.5}Co_{0.5})_{0.8}O_2$	137	2.82	386	1845	87%
$NaFe_{0.3}(Ni_{0.5}Co_{0.5})_{0.7}O_2$	140	2.91	407	1917	87%
$NaFe_{0.4}(Ni_{0.5}Co_{0.5})_{0.6}O_2$	142	2.98	423	1969	87%
$NaFe_{0.5}(Ni_{0.5}Co_{0.5})_{0.5}O_2$	143	3.06	437	2007	82%
$NaFe_{0.4}Co_{0.6}O_2$	150	3.05	458	2170	95%
$NaFe_{0.5}Co_{0.5}O_2$	156	3.11	485	2264	92%
$NaFe_{0.6}Co_{0.4}O_2$	150	3.03	455	2100	78%

Table 6.1: Results of the first discharge in $NaFe_x(Co_{0.5}Ni_{0.5})_{1-x}O_2$ and $NaFe_xCo_{1-x}O_2$ in a 1.5 - 4.0 V test, with calculated average voltage and 20th cycle discharge capacity retention. The calculated gravimetric and volumetric energy densities are included. Variation of the measured capacity was ~ 1 mAh/g.

Wang *et al.* reported the electrochemical performance of $NaFe_xNi_{1-x}O_2$ when $0.3 \leq x \leq 1$ [33]. It was found that the capacity retention and energy of $NaFe_xNi_{1-x}O_2$ deteriorates rapidly when x is increased from x = 0 to x = 0.3. The monoclinic $NaNiO_2$ discharge capacity retention was found to be 123 / 116 mAh/g in the 1^{st} / 20^{th} cycles using the 1.25-3.75 V test [57]. The O3- $NaFe_xNi_{1-x}O_2$ ($0.3 \leq x \leq 1$) is well reported in the paper by Wang *et al.* [33]. Capacity retention was reported to be 135 / 112 mAh/g and 112 / 76 mAh/g for x = 0.3 and 0.5 respectively in the 1^{st} / 20^{th} cycles of the 2.0 - 3.8 V test [33]. The presence of Fe^{4+} was measured in the de-intercalated $Na_{0.4}Fe_{0.3}Ni_{0.7}O_2$ sample [33]. Performance of $NaFeO_2$ in the 2.0-3.8 V range is poor [33, 56].

While addition of Fe to these systems can cause an increase in the energy density when Co is used, it is possible that the formation of Fe^{4+} is a source of capacity fade. Table 6.1 shows a comparison of the results of the electrochemistry for samples prepared in this work, so that observed trends in electrochemistry can be easily seen. For fixed values of x (constant Fe), samples with more Co have higher energy densities, less hysteresis and better capacity retention.

6.5 CHARACTERIZATION BY EX-SITU MÖSSBAUER SPECTROSCOPY

Figure 6.11 shows ^{57}Fe Mössbauer spectra for $NaFe_xCo_{1-x}O_2$ or $NaFe_x(Co_{0.5}Ni_{0.5})_{1-x}O_2$ samples with x = 0.5 and 0.4. All spectra were fit using one Fe site used to represent the Fe^{3+}. The fitting parameters are listed in Table 6.2. Fits are acceptable and indicate that

little Na loss occurs after or during the annealing procedure. Meaningful parameters could not be extracted from Fe^{4+} or Fe^{3+}(2) sites as described in previous sections with improvement in fit.

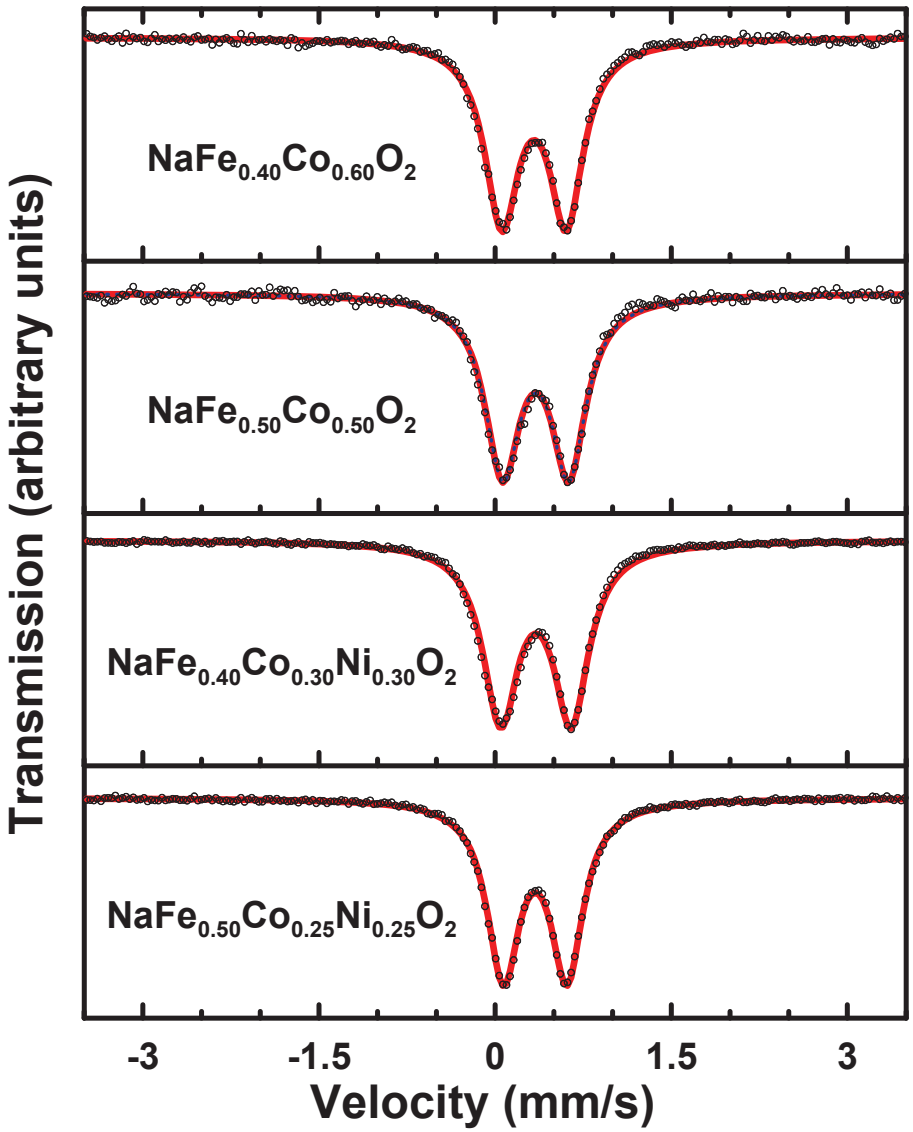

Figure 6.11: ^{57}Fe Mössbauer effect spectra from as-prepared $NaFe_xCo_{1-x}O_2$ and $NaFe_x(Co_{0.5}Ni_{0.5})_{1-x}O_2$ samples for x = 0.4 and 0.5. The Fe^{3+}(1) sites are shown as solid red lines.

Sample	Site	CS (mm/s)	QS (mm/s)	Area (%)
$NaFe_{0.4}Co_{0.6}O_2$	Fe^{3+}	+0.332	0.549	100
$NaFe_{0.5}Co_{0.5}O_2$	Fe^{3+}	+0.346	0.564	100
$NaFe_{0.4}Co_{0.3}Ni_{0.3}O_2$	Fe^{3+}	+0.344	0.601	100
$NaFe_{0.5}Co_{0.25}Ni_{0.25}O_2$	Fe^{3+}	+0.341	0.542	100

Table 6.2: Fitted room temperature ^{57}Fe Mössbauer effect parameters for the doublet sites for the as prepared materials indicated. Typical uncertainties for measured values of the centre shifts (CS) and quadrupole splittings (QS) are about ± 0.005 mm/s.

As expected, Fe^{3+} measured here have centre shifts in the range of 0.33-0.35 mm/s, which is consistent and similar with what is expected in the starting material of Fe^{3+}-containing O3- $NaMO_2$ phases measured here and elsewhere. Similar spectra were observed for the $NaFe_xNi_{1-x}O_2$ [33]. In this work, it is confirmed that other samples outside of this range have Fe^{3+}. This has been found in the $NaFe_xCo_{1-x}O_2$, $NaFe_x(Co_{0.5}Ni_{0.5})_{1-x}O_2$, and $NaFe_xNi_{1-x}O_2$ samples.

Figure 6.12 shows ex-situ Mossbauer spectra of the same materials after being charged to 4.0 V. Shown are fits with a simple two site model, one of which represents the Fe^{3+} and the other designated the Fe^{4+} site. The fitting parameters are listed in Table 6.3. The Fe^{3+} sites have centre shifts (CS) in the range of 0.24 - 0.26 mm/s which is within the acceptable range for octahedral Fe^{3+}, and is similar to previously reported Fe^{3+} centre shifts in charged $Na_xFe_{0.3}Ni_{0.7}O_2$ [33], charged $Na_xFe_{1/3}Mn_{1/3}Co_{1/3}O_2$ [60], charged

$Li_xFe_{0.1}Ni_{0.9}O_2$ [98], and others [46] [99] [100]. The lower value of the CS of the Fe^{3+} site, corresponding to a higher s-electron density, may be attributed to the different oxidation states of neighboring transition metal sites in comparison to uncharged materials, i.e. Co^{4+} or Ni^{4+}, which suppresses the screening effect from 3D electrons [33].

In the charged $NaFe_{0.4}Co_{0.6}O_2$ sample, the Fe^{3+} site the CS converged to a value near +0.1, which is below the traditionally accepted value for Fe^{3+} sites. Therefore, the result of this fit is questionable. When the value of the CS for the Fe^{3+} site is fixed near 0.24, as has been traditionally observed in similar materials [33] [46] [60] [98], there is an increase in the quadrupole splitting of the Fe^{3+} to 0.7 mm/s, and parameters for the Fe^{4+} remain similar. The relative area increases to 82% Fe^{4+}. The goodness of fit becomes significantly worse when the CS of the Fe^{3+} site is fixed at higher values. The results would suggest that most of the Fe has been oxidized in this material and would result in more Fe^{4+} existing in the charged $NaFe_{0.4}Co_{0.6}O_2$ sample in comparison to the charged $Na_xFe_{0.5}Co_{0.5}O_2$ sample.

The Fe^{4+} site is a doublet with a centre shift near -0.06 mm/s. Quadrupole splittings are small in the charged $NaFe_xCo_{1-x}O_2$ samples, near 0.3 mm/s. A low QS has also been reported for 1% Fe-doped P2- $Na_{0.82}CoO_2$, near 0.18 mm/s for the Fe^{4+} site [101]. It was speculated that this low QS is a result of the charge ordering of the Na-ions [101]. Additionally, there is an O3 → P3 transition in $NaFe_{0.5}Co_{0.5}O_2$ during the initial plateau on charge, with no other two phase regions in the voltage curve [31]. It is possible that Na vacancies in the neighboring prismatic sites are the origin of the low QS. This has

been observed in the charged P2-$Na_xMn_{1/3}Fe_{1/3}Co_{1/3}O_2$, where the P2 material had a QS near 0.32 mm/s when charged to 4.1 V [60]. In contrast, the quadrupole splittings of Fe^{4+} in the charged $NaFe_x(Ni_{0.5}Co_{0.5})_{1-x}O_2$ samples are significantly higher, between 0.8-0.9 mm/s. This is in line with the previously reported $Na_{0.4}Fe_{0.3}Ni_{0.7}O_2$ sample which was obtained electrochemically, where the QS is near 0.82 mm/s [33], and is also comparable to the Fe^{4+} site measured in charged $Li_xFe_{0.1}Ni_{0.9}O_2$, where the QS was reported in the 0.9-1.0 mm/s range [98]. Fe^{4+} in charged $Li_xNi_{0.70}Fe_{0.15}Co_{0.15}O_2$ were reported to have QS in the 0.9-1.2 mm/s range [100]. It is possible that nearby Na-vacancies also affect the quadrupole splittings of the Fe^{4+} sites, as seen with Fe^{3+}(2) sites reported in earlier sections.

Based on results reported in this thesis, it has been demonstrated that the creation of edge sharing Na-vacancies causes an increase in observed quadrupole splitting of Fe^{3+} sites. It is possible that Na-vacancies prefer the creation of Fe^{3+}(2) sites in the Ni^{3+}-containing samples, which induces the higher values of quadrupole splitting, due to the suppression of the O3 → P3 transition. Noticed is that the QS of the Fe^{3+} site increases as $NaFe_{0.3}Ni_{0.7}O_2$ is charged [33], which is consistent with the creation of Fe^{3+}(2) sites. It is also possible that the existence of a small component corresponding to tetrahedral Fe^{3+} in the charged material may also affect the validity of the two site models utilized in this and the previous work [33] [46].

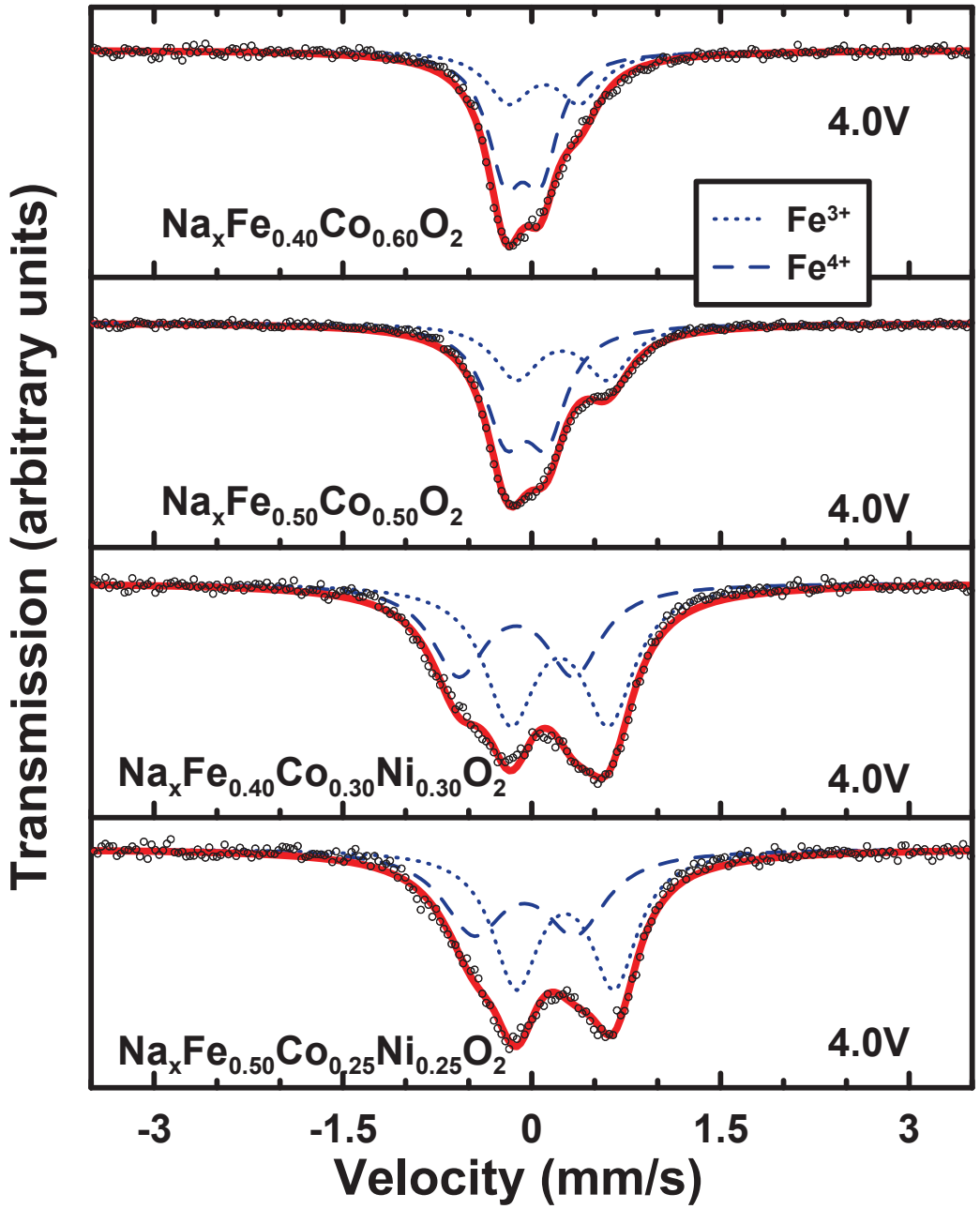

Figure 6.12: Ex-situ Mössbauer measurements for samples removed from cells charged to 4.0 V. Data and results of a two site model are shown, with the sum shown as solid red lines.

Sample	Site	CS (mm/s)	QS (mm/s)	Area (%)
$Na_xFe^{4+}_{0.27}Fe^{3+}_{0.13}Co_{0.6}O_2$ (charged to 4.0 V)	Fe^{3+} Fe^{4+}	+0.11(4) -0.07(1)	0.58(5) 0.28(2)	34 66
$Na_xFe^{4+}_{0.31}Fe^{3+}_{0.19}Co_{0.5}O_2$ (charged to 4.0 V)	Fe^{3+} Fe^{4+}	+0.240(7) -0.045(3)	0.72(1) 0.326(8)	37 63
$Na_xFe^{4+}_{0.15}Fe^{3+}_{0.25}(Co_{0.5}Ni_{0.5})_{0.6}O_2$ (charged to 4.0 V)	Fe^{3+} Fe^{4+}	+0.255(6) -0.11(1)	0.781(8) 0.91(1)	61 39
$Na_xFe^{4+}_{0.23}Fe^{3+}_{0.29}(Co_{0.5}Ni_{0.5})_{0.5}O_2$ (charged to 4.0 V)	Fe^{3+} Fe^{4+}	+0.225(8) -0.07(2)	0.787(7) 0.81(2)	59 41

Table 6.3: Fitted room temperature ^{57}Fe Mössbauer effect parameters for the doublet sites in charged samples as indicated. A two site model was used to extract the ratio of Fe^{4+} with estimated valence states of Fe indicated. All parameters were freed in the fits.

Samples with improved capacity retention and energy density with equal or more Fe^{4+} can be demonstrated with Co containing materials. The special placement of Na in the ordered phases observed during Na_xCoO_2 voltage plateaus [19, 102] may be the driving factor in producing highly symmetric Fe environments with low quadrupole splittings. The gradual emergence of voltage plateaus as less Fe is utilized is seen in the electrochemical results in Figures 6.4, 6.6, and 6.9, which has been shown to be due to presence of in-plane Na vacancy ordering and gliding of the CoO_2 layers in Na_xCoO_2 [19]. The ordered transition observed as a sharp change in voltage near 3.5 V and other

features line up when comparing the voltage curves of the $NaFe_{0.5}Co_{0.5}O_2$ and $NaCoO_2$ [31]. Materials having more resolved plateaus are correlated with improved cycling performance in the studied Fe-containing samples. While a two phase plateau or an order/disorder transition may be a source of capacity fade in other materials due to abrupt changes in volume [103], it is possible that formation of Na-vacancy ordered phases having prismatic sites in the M = Co samples mitigates the Fe migration by suppressing the creation of Fe^{3+}(2) sites. A detailed study of in-situ or ex-situ XRD patterns of charged materials are necessary to help determine the phases present and to model Na positions. This is necessary to better understand the observed Mössbauer parameters and to develop more complex models. Good stability is seen for the $NaFe_{0.4}Co_{0.6}O_2$ sample, having the best combination of capacity retention, and energy density and other electrochemical features of all samples evaluated in this work, using the active $Fe^{3+} \leftrightarrow Fe^{4+}$ redox couple.

6.6 CONCLUSIONS

It was found that addition of Fe is a source of capacity fade for each system in all galvanostatic cycling tests conducted in the 1.5-4.0 V range. Improved capacity retention was also observed when M = Co in comparison to M = $Ni_{0.5}Co_{0.5}$ in $NaFe_xM_{1-x}O_2$ for fixed amounts of iron (x = 0.4, 0.5).

An investigation of new $NaFe_x(Co_{1/2}Ni_{1/2})_{1-x}O_2$ phases belonging to the α-$NaFeO_2$ type structure is reported. Increasing the value of x from 0 to 0.1 results in an increase in

capacity retention and energy density. Further increasing the value of x from 0.1 to 0.5 results in an increase of energy density, but capacity retention on a percentage basis after 20 cycles is reduced in samples containing more Fe. Use of Fe causes an increase in first cycle energy density from 320 Wh/kg to 440 Wh/kg when x is increased from 0 to 0.5 when cycled with constant current between 1.5-4.0 V. Samples have been directly compared to $NaFe_xCo_{1-x}O_2$ and it is found that there is roughly 10% difference in the volumetric energy density in the $NaFe_{0.5}Co_{0.5}O_2$ and $NaFe_{0.5}(Ni_{0.5}Co_{0.5})_{0.5}O_2$ samples. However, use of Ni in place of Co results in lower capacity retention. Capacity retention and energy density increases have now been observed when Fe is added to $NaCoO_2$ [31], with improvement in cycling stability seen in the $NaFe_{0.4}Co_{0.6}O_2$ sample over the $NaFe_{0.5}Co_{0.5}O_2$ sample. Given this improvement, the value of x can still be optimized in $NaFe_xCo_{1-x}O_2$ with $0 < x \leq 0.4$.

The optimal value of x in $NaFe_xCo_{1-x}O_2$ is much higher than the optimal value of x in $NaFe_x(Co_{0.5}Ni_{0.5})_{1-x}O_2$ on the basis of capacity retention. It is possible that Fe can be stabilized in the transition metal layer during cycling with large amounts of vacancies only when used in conjunction with Co. The use of Co^{3+} in the synthesized materials has been demonstrated to be preferred over Ni^{3+} when paired with Fe on the basis of electrochemistry. Ex-situ Mössbauer results of charged $NaFe_x(Co_{0.5}Ni_{0.5})_{1-x}O_2$ and $NaFe_xCo_{1-x}O_2$ show that poor cycling performance is correlated to larger quadrupole splittings measured at the Fe sites, and indicate that the amount of Fe^{4+} present in each respective sample is not the only factor in determining the capacity fade. It is possible that Fe migration to the adjacent Na layer occurs in these samples during cycling due to

the creation of more Fe^{3+}(2) sites during charge. Use of Co appears to be most effective for stabilizing Fe in the transition metal layer in Fe-containing layered cathodes thus far when the $Fe^{3+} \leftrightarrow Fe^{4+}$ is used during cycling [31].

CHAPTER 7 STUDIES OF $Na_{2/3}Fe_xMn_xCo_{1-2x}O_2$

7.1 INTRODUCTION

Many new ternary systems have been introduced as layered Na-ion battery cathodes using elements Ni, Mn, and Co which are commonly used in layered Li-ion battery cathodes. These have been introduced in the form of O3-$NaFe_{1/3}Co_{1/3}Ni_{1/3}O_2$ [34] O3-$NaMn_{1/3}Co_{1/3}Ni_{1/3}O_2$ [104] and O3-$NaMn_{1/3}Fe_{1/3}Ni_{1/3}O_2$ [15]. In this chapter, a new P2-$Na_{2/3}Mn_{1/3}Fe_{1/3}Co_{1/3}O_2$ material is synthesized and used in sodium half cells to introduce the $Na_{2/3}Mn_xFe_yCo_zO_2$ system, including ex-situ Mössbauer studies of the charged electrodes to help determine the mechanism of oxidation / reduction during cycling. Work on $Na_{2/3}Mn_{1/3}Fe_{1/3}Co_{1/3}O_2$ presented in this chapter was published in 2014 [60]. Other compositions in the $Na_{2/3}Fe_xMn_xCo_{1-2x}O_2$ system are presented for potential application to Na-ion battery positive electrodes. Exploration of new Fe and Co containing layered cathodes aid in the understanding of the role of the various transition metals for design of new cathodes.

7.2 SYNTHESIS

Stoichiometric amounts of MnO_2, Fe_3O_4, Co_3O_4 and Na_2O_2 were ball milled for 4 hours in Argon. The resulting powders were then pressed into a pellet and heated in O_2 for 12 hours at 950 °C, followed by immediate removal from the furnace to quench to room temperature without air exposure. Samples were not exposed to the atmosphere.

7.3 CHARACTERIZATION BY XRD

Figure 7.1 shows the XRD pattern of the synthesized $Na_{2/3}Mn_{1/3}Fe_{1/3}Co_{1/3}O_2$. No noticeable impurities were detected. The XRD pattern was fit to the $P6_3/mmc$ space group using Rietveld refinement, which indicates that this oxide has the P2 structure. Details of the refinement are summarized in Table 7.1. Previous studies have shown that Co is in the 3+ oxidation state in $Na_{2/3}Mn_{1/3}Co_{2/3}O_2$ [25], implying that all Mn is in the 4+ oxidation state. Furthermore the Fe has been found to be 3+ in $Na_xFe_xMn_{1-x}O_2$ ($1.0 \geq x \geq 0.5$) [27]. Therefore it is reasonable to assume that all Mn is in its 4+ oxidation state in $Na_{2/3}Mn^{4+}_{1/3}Fe^{3+}_{1/3}Co^{3+}_{1/3}O_2$.

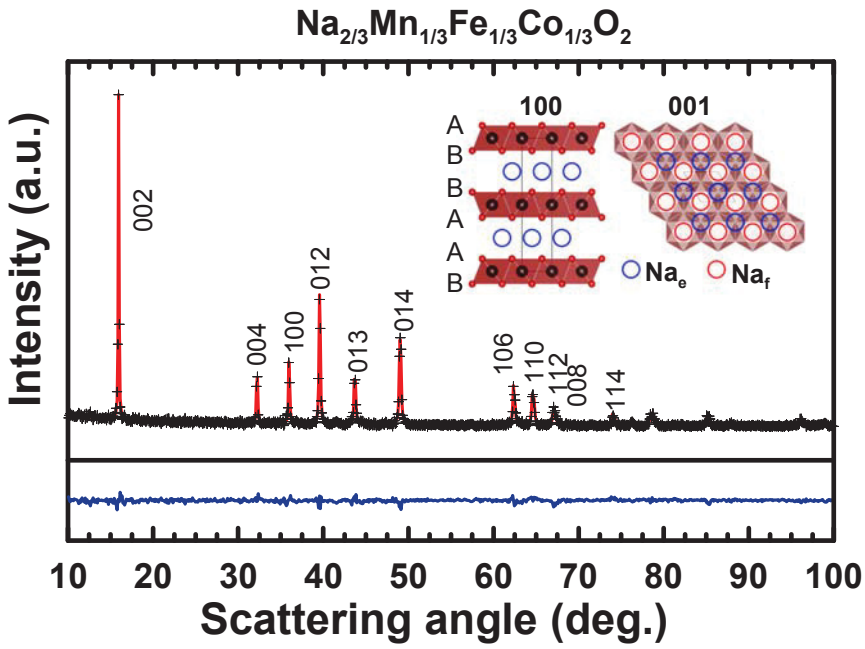

Figure 7.1: XRD pattern of $Na_{2/3}Mn_{1/3}Fe_{1/3}Co_{1/3}O_2$ with results of Rietveld refinement and difference plot. An illustration of the (001) and (100) projections are shown. Na_e and Na_f are shown for a given atomic layer. Solid black and solid red atoms correspond to the transition metals and oxygen respectively. A difference plot is shown.

Atom	**Site**	**x**	**y**	**z**	**Occupancy**	**B (Å^2)**
Na_f	2b	0	0	¼	0.23	0.4
Na_e	2d	1/3	2/3	¼	0.43	0.4
Mn	2a	0	0	0	1/3	0.2
Fe	2a	0	0	0	1/3	0.2
Co	2a	0	0	0	1/3	0.2
O	4f	2/3	1/3	0.095(1)	1	0.5
a_{hex} = 2.884(5) Å. c_{hex} = 11.123(7) Å. Bragg R-factor = 4.24.						

Table 7.1: Parameters used for Rietveld refinement of the $Na_{2/3}Mn_{1/3}Fe_{1/3}Co_{1/3}O_2$ using space group $P6_3/mmc$. Errors in the fitted parameters are shown. All other parameters were fixed.

Many layered oxide solid solution compositions containing Mn, Fe and Co can be synthesized. Figure 7.2 shows XRD patterns of P2- $Na_{2/3}Fe_xMn_xCo_{1-2x}O_2$ compounds. In some samples, an O3 impurity can be seen, suggesting that changing the annealing temperature and time as well as the Na content in the starting material can likely lead to the formation of phase pure O3- materials such as $NaMn_{1/3}Fe_{1/3}Co_{1/3}O_2$.

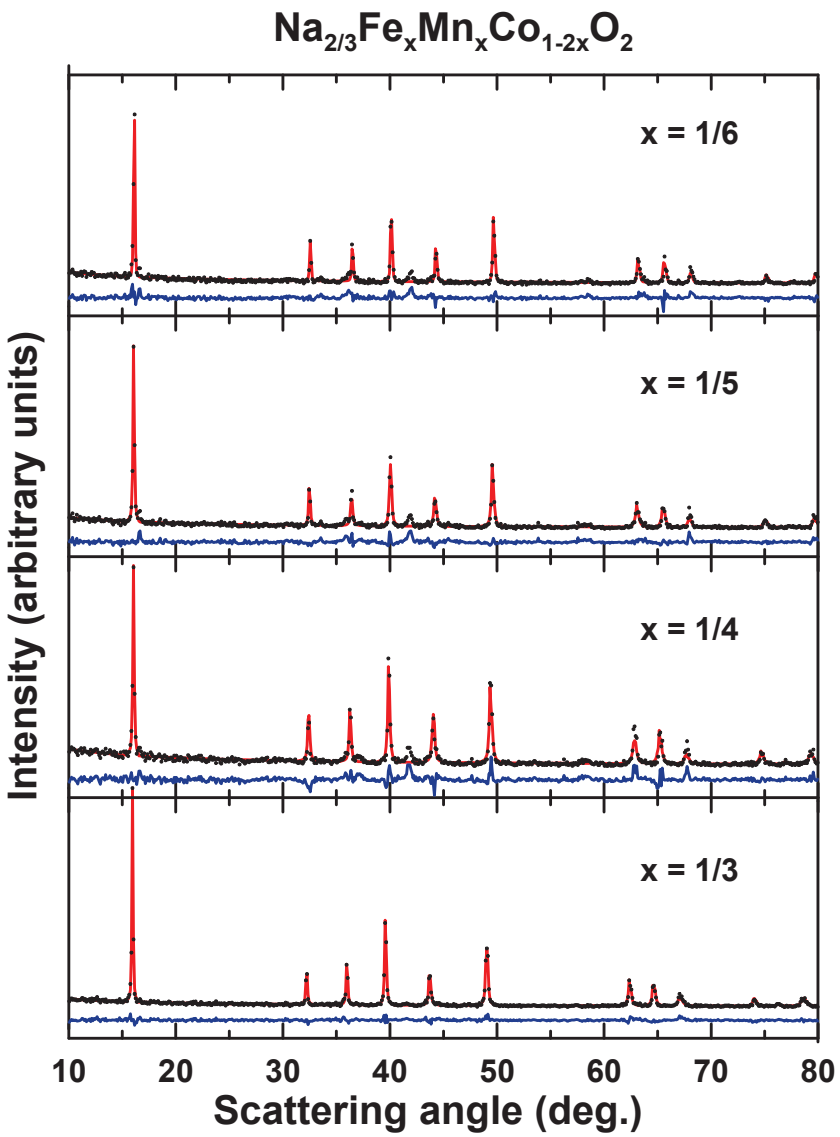

Figure 7.2: XRD patterns of the P2- $Na_{2/3}Fe_xMn_xCo_{1-2x}O_2$ samples ($1/6 \leq x \leq 1/3$) with results of Rietveld refinement. O3 impurities can be seen near 42.5 deg in some samples. Difference plots are shown in blue.

7.4 ELECTROCHEMISTRY

Figure 7.3 shows the first cycle voltage curves of P2-$Na_{2/3}Mn_{1/3}Fe_{1/3}Co_{1/3}O_2$ cycled between 1.5 V and different upper cut-off voltages of 4.0 V, 4.25 V and 4.5 V. This

resulted in first charge/discharge capacities of 86/125mAh/g, 133/162 mAh/g, and 153/173 mAh/g, respectively. Figure 7.4 shows the corresponding differential capacity curves for the cells cycled between 1.5 - 4.0 V and 1.5 - 4.5 V.

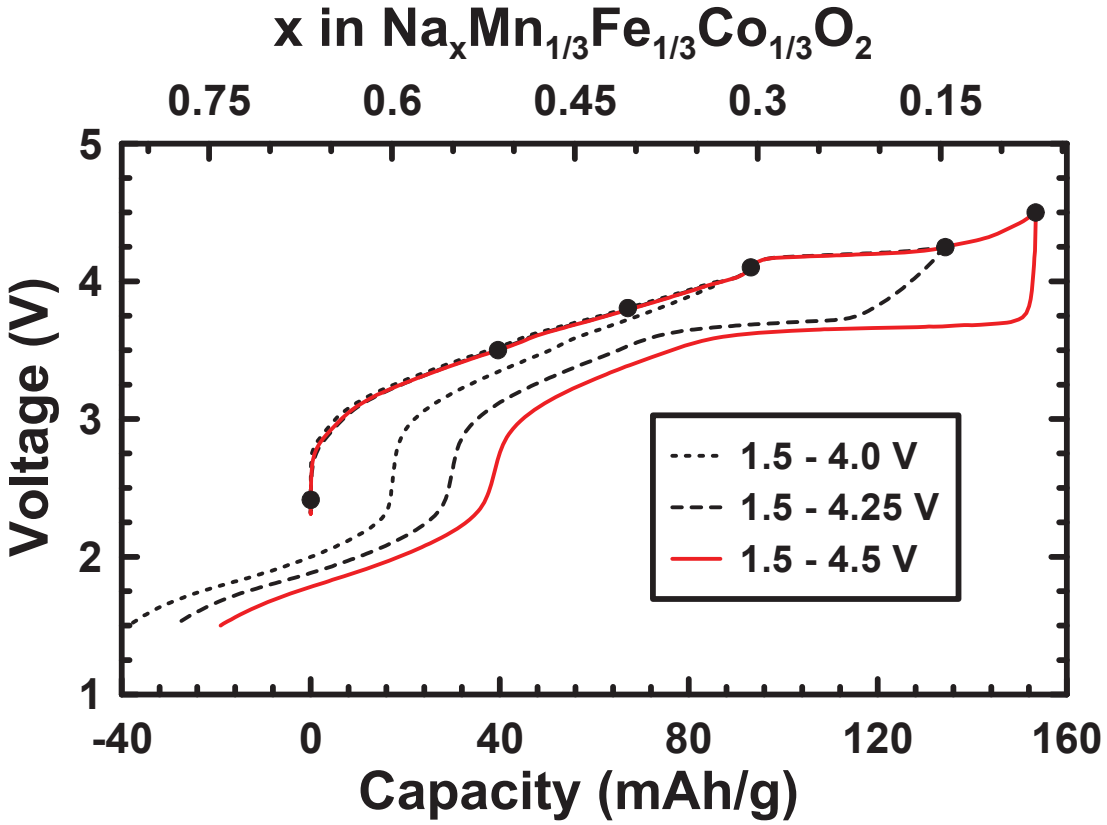

Figure 7.3: First cycle voltage profile of $Na_{2/3}Mn_{1/3}Fe_{1/3}Co_{1/3}O_2$ between 1.5 V and various cutoff voltages using 10 mA/g current density. Data points for voltages selected for ex-situ Mössbauer measurements are shown.

The voltage curves of Figure 7.3 are characterized by an initially sloping plateau between 3 V – 4.1 V, characteristic of a single-phase region (corresponding to the broad features observed in differential capacity between 3 - 4.1 V in Figure 7.4). Assuming the starting material has a composition corresponding to x = 2/3 in $Na_xMn_{1/3}Fe_{1/3}Co_{1/3}O_2$, the charge

capacity associated with this sloping plateau corresponds to the theoretical formation of $Na_{0.31}Mn_{1/3}Fe_{1/3}Co_{1/3}O_2$ at 4 V. If the cell is subsequently discharged, this sloping plateau is completely reversible. If the discharge is allowed to proceed further, a low voltage sloping plateau starting at about 2.2 V results. This corresponds to a broad peak in the differential capacity centred at about 1.8 V. During this low voltage plateau, more sodium is introduced than was present in the initial material, resulting in endpoint discharge capacity of -39 mAh/g, corresponding to the theoretical formation of x = 0.82 in $Na_xMn_{1/3}Fe_{1/3}Co_{1/3}O_2$.

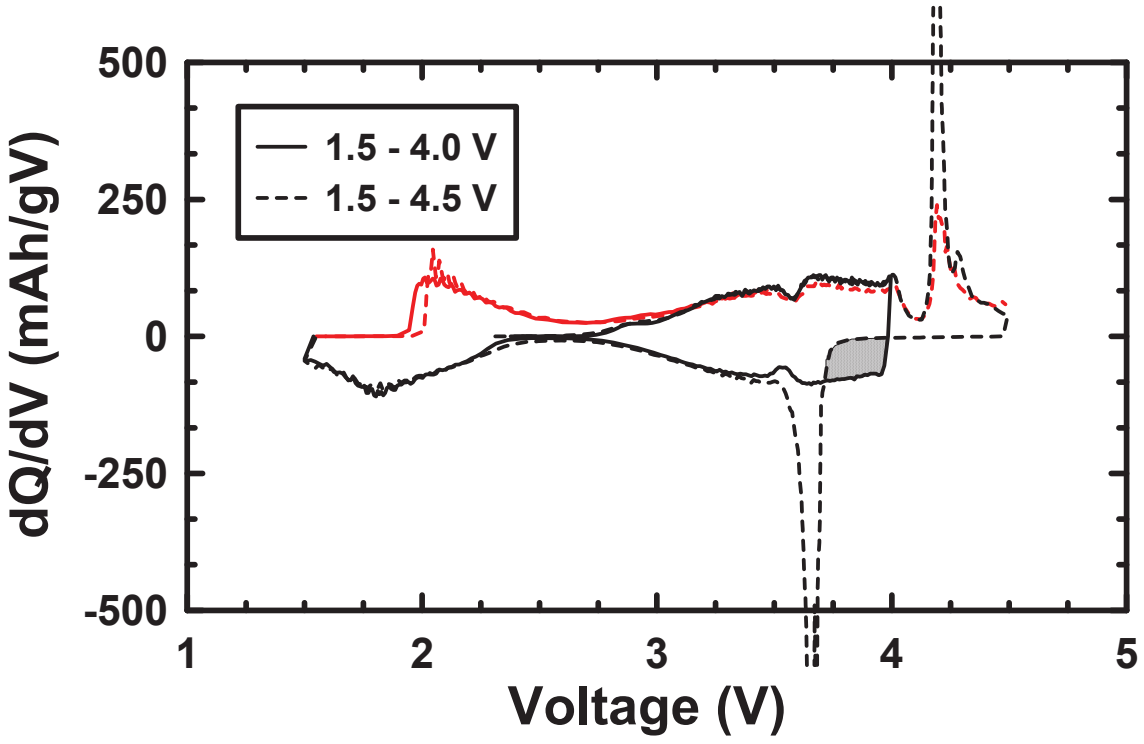

Figure 7.4: differential capacity (dQ/dV) as a function of voltage for the first 1.5 cycles for cells cycled between 1.5-4.0 V and 1.5-4.5 V. The second half-cycle is shown in red. The shaded region indicates the capacity of the 3 - 4.1 V plateau that is lost when the full 4.2 V plateau is accessed.

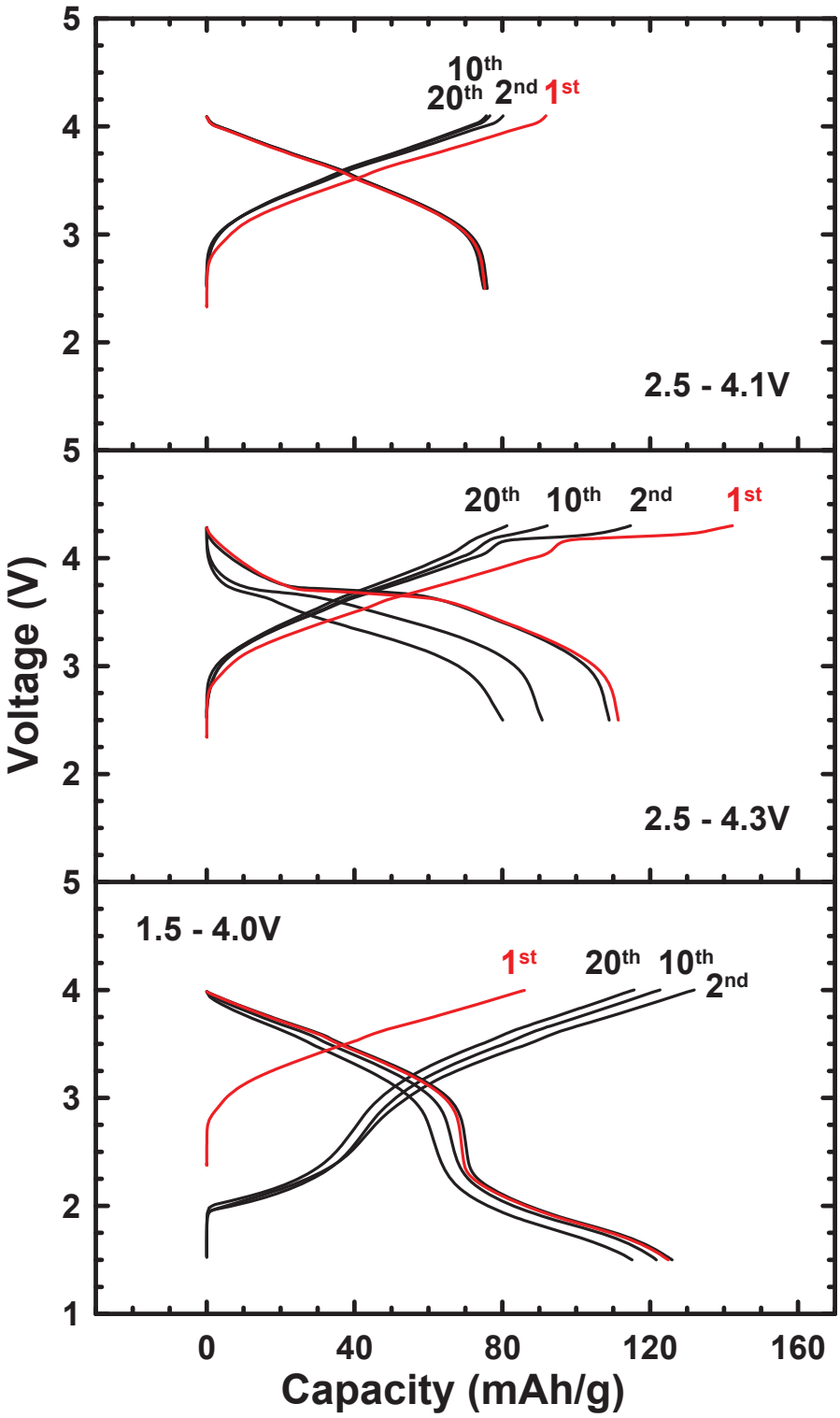

Figure 7.5: Voltage vs. capacity profiles for selected cycles with voltage ranges indicated using 10mA/g current density.

Below 3.7 V the differential capacity curves are nearly identical during the first and second cycles for all voltage ranges. Accessing voltages above 4.1 V results in a voltage plateau and a peak in the differential capacity at about 4.2 V. The full capacity of this plateau is accessed by charging to 4.5 V and results in a plateau capacity of about 61 mAh/g, corresponding to the removal of 0.23 Na and the theoretical formation of $Na_{0.08}Mn_{1/3}Fe_{1/3}Co_{1/3}O_2$. However, this may not be the actual stoichiometry at this voltage as will be discussed below.

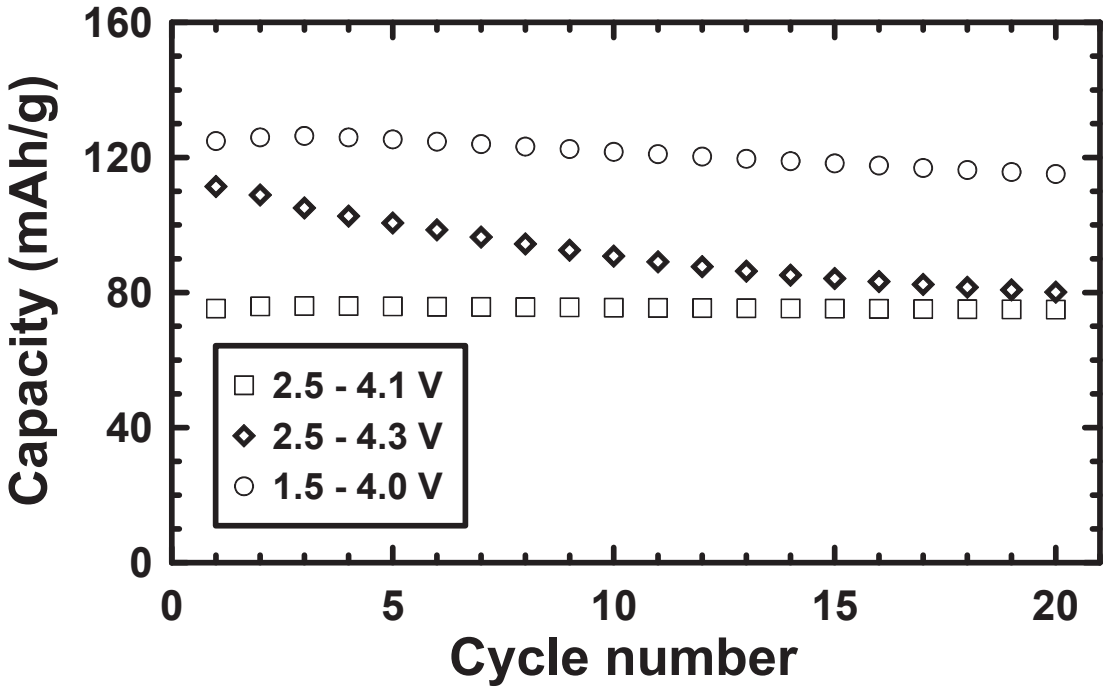

Figure 7.6: Discharge capacity vs. cycle number corresponding to samples from Figure 7.5 with indicated voltage ranges.

The 4.2 V plateau is fully reversible, but is associated with considerable hysteresis, as its corresponding discharge plateau occurs at about 3.6 V. Below this voltage the differential capacity is identical to cells that were charged to voltages below 4.1 V.

However, accessing the 4.2 V plateau causes discharge capacity above 3.7 V of the 3 V – 4.1 V sloping plateau to be lost. This is most easily seen in the differential capacity curve, where this capacity loss is shown as a shaded region in Figure 7.4. The amount of 3 V – 4.1 V plateau capacity loss increases as more of the 4.2 V plateau is accessed. This results in the voltage curves becoming shifted progressively to higher capacities as the upper cut-off voltage is increased above 4.1 V. The reduction of the 3 V – 4.1 V capacity as a result of accessing higher voltage and the large hysteresis of the 4.2 V voltage plateau indicate that structural changes occur during the 4.2 V plateau.

Figure 7.5 and 7.6 illustrate cycling performance of samples cycled between 2.5-4.1 V and 2.5 - 4.3 V. Despite the formation of roughly 0.13 Fe^{4+} at the top of charge (shown in section 7.5), the sample cycled between 2.5 - 4.1 V has very little hysteresis and excellent cycling characteristics, having 99.7% capacity retention after 20 cycles (76 mAh/g, 3.55V), with ~15 mAh/g irreversible capacity. The preceding shows that it is possible to access reversible $Fe^{3+} \rightarrow Fe^{4+}$ oxidation with excellent capacity retention and negligible hysteresis. However, when attempts were made to extend the upper voltage cut-off to 4.3V, the irreversible capacity increased to 31 mAh/g. The first cycle gravimetric energy density increased significantly to 400 Wh/kg (111 mAh/g, 3.58V) at the expense of cycling stability: just 72% discharge capacity retention remains after 20 cycles. When cells are cycled between 1.5 - 4.0 V range (125 mAh/g, 2.77V), there is an increase in voltage hysteresis and deterioration to just 92% capacity retention after 20 cycles.

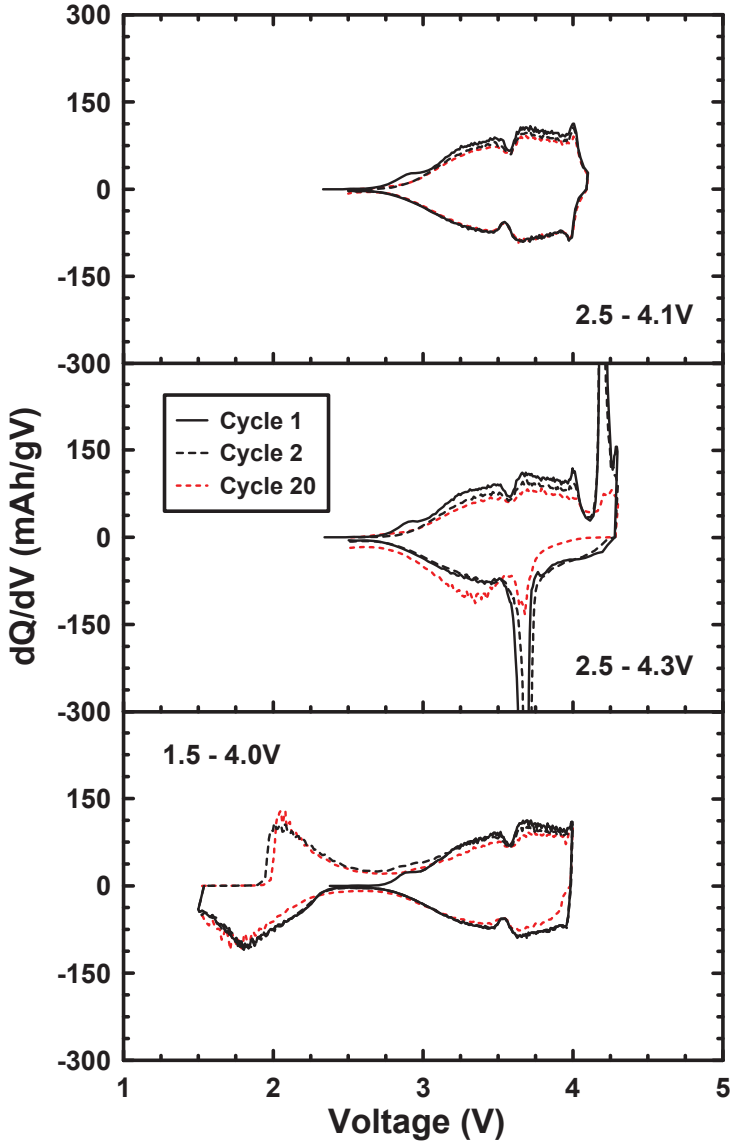

Figure 7.7: Voltage vs. dQ/dV plots for selected cycles with voltage ranges indicated using 10 mA/g current density. Features which may be characteristic of Na-ordered phases are seen near near 3.5 V and 4.1 V.

Figure 7.7 shows the differential capacity curves of the cells shown in Figure 7.5. The differential capacity is completely reversible when cells are cycled below 4.1 V, indicating structural stability. Accessing the 4.2 V plateau during charge results in the

loss of some of the 3 - 4.1 V sloping plateau capacity during the subsequent discharge. During the next cycle the 3 - 4.1 V sloping plateau remains unchanged during charge from the first cycle, however the 4.2 V plateau capacity is significantly reduced. After 20 cycles the 4.2 V plateau capacity has almost disappeared, which is indicative that major structural changes have occurred. Interestingly the 3 - 4.1 V sloping plateau remains unchanged during charge from the first cycle. During discharge the capacity of this plateau is much reduced above 3.7 V.

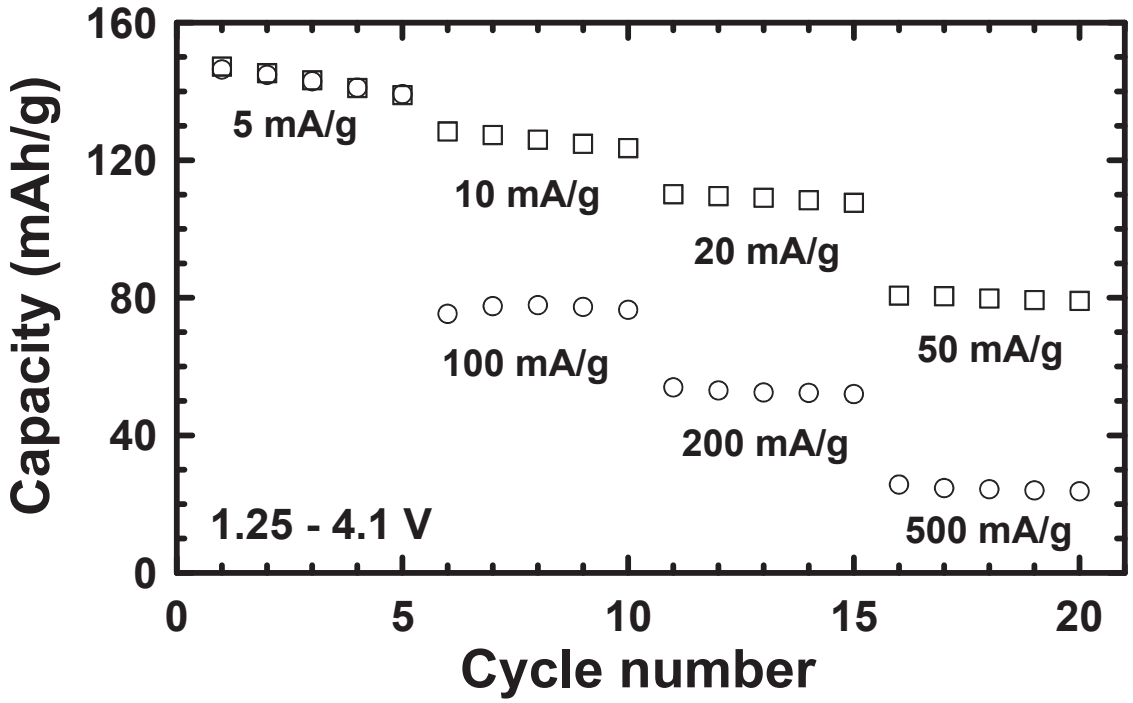

Figure 7.8: Cycle number vs. discharge capacity for various current densities indicated when cycled between 1.25-4.1 V.

Figure 7.8 shows the discharge capacity of P2-$Na_{2/3}Mn_{1/3}Fe_{1/3}Co_{1/3}O_2$ cycled between 1.25 - 4.1V at different cycling rates varying from roughly C/20 (5 mA/g) to 5C (500 mA/g) based on the first charge capacity. Results are found to be similar to rate tests

between 1.5-4.0V. The rate performance is relatively poor with roughly 60% of the C/10 rate capacity (10 mA/g, cycles 6-10, ~126 mAh/g) measured at 1C rate (100mA/g, cycles 6-10, ~78 mAh/g). There is a large increase in polarization at higher rates. Results are similar to comparable tests of $Na_{0.71}CoO_2$ [20].

7.5 CHARACTERIZATION BY EX-SITU MÖSSBAUER SPECTROSCOPY

Figure 7.9 shows ex-situ Mössbauer spectra of P2-$Na_{2/3}Mn_{1/3}Fe_{1/3}Co_{1/3}O_2$ electrodes removed from cells at different points in the voltage curve, as indicated in Figure 7.3. A simple two site model using Lorentzian doublets was employed to fit the Mössbauer spectra. Mössbauer spectra fitting parameters are listed in Table 7.2. The Mössbauer spectra of the as prepared $Na_{2/3}Mn_{1/3}Fe_{1/3}Co_{1/3}O_2$ correspond entirely to Fe^{3+}. This is in agreement with the assumption that all Mn is 4+ in the as prepared material which is presumed to be $Na_{2/3}Mn^{4+}{}_{1/3}Fe^{3+}{}_{1/3}Co^{3+}{}_{1/3}O_2$.

Figure 7.10 shows a plot of the percentage of Fe in the 4+ state plotted from Table 7.2, along with the best fit line for values below 4.1 V. During charge on the 3 – 4 V sloping plateau, it was found that $Fe^{3+} \rightarrow Fe^{4+}$ oxidation occurs linearly as a function of x in $Na_xMn_{1/3}Fe_{1/3}Co_{1/3}O_2$. Based on the relative areas of the spectral components, roughly 40% of Fe has an oxidation state of 4+ at 4.1 V. This degree of iron oxidation can account for the removal of about 0.13 Na of the theoretical ~0.35 Na removed at this voltage. This indicates that the 3 - 4 V plateau is most likely associated with

simultaneous Fe^{3+} and Co^{3+} oxidation, with the theoretical formation of $Na_{0.31}Mn^{4+}_{1/3}Fe^{3+}_{0.2}Fe^{4+}_{0.13}Co^{3+}_{0.12}Co^{4+}_{0.22}O_2$ at 4.1 V.

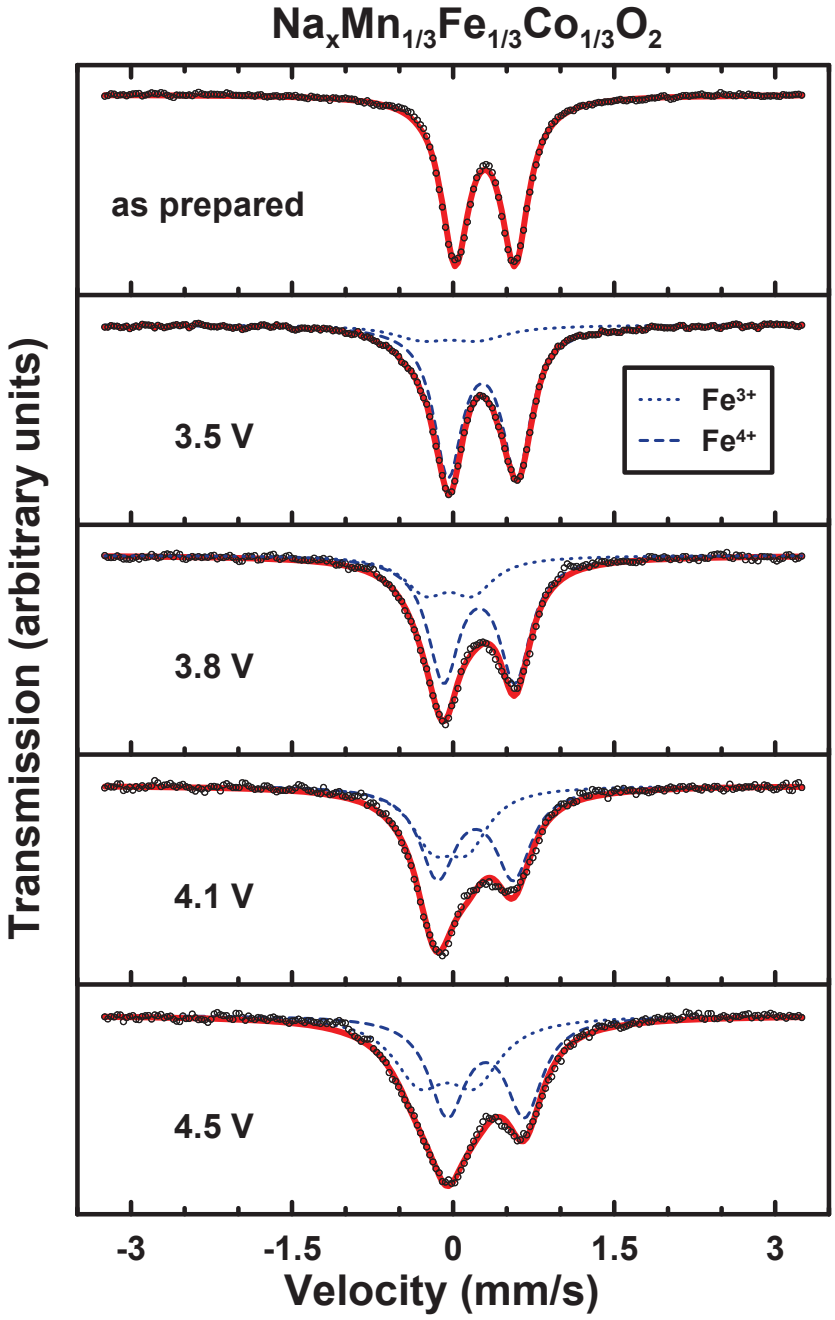

Figure 7.9: Ex-situ Mössbauer measurements for the as prepared sample and samples removed from cells charged to 3.5 V, 3.8 V, 4.1 V, and 4.5 V. Data and results of a two site model are shown.

Sample	**Capacity (mAh/g)**	**Site**	**CS (mm/s)**	**QS (mm/s)**	**A (%)**
As prepared	0	Fe^{3+}	+0.297	0.555	100
$Na_xFe^{4+}_{0.06}Fe^{3+}_{0.27}Co_{1/3}Mn_{1/3}O_2$	40	Fe^{3+}	+0.273	0.639	82
(charged to 3.5 V)		Fe^{4+}	-0.029	0.532	18
$Na_xFe^{4+}_{0.11}Fe^{3+}_{0.22}Co_{1/3}Mn_{1/3}O_2$	67	Fe^{3+}	+0.244	0.665	68
(charged to 3.8 V)		Fe^{4+}	-0.037	0.432	32
$Na_xFe^{4+}_{0.14}Fe^{3+}_{0.19}Co_{1/3}Mn_{1/3}O_2$	92	Fe^{3+}	+0.208	0.707	58
(charged to 4.1 V)		Fe^{4+}	-0.026	0.320	42
$Na_xFe^{4+}_{0.14}Fe^{3+}_{0.19}Co_{1/3}Mn_{1/3}O_2$	92	Fe^{3+}	+0.224	0.726	59
(charged to 4.1 V)		Fe^{4+}	-0.014	0.343	41
$Na_xFe^{4+}_{0.15}Fe^{3+}_{0.18}Co_{1/3}Mn_{1/3}O_2$	134	Fe^{3+}	+0.299	0.742	55
(charged to 4.25 V)		Fe^{4+}	-0.032	0.508	45
$Na_xFe^{4+}_{0.16}Fe^{3+}_{0.17}Co_{1/3}Mn_{1/3}O_2$	153	Fe^{3+}	+0.306	0.725	52
(charged to 4.5 V)		Fe^{4+}	-0.025	0.512	48

Table 7.2: Room temperature ^{57}Fe Mössbauer effect parameters for two doublet sites extracted from charged $Na_xMn_{1/3}Fe_{1/3}Co_{1/3}O_2$ materials. Typical uncertainties in measured velocities are ±0.005 mm/s.

Ex-situ Mössbauer measurements at voltages higher than 4.1 V indicate that $Fe^{3+} \rightarrow Fe^{4+}$ continues to occur during the 4.2 V plateau, as the Fe^{4+} spectral component becomes more prominent, though there is a sharp increase in the value of the quadrupole splitting.

However, the rate of increase of the estimated fraction of Fe^{4+} as a function of x is much lower on the 4.2 V plateau, compared to the 4.1 V plateau, as shown in Figure 7.10. The spectra obtained at 4.5 V suggest that only about half of Fe is in the 4+ oxidation state. Assuming all Mn and Co are 4+ at 4.5 V, this only accounts for the removal of 0.15 Na during the 4.2 V plateau, whereas 0.24 Na is removed according to the voltage curve. This unaccounted Na loss may be due to electrolyte decomposition. However, considering that the 4.5 V plateau is almost completely reversible, the amount of Na loss due to electrolyte decomposition may be small compared to this unaccounted Na.

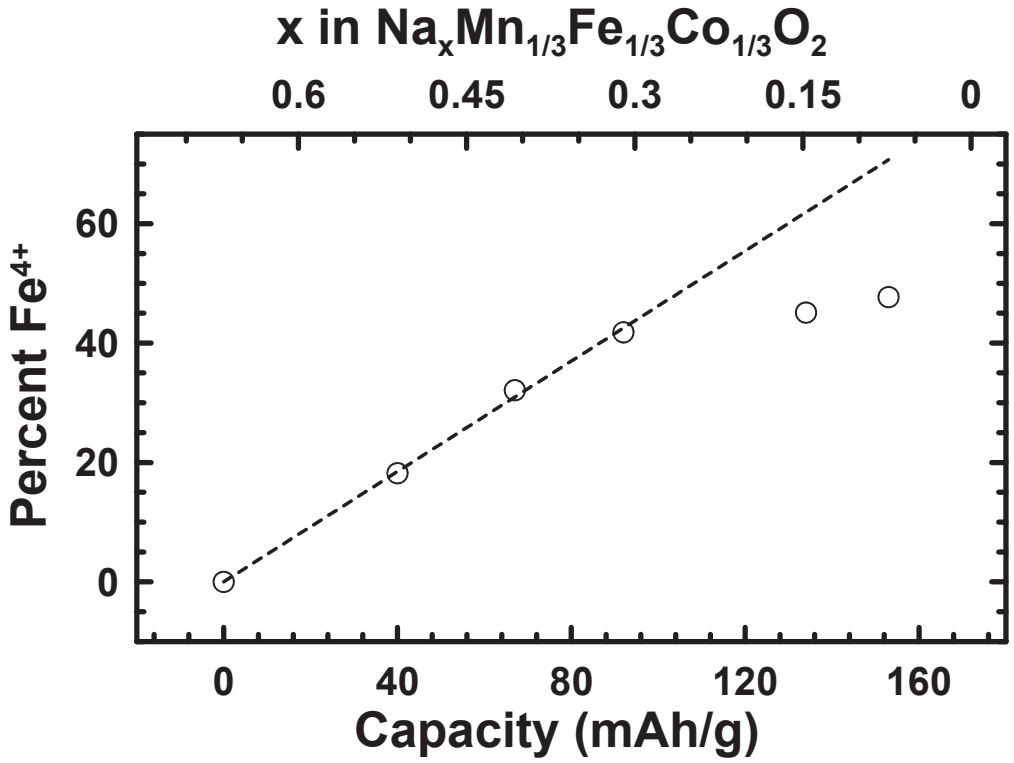

Figure 7.10: Fraction of Fe^{4+} plotted as a function of capacity. The line of best fit for values extracted from 4.1 V and below is used to help isolate sources of irreversible capacity.

This suggests that the majority of unaccounted capacity at 4.5 V may be a result of structural damage. This would result in Na^+ removal from the material with little change in the oxidation state of the transition metals, as is observed here. The structural damage resulting from this results in the lowering of the 3 - 4.1 V plateau capacity and in the reduction of the 4.2 V plateau capacity during subsequent cycles. To confirm this model, in-situ XRD studies and studies including electrolytes that are known to be stable at high voltages are needed. Accessing the 4.2 V plateau results in severe capacity loss, indicative of some structural change, which may be associated with oxygen oxidation. More experiments are necessary to confirm this mechanism.

Recent work on $Na_{0.7}Fe_{0.4}Mn_{0.4}Co_{0.2}O_2$ has confirmed that the plateau above 4.1 V in that material is indicative of a structural change from the P2 phase to an O2 phase, and that the P2 structure is restored during discharge. However, a large volumetric contraction was observed during this transition [105], which is associated with capacity loss.

Charged $Na_xMn_{1/3}Fe_{1/3}Co_{1/3}O_2$ samples were also fit using the three site model. Figure 7.11 shows the results of these fits for the 4.1 V spectrum which was repeated and fit with nearly identical parameters from start to finish. Parameters and estimated valence states are shown in Table 7.3. Parameters for the ratio of Fe^{4+} are found to be similar to the two site model. Noticed is the small centre shift of the Fe^{3+} site, as well as the relatively low quadrupole splitting of the Fe^{4+} site near 0.35 mm/s. The quadrupole splittings of the Fe^{3+}(1) and Fe^{3+}(2) sites are typical for samples in this thesis. Smaller values of the quadrupole splitting and low values of the centre shifts for Fe sites may be

characteristic of the improved cycling characteristics seen for these samples (92% using 1.5-4.0 V), comparable to that of the $NaFe_{0.4}Co_{0.6}O_2$ (95%). Though there is more Fe^{4+} measured in the $NaFe_{0.4}Co_{0.6}O_2$ measured at 4.0 V, quadrupole splittings and centre shifts are significantly lower in the Fe sites in that sample (presented in Chapter 6), which appear to be correlating factors in cycling performance and hysteresis.

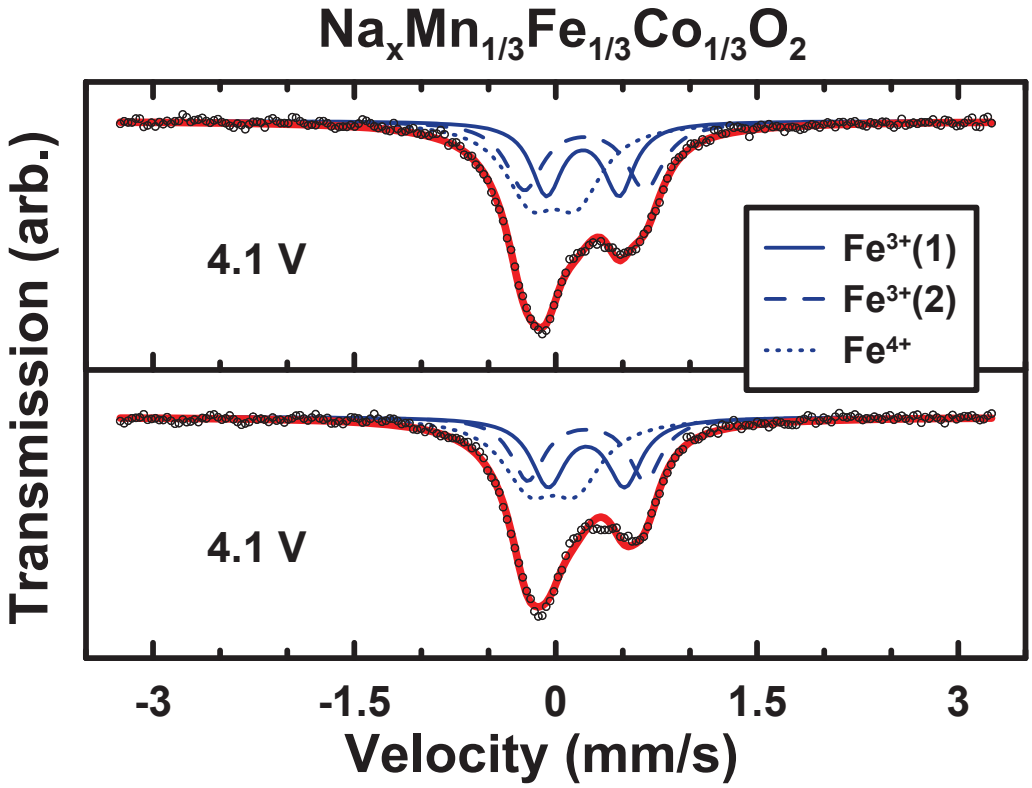

Figure 7.11: Ex-situ Mössbauer measurements for the sample charged to 4.1 V. The measurement and fit were repeated to strengthen the result. Data and results of a three site model are shown.

Sample	Site	CS (mm/s)	QS (mm/s)	Area (%)
$Na_xFe^{4+}_{0.14}Fe^{3+}_{0.19}Co_{0.33}Mn_{0.33}O_2$	Fe^{3+}(1)	+0.202*	0.541	27
(charged to 4.1 V)	Fe^{3+}(2)	+0.216	0.898	30
	Fe^{4+}	-0.014*	0.344	43
$Na_xFe^{4+}_{0.14}Fe^{3+}_{0.19}Co_{0.33}Mn_{0.33}O_2$	Fe^{3+}(1)	+0.229*	0.569	30
(charged to 4.1 V)	Fe^{3+}(2)	+0.228	0.875	27
	Fe^{4+}	-0.024*	0.351	43

* fixed parameter

Table 7.3: Fitted room temperature ^{57}Fe Mössbauer effect parameters for the doublet sites in charged samples (indicated). A three site model was used to extract the valence of Fe and the ratio of Fe^{3+}(1) to Fe^{3+}(2). Typical uncertainties for measured values of the centre shifts (CS) and quadrupole splittings (QS) are about ± 0.005 mm/s.

7.6 CONCLUSIONS

The preparation and electrochemical properties of a new P2-$Na_{2/3}Mn_{1/3}Fe_{1/3}Co_{1/3}O_2$ phase was reported, as well as synthesis of other samples in the P2-$Na_{2/3}Fe_xMn_xCo_{1-2x}O_2$ pseudo binary series. This material has sloping charge voltage plateaus between about 1.3-2.5 V, 3-4.1 V and a flat voltage plateau at 4.2 V, resulting in a total discharge capacity of about 173 mAh/g, and an average discharge voltage of 3.00 V, corresponding to an energy density of about 520 Wh/kg or 2240 Wh/L. It was found by ex-situ

Mössbauer measurements that simultaneous Co^{3+} and Fe^{3+} oxidation occurs during the 3 - 4.1 V charge plateau. This plateau is highly reversible and has low hysteresis. At 4.1 V (91 mAh/g first charge) an estimated 40% of the iron present is 4+. Excellent cycling characteristics with very low voltage hysteresis can be obtained using this cut-off voltage. This demonstrates that octahedral Fe^{4+} can be accessed with high efficiency. While formation of Fe^{4+} may adversely affect stability in binary layered $Na_xFe_yM_{1-y}O_2$ with M = Mn and Ni [27, 33], the use of Co with Fe in binary or ternary systems may be sufficient to stabilize the Fe^{4+} when cycled with selected voltage windows [31, 34]. Accessing the 4.2 V plateau results in severe capacity loss, indicative of some structural change, which may be associated with oxygen oxidation. More experiments are necessary to confirm this mechanism.

CHAPTER 8 TRENDS AND DISCUSSION

8.1 INTRODUCTION

A review of the currently available systematic studies on $Na_xFe_yM_{1-y}O_2$ layered cathodes with M = Co, $Co_{0.5}Ni_{0.5}$, Ni, $Ni_{0.5}Mn_{0.5}$, Mn, and Ti is presented. Of these systems, the highest available energy density below 4.0 V is reported to be the M = Co system, with over 520 Wh/kg and 2400 Wh/L in $NaFe_{1/2}Co_{1/2}O_2$ [31, 59]. Similar energy densities can be achieved with higher voltage limits using O3- $NaFe_{1/3}Co_{1/3}Ni_{1/3}O_2$ cycled to 4.2 V having 500 Wh/kg and 2340 Wh/L [34]. P2- $Na_{2/3}Fe_{1/2}Mn_{1/2}O_2$ cycled to 4.3 V yields 520 Wh/kg and 2130 Wh/L [9]. $Na_{2/3}Fe_{1/3}Mn_{1/3}Co_{1/3}O_2$ discharged from 4.5 V has 520 Wh/kg and 2240 Wh/L [60]. Quaternary systems are also beginning to be explored in the literature, with $NaFe_{1/4}Mn_{1/4}Co_{1/4}Ni_{1/4}O_2$ discharged from 4.3 V yielding 580 Wh/kg and 2690 Wh/L [53], the highest yet reported (digitized and shown in Figure 8.1). These are comparable to $LiCoO_2$ vs. Li with 2950 Wh/L.

In the early stages of cathode research, the reversible energy density after 20 cycles or more needs be evaluated for a practical battery material, preferably one which holds up under moisture exposure. The use of Co in Fe-containing materials may be necessary to achieve competitive energy densities comparable to Li-ion systems. The problem of Fe-migration or capacity loss from use of $Fe^{3+} \leftrightarrow Fe^{4+}$ is shown to be a possible factor that adversely affects cycling stability in these systems. Here, the feasibility of selected Fe-

containing binary layered oxides systems is evaluated, with a look into linking ternary systems.

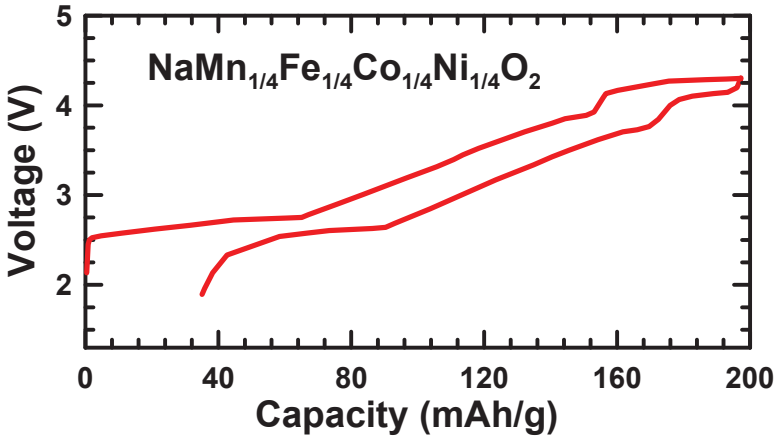

Figure 8.1: Digitized first cycle voltage capacity plot of $NaMn_{1/4}Fe_{1/4}Co_{1/4}Ni_{1/4}O_2$ reported by Li *et al.* [53].

All the data presented in this chapter are original data except for the $NaFe_xNi_{1-x}O_2$ system [33, 57], the $NaFe_x(Ni_{0.5}Mn_{0.5})_{1-x}O_2$ system [35], and $NaFeO_2$ cycled between 2.0-3.8 V [33]. For these samples, capacities were digitized from the literature and the capacity was calculated as a percentage of the first discharge capacity, and the relevant citation is included. Capacity retention of these systematic studies on the basis of percentage capacity retention has not previously been considered.

8.2 ELECTROCHEMISTRY

Figure 8.2 shows the percent capacity retention of $NaFe_xCo_{1-x}O_2$ samples calculated as a percentage of the first discharge capacity for 20 cycles cycled in the 1.5–4.0 V range. There is a deterioration in capacity retention and energy density as Fe is added. Capacity

retention for the $NaFe_{0.4}Co_{0.6}O_2$ material is the best performing cathode presented in this work on the basis of capacity retention. Activation of the $Fe^{3+} \rightarrow Fe^{4+}$ redox couple has been measured directly and quadrupole splittings and centre shifts in this material were found to be abnormally low, similar to those found for tetrahedral Fe^{3+}, as will be discussed.

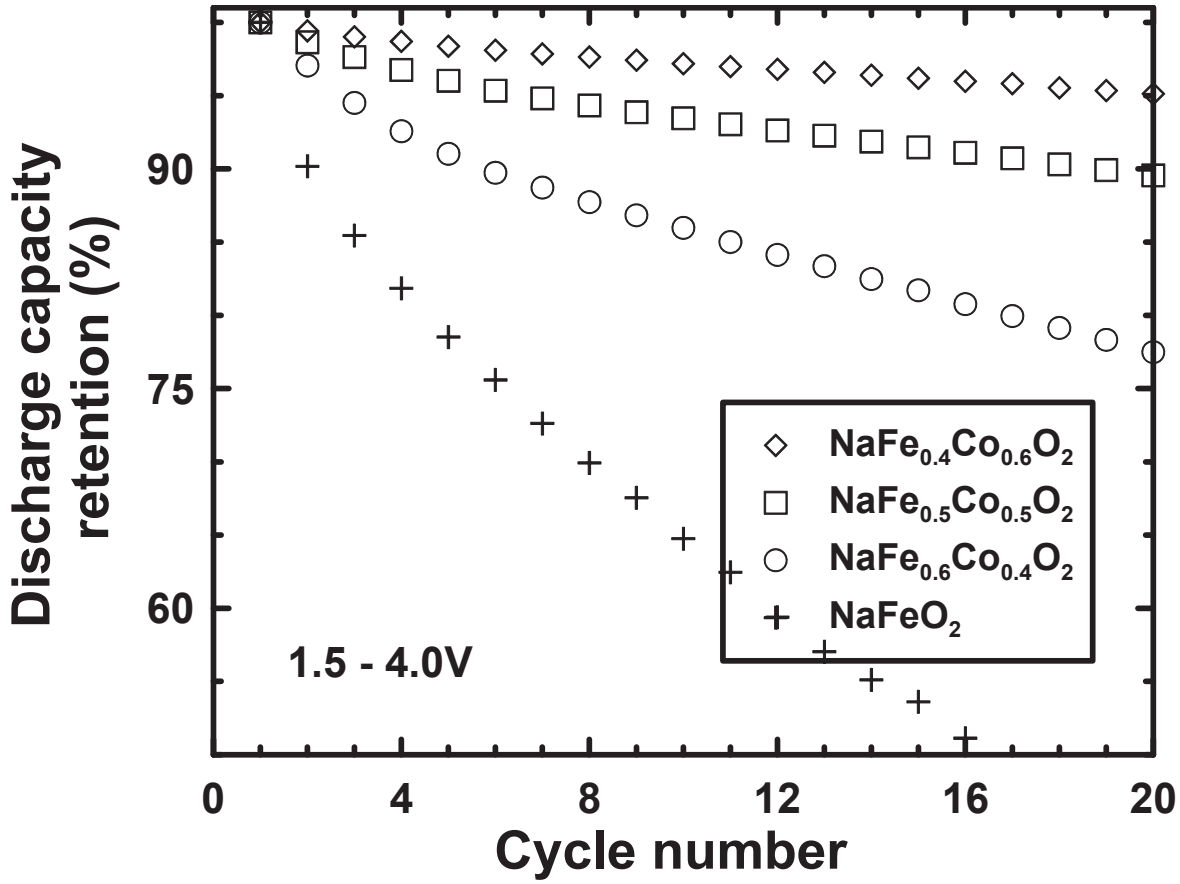

Figure 8.2: Percent discharge capacity retention vs. cycle number of various $NaFe_xCo_{1-x}O_2$ cycled in the 1.5-4.0 V range.

Figure 8.3 shows a comparison of the percentage capacity retention vs. cycle number for the $NaFe_{0.5}Co_{0.5}O_2$ presented here. Slightly more hysteresis is calculated compared to Kubota *et al.* [59], and roughly 5% less capacity is observed during the initial desodiation

plateau. This is likely indicative of minimal damage due to trace moisture exposure and/or slight Na loss during annealing in this work. However, cycling performance is virtually indistinguishable from Yoshida *et al.* [31], which does not appear to be affected by use of a 2.0 V cutoff potential vs. 1.5 V used here and different electrolyte purity. The cycling performance of the $NaFe_{0.4}Co_{0.6}O_2$ presented in this work exceeds that of the $NaFe_{0.5}Co_{0.5}O_2$ previously reported, despite claims that improved cycling performance is not achieved with the use of less Fe [59].

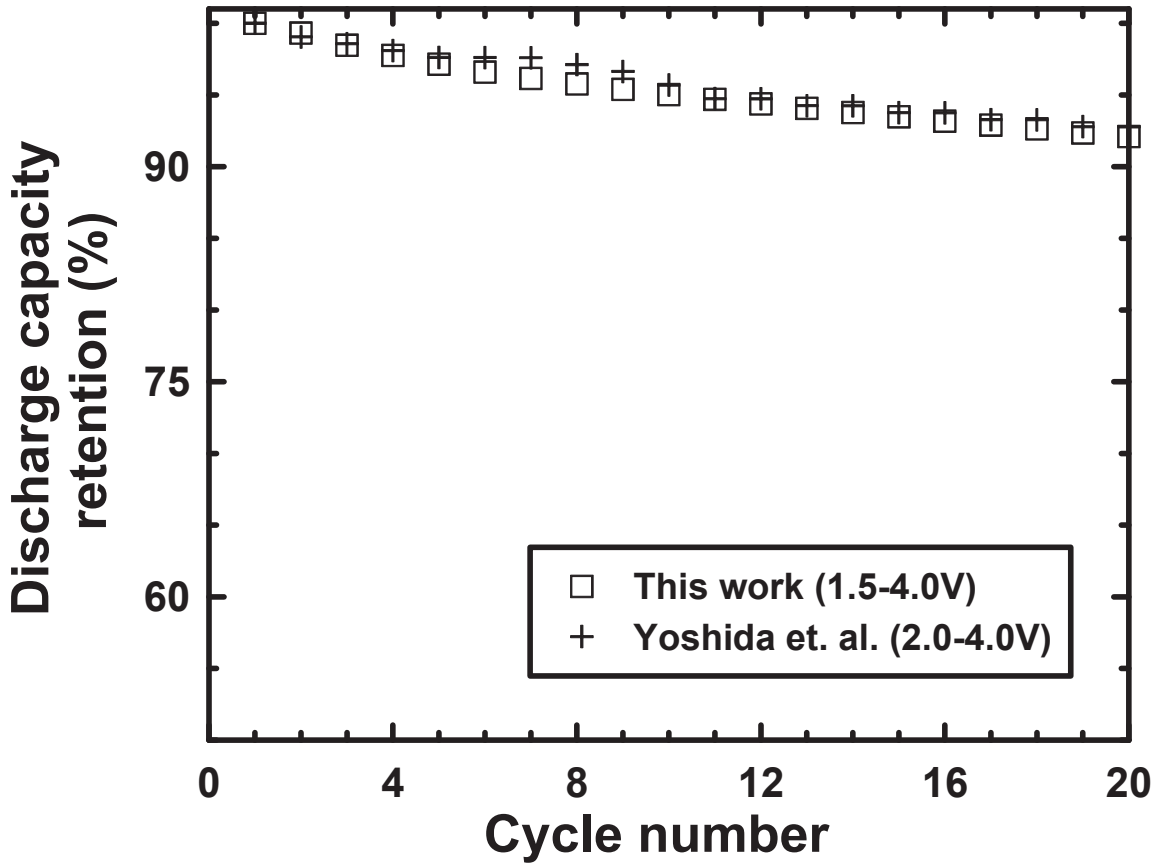

Figure 8.3: percentage discharge capacity retention vs. cycle number for $NaFe_{0.5}Co_{0.5}O_2$ cycled between 1.5-4.0 V in this work compared to $NaFe_{0.5}Co_{0.5}O_2$ digitized from Yoshida *et al.* [31] cycled between 2.0-4.0 V.

A highly symmetric environment for Fe^{4+}, with a limited use of the $Fe^{3+} \rightarrow Fe^{4+}$, may be necessary to maximize cycling performance of Fe-containing layered oxides for Na-ion cathode materials. Of note is a large improvement in capacity, and largely improved capacity retention when comparing the O3- $NaCoO_2$ [31] to O3- $NaCo_{0.4}Fe_{0.6}O_2$ presented here and elsewhere [59]. The optimal ratio of Co and Fe has yet to be determined and is most likely between $0.2 \leq x \leq 0.4$ in $NaFe_xCo_{1-x}O_2$, as is evidenced by the exceptional capacity retention observed in the $NaFe_{0.4}Co_{0.6}O_2$ sample.

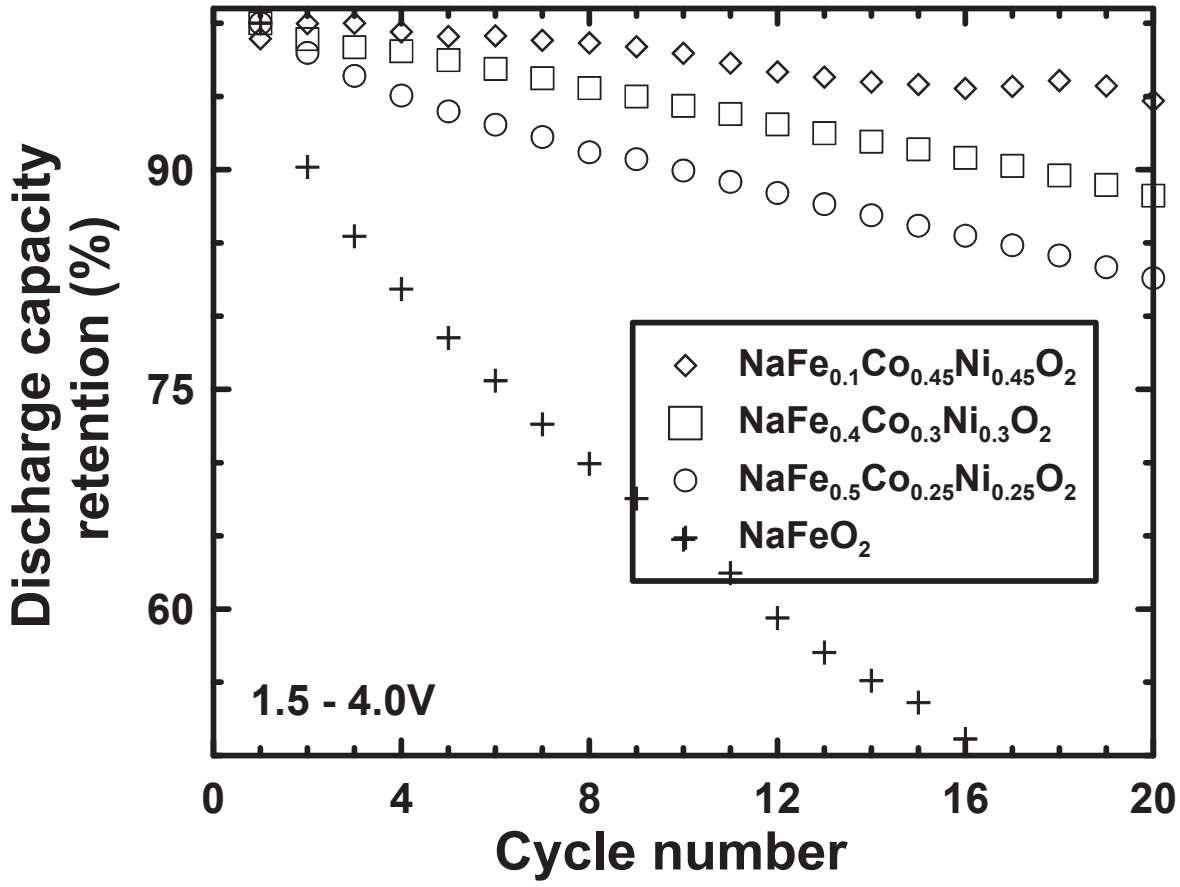

Figure 8.4: Percentage discharge capacity retention vs. cycle number for various $NaFe_x(Co_{0.5}Ni_{0.5})_{1-x}O_2$ samples cycled in the 1.5-4.0 V range.

When Ni^{3+} is used in place of Co^{3+} in the starting material, initial studies have revealed the optimal amount of Fe that maximizes cycling performance is reduced in comparison to binary $NaFe_xCo_{1-x}O_2$. Figure 8.4 shows a comparison of the cycling performance of $NaFe_x(Co_{0.5}Ni_{0.5})_{1-x}O_2$ samples calculated on a percentage basis. In this work, the capacity retention was shown to be optimized for $NaFe_{0.1}(Co_{0.5}Ni_{0.5})_{0.9}O_2$, which yields the same 95% capacity retention as the $NaFe_{0.4}Co_{0.6}O_2$. When x is increased in $NaFe_x(Co_{0.5}Ni_{0.5})_{1-x}O_2$ above 0.1, the resulting increase in energy density is at the cost of capacity retention. Capacity retention is similar for x = 0.2, 0.3 and 0.4 samples, but the energy density is largely increased in this range, indicating there are other possible sources of capacity fade in addition to the possibility of capacity fade resulting from use of $Fe^{3+} \leftrightarrow Fe^{4+}$. Mössbauer spectra indicate a substantial increase in the quadrupole splittings of the Fe^{3+} and Fe^{4+} sites in the charged materials when Ni is used in place of Co, as will be discussed.

Excellent capacity retention is seen in monoclinic $NaNiO_2$ cycled to 3.75 V [57] having 95% capacity retention. Addition of Fe to this system results in a two phase region between x = 0.14 and x = 0.20. Monoclinic $NaNiO_2$ and $NaFe_{0.14}Ni_{0.86}O_2$ are extremely hygroscopic and sensitive to the commonly used solvents such as NMP and thus are not practical for cost reduction in battery production. The electrochemistry of monoclinic $NaFe_{0.14}Ni_{0.86}O_2$ and O3- $NaFe_{0.2}Ni_{0.8}O_2$ has not been evaluated.

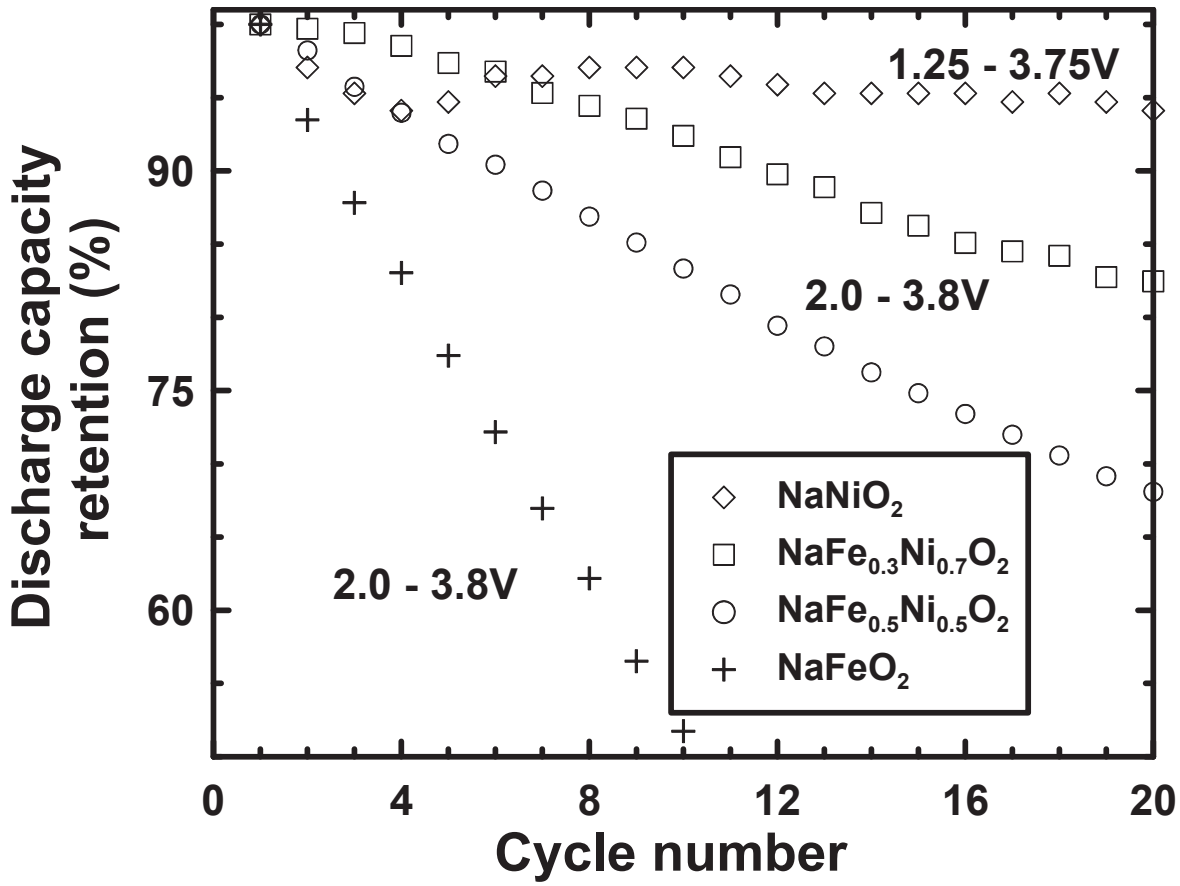

Figure 8.5: Percentage capacity retention as a function of cycle number for $NaFe_xNi_{1-x}O_2$ cycled between 2.0-3.8 V (capacity digitized from Wang *et al.* [33]) and $NaNiO_2$ cycled between 1.25-3.75 V (capacity digitized from Vassilaras *et al.* [57]).

Figure 8.5 shows the capacity retention vs. cycle number for the available $NaFe_xNi_{1-x}O_2$ samples. A rapid deterioration occurs as Fe is added above x = 0.3. It is likely that the optimal composition on the basis of capacity retention in this series is $NaNiO_2$, but this has yet to be confirmed. Addition of Fe to this system causes a decrease in capacity and energy density across the board. Of the transition metals evaluated, Ni^{3+} appears to be the worst performer when combined with Fe.

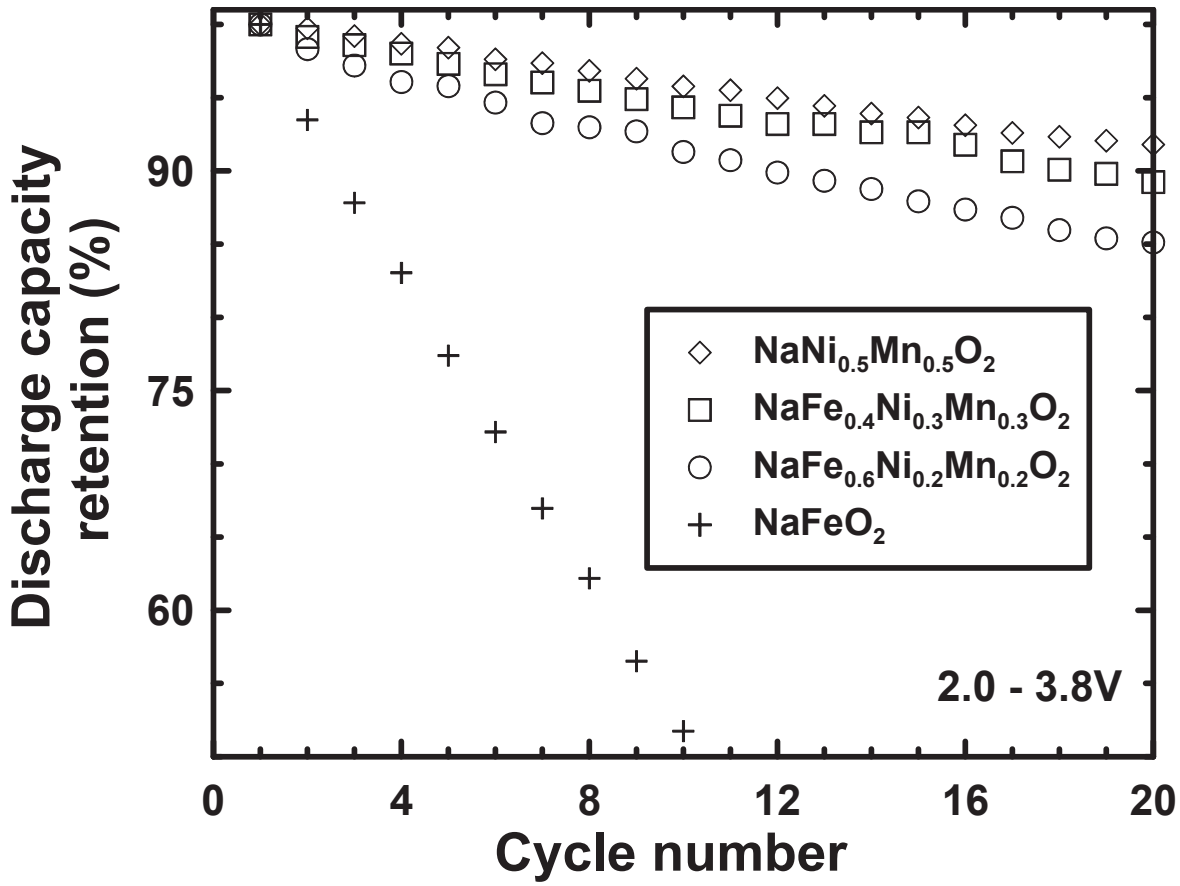

Figure 8.6: Percentage capacity retention as a function of cycle number for various $NaFe_x(Ni_{0.5}Mn_{0.5})_{1-x}O_2$ (capacity digitized from Yabuuchi *et al.* [35]) and $NaFeO_2$ (capacity digitized from Wang *et al.* [33]) cycled between 2.0-3.8 V.

Figure 8.6 shows the calculated capacity retention for the samples in Yabuuchi et. al for the $NaFe_x(Ni_{0.5}Mn_{0.5})_{1-x}O_2$ series when $0 \leq x \leq 1$ [35]. Though limited samples are presented, the $x = 0.4$ sample is said to be optimal in this series. The voltage plateaus are suppressed with the addition of Fe. However, noted is the deterioration in cycling stability and a significant reduction in energy density, which is correlated with access of the Fe^{4+}.

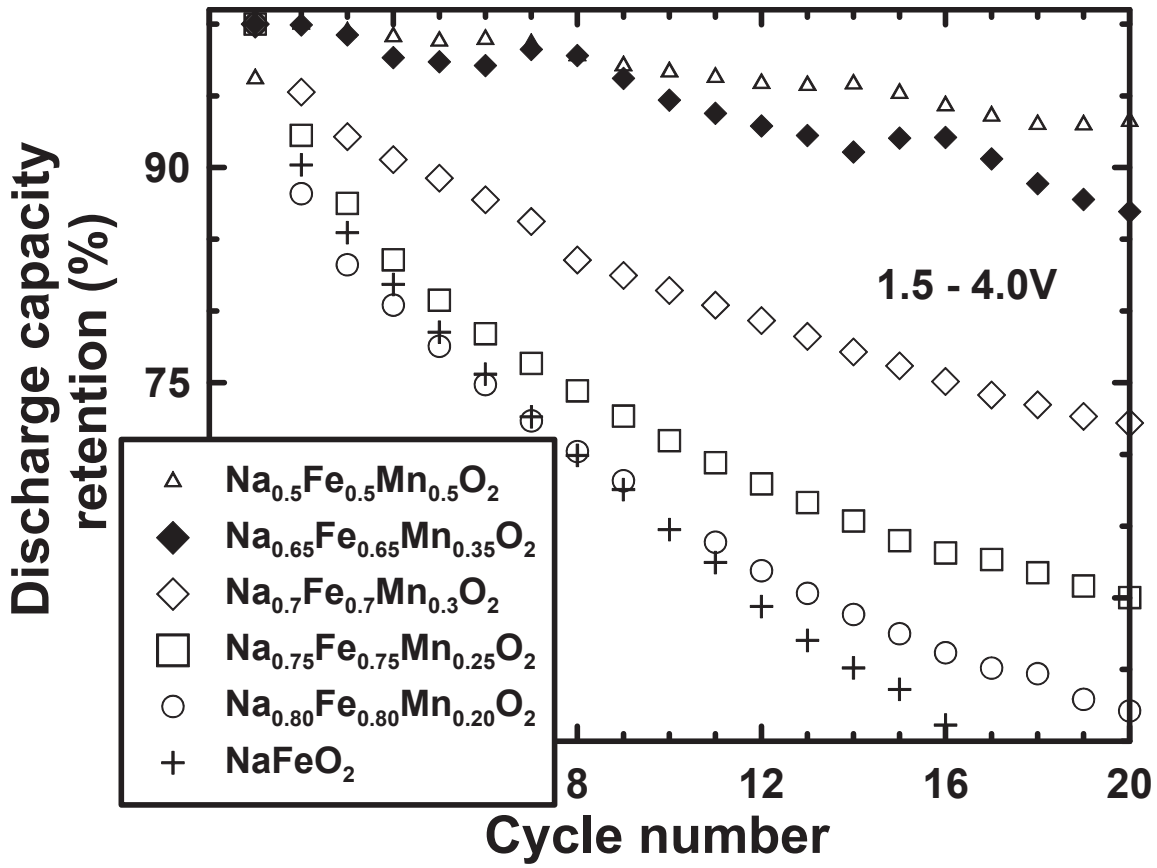

Figure 8.7: Percentage capacity retention vs. cycle number for various $Na_xFe_xMn_{1-x}O_2$ samples.

Figure 8.7 shows the calculated capacity retention for $Na_xFe_xMn_{1-x}O_2$ samples, which have similar electrochemical features to recently reported samples in this system with similar Fe to Mn ratios [26-30]. Results of the current study presented in Figure 8.7 are affected by moisture exposure and may result in slightly increased voltage hysteresis which may have a marginal and increasing effect on other electrochemical properties for samples with higher amounts of Fe. However, it is noted that the cycling performance is not affected and electrochemical features are similar in the 1.5-4.0 V range when comparing samples to the literature [9].

Figure 8.8 shows the percentage capacity retention as a function of cycle number for cells prepared in this work using $Na_{0.5}Fe_{0.5}Mn_{0.5}O_2$ annealed at 700 °C in open air atmosphere for 2 hours in comparison to P2- $Na_{2/3}Fe_{1/2}Mn_{1/2}O_2$ annealed at 900 °C in dry compressed air for 12 hours [9]. This figure shows that the capacity retention of these two samples is similar, suggesting that the different electrolytes and preparation method are not a primary factor in the fading mechanism. A lower capacity retention due to the higher cutoff voltage is seen in comparison to Figure 8.7 for the $Na_{0.5}Fe_{0.5}Mn_{0.5}O_2$ sample. While there is a 10% reduction in reversible capacity when comparing $Na_{0.5}Fe_{0.5}Mn_{0.5}O_2$ to the P2- $Na_{2/3}Fe_{1/2}Mn_{1/2}O_2$ [9] this discrepancy has been previously demonstrated to be due to use of low purity electrolyte and absence of FEC in this work. Therefore, exposure to moisture and CO_2 from handling materials in atmospheric conditions [86] and the differing electrolyte salts appear to have a marginal effect on percentage capacity retention seen in these samples as Mn is increased. Cycling of $Fe^{3+} \leftrightarrow Fe^{4+}$ appears to be associated with capacity fade in this binary system.

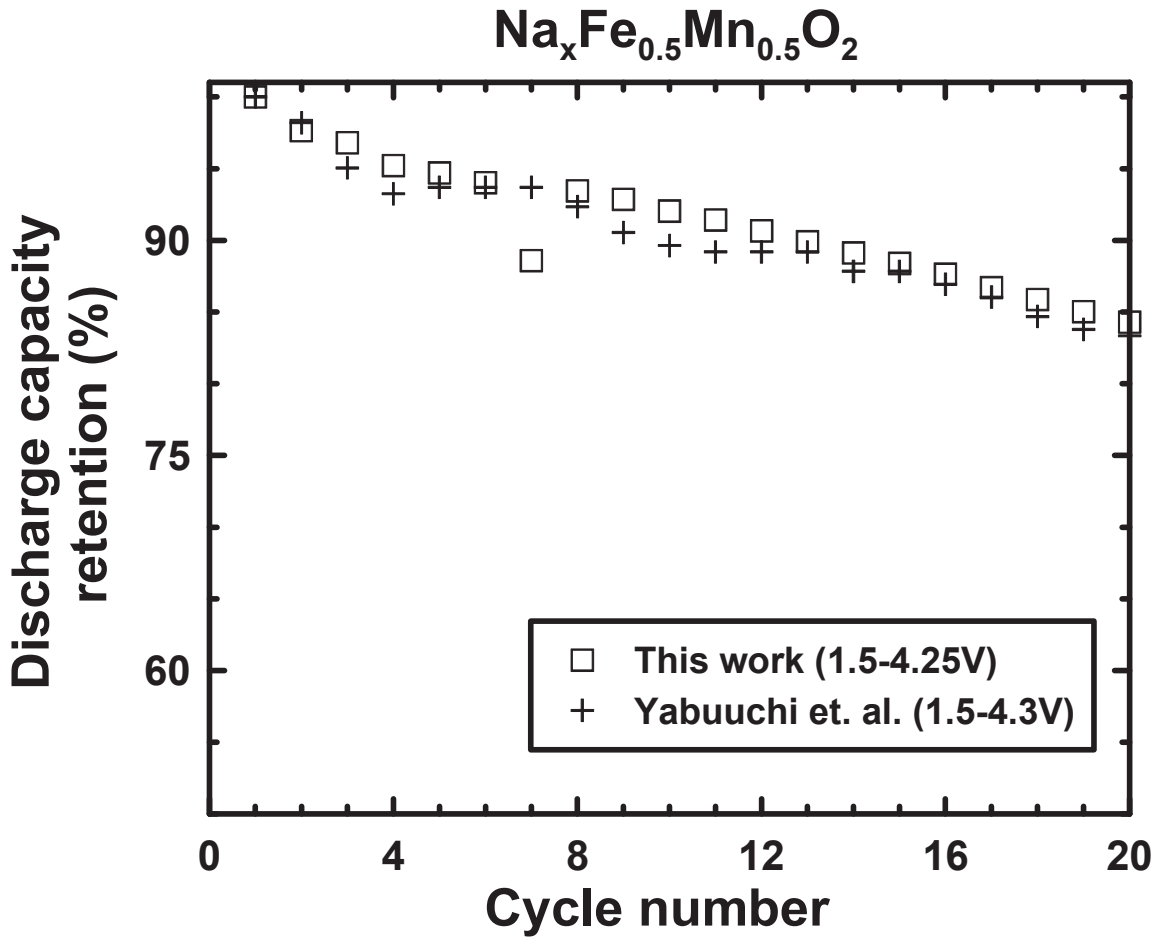

Figure 8.8: Percentage capacity retention vs. cycle number for $Na_{0.5}Fe_{0.5}Mn_{0.5}O_2$ cycled between 1.5-4.25 V using 1M $NaPF_6$ in PC compared to the P2-$Na_{2/3}Fe_{1/2}Mn_{1/2}O_2$ (capacity digitized from Yabuuchi *et al.* [9]) cycled between 1.5-4.3 V using 1M $NaClO_4$ in PC with 2% FEC.

Figure 8.9 shows percentage discharge capacity retention for samples $Na_xFe_{0.5}M_{0.5}O_2$ with M = Fe, Mn, Co, $Co_{0.5}Ni_{0.5}$, and Ni, all of which cycled in the 1.5-4.0 V range except for the M = Ni sample, which was cycled with a 3.8 V cutoff [33]. Of these, the best performing samples are observed to be the M = Mn sample on the basis of capacity retention, followed by Co, $Co_{0.5}Ni_{0.5}$, Ni, and the worst being $NaFeO_2$. Of these, it is

possible that Fe migration observed in $NaFeO_2$ is not eliminated in the M = Ni, $Co_{0.5}Ni_{0.5}$ and Mn systems when $Fe^{3+} \leftrightarrow Fe^{4+}$ is utilized during cycling. The approach in these systems appears to be to synthesize and select the correct upper voltage cutoff such that the presence of Fe^{4+} is eliminated in the charged electrodes.

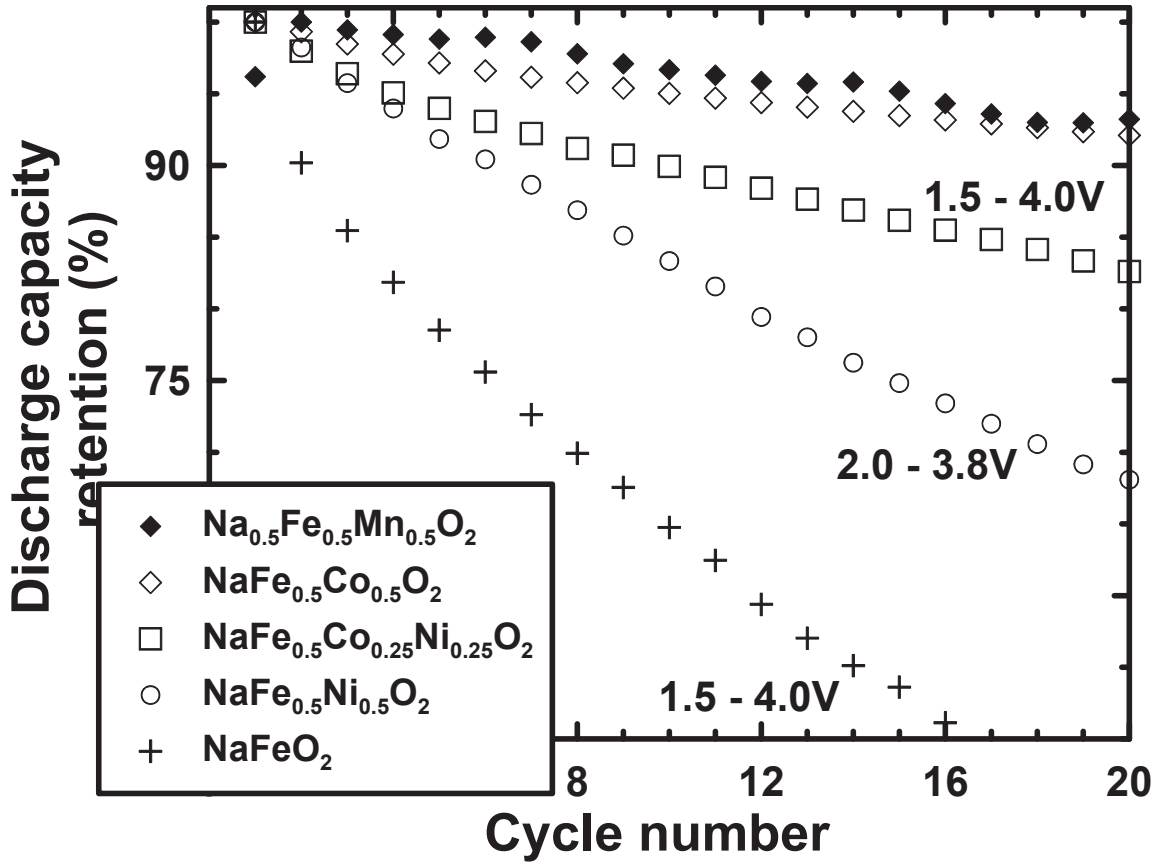

Figure 8.9: Percentage discharge capacity retention vs. cycle number for various $Na_xFe_yM_{1-y}O_2$ cycled in voltage ranges as indicated. Values of capacity of $NaFe_{0.5}Ni_{0.5}O_2$ were digitized from Wang *et al.* [33].

Although the M = Mn system provides the best capacity in this selection, this is resulting from very little use of Fe^{4+} in the $Na_{0.5}Fe_{0.5}Mn_{0.5}O_2$. A strong case has been presented

that activation of Fe^{4+} is a source of capacity fade in the M = Mn series. The next best sample is shown to be the M = Co, which appears to be the most effective for preventing Fe migration into the Na layer. Although capacity retention is less than the M = Mn sample, the M = Co sample boasts a significant amount of Fe^{4+} when charged to 4.0 V, utilizing 50% or more of the available Fe.

Figure 8.10 shows the capacity retention for the $Na_xFe_xTi_{1-x}O_2$ binary series. Capacity from the $Fe^{3+} \leftrightarrow Fe^{4+}$ redox couple is shown to rapidly deteriorate until the all of the reversible capacity is due to access of the $Ti^{3+} \leftrightarrow Ti^{4+}$ redox couple. The high voltage $Fe^{3+} \rightarrow Fe^{4+}$ deintercalation plateau is shown to rapidly diminish in the selected voltage ranges. As can be seen in the $Na_{0.75}Fe_{0.75}Ti_{0.25}O_2$ sample, the shape of the voltage curve becomes constant as the sample is cycled (presented in Chapter 5). In later cycles in the $Na_{0.8}Fe_{0.8}Ti_{0.2}O_2$ (cycle 13 and higher), a similar shaped voltage curve due to the $Ti^{3+} \leftrightarrow Ti^{4+}$ is seen to stabilize. In general, the addition of Ti^{4+} to these samples is less simple than other transition metals, as there appear to be instabilities associated with the presence of Ti at high voltages. A series of two $NaFe_x(Ni_{0.5}Ti_{0.5})_{1-x}O_2$ with x = 0.2 and 0.4 [54] in which the Ti is in the 4+ state and Ni in the 2+ state produces worse capacity retention for the Fe containing materials in comparison to the $NaNi_{0.5}Ti_{0.5}O_2$ [73] but the x = 0.4 sample had better capacity retention. In tests from this work, lower values of x in $Na(Fe_{0.5}Co_{0.5})_xTi_{1-x}O_2$ resulted in worse cycling stability. The increasing use of $Fe^{3+} \rightarrow Fe^{4+}$ oxidation in these Ti containing systems is associated with increasing capacity fade.

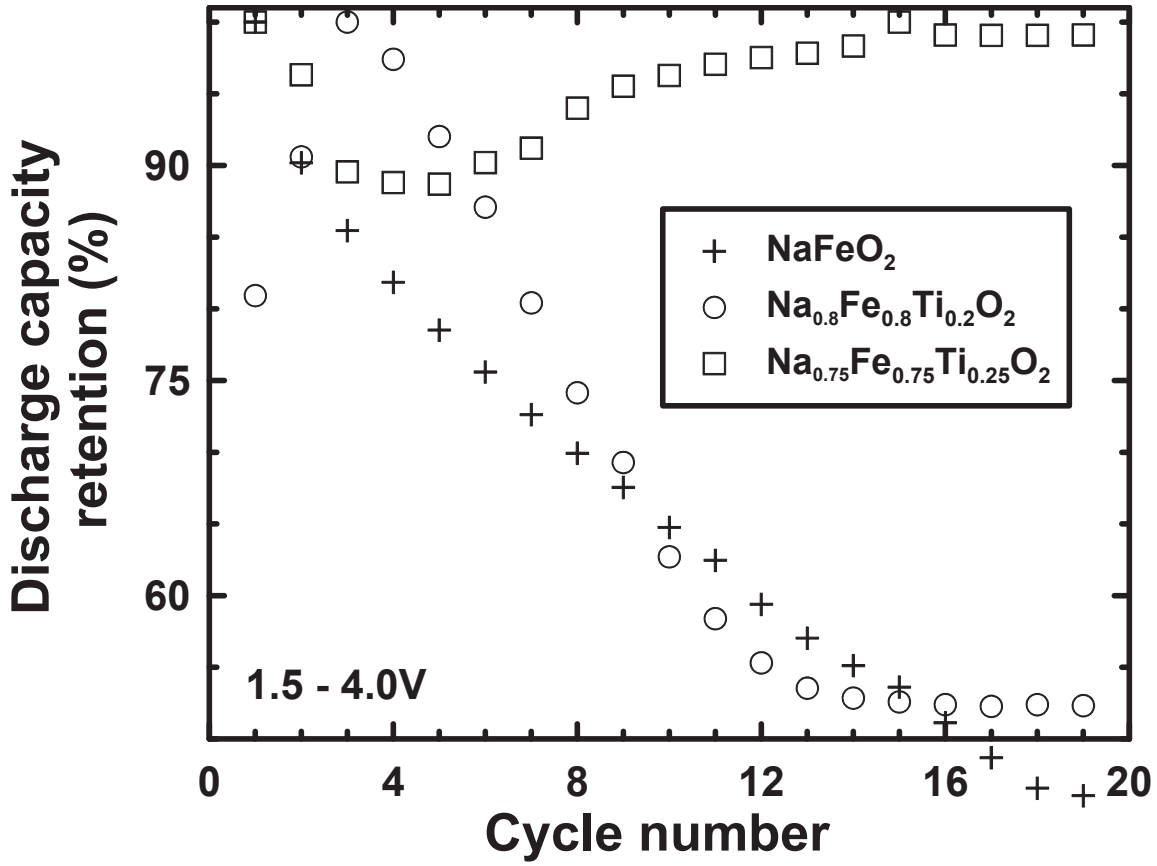

Figure 8.10: Percentage discharge capacity retention vs. cycle number for various $Na_xFe_xTi_{1-x}O_2$ samples using 1M $NaPF_6$.

8.3 CONCLUSIONS

Systematic studies of binary $NaFe_xM_{1-x}O_2$ systems have been evaluated here and in the literature, with M = Sn, Fe, Mn, Ni, Co, and Ti, and the ternary M = $Ni_{0.5}Co_{0.5}$, $Ni_{0.5}Mn_{0.5}$, and $Ni_{0.5}Ti_{0.5}$. The use of Fe^{4+} appears to be a source of capacity fade in samples evaluated thus far. Of the available literature, the best capacity retention, energy density in the mentioned systems is achieved with the $NaFe_{0.4}Co_{0.6}O_2$. In this sample, the $Fe^{3+} \leftrightarrow Fe^{4+}$ redox couple marks a significant portion of the measured capacity. In the

other systems evaluated, the use of the Fe^{4+} is determined to be a source of capacity fade. In the efforts to create a more environmentally sustainable layered Fe-containing sodium cathode material, cost reductions are limited by the necessity of Co in order for competitive energy densities and capacity retention to be achieved. More work is needed on the ternary, quaternary systems in order to evaluate the feasibility of elimination or minimization of the $Fe^{3+} \leftrightarrow Fe^{4+}$ in Fe-containing layered cathodes, or by use of Co to stabilize Fe ions in the transition metal layer when large numbers of vacancies are present. It is possible that Na-vacancy ordering induced by Co substitution is helpful to prevent Fe migration in to the Na layer from occurring. More experiments are necessary to confirm this mechanism.

CHAPTER 9 CONCLUSIONS AND FUTURE WORK

More work is necessary to evaluate the feasibility of Fe-containing layered cathodes for Na-ion batteries. Large portions of the ternary or quaternary systems using the aforementioned transition metals have not been explored. The preceding offers a guide to further optimization of Fe-containing cathodes. Spaces in between the binary solid solution series mentioned here where use of $Fe^{3+} \leftrightarrow Fe^{4+}$ can be eliminated, or reduced with use of Co, can be further optimized. It is likely that the binary $NaFe_xNi_{1-x}O_2$ is unfeasible due to poor performance and extreme sensitivity to the environment, and the binary $NaFe_xMn_{1-x}O_2$ has limited energy density by use of the $Mn^{3+} \leftrightarrow Mn^{4+}$ and/or $Fe^{2+} \leftrightarrow Fe^{3+}$ couples. This can be followed by exploration of the ternary or quaternary systems.

In the quaternary systems, it is advisable to explore those phases where use of lower voltage $Mn^{3+} \leftrightarrow Mn^{4+}$ or $Ti^{3+} \leftrightarrow Ti^{4+}$ is avoided during cycling. This can be achieved by use of Ni, where the ratio is chosen such that Ni^{2+} and Mn^{4+} and/or Ti^{4+} are used in the starting material. The use of active Fe^{4+} should be eliminated, or alternatively used in small amounts when coupled with Co. This approach, or the coupling of Ni^{2+} with Co^{3+} and Fe^{3+} in quaternary or higher order systems has yet to be reported thoroughly in systematic studies. Additionally, it is possible that Fe-containing layered oxides are more reactive with the chosen electrolytes, or might be related to the deterioration of Na foil. Though, varying the electrode loading by 20% or more with the same samples did not appear to alter the mechanism of capacity fade, suggesting Na foil deterioration may not

be a primary factor in the observed differences. Na foil deterioration is still a possible contributing factor even with the use of FEC in half cells from the standpoint of the coulombic efficiency [51]. Further investigation using full cells are necessary to determine if the $Fe^{3+} \leftrightarrow Fe^{4+}$ couple is commercially feasible in this class of material. It is conceivable that a cost reduction can be achieved with an Fe and Co containing cathode in a ternary or quaternary mixture. This is due to the relatively good combination of capacity retention (which still must be evaluated and improved in full cells) low hysteresis and high energy density in a relatively narrow voltage window which are comparable to Li-ion systems. Studies on new electrolytes are necessary.

In the preceding, Fe-containing layered phases O3- $Na_xFe_xMn_{1-x}O_2$, O3- $Na_xFe_xSn_{1-x}O_2$, O3- $NaFe_x(Co_{0.5}Ni_{0.5})_{1-x}O_2$, and the ternary system with flagship P2- $Na_{2/3}Fe_{1/3}Mn_{1/3}Co_{1/3}O_2$ were synthesized, characterized and reported, among others. Substantial progress has been made toward the feasibility of Fe-containing layered oxides for use in Na-ion battery positive electrodes and directions are suggested for future work.

A new model has been presented which suggests that the positions of Na^+ ions or vacancies in the Na layer is a decisive factor in the quadrupole splitting (electronic symmetry) of the Fe^{3+} environments. Samples with worse capacity retention are correlated to Fe^{3+} sites with higher quadrupole splittings, and high values of the parameter β which was introduced in Chapter 4. Furthermore, the quadrupole splitting of electrochemically induced Fe^{4+} is a decisive factor. The sample where the lowest values of quadrupole splittings were identified was the best performer on the basis of capacity

retention and energy density among those evaluated. It is feasible that Co influences the Na-ion positions during deintercalation in a favourable way that stabilizes the chemical environment of the Fe in the presence of a large number of vacancies, even during cycling of the $Fe^{3+} \leftrightarrow Fe^{4+}$ redox couple. In Na_xCoO_2, voltage plateaus result from abrupt changes in Na-ordering in the layered phases [19, 102]. One possible direction for Fe-containing layered cathodes is to determine the location of the Na-ions of the deintercalated phase in $NaFe_yCo_{1-y}O_2$ samples, and determine how they relate to the quadrupole splittings of the Fe^{3+} and Fe^{4+} sites discussed here. It is possible that the positions of the Na atoms relative to the Fe^{3+} and Fe^{4+} sites is key to good cycling performance and high energy density with use of the $Fe^{3+} \leftrightarrow Fe^{4+}$ redox couple.

REFERENCES

[1] G.H. Newman and L.P. Klemann. *J. Electrochem. Soc.***127** (1980) 2097-2099.

[2] K.M. Abraham. *Solid State Ion.***7** (1982) 199-212.

[3] C. Delmas, J.J. Braconnier, C. Fouassier and P. Hagenmuller. *Solid State Ion.* **3-4** (1981) 165-169.

[4] K. Mizushima, P.C. Jones, P.J. Wiseman and J.B. Goodenough. *Mat. Res. Bull.* **15** (1980) 783-789.

[5] R. Yazami and P. Touzain. *J. Power Sources* **9** (1983) 365-371.

[6] M.M. Thackeray, W.I.F. David, P.G. Bruce, and J.B. Goodenough. *Mat. Res. Bull.* **18** (1983) 461-472.

[7] Y. Akira, S. Kenichi and N. Takayuki. US patent #4668595 (1985).

[8] Z. Lu, D.D. MacNeil and J.R. Dahn. *Electrochem. Solid State Lett.* **4** (2001) A191-A194.

[9] N. Yabuuchi, M. Kajiyama, J. Iwatate, H. Nishikawa, S. Hitomi, R. Okuyama, R. Usui, Y. Yamada and S. Komaba, *Nature Materials*, **11** (2012) 512-517.

[10] N. Yabuuchi and S. Komaba. *Sci. Techol. Adv. Mater.* **15** (2014) 043501.

[11] S. Okada and J. Yamaki. *Lithium Ion Rechargeable Batteries*, WILEY-VCH Verlag GmbH & Co. KGaA, Weinheim (2009).

[12] S. Komaba, C. Takei, T. Nakayama, A. Ogata and N. Yabuuchi, *Electrochem. Comm.* **12** (2010) 355-358.

[13] S. Komaba, N. Yabuuchi, T. Nakayama, A. Ogata, T. Ishikawa, and I. Nakai. *Inorg. Chem.* **51** (2012) 6211-6220.

[14] C. Didier, M. Guignard, C. Denage, O. Szajwaj, S. Ito, I. Saadoune, J. Darriet, and C. Delmas, *Electrochem. Solid-State Lett.*, **14** (2011) A75-A78.

[15] D. Kim, E. Lee, M. Slater, W. Lu, S. Rood, and C.S. Johnson, *Electrochem. Comm.* **18** (2012) 66-69.

[16] X. Ma, H. Chen and G. Ceder, *J. Electrochem. Soc.* **158** (2011) A1307-A1312.

[17] C. Delmas, J.-J. Braconnier, C. Fouassier and P. Hagenmuller, *Solid State Ion.* **3-4** (1981) 165-169.

[18] H. Pan, Y.-S. Hu and L. Chen. *Energy Environ. Sci.* **6** (2013) 2338-2360.

[19] R. Berthelot, D. Carlier and C. Delmas. *Nature Mat.* **10** (2011) 74-80.

[20] M. D'Arienzo, R. Ruffo, R. Scotti, F. Morazzoni, C.M. Mari, and S. Polizzi. *Phys. Chem. Chem. Phys.* **14** (2012) 5945-5952.

[21] J. J. Ding, Y.N. Zhou, Q. Sun, X.Q. Yu, X.Q. Yang, and Z.W. Fu, *Electrochimica Acta* **87** (2013) 388-393.

[22] J.M. Paulsen and J.R. Dahn. *Solid State Ionics.* **126** (1999) 3-24.

[23] D. Carlier, J. H. Cheng, R. Berthelot, M. Guigard, M. Yoncheva, R. Stoyanova, B. J. Hwang and C. Delmas. *Dalton Trans.* **40** (2011) 9306-9312.

[24] X. Wang, M. Tamaru, M. Okubo and A. Yamada. *J. Phys. Chem. C.* **117** (2013) 15545-15551.

[25] J. Cheng, C. Pan, J. Lee, J. Chen, M. Guignard, C. Delmas, D. Carlier and B. Hwang. *Chem. Mater.* **26** (2014) 1219-1225.

[26] N. Yabuuchi, J. Iwatate, M. Kajiyama, Y. Yamamoto, S. Hitomi, R. Okuyama and S. Komaba, *220th ECS Meeting* (2011) Abstract #649.

[27] J.S. Thorne, R.A. Dunlap and M.N. Obrovac. *J. Electrochem. Soc.* **160** (2013) A361-A367.

[28] M. Sendova-Vassileva, R. Stoyanova, D. Carlier, M. Yoncheva, E. Zhecheva and C. Delmas. *Adv. Sci. Tech.* **74** (2010) 60-65.

[29] B. M. de Boisse, D. Carlier, M. Guignard and C. Delmas. *J. Electrochem. Soc.* **160** (2013) A569-A574.

[30] J. Zhao, J. Xu, D.H. Lee, Y.S. Meng and S. Okada, *224th ECS meeting* (2013) Abstract #553.

[31] H. Yoshida, N. Yabuuchi, and S. Komaba. *Electrochem. Comm.* **34** (2013) 60-63.

[32] S. Okada, Y. Takahashi, T. Kiyabu, T. Doi, J. Yamaki and T. Nishida. *210th ECS meeting* (2006) Abstract #201.

[33] X. Wang, G. Liu, T. Iwao, M. Okubo and A. Yamada. *J. Phys. Chem. C.* **118** (2014) 2970-2976.

[34] P. Vassilaras, A.J. Toumar, G. Ceder. *Electrochem, Comm.* **38** (2014) 79-81.

[35] N. Yabuuchi, M. Yano, H. Yoshida, S. Kuze and S. Komaba. *J. Electrochem. Soc.* **160** (2013) A3131-A3137.

[36] D. Yuan, X. Hu, J. Qian, F. Pei, F. Wu, R. Mao, X. Ai, H. Yang, Y. Cao. *Electrochimica Acta.* **116** (2014) 300-305.

[37] S.-M. Oh, S.-T. Myung, C.S. Yoon, J. Lu, J. Hassoun, B. Scrosati, K. Amine and Y.-K. Sun. *Nano Lett.* **14** (2014) 1620-1626.

[38] M. Kajiyama, N. Yabuuchi, J. Iwatate and S. Komaba, *PRiME* (2012) Abstract #126.

[39] D. Zhou, M. Slater, D. Kim, E. Lee, J. Jorne, and C.S. Johnson. *224th ECS meeting* (2013) Abstract #487.

[40] J. Billaud, G. Singh, A. R. Armstrong, E. Gonzalo, V. Roddatis, M. Armand, T. Rojo, and P. G. Bruce. *Energy Environ. Sci.* **7** (2014) 1387-1391.

[41] H. Yu, S. Guo, Y. Zhu, M. Ishida and H. Zhou. *Chem. Comm.* **50** (2014) 457-459.

[42] H. Yoshida, N. Yabuuchi, K. Kubota, I. Ikeuchi, A. Garsuch, M. Schulz-Dobrick and S. Komaba. *Chem. Comm.* **50** (2014) 3677-3680.

[43] N. Yabuuchi, J. Iwatate, M. Kajiyama, Y. Yamamoto, S. Hitomi, R. Okuyama and S. Komaba, *220th ECS Meeting* (2011) Abstract #649.

[44] J. Zhao, J. Xu, D.H. Lee, Y.S. Meng and S. Okada, *224th ECS Meeting* (2013) Abstract #553.

[45] S. Okada, Y. Takahashi, T. Kiyabu, T. Doi, J. Yamaki and T. Nishida. *210th ECS Meeting* (2006) Abstract #201.

[46] E. Talaie, V. Duffort, H.L. Smith, B. Fultz, and L.F. Nazar. *Energy Environ. Sci.* **8** (2015) 2512-2523.

[47] R. Fielden and M. N. Obrovac. *J. Electrochem. Soc.* **161** (2014) A1158-A1163.

[48] R. Shanmugam and W. Lei. *ECS Electrochem. Lett.* **3** (2014) A23-A25.

[49] G. Singh, F. Arguesse, L. Otaegui, E. Goikolea, E. Gonzalo, J. Segalini and T. Rojo. *J. Power Sources* **273** (2014) 333-339.

[50] S. Komaba, T. Ishikawa, N. Yabuuchi, W. Murata, A. Ito, and Y Ohsawa. *ACS Appl. Mater. Interfaces* **3** (2011) 4165-4168.

[51] T.D. Hatchard and M.N. Obrovac, *J. Electrochem. Soc.* **161** (2014) A1748-A1752.

[52] X. Sun, Y. Jin, C.-Y. Zhang, J.-W. Wen, Y. Shao, Y. Zang and C.-H. Chen. *J. Mater. Chem. A*. **2** (2014) 17268-17271.

[53] X. Li, D. Wu, Y.-N. Zhou, L. Liu, X.-Q. Yang, and G. Ceder. *Electrochem. Comm.* **49** (2014) 51-54.

[54] J.S. Thorne, S. Chowdhury, R.A. Dunlap and M. N. Obrovac. *J. Electrochem. Soc.* **161** *(*2014) A1801-A1805.

[55] D. Wu, X. Li, B. Xu, N. Twu, L. Liu and G. Ceder. *Energy Environ. Sci.* **8** (2015) 195-202.

[56] N. Yabuuchi, H. Yoshida and S. Komaba. *Electrochemistry* **80** (2012) 716-719.

[57] P. Vassilaras, X. Ma, X. Li, and G. Ceder. *J. Electrochem. Soc.* **160** (2013) A207-A211.

[58] J.S. Thorne, S. Chowdhury, R.A. Dunlap and M.N. Obrovac. *224th ECS Meeting* (2013) Abstract #1232.

[59] K. Kubota, H. Yoshida, N. Yabuuchi, H. Shiiba, M. Nakayama and S. Komaba. *226th ECS Meeting* (2014) Abstract #151.

[60] J.S. Thorne, R.A. Dunlap and M.N. Obrovac. *J. Electrochem. Soc.* **161** (2014) A2232-A2236.

[61] C. Li, A. Reid and S. Saunders, *J. Solid State Chem.*, **3** (1971) 614-620.

[62] C. Kittel, *Introduction to Solid State Physics*, 5th Edition. New York. (John Wiley & Sons, Inc., 1976).

[64] H.M. Rietveld. *J. Appl. Crystallogr.* **2** (1969) 65.

[65] H.M. Rietveld. *Acta Crystallogr.* **22** (1967) 151.

[66] B. Hunter. *International Union of Crystallography Commission on Powder Diffraction Newsletter* **20** (1998).

[67] Richard B. Firestone, *Table of Isotopes, 8th Edition* (Wiley-Interscience, 1996).

[68] N.N. Greenwood and T.C. Gibb. *Mössbauer Spectroscopy*. Chapman and Hall

Ltd., London. (1971).

[69] http://www.rsc.org/membership/networking/interestgroups/mossbauerspect/intro.asp

[70] P. A. Flinn, G. K. Shenoy and F. E.Wagner (eds), *Mössbauer Isomer Shifts*, North-Holland, Amsterdam, (1978).

[71] Y. Takeda, K. Nakahara, M. Nishijima, N. Imanishi and O. Yamamoto, *Mat. Res. Bull.*, **29** (1994) 659-666.

[72] Z. Homonnay, E. Kuzmann, Z. Németh, Z. Klenscár, S. I. Nagy, and A. Vértes. *Ceramics* **4** (2004) 197-205

[73] G. Shirane, D.E. Cox and S.L. Ruby, *Phys. Rev.* **125** (1962) 1158.

[74] W. Ross McKinnon. "Physical Mechanisms of Intercalation Batteries." Ph.D. thesis. University of British Colombia (1979).

[75] C. Delmas, C. Fouassier, P. Hagenmuller. *Physica B+C*, **99** (1980) 81-85.

[76] Y. Takeda, J. Akagi, A. Edagawa, M. Inagaki, and S. Naka. *Mat. Res. Bull.* **15** (1980) 1167-1172.

[77] K. Kubota, I. Ikeuchi, T. Nakayama, C. Takei, N. Yabuuchi, H. Shiiba, M. Nakayama, and S. Komaba. *J. Phys. Chem. C.*, **119** (2015) 166-175.

[78] A. J. Smith, J.C. Burns, D. Xiong and J.R. Dahn. *J. Electrochem. Soc.* **158** (2011) A1136-A1142.

[79] http://en.wikipedia.org/wiki/Crystal_field_theory (accessed April 30th, 2015)

[80] X. Li, X. Ma, D. Su, L. Liu, R. Chisnell, S.P. Ong, H. Chen, A. Toumar, J.-C. Idrobo, Y. Lei, J. Bai, F. Wang, J.W. Lynn, Y.S. Lee, and G. Ceder, *Nature Mat.* **13** (2014) 586-592

[81] J.M. Paulsen and J.R. Dahn. *Solid State Ionics* **126** (1999) 3-24.

[82] S. Kikkawa, S. Miyazaki and M. Koizumi. *Mat. Res. Bull.*, **20** (1985) 373-377.

[83] S. Okada, Y. Takahashi, T. Kiyabu, T. Doi, J. Yamaki and T. Nishida, *ECS Meeting Abstr.* **602** (2006) 201.

[84] M. Richard, "The Behaviour of Lithium and Sodium Iron Oxides as Cathode Materials for Lithium Ion Batteries." B.Sc. thesis. University of New Brunswick, Fredericton (1994).

[85] Y. Takeda, J. Akagi, A. Edagawa, M. Inagaki, and S. Naka. *Mat. Res. Bull.* **15** (1980) 1167-1172.

[86] V. Duffort, E. Talaie, R. Black, and L.F. Nazar. *Chem. Mater.* (2015) DOI: 10.1021/acs.chemmater.5b00097.

[87] Z. Chen, Z. Lu and J.R. Dahn. *J. Electrochem. Soc.* **149** (2002) A1604-A1609.

[88] J.S. Thorne, R.A. Dunlap and M.N. Obrovac. *PRiME* (2012) Abstract #1835.

[89] E. Gonzalo, M. H. Han, J.M. López del Amo, B. Acebedo, M. Casas-Cabanas, and T. Rojo. *J. Mat. Chem. A.* **2** (2014) 18523-18530.

[90] M. Guignard, C. Didier, J. Darriet, P. Bordet, E. Elkaïm and C. Delmas. *Nature Mat.* **12** (2013) 74-80.

[91] T. Zheng, W. R. McKinnon, and J. R. Dahn. *J. Electrochem. Soc.* **143** (1996) 2137-2145.

[92] M.A. Al-Maghrabi, J. Suzuki, R. J. Sanderson, V.L. Chevrier, R.A. Dunlap and J.R. Dahn. *J. Electrochem. Soc.* **160** (2013) A1587-A1593.

[93] M. R. Palacin, Y. Chabr, L. Dupont, M. Hervieu, P. Strobel, G. Rousse, C.Masquelier, M. Anne, G.G. Amatucci, and J.M. Tarascon. *J. Electrochem. Soc.* **147** (2000) 845-853.

[94] J. Reed, G. Ceder, and A. Van Der Ven. *Electrochem. Solid-State Lett.* **4** (2001) A78-A81.

[95] I. Saadoune, A. Maazaz, M. Ménétrier, and C. Delmas. *J. Solid State Chem.* **122** (1996) 111-117.

[96] M.H. Han, E. Gonzalo, M. Casas-Cabanas, and T. Rojo. *J. Power Sources* **258** (2014) 266-271.

[97] D. Buchholz, L. G. Chagas, C. Vaalma, L. Wu and S. Passerini. *J. Mater. Chem. A.* **2** (2014) 13415-13421.

[98] G. Prado, A. Rougier, L. Fournès and C. Delmas. *J. Electrochem. Soc.* **147** (2000) 2880-2887.

[99] H. Kobayashi, H. Shigemura, M. Tabuchi, H. Sakaebe, K. Ado, H. Kageyama, A. Hirano, R. Kanno, M. Wakita, S. Morimoto and S. Nasu. *J. Electrochem. Soc.* **147** (2000) 960-969.

[100] G. Prado, L. Fournès, and C. Delmas. *J. Solid State Chem.* **159** (2001) 103-112.

[101] M. Pissas, V. Psycharis, D. Stamopoulos, G. Papavassiliou, Y. Sanakis,and A. Simopoulos. cond-mat/0503662v1 (unpublished, 2005).

[102] L. Viciu, J.W.G. Bos, H.W. Zandbergen, Q. Huang, M.L.Foo, S. Ishiwata, A.P. Ramirez, M. Lee, N.P. Ong and R.J. Cava. *Phys. Rev. B*.**73** (2006).

[103] Y. Shin and A. Manthiram. *Chem. Mater.* **15** (2003) 2954-2961.

[104] M. Sathiya, K. Hemalatha, K. Ramesha, J.-M. Tarascon, and A.S. Prakash. *Chem. Mater.* **24** (2012) 1846-1853.

[105] Y.H. Jung, A.S. Christiansen, R.E. Johnsen, P. Norby, and D. K.. Kim. *Advanced Functional Materials* **25** (2015) 3227-3237.

[106] K. Kubota, N. Yabuuchi, H. Yoshida, M. Dahbi and S. Komaba. *MRS Bulletin.* **39** (2014) 416-422.

[107] D. Buchholz, A. Moretti, R. Klopsch, S. Nowak, V. Siozios, M. Winter and S. Passerini. *Chem. Mater.* **25** (2013) 142-148.